



THE HONG KONG
POLYTECHNIC UNIVERSITY

香港理工大學

Pao Yue-kong Library

包玉剛圖書館

Copyright Undertaking

This thesis is protected by copyright, with all rights reserved.

By reading and using the thesis, the reader understands and agrees to the following terms:

1. The reader will abide by the rules and legal ordinances governing copyright regarding the use of the thesis.
2. The reader will use the thesis for the purpose of research or private study only and not for distribution or further reproduction or any other purpose.
3. The reader agrees to indemnify and hold the University harmless from and against any loss, damage, cost, liability or expenses arising from copyright infringement or unauthorized usage.

IMPORTANT

If you have reasons to believe that any materials in this thesis are deemed not suitable to be distributed in this form, or a copyright owner having difficulty with the material being included in our database, please contact lbsys@polyu.edu.hk providing details. The Library will look into your claim and consider taking remedial action upon receipt of the written requests.

**COMPUTATIONAL AND DIGITAL ANALYSIS OF
YARN FABRICATION, STRUCTURE AND SURFACE
APPEARANCE**

LI SHENGYAN

Ph.D

The Hong Kong Polytechnic University

2016

The Hong Kong Polytechnic University

Institute of Textiles and Clothing

Computational and Digital Analysis of Yarn Fabrication,

Structure and Surface Appearance

LI SHENGYAN

A thesis submitted in partial fulfilment of the
requirements for the degree of **Doctor of Philosophy**

March 2015

CERTIFICATE OF ORIGINALITY

I hereby declare that this thesis is my own work and that, to the best of my knowledge and belief, it reproduces no material previously published or written, nor material that has been accepted for the award of any other degree or diploma, except where due acknowledgement has been made in the text.

_____ (Signed)

_____ **LI Shengyan** (Name of student)

ABSTRACT

Spun yarns are used worldwide for making a broad range of textiles and apparel. With an output of 32.9 million tons in 2009, spun yarns satisfy more than half the needs of the global textiles and clothing industry. The present study is devoted to developing computational and digital methods and systems for the accurate and efficient analysis of three predominant aspects of spun yarns: yarn formation, internal structure and surface appearance.

In this study, a new generalized theoretical model has been developed by using Finite Element Method (FEM) for the theoretical and numerical analysis of yarn formation in spinning triangle. In this proposed model, the initial conditions are formulated together with an algorithm for fiber buckling. Compared with the earlier models, some important parameters ignored previously, such as inclined angle of spinning tension, frictional contact of fibers with bottom roller and fiber torsional strains, are considered. Numerical simulations were then carried out to explore the quantitative relationships between the mechanical performance of ring spinning triangle and various spinning parameters. Further comparison results showed that fiber tensions predicted by the proposed model are in good agreements with earlier models while the calculated torque of yarns is generally closer to experimental measurements.

Moreover, a dynamic model of spinning triangle has been further developed in this study based on the above static FEM model with consideration of the dynamic characteristics of fiber inertia and damping for a more complete and accurate description. By this model, the dynamic behavior of fibers in spinning triangle, such as the natural frequency, mode shape, resonant response, harmonic analysis and response under a time-varying tension, has been originally studied. The results showed that dynamic parameters have a great influence on the amplitude and attenuation of the response of constituent fibers in spinning triangle.

Tracer fiber measurement has been widely used for analysis of yarn internal structure by tracing the fiber path in a transparent liquid. Currently, the image mosaic and segmentation of tracer fiber images largely involve manual operation. It is extremely time-consuming. Therefore, in this study, an intelligent computer method has been developed for automatic mosaic and segmentation of tracer fiber images. In this method, an extended QRS complex detection method is developed for tracer fiber detection. A decision function, integrating several matching functions extracted from tracer fiber and gradient image, is proposed for image mosaic. An objective method is then proposed to evaluate the qualities of image mosaic and segmentation of the proposed method. Fifty series of tracer fiber images (total 872 images) with five different yarn counts (10Ne~60Ne) were prepared and used for a full evaluation of

the proposed image processing method with respect to conventional manual method.

Evaluation results showed that the proposed method works well in mosaic and segmentation for tracer fiber images and presents a much higher efficiency than the conventional method.

For yarn surface evaluation, an intelligent computer method has been developed to analyze yarn blackboard image and objectively evaluate yarn quality using computer vision and artificial intelligence. The evaluation method for yarn surface quality currently in use is mainly based on manual inspection. Although some works have been done on digital yarn analysis in order to resolve the limitations of human visual inspection, none of them can fully imitate human behavior in the inspection of yarn quality on a blackboard according to ASTM D2255 standard. In the proposed method, a multi-scale attention model is proposed and developed, which can fully imitate human attention at different observation distances for the whole and detailed yarn information. A Spectral Residual method is then extended to establish a general benchmark for the comparison among different grade yarns. In the developed system, Fourier transform is employed to separate yarn diameter and hairs, and image conspicuity is obtained by the multi-scale attention model. Total sixteen features, obtained from yarn diameter, hairiness and image conspicuity, are extracted to present the yarn surface characteristics and then used to classify and grade yarn

surface qualities using Probabilistic Neural Network (PNN). Two kinds of PNNs, i.e. global and individual PNNs, and two types of classification, i.e. eight-grade and five-grade classifications, are designed and developed for various yarn quality classification purposes. For the evaluation of the proposed method, a database was constructed with 296 yarn board images, covering eight yarn counts (7Ne~80Ne) and different grades. Experimental results showed that the accuracy for eight- and five-grade global PNNs are 92.23% and 93.58%, respectively, demonstrating a good classification performance of the proposed digital method in yarn surface grading.

Finally, with the above developed computer methods, two intelligent digital systems have been developed for the computerized analysis and evaluation of yarn internal structure and surface appearance, respectively. The systems were designed for controlling and visualizing the whole process of yarn measurement and analysis, covering image acquisition, image processing and data analysis with interactive and user-friendly interface. Both digital systems are potential for application in textile laboratories and spinning mills for yarn structure and surface analyses.

PUBLICATIONS ARISING FROM THE THESIS

Journal Paper:

1. Li SY, Xu BG, Tao XM and Feng J. Numerical Analysis of the Mechanical Behavior of a Ring-spinning Triangle Using the Finite Element Method. Textile Research Journal 81(9): 959-971, 2011.
2. Li SY, Xu BG, Tao XM and Hu H. A Generalized FEM Model for Fiber Structural and Mechanical Performance in Fabrication of Slender Yarn Structures. CMES-Computer Modeling in Engineering & Sciences 77(1): 33-55, 2011.
3. Li SY, Xu BG and Tao XM. Dynamic Modeling and Evaluation for Constituent Fibers in Fabrication of Twisted Flexible Yarns with Consideration of Fiber Mass and Viscoelasticity. Journal of Materials Science 48(3): 1090-1099, 2013.
4. Li SY, Xu BG, Tao XM and Chi ZR. An Intelligent Computer Method for Automatic Mosaic and Segmentation of Tracer Fiber Images for Yarn Structure Analysis. Textile Research Journal 85 (7): 733-750, 2015.

Journal Paper under Preparation:

1. Li SY, Xu BG, Tao XM and Chi ZR. An Intelligent Method and System for Yarn Surface Appearance Grading Based on Digital Blackboard Images. To be submitted to Journal of Electronic Imaging.

Conference Paper:

1. Li SY, Feng J, Xu BG and Tao XM. Integrated Digital System for Yarn Surface Quality Evaluation Using Computer Vision and Artificial Intelligence. The 2012 International Conference on Image Processing, Computer Vision, and Pattern Recognition (WORLDCOMP/ IPCV'12), Las Vegas, USA, 472-476, July 16-19, 2012.
2. Li SY, Xu BG, Tao XM and Chi ZR. A Novel Digital Approach for Automatic and Continuous Image Segmentation of Tracer Fiber Image. Fibers Interfacing the World (Fiber Society Fall 2013 Conference), Clemson, South Carolina, USA, October 23-25, 2013.

ACKNOWLEDGEMENTS

Firstly, I would like to express my deepest gratitude and sincere appreciation to my chief supervisor Dr. Bingang XU, Associate Professor of Institute of Textiles and Clothing, The Hong Kong Polytechnic University, who provides me with his professional and patient guidance, continuous encouragement and constructive criticism throughout this study. He gave me a lot of excellent suggestions and expert advices in research. And his firm support and patience help me to overcome the difficulties encountered.

I would also like to express my deepest appreciation to my co-supervisors Professor Xiaoming TAO and Dr. Zheru CHI for their valuable advices, critical comments and consistent supports during the course of my PhD study.

My grateful thanks are given to my team members, particularly Dr. Jie FENG for his great support and assistance in preparing yarn samples and grading yarn surface appearance and great care in daily life, Dr. Ying GUO for her great support and assistance in the sample preparation and image acquisition of tracer fiber measurement and great care in daily life, Dr. Huifen GUO and Mr. Jianliang GONG for their great supports.

My sincere thanks are also given to Mr. Waiman CHU for great support in yarn sample preparation and grading surface appearance of yarn samples. My sincere thanks are also given to Dr. Tao HUA for great assistance in theoretical analysis of spinning triangle.

My sincere thanks are given to Mr. K.K. FAN in spinning workshop, Mr. W.K. TAN in dying & finishing lab, Mr. W.K. HO in analytical lab, Ms. M.N. SUN and Mr. K.O. CHOI in the physical lab for their technical support and help.

Many grateful thanks are given to all my friends in Professor Tao's group, Ms. Xinxin HUANG, Mr. Rong YIN, Dr. Qiao LI, Dr. Lin SHU, Dr. Wei ZHENG, Mr. Fei WANG, Mr. Song CHEN, Mr. Xi WANG, Dr. Bao YANG, Ms. Ying LI, Dr. Wei ZENG et al.

Many grateful thanks are given to all my friends in Dr. CHI's group, Dr. Hong FU, Dr. Zhen LIANG, Dr. Zenghai CHEN, Mr. Junkai CHEN and Mr. Yu HU.

Finally, I would like to express my special thanks to my parents for their endless support, understanding and great care during my PhD study.

TABLE OF CONTENTS

TABLE OF CONTENTS	IX
LIST OF TABLES	XVI
LIST OF FIGURES	XVIII
CHAPTER 1 INTRODUCTION.....	1
1.1. Research background	1
1.2. Objectives.....	5
1.3. Significance and originality	6
1.4. Research methodology	9
1.5. Thesis outline	14
CHAPTER 2 LITERATURE REVIEW	17
2.1. Analysis of spinning triangle in yarn fabrication.....	17
2.1.1. Spinning triangle in yarn formation	18
2.1.2. Theoretical analysis of spinning triangle	21
2.1.3. Measurement of fiber performance in spinning triangle.....	32
2.2. Analysis of yarn internal structure	36
2.2.1. Cross section technique.....	36
2.2.2. Tracer fiber technique	37
2.2.2.1. Hi-scope video microscope system.....	39
2.2.2.2. Measurement system based on depth from focus	40
2.2.2.3. Measurement system for two views of yarn by using a mirror.....	41

2.2.3.	Image mosaic	43
2.2.4.	Yarn segmentation.....	46
2.2.4.1.	Optical method.....	47
2.2.4.2.	Image processing method	48
2.2.4.3.	Segmentation of tracer fiber image.....	50
2.3.	Analysis of yarn surface appearance.....	52
2.3.1.	Digital yarn grading methods.....	53
2.3.1.1.	Yarn grading based on 1D continuous measurement.....	53
2.3.1.2.	Yarn grading based on 2D yarn black board.....	58
2.3.2.	Attention model	63
2.3.2.1.	Static attention model	64
2.3.2.2.	Dynamic attention model.....	71
2.4.	Summary	72

**CHAPTER 3 THEORETICAL AND NUMERICAL ANALYSIS OF
MECHANICAL PERFORMANCE OF FIBERS IN SPINNING TRIANGLE
USING FINITE ELEMENT METHOD 75**

3.1.	Introduction.....	75
3.2.	Initial height of spinning triangle.....	77
3.3.	Initial strain of constituent fibers	83
3.4.	Static analysis of spinning triangle	86
3.4.1.	Static modelling using finite element method	86
3.4.1.1.	Governing equations	86
3.4.1.2.	Generation of yarn torque	88
3.4.1.3.	Element selection	90

3.4.1.4.	Boundary conditions	92
3.4.1.5.	Algorithms for fiber buckling	95
3.4.2.	Simulation results for fiber tension distributions	96
3.4.2.1.	Effect of spinning tension	97
3.4.2.2.	Effect of spinning tension angle.....	100
3.4.2.3.	Effect of yarn twist.....	102
3.4.2.4.	Effect of yarn count.....	104
3.4.2.5.	Effect of the frictional contact with bottom roller	105
3.4.3.	Simulation results for fiber torsion distributions	107
3.4.4.	Yarn torque comparison	110
3.5.	Dynamic analysis of spinning triangle.....	112
3.5.1.	Dynamic modelling using finite element method	114
3.5.2.	Modal analysis	118
3.5.3.	Harmonic analysis.....	120
3.5.4.	Resonant response.....	122
3.5.5.	Transient analysis.....	123
3.5.5.1.	Dynamic spinning tension.....	123
3.5.5.2.	Solution methodology	128
3.5.5.3.	Simulation results.....	129
3.5.6.	Fiber tension comparison	130
3.6.	Conclusions	134

CHAPTER 4	INTELLIGENT COMPUTER METHOD AND SYSTEM FOR	
	AUTOMATIC MOSAIC AND SEGMENTATION OF TRACER FIBER	
	IMAGES IN YARN STRUCTURE ANALYSIS.....	137

4.1.	Introduction.....	137
4.2.	Image acquisition.....	139
4.3.	Image mosaic.....	142
4.3.1.	Matching function related to the tracer fiber.....	147
4.3.2.	Matching function related to gradient image.....	158
4.3.3.	Results of the image mosaic.....	160
4.4.	Image segmentation.....	162
4.5.	Quality evaluation of the image mosaic and segmentation.....	168
4.5.1.	Application on a whole series of images.....	168
4.5.2.	Evaluation of the image mosaic.....	171
4.5.3.	Evaluation of the image segmentation.....	174
4.5.4.	Evaluation of efficiency.....	180
4.6.	Experiments.....	181
4.6.1.	Database construction of tracer fiber images.....	181
4.6.2.	Results of the image mosaic.....	185
4.6.3.	Results of the image segmentation.....	190
4.6.4.	3D configuration and structural analysis.....	195
4.7.	System development for image processing of tracer fiber images.....	198
4.7.1.	Video acquisition.....	201
4.7.2.	Image acquisition.....	202
4.7.3.	Image mosaic.....	204
4.7.3.1.	Mosaic of pair images.....	207
4.7.3.2.	Tracer fiber detection.....	211
4.7.4.	Image segmentation.....	214
4.7.5.	Parameter analysis.....	218
4.8.	Conclusions.....	226

CHAPTER 5 INTELLIGENT METHOD AND SYSTEM FOR YARN

SURFACE GRADING BASED ON DIGITAL BLACKBOARD IMAGES.....229

5.1.	Introduction.....	229
5.2.	Methodology	230
5.2.1.	Fourier analysis and filtering	231
5.2.2.	Multi-scale information.....	237
5.2.3.	Extended spectral residual (SR) approach	243
5.2.4.	Attention based on information maximization (AIM model)	245
5.2.5.	Probabilistic Neural Networks (PNNs).....	246
5.3.	Implementation	248
5.3.1.	Segmentation of yarn body and hairs.....	249
5.3.1.1.	Image processing.....	249
5.3.1.2.	Feature extraction.....	254
5.3.2.	Image residual of extended SR model	260
5.3.2.1.	Image processing.....	260
5.3.2.2.	Feature extraction.....	263
5.3.3.	Image conspicuity from multi-scale attention models	265
5.3.3.1.	Image processing.....	265
5.3.3.2.	Feature extraction.....	271
5.3.4.	Database construction of yarn board images	272
5.3.5.	Yarn classification results.....	276
5.3.5.1.	Performance assessment method	276
5.3.5.2.	Eight-grade classification.....	279
5.3.5.3.	Five-grade classification	285
5.4.	Development of yarn grading system	287

5.4.1.	Main interface	287
5.4.2.	Image acquisition and image loading	289
5.4.3.	Image processing	290
5.4.4.	Yarn classification.....	294
5.5.	Conclusions.....	296

CHAPTER 6 CONCLUSIONS AND SUGGESTIONS FOR FUTURE

RESEARCH 299

6.1.	Conclusions.....	299
6.1.1.	Theoretical modeling and numerical simulation of spinning triangle for yarn formation analysis.....	299
6.1.2.	Automatic and efficient processing of tracer fiber images for yarn structure analysis.....	301
6.1.3.	Intelligent and objective evaluation of yarn board images for yarn surface appearance analysis.....	303
6.2.	Limitations of the study and suggestions for future research	307
6.2.1.	Instant measurement of fiber dynamic behavior inside the spinning triangle	307
6.2.2.	Algorithm and measurement optimizations for yarn structural analysis	309
6.2.3.	Development of global yarn database and high-resolution image for precise yarn surface classification	311
6.2.4.	Integration of spinning triangle, yarn internal structure and surface appearance for a better analysis of yarn quality.....	312

APPENDICES 314

Appendix A: Results of the image mosaic and segmentation	314
Appendix B: Evaluation results of the image mosaic	323
Appendix C: Evaluation results of the image segmentation	325
Appendix D: 3D configurations of tracer fiber in yarn.....	327
Appendix E: Time taken and the migration parameters.....	332
Appendix F: Features of yarn board image.....	334
REFERENCES.....	351

LIST OF TABLES

Table 2.1 The attributes and their values of yarn quality of Amin [58].....	55
Table 3.1 Parameters adopted for the simulation of spinning triangle.....	97
Table 3.2 The number of elongated fibers under different spinning tensions with fiber buckling.....	100
Table 3.3 The spinning parameters and calculated components of yarn torque	111
Table 4.1. Mosaic results of the 20Ne yarn sample ($N=614$ pixels, $D=21$ pixels)	174
Table 4.2. Evaluation of the yarn diameter and relative differences ($D=21$ pixels) .	177
Table 4.3. Comparison of migration parameters using computer and manual methods	180
Table 4.4. Comparison of time taken by the proposed computer and manual methods	181
Table 4.5. Database of yarn samples.....	182
Table 4.6. Number of images for each complete tracer fiber in the database	184
Table 4.7. Relative errors of image mosaic for each yarn count.....	188
Table 4.8. Evaluation results of image segmentation for each count in the database	192
Table 4.9. Structural parameters of the yarn samples in Figure 4.41.....	197

Table 4.10. Time taken for image mosaic and segmentation	198
Table 5.1 Features and their meanings	237
Table 5.2 The observation distance and image resolution.	242
Table 5.3 Features and their meanings	243
Table 5.4 Requirements for preparations of specimens	274
Table 5.5 Database of yarn images for grading system	275
Table 5.6 Confusion matrix for multi-classification problem.....	278
Table 5.7 Confusion matrix for classification performance (spread = 0.06).	281
Table 5.8 Importance of individual feature	283
Table 5.9 Classification results for eight-grade network (accuracy).....	284
Table 5.10 Database of yarn images for five-grade system	285
Table 5.11 Classification results for five-grade network (accuracy).....	286
Table 5.12 Visualized maps for selected button.....	293
Table 5.13 Relation of yarn count and yarn diameter (cotton).	296

LIST OF FIGURES

Figure 2.1 Rieter yarns by ring, compact, rotor and air-jet spinning [69].	17
Figure 2.2 Yarn formation in ring spinning system	18
Figure 2.3 A schematic diagram of yarn formation in rotor spinning [74]	19
Figure 2.4 Yarn formation in air-jet spinning [75].....	20
Figure 2.5 A CNT yarn twisted from a carbon nanotube array [76]......	20
Figure 2.6 An electrospinning process of nanofiber yarns [79].....	21
Figure 2.7 Spinning triangle model for fiber tensile strain developed by Najjar [20].	22
Figure 2.8 Images and theoretical model of the electrospinning triangles [24].....	25
Figure 2.9 Spinning triangle model for fiber tension by Hua et al.[22].....	26
Figure 2.10 Spinning triangle model for fiber tension by Feng et al. [25]	28
Figure 2.11 Spinning triangle model for fiber tension by Su et al [26]	30
Figure 2.12 Spinning triangle model with fiber concentric circular cones arrangement at front nip line [27].	31
Figure 2.13 Schematic diagram of experimental set-up for fiber tension measurement	33
Figure 2.14 Tension force patterns of wool fiber in the spinning triangle [20]	34
Figure 2.15 CCD system to capture spinning triangle and the relevant result [28]...	36
Figure 2.16 Cross-sectional image of a high-twist ring spun yarn (Tencel) [32].	37

Figure 2.17 A section of a spun yarn with tracer fiber by Hearle and Gupta [38].	38
Figure 2.18 Standard Hi-scope video microscope system [48].....	40
Figure 2.19 Measurement principle and images based on depth from focus [50].	41
Figure 2.20 Apparatus for observing the yarn and its image in mirror.	42
Figure 2.21 Measurement of tracer fiber and yarn surface [45].	43
Figure 2.22 An example of image mosaic [88].....	44
Figure 2.23 Stitched tracer fiber image of vortex yarns using Spin Panorama [30]..	45
Figure 2.24 A part of panoramas by MergeMagic with different fineness yarn [47].	46
Figure 2.25 Developed optical yarn measurement hardware [109]	48
Figure 2.26 Example of an image resulting from the application of a (a) high-pass spatial filter [109], (b) low-pass spatial filter [111].	48
Figure 2.27 Comparison of four histogram-based methods for yarn image	49
Figure 2.28 Yarn segmentation by a region growing-based approach [100]	50
Figure 2.29 Traditional method for yarn surface evaluation.....	53
Figure 2.30 Optical measuring principle of YAS [65]. D is yarn diameter.....	57
Figure 2.31 A sample for elimination of yarn body from yarn board [52].....	58
Figure 2.32 Perceptron artificial neural network with a fuzzy layer [57].....	59
Figure 2.33 The process of attention-driven fault features detection [55].	60
Figure 2.34 Fuzzy ARTMAP architecture [122].....	61

Figure 2.35 Example of fitting curve for one feature [56].....	62
Figure 2.36 General architecture of the Itti model [123].....	65
Figure 2.37 Saliency map generation by using Itti model. [123].....	66
Figure 2.38 Spectral residual approach [125].	68
Figure 2.39 The framework of AIM [130].....	70
Figure 3.1 A sketched view and geometry model of a symmetric spinning triangle.	78
Figure 3.2 An ideal structure of a yarn (5 layers).	78
Figure 3.3 Fiber bending due to flexural rigidity of fiber.	79
Figure 3.4 An idealized helical fiber on the surface of yarn.	82
Figure 3.5 Examples of fiber initial strain for 58tex yarn.....	86
Figure 3.6 A geometric model of spinning triangle.	87
Figure 3.7 The adopted beam element. W , V , and P are the nodes of the element, L_e is the orientation node, x , y and z are the directions of element coordinate system.	91
Figure 3.8 The finite element model of spinning triangle.	94
Figure 3.9 Finite element model of spinning triangle considering fiber-roller contact.	95
Figure 3.10 Fiber buckling in spinning triangle.....	96
Figure 3.11 Fiber tensions under different spinning tensions without fiber buckling.	98

Figure 3.12 Fiber tensions under different spinning tensions with fiber buckling. ...	98
Figure 3.13 Fiber tensions under different spinning tension angles in Case 3.	102
Figure 3.14 Fiber tensions under different yarn twists in Case 4.....	103
Figure 3.15 Comparison of fiber tensions under different yarn twists with [22, 23].	104
Figure 3.16 Fiber tensions at different yarn counts in Case 5 (yarn twist: 523tpm)	105
Figure 3.17 Fiber tensions at different contact lengths with roller in Case 6.	106
Figure 3.18. Effect of spinning parameters on fiber torsion distribution.....	108
Figure 3.19 Effect of the fiber contact lengths with bottom roller in Case 6.....	108
Figure 3.20 Contour plots of fiber torsion without roller contact.....	109
Figure 3.21 Contour plots of fiber torsion with $H/2$ roller contact.....	110
Figure 3.22 Comparison of the total yarn torque obtained by the theoretical models [14, 23] with experimental results [14]......	112
Figure 3.23 A geometric model of the spinning triangle.....	113
Figure 3.24 The Voigt model.....	114
Figure 3.25 Mass-spring-damper system of spinning triangle.....	116
Figure 3.26 The finite element model of spinning triangle.....	117
Figure 3.27 Mode shapes and natural frequencies (Hz) for the first 6 modes.	118
Figure 3.28 Effects of spinning parameters on natural frequency of first 3 modes.	119

Figure 3.29 Harmonic responses without consideration of fiber damping (Case 3) 121

Figure 3.30 Harmonic responses with consideration of fiber damping (Case 4)..... 121

Figure 3.31 Resonant responses without consideration of fiber damping (Case 3). 123

Figure 3.32 Resonant responses with consideration of fiber damping (Case 4)..... 123

Figure 3.33 Force analysis in yarn formation of ring spinning [154]...... 125

Figure 3.34 Simulated dynamic spinning tension according to Equation (3.39)..... 126

Figure 3.35 Dynamic inclined spinning tension with a periodical oscillation..... 127

Figure 3.36 Simulated spinning tension on twisting point of spinning triangle ... 128

Figure 3.37 Response of fiber tension (on left edge) to spinning tension in Figure
3.36..... 130

Figure 3.38 Comparison of fiber tensions under different twist angles with Najar[20].
..... 131

Figure 3.39 Geometric shapes of spinning triangle with different twist angles. 132

Figure 3.40 The fiber tension distribution of spinning triangle in different shape. . 133

Figure 3.41 Comparison of the proposed model with experimental measurements of
Najar [20] under different spinning tensions 134

Figure 4.1 Framework of the proposed computer method for tracer fiber analysis. 139

Figure 4.2 Configuration of the measurement system developed by Guo et al. [44].
..... 140

Figure 4.3. A series of consecutive 20Ne yarn images (twist multiplier of 3.3).....	141
Figure 4.4 Panorama created by (a)ArcSoft Panorama Maker and (b) manual stitching.....	143
Figure 4.5 Principle of the proposed computer method for automatic image mosaic	144
Figure 4.6 Procedure of the proposed computer algorithms for image mosaics.....	146
Figure 4.7 Intensity profile of the i^{th} column of the tracer fiber image.....	148
Figure 4.8 Schematic representation of normal ECG [158].....	148
Figure 4.9 Block diagram of Pan-Tompkins algorithm for QRS complex detection.	149
Figure 4.10 Signal de-noising.	150
Figure 4.11 Baseline fitting.....	150
Figure 4.12 Processing results of tracer fiber detection.....	152
Figure 4.13 Tracer fibers in image 1 and A_2 of image 2.	153
Figure 4.14 Matching function related to correlation coefficients of the tracer fiber.	155
Figure 4.15 Matching functions related to standard deviation of the tracer fiber. ...	156
Figure 4.16 Gradient images of the example images 1 and 2.....	158
Figure 4.17 2D correlation coefficients of the gradient image.	159

Figure 4.18 Matching function $G(u)$ from correlation coefficients of gradient image.	160
Figure 4.19 Decision function and its components.....	161
Figure 4.20 Panorama of images 1 and 2.....	162
Figure 4.21 Histogram and binary image of the panorama in Figure 4.20.....	163
Figure 4.22 The algorithms diagram for yarn boundary detection.	164
Figure 4.23 Average the image using a moving window.	164
Figure 4.24 Image preprocessing results.	165
Figure 4.25 Threshold segmentation.....	166
Figure 4.26 Panorama with identified yarn boundaries and tracer fibers.	167
Figure 4.27 Segmentation signals and the coordinate system.	167
Figure 4.28 3D configurations of a pair of yarn images.	168
Figure 4.29. Results of image mosaic and segmentation for whole series.	169
Figure 4.30. Panorama for whole series created by Panorama Maker.....	169
Figure 4.31. 3D configuration of the 20Ne yarn sample containing a whole complete tracer fiber.	170
Figure 4.32. Parameters $(z_i, y_i$ and $x_i)$ for the stitching point of the tracer fiber.	171
Figure 4.33 Comparison of segmentation results using the proposed computer method and manual method for the 20Ne yarn sample (unit: pixel).	175

Figure 4.34 Differences $l_i-l_i^m$ (pixel) between the computer and manual method. ..	175
Figure 4.35 Radial position of the tracer fiber in the 20Ne yarn sample.	178
Figure 4.36 Examples of yarn images of different counts with different magnifications.	183
Figure 4.37 Examples of the panoramas for different yarn counts.	186
Figure 4.38 Errors of image mosaic in quality evaluation.	189
Figure 4.39 Identified yarn boundaries and tracer fiber on the panoramas.	191
Figure 4.40 Relative errors for the image segmentation.	194
Figure 4.41 3D configuration of the examples shown in Figure 4.37.	196
Figure 4.42 Interface outline of the proposed system for tracer fiber images.	199
Figure 4.43 Main interface of the system.	200
Figure 4.44 Main steps for the image processing in the system.	201
Figure 4.45 Interface of image acquisition	203
Figure 4.46 Scale image in image acquisition.	204
Figure 4.47 Interfaces of image mosaic	205
Figure 4.48 Parameter setting for image mosaic.	206
Figure 4.49 Interface for the details of pair image mosaic	208
Figure 4.50 Processing results of gradient image and tracer fibers in the interface.	209
Figure 4.51 Statistical measures for image mosaic shown in the interface.	210

Figure 4.52 Selection windows for tracer fiber detection.....	211
Figure 4.53 Tracer fiber detection window.....	212
Figure 4.54 Windows for the results of high- and low-pass filter methods.....	213
Figure 4.55 Tracer fiber locations detected in image.....	214
Figure 4.56 Dialog box for the panorama setting in image segmentation.....	215
Figure 4.57 Interface for image segmentation.....	216
Figure 4.58 Results of image segmentation shown in the interface.....	217
Figure 4.59 Precessing results of yarn boundary detection shown in the interface.....	218
Figure 4.60 Interface for parameter analysis of yarn.....	219
Figure 4.61 Fiber radial position and frequency-amplitude curve.....	221
Figure 4.62 2D fiber paths and their frequency-amplitude curve.....	222
Figure 4.63 Zonal distribution of individual fiber.....	223
Figure 4.64 Fiber spatial orientation and the relation with radial position.....	224
Figure 4.65 Yarn diameter and its histogram.....	225
Figure 4.66 Manu and tools.....	225
Figure 5.1 Proposed computer method for yarn grading.....	231
Figure 5.2 Fourier transform of vertical and horizontal periodic structures [160].....	232
Figure 5.3 Amplitude of yarn board image in frequency domain.....	233
Figure 5.4 Maximum amplitude of yarn board image in frequency domain.....	234

Figure 5.5 Proposed strategy for feature extractions of yarn diameter and hairs. ...	236
Figure 5.6. Retinal image of an object at different observation locations.	238
Figure 5.7 Yarn board image with different resolutions.....	240
Figure 5.8 Visual distance and resolution.	240
Figure 5.9 Proposed strategy for feature extractions from saliency value and region.	242
Figure 5.10 Architecture of probabilistic neural network (PNN) [166].....	247
Figure 5.11 Architecture of probabilistic neural network (PNN) in Matlab. [167] .	248
Figure 5.12 Steps for the segmentation of yarn board image.	249
Figure 5.13 Example of yarn board image.....	250
Figure 5.14 Yarn board image in frequency domain by FFT.	251
Figure 5.15 De-noised image using FFT and BLPF.....	252
Figure 5.16 Binary image.....	252
Figure 5.17 Separated yarn board image.....	253
Figure 5.18 Histogram of yarn diameter.	254
Figure 5.19 Bar charts of features extracted from diameter and hairs (60Ne).....	259
Figure 5.20 General shape of log spectrum of all 60Ne yarn samples.	260
Figure 5.21 A 60Ne yarn sample with B+ grade.....	261
Figure 5.22 Image processing by SR method for the B+ grade 60Ne yarn.	262

Figure 5.23 Ordered curve of spectral residual of all 60Ne images.	263
Figure 5.24 Bar charts of the features extracted from image residual of 60Ne yarns.	265
Figure 5.25 Original SR saliency map.....	267
Figure 5.26 Original AIM saliency map divided into 4 pieces.....	268
Figure 5.27 Saliency map by SR method in Scale 1 (resolution of 100dpi).....	269
Figure 5.28 Saliency map by AIM model in Scale 2 (resolution of 300dpi).	270
Figure 5.29 Features of 60Ne yarns extracted from the top 20 regions in multi-scale.	272
Figure 5.30 System for image acquisition.	273
Figure 5.31 A series of 60Ne yarn board images with different grades.....	276
Figure 5.32 Spread-accuracy curve for spread selection (296 samples, 8 grades). .	280
Figure 5.33 Outline for yarn grading system.	287
Figure 5.34 Main interface of the digital yarn grading system.....	288
Figure 5.35 Flow chart of the digital yarn grading system.	288
Figure 5.36 Digital image acquisition.....	289
Figure 5.37 Image loading.	289
Figure 5.38 Interface for image processing and feature extraction.	292
Figure 5.39 Interface of yarn classification.	295

Chapter 1 Introduction

1.1. Research background

Spun yarn is the fundamental material for making a broad range of textile structures and composites. Yarn structure and appearance have significant influences on the properties and performance of the yarn and its end-products. Therefore, the analysis of yarn fabrication, structure and appearance is important in ensuring yarn qualities in the textile industry.

During fabrication, yarn is formed by twisting an assembly of short or long fibers in a small area called spinning triangle. Many novel ring spinning technologies [1-11] have been developed to control the fiber performance in spinning triangle for the improvement of yarn quality. Fiber physical performance in spinning triangle, such as fiber tension distribution, torsional distribution and geometric shape, will influence yarn characteristics and properties. For instance, the main source of fiber migration is acknowledged to the differences of fiber tension during the yarn formation [12] and yarn torque is mainly generated by fiber tension, fiber bending and fiber torsion in the yarn [13-14].

In the past, the investigations on the physical characteristics of spinning triangle were

mainly based on the force method [15-19] and energy method [20-27]. Due to the limitations of these methods, some important parameters, such as the inclined angle of spinning tension, the fiber contact with bottom roller, yarn torque and the fiber torsional distribution, cannot be considered. Particularly, with some recent developments in staple yarn spinning [8-11], the working condition for spinning triangle becomes more complex, and thus requires a more realistic model to analyze the properties of yarn and its constituent fibers. Therefore, a new theoretical model of spinning triangle should be established to fully examine the quantitative relationships between the spinning triangle and various spinning parameters, including the above-mentioned factors ignored previously.

Furthermore, in most existing models, the performance of constituent fibers in spinning triangle was considered as a steady-state process. In fact, the magnitude of spinning tensions used to draw out the yarn is time-variable. The fiber tension and shape of spinning triangle were also presented with a high-speed variation during yarn formation [20, 28]. Therefore, the dynamic characteristics such as the inertia and damping of constituent fibers should be considered in the analysis the mechanical and geometric performance of spinning triangle.

Tracer fiber technique is a popular method to study yarn internal structure by tracing

the trajectory of individual fiber in the yarn [29-50]. In this method, an extremely small percentage of color fibers are introduced in a spun yarn. The yarn sample is then immersed in a trough of special solvent so as to optically dissolve other fibers based on their different refractive indexes for capturing the tracer fibers by a microscope. During image acquisition, a series of consecutive yarn images are obtained and each image only covers a part of tracer fiber. So image mosaic method has to be used to stitch them together into a panorama for a whole tracer fiber. Then the yarn boundaries and tracer fiber will be identified from the panorama image. Based on the identified spatial distribution of fibers, the geometrical parameters of yarn, such as fiber migration and yarn diameter, could be obtained. Nevertheless, the existing general image processing methods and software cannot work well in most cases for automatic mosaic and segmentation of tracer fiber images. Therefore, the image mosaic and segmentation currently in use are mainly based on manual operation for the analysis of tracer fiber images. It is extremely time-consuming and becomes a bottleneck problem in yarn structure analysis.

Traditionally, the evaluation of yarn surface quality is based on human vision inspection of yarn sample appearance according to ASTM D2255 [51]. In this method, yarn sample is wound on a black board and then compared with a series of

grade-labeled photographic standards with consideration of the unevenness, fuzziness, neppiness and visible foreign matter. But the current method is subjective, time-consuming and sometimes inconsistent. Although some works [52-65] have been done on digital yarn analysis, none of them can fully imitate the human visual behavior in the evaluation of yarn surface appearance on blackboards according to ASTM D2255.

Therefore, based on all the above, the present study aims to develop computational and digital methods and systems for the accurate and efficient analysis of yarn fabrication, internal structure and surface appearance. In this study, a new theoretical model of spinning triangle will be built up to investigate the effects of spinning parameters on the mechanical performance of fibers in yarn formation by using Finite Element Method (FEM). Intelligent digital methods will be also developed to solve the limitations of manual operation and human inspection currently used for yarn internal structure and surface appearance by using computer vision and artificial intelligence. Both digital methods and systems will be developed for automatic image mosaic and segmentation of tracer fiber images and intelligent feature extraction and classification of yarn surface quality based on yarn board images.

1.2. Objectives

The present study mainly focuses on the computational and digital analysis of yarn fabrication, structure and surface quality with following specific objectives:

(1) to develop new theoretical models for analyzing the geometric shape and fiber mechanical behavior of spinning triangle during yarn formation with consideration of various operating parameters ignored previously, including inclined angle of spinning tension, frictional contact of fibers with bottom roller and fiber torsional strains, and the dynamic effects, such as inertia and damping of the fibers;

(2) to develop a new integrated computer method, based on the digital signal and image processing methods, for automatic and efficient mosaic and segmentation of a series of consecutive tracer fiber images for yarn structure analysis;

(3) to design and build up a digital system, based on the above developed new computer method, to integrate and control the whole process of yarn measurement and structure analysis, including yarn image acquisition, image mosaic, image segmentation, and parameter analysis, for an accurate and efficient analysis of yarn internal structure, with an interactive and user-friendly interface;

(4) to develop a new intelligent computer method, based on recent advances in image processing and artificial intelligence, for quantitative characterization and objective

evaluation of yarn surface quality; and

(5) to design and develop a digital system for the computerized measurement and evaluation of yarn surface quality, including image acquisition, digital feature extraction, characteristics computation and surface quality classification, with an interactive and user-friendly interface.

1.3. Significance and originality

This study aims at developing computational and digital methods and systems for accurate and efficient analysis of yarn fabrication, structure and surface appearance.

In recent years, some novel spinning systems such as compact spinning [1-2], siro-spinning [3-4], solo-spinning [5-6], cluster spinning [7] and low-torque spinning [8-11] have been developed for higher yarn performance and they are all concentrated on alteration or control of yarn formation in the spinning triangle to improve fiber arrangement or migration. For example, compact spinning produces high-performance yarn by minimizing or eliminating the spinning triangle and low-torque spinning reduces yarn residual torque by shortening and symmetrizing the spinning triangle. In the past, the investigations on the mechanical characteristics of spinning triangle were mainly based on the force method [15-19] and energy method [20-27]. Due to the limitations of these methods, some

important spinning parameters, such as the inclined angle of spinning tension, frictional contact of fibers with the bottom roller and fiber torsional strains, cannot be considered. Besides, experimental observations [20, 28] showed that the performance of constituent fibers in spinning triangle during yarn formation is a real dynamic process. However the existing methods for analysis of spinning triangle are mainly based on static assumptions. In this study, new generalized theoretical models of spinning triangle will be developed for a more complete and accurate description of yarn fabrication using Finite Element Method (FEM). In the proposed models, besides the operating parameters of spinning tension, yarn count and yarn twist, some important parameters ignored previously, including inclined angle of spinning tension, fiber torsional strains and frictional contact of fibers with the bottom roller, and system dynamic effects such as inertia and damping forces of constituent fibers, will be considered.

Traditionally, yarn internal structure and surface appearance are mainly measured and evaluated by manual methods in textile industry and these methods are subjective, time-consuming and sometimes inconsistent. Recent developments of computer vision, digital image processing and artificial intelligence bring new acquisition apparatus, data analysis and recognition approaches, thus may provide solutions to the above limitations of human vision and operation.

Tracer fiber technique is a popular method for the analysis of yarn internal structure.

As image mosaic and segmentation for the two-viewed tracer fiber images are complex in nature, the general image-processing methods or software may fail in most cases. Currently, the image mosaic and segmentation for tracer fiber images are mainly conducted by manual operation. In order to analyze a structure of spun yarn, a series of yarns produced with different yarn counts and twists would be examined, so hundreds of or even thousands of yarn images have to be processed. It is extremely time-consuming and becomes a bottleneck problem of yarn structure analysis. In this study, an integrated computer method for image mosaic and segmentation will be developed for automatically and efficiently stitching a series of consecutive yarn images into a panorama and identifying the yarn boundaries and tracer fiber from the panorama. Moreover, based on the proposed image processing method, an intelligent image processing system will be developed for intelligent and efficient tracer fiber measurement and yarn structure analysis. The developed method and system will be potentially for textile laboratorial and industrial applications, such as the analysis of yarn structural characteristics for an innovative spinning method and the study of effect of spinning parameters on fiber arrangement inside the yarn.

In textile industry, yarn surface appearance is subjectively evaluated by human

vision. It is subjective, time-consuming and sometimes inconsistent. Although some digital methods [52-65] have been developed for yarn grading, none of them can fully imitate human visual behavior in the inspection of yarn segments on a blackboard and consider all influential factors of yarn unevenness, fuzziness, neppiness and visible foreign matter for yarn grading according to the standard of ASTM D2255. In this study, a new digital method will be developed for an objective, efficient and accurate evaluation of yarn surface appearance. Moreover, based on the proposed computer method, a digital system will also be built up for intelligent and automatic measurement and evaluation of yarn surface quality. This computerized system is tailor-made for yarn board grading and thus potential for application in textile testing laboratories and spinning mills for yarn surface quality control and assurance.

1.4. Research methodology

In this project, computational and digital methods will be developed for the systematic analysis of yarn formation, structure and surface appearance. The following research methodologies will be adopted in this study.

(1) Theoretical analysis of spinning triangle by finite element method (FEM)

Finite element method (FEM) will be employed in this study to investigate fiber

performance and yarn fabrication in the spinning triangle. FEM is a numerical method for solving physical problems governed by differential equations or an energy theorem. The method uses continuous piecewise smooth functions for approximating the unknown quantities. In this study, the governing equation for the dynamic system of spinning triangle can be written as:

$$[M]\{\ddot{u}\} + [C]\{\dot{u}\} + [K]\{u\} = [F] \quad (1.1)$$

where $[M]$ is the mass matrix, $\{\ddot{u}\}$ is the second time derivative of the displacement $\{u\}$ (i.e. the acceleration), $[C]$ is the damping matrix, $\{\dot{u}\}$ is the velocity, $[K]$ is the elastic stiffness matrix and $[F]$ is the force vector.

FEM is a powerful computational technique for approximate solutions to a variety of physical problems having complex domains subject to general boundary conditions [66]. To deal with fiber buckling in the FEM model, the algorithm of element birth and death should be employed to delete compressive capability of fiber because the critical fiber strain at which fiber buckling occurs is approximately 10^{-6} [22].

With the developed theoretical model of spinning triangle, the quantitative relationships between the mechanical performance of fibers in spinning triangle and various spinning parameters will be numerically studied. In the static model, the effects of spinning parameters, such as spinning tension, spinning tension angle, yarn

twist, yarn count, and frictional contact of fibers with bottom roller, on fiber tension and torsion distributions of spinning triangle, will be fully examined and analyzed.

In the dynamic model, the dynamic behavior of fibers in spinning triangle, such as the natural frequency, mode shape, resonant response, harmonic analysis and fiber response under a dynamic spinning tension, will also be numerically studied.

In addition, simulation results of the developed models, such as fiber tension distribution and their influences on yarn torque, should also be compared with those of earlier models [20-23] and experimental data [14].

(2) Automatic mosaic and segmentation of tracer fiber images

Image mosaic is a process of finding a global transformation that resamples a set of images of a scene into a common coordinate system. In tracer fiber technique concerned in this study, image mosaic is used to stitch a series of consecutive overlapped yarn images into a panorama for further yarn structure analysis. In order to gather more image information for an accurate mosaic, a decision function $H(u)$ will be proposed to identify the optimal matching position by incorporating various matching functions extracted from tracer fibers and gradient image:

$$H(u) = \sum_{i=1}^n w_i H_i(u) \quad (1.2)$$

where $H_i(u)$ is i^{th} normalized matching function, w_i is the weight for $H_i(u)$ and n is the number of matching functions.

In addition, an extended Pan-Tompkins algorithm [67] will be developed for accurate and efficient detection of tracer fiber and a piecewise cubic Hermite interpolation method [68] will be used to eliminate the effect of uneven light condition.

An objective method should also be proposed to evaluate the qualities of the proposed image mosaic and segmentation method with respect to those from manual method. Furthermore, a yarn image database, obtained from various samples at different counts (linear density) under different acquisition conditions, will be constructed to fully evaluate the proposed computer method of image mosaic and segmentation.

(3) Quantitative characterization and classification of yarn surface appearance

In this study, a multi-scale attention model will be developed to fully imitate human observation at different observation distances for both a whole and a detailed analyses of yarn information. As the yarn board images have regular periodic pattern, Fourier transform, Butterworth low-pass filter and inverse Fourier transform will be used to segment yarn board image into yarn body image and yarn hairiness

image. Then various digital features should be extracted from yarn body image, yarn hairiness image and multi-scale attention maps, to present all influential factors of the yarn surface appearance. With these digital features, Probabilistic Neural Network (PNN) will be employed for yarn classification.

In order to evaluate the proposed digital method, a series of spun yarns with different yarn counts and different qualities of surface appearance will be prepared by using different spinning parameters. Leave-one-out cross validation (LOOCV) will be used to evaluate the classification results of the proposed method with respect to those given by the experienced yarn graders according to ASTM D2255.

(4) System developments for analysis and evaluation of yarn internal structure and surface appearance

Based on the above developed computer methods, two digital systems will also be designed and developed for computerized analysis and evaluation of yarn internal structure and surface appearance, respectively. In these systems, all the digital processing algorithms will be integrated to implement and control the whole process of measurement, analysis and evaluation of yarn internal structure and surface appearance with an interactive and user-friendly interface. More specifically, the digital system for tracer fiber analysis should contain the functions for video

acquisition, image acquisition, image mosaic, image segmentation and parameter analysis. The digital system for yarn surface grading should contain hardware for sample preparation and image acquisition, and software for image acquisition, image loading, image processing and yarn classification.

1.5. Thesis outline

This thesis covers the following six chapters.

Chapter 1 introduces research background, objectives, significance and originality, and methodology of the study. The outline of this thesis is also provided.

Chapter 2 offers a literature review of previous and current research works associated with this study. It includes the theoretical analysis and measurement of spinning triangle in yarn fabrication, the measurement techniques and related image analysis methods for yarn internal structure, as well as the analysis and evaluation methods for yarn surface quality.

Based on the literature review, in order to overcome the limitations of current theoretical models of spinning triangle, Chapter 3 proposes two new theoretical models of spinning triangle in yarn fabrication using finite element method (FEM).

The static model of spinning triangle is developed by taking account of some

important factors ignored previously, including the inclined angle of spinning tension, the fiber contact with bottom roller and fiber torsional strain. Then, a dynamic theoretical model of spinning triangle is further developed model by extending the proposed static model with consideration of the dynamic effects such as the inertia and damping of constituent fibers, for a more complete and accurate description. The relevant simulations on fiber mechanical performance in spinning triangle are also carried out.

Chapter 4 proposes an intelligent computer method for automatic mosaic and segmentation of a series of consecutive two-viewed tracer fiber images for the analysis of yarn internal structure. In this method, an extended Pan-Tompkins algorithm is developed for tracer fiber detection, and a decision function is proposed by combining several special statistical measures to identify the optimal position for image mosaic. Moreover, a piecewise cubic Hermite interpolation method is employed to eliminate the effect of uneven light condition. An objective evaluation method is also proposed for evaluating the precision of image mosaic and segmentation with respect to manual method. For this purpose, a database containing a series of yarn samples (total 872 images) was constructed. Finally, based on the developed algorithms, an integrated system for the image analysis of yarn internal structure is designed and developed for implementing and visualizing

the whole image processing of tracer fiber images for yarn structure analysis.

In Chapter 5, an intelligent digital method is developed for the objective and automatic evaluation of yarn surface appearance using computer vision and artificial intelligence. The method can fully imitate the human visual behavior in yarn grading according to standard of ASTM D2255. In this method, Fourier transform, Butterworth low-pass filter and inverse Fourier transform are used to segment yarn board image into yarn body image and yarn hairiness image. A multi-scale attention model is developed to fully imitate human observation at different observation distances for both a whole and a detailed analyses of yarn information. Then, sixteen digital features are extracted from yarn body image, yarn hairiness image and the multi-scale saliency maps to present the characteristics of yarn surface appearance. Based on the digital features, Probabilistic Neural Network (PNN) is utilized to classify yarn surface grade. A database containing 296 yarn samples with various surface qualities and yarn counts is constructed to evaluate the performance of the proposed method. Finally, based on the proposed algorithms, an intelligent digital evaluation system is also designed and developed for the computerized measurement and evaluation of yarn surface quality.

Finally, Chapter 6 makes a brief summary for the whole work in this thesis and brings up some suggestions for further work.

Chapter 2 Literature Review

2.1. Analysis of spinning triangle in yarn fabrication

Spinning is a process which converts short or long fibers into a continuous useful yarn in order to obtain sufficient strength, smoothness and abrasion resistance for the downstream processing. In the spinning process, yarns are eventually formed in a small area called spinning triangle by twisting an assembly of natural or polymeric fibers, therefore the geometric and mechanical performances of spinning triangle play an important role in determining the physical performance of these yarns.

Figure 2.1 shows the yarns produced by different methods of ring, compact, rotor and air-jet spinning.

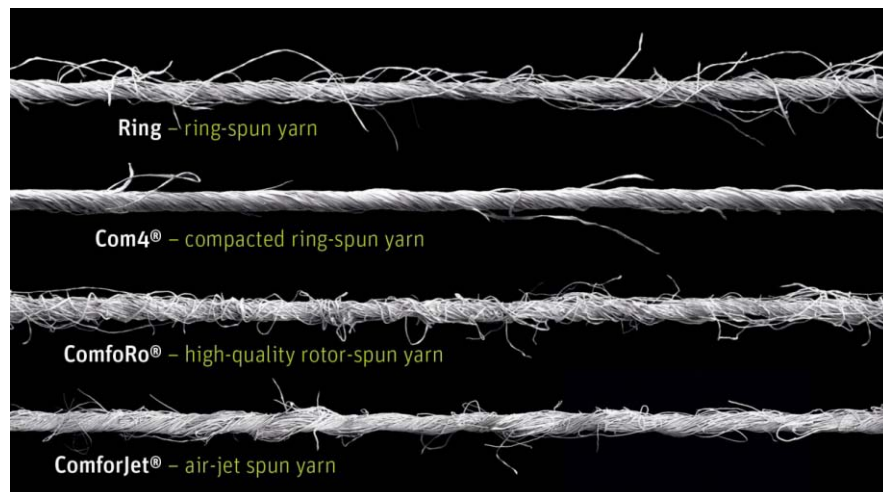
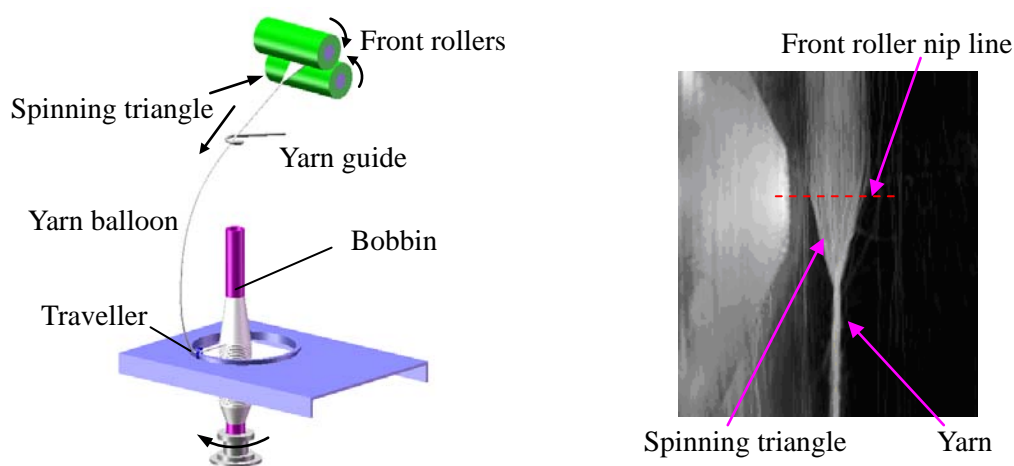


Figure 2.1 Rieter yarns by ring, compact, rotor and air-jet spinning [69].

2.1.1. Spinning triangle in yarn formation

Ring spinning is the most important system of making high quality yarns in the textile industry. In the ring twisting process (see Figure 2.2(a)), roving fibers are first reduced in size by the drafting rollers and then twisted together to form a spun yarn in the spinning triangle by a twist propagated from the bottom traveller.

Figure 2.2(b) shows a photo of real spinning triangle of cotton fibers obtained by a CCD Micro-Camera [21], in which a special transparent roller is designed to replace the top rubber roller and used for clear observation and image acquisition of yarn formation at spinning triangle.



(a) a schematic diagram of ring spinning (b) a photo of real spinning triangle [21]

Figure 2.2 Yarn formation in ring spinning system

Rotor spinning is a kind of open-end spinning. In rotor spinning, the twist is applied to the newly added fibers for converting them into a yarn, and new elements of the

yarn are continuously taken out from the twisting zone (see [Figure 2.3](#)). Real twist is generated by the rotating action of rotor and it interacts with the false twist generated on the rotor groove. The mechanical models of fibers in yarn-forming zone of rotor spinning, such as the twist distribution [70-71], yarn motion [72] and twisting convergent point [73], have been developed for analyzing the effects of spinning parameters on yarn dynamic behaviors.

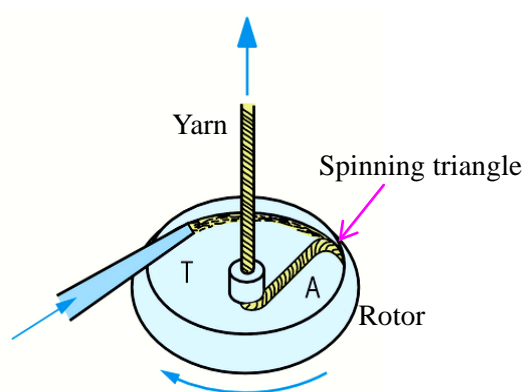


Figure 2.3 A schematic diagram of yarn formation in rotor spinning [74]

In air-jet spinning, a twist triangle is formed near a roller drafting system to twist fibers together. As shown in [Figure 2.4](#), zones marked with T contain fibers under tension derived from the pull of air-jet and the zone marked with M contains fibers that go slack due to their shorter path length (as compared with the others) between the nip of the drafting rolls and the vertex of triangle [75]. Slack fibers migrate laterally in yarn body to interlock the structure, giving fiber cohesion and yarn strength.

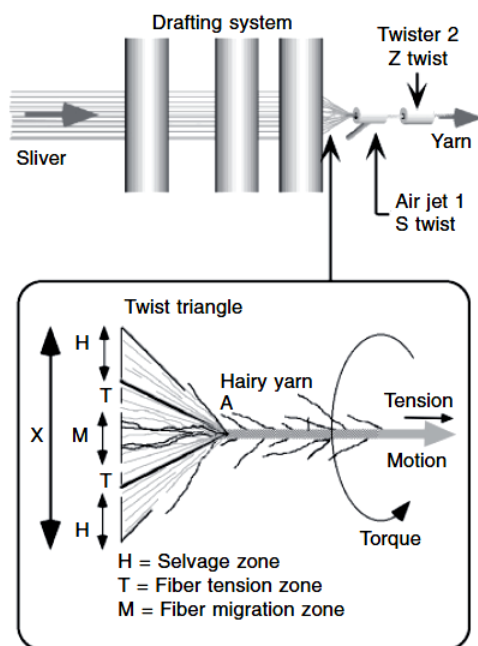


Figure 2.4 Yarn formation in air-jet spinning [75]

Besides the above conventional methods, researchers have also attempted to develop novel spinning methods to twist nano-scale fibers into the continuous nanofiber yarns such as carbon nanotube (CNT) yarn [76-78] and electrospun yarn [79]. As illustrated in Figure 2.5 and Figure 2.6, spinning triangles can also be observed in twisting nanofibers into the yarns by CNT array and electrospinning.

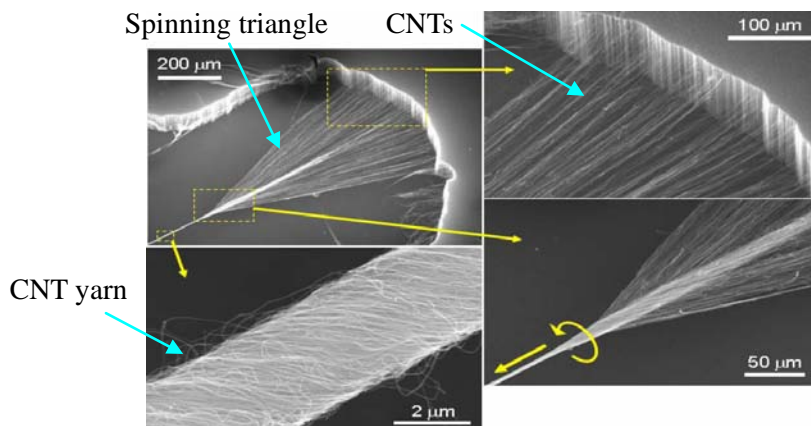


Figure 2.5 A CNT yarn twisted from a carbon nanotube array [76].

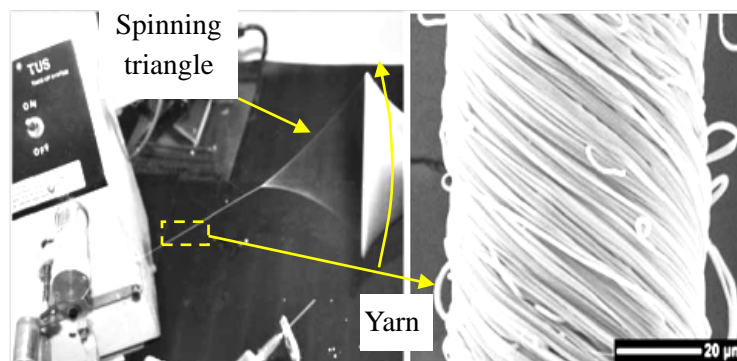


Figure 2.6 An electrospinning process of nanofiber yarns [79].

2.1.2. Theoretical analysis of spinning triangle

In the past, performance of constituent fibers in spinning triangle was mainly considered as a steady-state process and researchers have investigated the physical characteristics and geometry of spinning triangle using the static models. In the earlier stage of studies, the force method was the mainstream for the geometric and strength study of spinning triangle [15-19]. For instance, Fujino et al. [15] examined the twist irregularity of yarns with a theoretical consideration of force balances in the spinning triangle. In a study of the fiber strength, structural transformations of the fibers at the instant rupture in yarn formation were studied by Pavlov [16]. Krause et al. [19] also carried out a similar theoretical investigation on the strength of spinning triangle by taking different extensions of fiber into consideration. Based on the photographic experiments [17, 20-21, 28], the mechanical behavior of fibers, such as fiber buckling, fiber migration and the profile

of spinning triangle, were partially observed.

The theoretical models of spinning triangle currently in use are mainly based on the energy method. The advantage of this method lies that the full description of geometry is not required before hand. In those models [20-27], the total potential energy, composed of the total elastic strain energy of fibers and the work done by the spinning tension, is minimized with respect to a generalized coordinate. Najjar [20] originally carried out a theoretical study of symmetric spinning triangle (see Figure 2.7) using the energy method. The distribution of fiber tensions in the symmetric spinning triangle was systematically studied with respect to its influential parameters of twisting angle, spinning tension and yarn count.

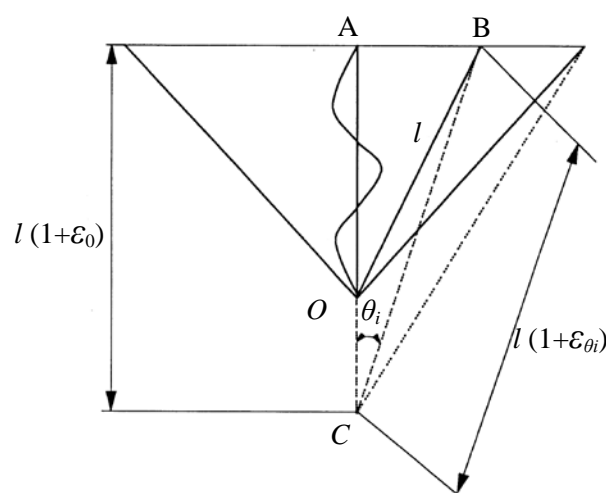


Figure 2.7 Spinning triangle model for fiber tensile strain developed by Najjar [20].

According to the principle of stationary total potential energy, it follows that:

$$\Pi_p = U + \Omega \quad (2.1)$$

where Π_p is the total potential energy, U is the strain energy and Ω is the potential energy done by external loads.

Thus in equilibrium conditions, Equation (2.1) leads to:

$$\frac{d\Pi_p}{du} = \frac{d}{du}(U + \Omega) = 0 \quad (2.2)$$

And the strain energy U can be expressed as:

$$\begin{aligned} U(u) = & Al \left[\frac{E}{2} \left(\frac{u}{l} \right)^2 \right] + 2Al \left[\frac{E}{2} \left(\frac{u(1 + \tan^2 \theta_1) + \frac{1}{2}l \tan^2 \theta_1}{l} \right)^2 \right] \\ & + 2Al \left[\frac{E}{2} \left(\frac{u(1 + \tan^2 \theta_2) + \frac{1}{2}l \tan^2 \theta_2}{l} \right)^2 \right] + \dots \\ & + 2Al \left[\frac{E}{2} \left(\frac{u(1 + \tan^2 \theta_n) + \frac{1}{2}l \tan^2 \theta_n}{l} \right)^2 \right] \end{aligned} \quad (2.3)$$

where u is the generalised coordinate, l is the initial length of fiber, E is the fiber tensile elastic modulus, and θ_i is the individual fiber angle with the axial direction.

Besides, the potential energy Ω can be written as:

$$\Omega(u) = -F_s u \quad (2.4)$$

where F_s is the external force.

Therefore, substituting Equation (2.3) and Equation (2.4) into Equation (2.2), the fiber tension force in the central of the spinning triangle F_0 can be expressed:

$$F_0 = \frac{F_s - AE \sum_{i=1}^n (1 + \tan^2 \theta_i) \tan^2 \theta_i}{2 \sum_{i=1}^n (1 + \tan^2 \theta_i)^2 - 1} \quad (2.5)$$

Finally, the tension force of fibers in general terms can be derived as follows:

$$F_{i=0,1,2,\dots,n} = \frac{F_s - AE \sum_{i=1}^n (1 + \tan^2 \theta_i) \tan^2 \theta_i}{2 \sum_{i=1}^n (1 + \tan^2 \theta_i)^2 - 1} (1 + \tan^2 \theta_i) + \frac{AE}{2} \tan^2 \theta_i \quad (2.6)$$

Hajiani et al. [24] then applied Najjar's method to investigate the effects of twist on the symmetric electrospinning triangle (as shown in Figure 2.8). Based the theoretical and experimental work, they concluded that mechanical properties of nanofiber yarn can be improved by increasing the twist rate and changing the shape of the electrospinning triangle.

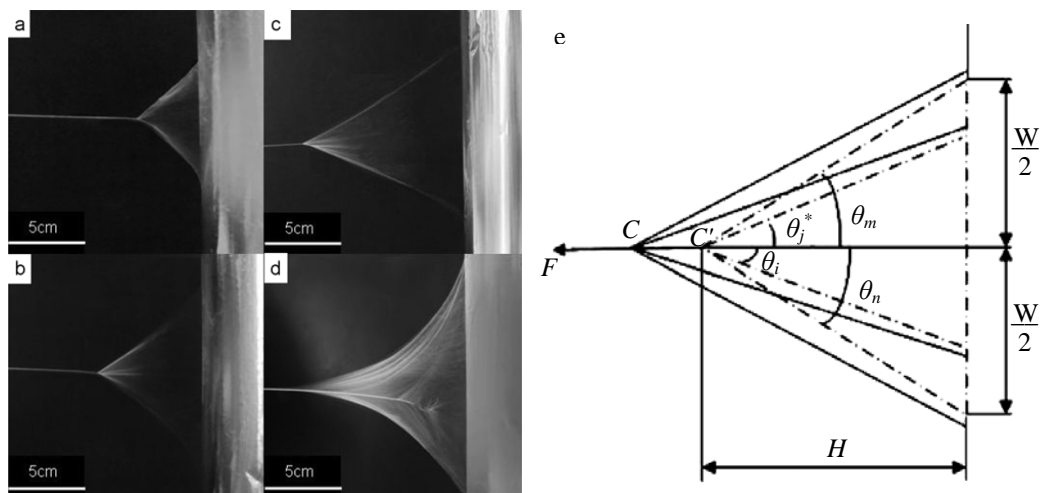


Figure 2.8 Images and theoretical model of the electrospinning triangles [24].

Electrospinning triangles produced for spinning continuous nanofiber yarn at different twists: (a) 288rpm, (b) 224rpm, (c) 160rpm, and (d) 96rpm; (e) symmetric electrospinning triangle model for tension on nanofibers.

Afterwards, Hua et al. [21-23] extended the work of Najjar [20] to an asymmetric spinning triangle with a consideration of fiber buckling and a shape parameter β .

As shown in Figure 2.9, the shape parameter β was defined below to represent the skew level of the geometry of spinning triangle:

$$\beta = \frac{w - d}{w + d} \quad (2.7)$$

where w is the half width of spinning triangle.

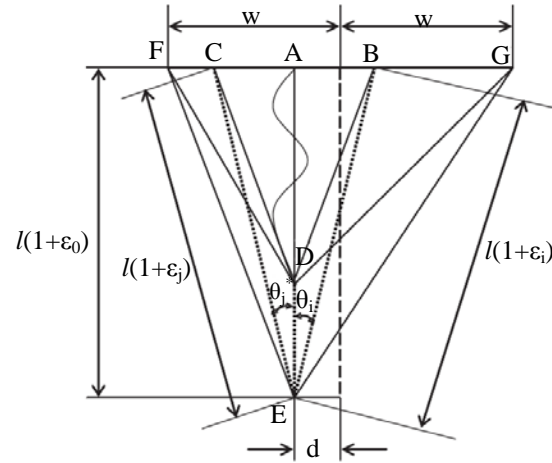


Figure 2.9 Spinning triangle model for fiber tension by Hua et al.[22].

With consideration of the fiber buckling, if the fiber is treated as an elastic thin rod under an axial compressive load with both ends clamped, the critical compressive load required to cause fiber buckling is given by [80]:

$$P_{cr} = \frac{4\pi^2 EI}{l_c^2} \quad (2.8)$$

where I is the moment of inertia of the fiber with a circular cross-section of radius r , and l_c is the clamped length of fiber.

Then, the critical fiber strain beyond which fiber buckling occurs can be given as:

$$\varepsilon_{cr} = \frac{\pi^2 r^2}{l_c^2} \quad (2.9)$$

Hua et al. [22] found that the fiber tension distribution with consideration of fiber buckling is much lower than without buckling. In order to evaluate the model of

spinning triangle, Hua et al. [23] further calculated yarn torque L generated by fiber tension P_i for comparison with published experimental data:

$$L = \sum_{i=1}^{m+n+1} L_i = \sum_{i=1}^{m+n+1} P_i r_i \sin q_i \quad (2.10)$$

where $m+n+1$ is the number of fibers in the yarn, L_i is the component of yarn torque due to the fiber tension, r_i is the distance of fiber from the yarn axis and q_i is the helix angle of the fiber tension.

The simulation results by Hua et al. [23] showed that the case with fiber buckling is much closer to the experimental data and thus the assumption of no fiber buckling is not realistic.

Feng et al. [25] further extended the work of Hua et al. [21-23] with consideration of an imaginary (specifically defined) inclined spinning tension F_s , as shown in [Figure 2.10](#).

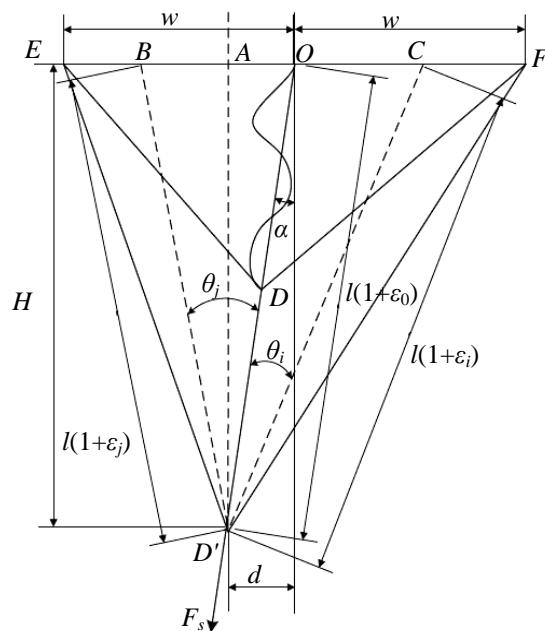


Figure 2.10 Spinning triangle model for fiber tension by Feng et al. [25]

In the model of Feng et al. [25], spinning tension F_s is assumed to depend on the shape of the spinning triangle and can only specifically act along a particular direction on the connection of the middle point O of the nip line and the twisting point D . Thus, the inclination angle α of the yarn spinning tension can be expressed as:

$$\alpha = \arctan\left(\frac{d}{H}\right) \quad (2.11)$$

Then the fiber strain can be written as:

$$\varepsilon_i = M\varepsilon_0 + M - 1 \quad \text{and} \quad \varepsilon_j = M'\varepsilon_0 + M' - 1 \quad (2.12)$$

where $M = \frac{1}{\cos \theta_i (1 - \tan \alpha \times \tan \theta_i)}$ and $M' = \frac{1}{\cos \theta_j (1 + \tan \alpha \times \tan \theta_j)}$.

Finally, a general formula of fiber tension can be obtained as:

$$F_{i=0, \dots, n} = \frac{F_s - AE \left(\sum_{i=0}^n M(M-1) + \sum_{j=0}^n M'(M'-1) \right)}{\sum_{i=0}^n M^2 + \sum_{j=0}^n M'^2 - 1} \times M + AE(M-1) \quad (2.13)$$

$$F_{j=0, \dots, n} = \frac{F_s - AE \left(\sum_{i=0}^n M(M-1) + \sum_{j=0}^n M'(M'-1) \right)}{\sum_{i=0}^n M^2 + \sum_{j=0}^n M'^2 - 1} \times M' + AE(M'-1) \quad (2.14)$$

Feng et al. [25] quantitatively investigated the effect of speed ratio on the distribution of fiber tensions at the spinning triangle and the results showed that the magnitudes of fiber tension are slightly larger than those of previous models [22-23].

More recently, Su et. al. [26] extended the energy model of Feng et al. [25] by introducing one more parameter (d_1), as shown in Figure 2.11. Thus, in order to describe the geometric skewness of the spinning triangle, the two shape parameters

δ_1 and δ_2 can be defined as:

$$\delta_1 = \frac{d_1}{m} \quad \text{and} \quad \delta_2 = \frac{d_2}{m} \quad (2.15)$$

Then according to the Equations (2.12)~(2.14) of Feng et al., the effects of shape

parameters δ_1 and δ_2 on fiber tension distribution in the spinning triangle were investigated without considering fiber buckling.

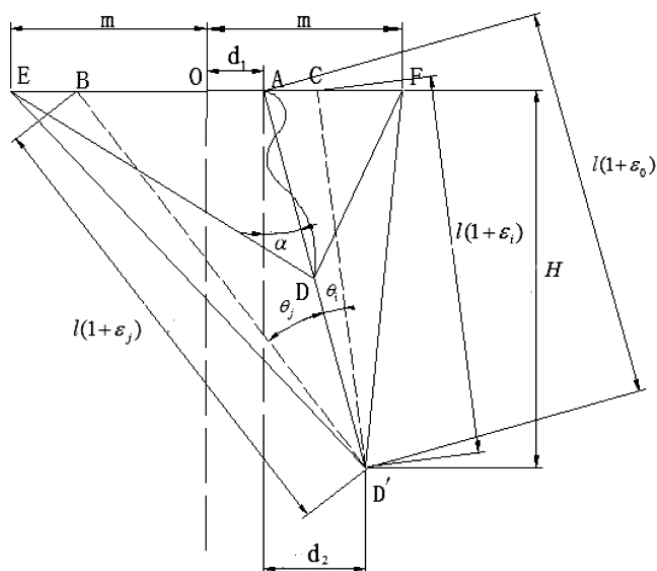


Figure 2.11 Spinning triangle model for fiber tension by Su et al [26]

Moreover, Liu et al [27] further applied the energy-method based theoretical model of spinning triangle to the case of fiber concentric circular cone-arrangement at front nip line (see Figure 2.12), such as compact spinning. Based on the energy models of Feng et al. [25] and Hua et al. [22], and with considering the spatial angle of individual fiber with the axial direction, the fiber tension in the spinning triangle can be obtained as:

$$F_{j=0,\dots,m;i=1,2,\dots,N_j} = \frac{F_s - AE \sum_{i=1}^m N_j M_j (M_j - 1)}{\sum_{i=1}^m N_j M_j^2} M_j + AE(M_j - 1) \quad (2.16)$$

where $M_j = \frac{1}{\cos \theta_j}$, $\tan \theta_j = \frac{r_j}{h'}$ and $\begin{cases} N_j = 1 & j = 1 \\ N_j = 6(j-1) & j \geq 2 \end{cases}$

According to Equation (2.16), the numerical simulations of fiber tension distribution in compact spinning were carried out. Comparison of residual torques generated by fiber tension was made between the ring and compact spinning triangles, and the results showed that the torque of compact spun yarn is a little larger than that of ring spun yarn.

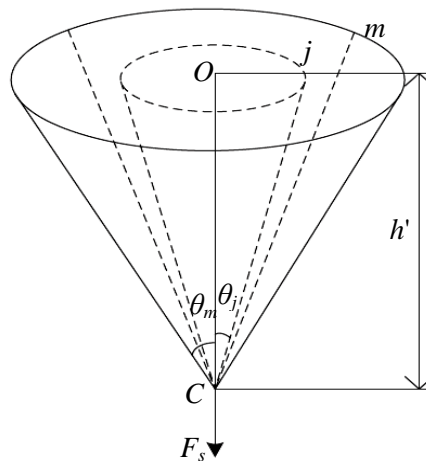


Figure 2.12 Spinning triangle model with fiber concentric circular cones arrangement at front nip line [27].

From the above-mentioned, many energy-based theoretical models have been developed for studying the mechanical characteristics of spinning triangle. However, with energy method, due to the problem of dissipated friction energy and the mathematical complexities in formulating fiber bending and torsional strains,

some important spinning parameters and properties of spinning triangle, such as the inclined angle of spinning tension, fiber torsion distribution and the fiber frictional contact with bottom roller, are hardly to be considered. Most importantly, the performance of constituent fibers in spinning triangle was only considered as a steady-state process in these models. In fact, the magnitude of spinning tensions used to draw out the yarn is variable and the experimental measurements [20] show that the fibers in spinning triangle are apparently subject to dynamic loads.

2.1.3. Measurement of fiber performance in spinning triangle

Because spinning triangle is a very small region with a high-speed variation and the constituent fibers inside the spinning triangle are discontinuous, it is extremely difficult to measure its dynamical parameters during spinning, such as the tension force of individual fibers and the position of twisting point. Besides, the measurement apparatus may also interact with and even disturb the twisting and movement of fibers in the spinning triangle. Najar [20] designed a special experimental device and used a continuous nylon monofilament to investigate the dynamic behavior of wool fiber tension at the ring spinning triangle. [Figure 2.13](#) shows the schematic diagram of the experimental set-up for fiber tension measurement.

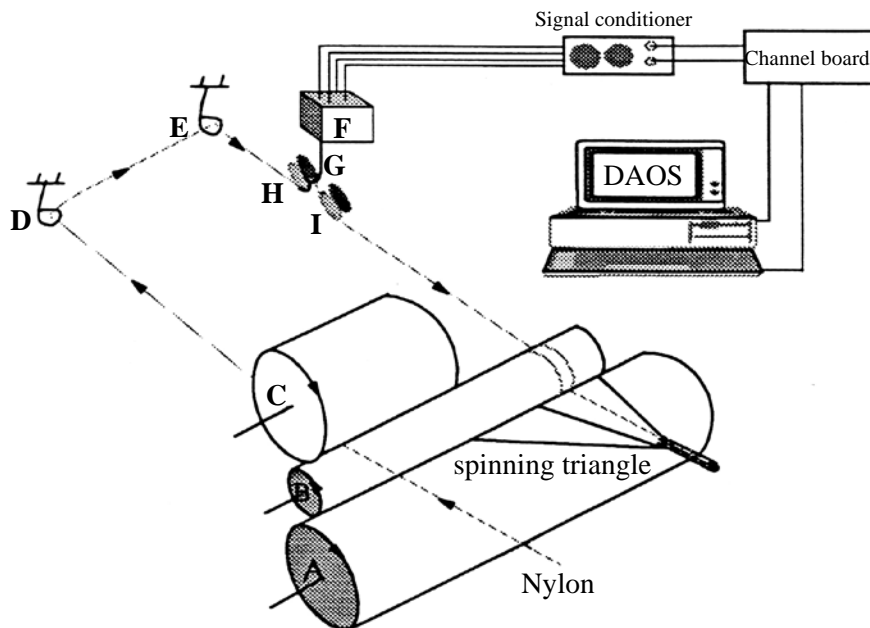


Figure 2.13 Schematic diagram of experimental set-up for fiber tension measurement
 A: Existing bottom roller, B: designed top roller with a narrow groove, C: free rotating additional top roller, D&E: yarn guide, F: strain gauge, G: strain gauge hook attachment, H&I: free rotating pin, DAOS: data acquisition operating system. [20]

The tension of the nylon monofilament can be detected by a designed tensiometer, which includes a strain gauge (F), a hook attachment (G), and two free rotating pins (H and I). The stress of nylon monofilament and wool fiber is assumed to be equal, and then the wool fiber tension F_{wool} can be calculated from that of nylon F_{nylon} with the cross sectional areas of wool fiber and nylon monofilament (A_{wool} and A_{nylon}):

$$F_{\text{wool}} = F_{\text{nylon}} \cdot \frac{A_{\text{wool}}}{A_{\text{nylon}}} = F_{\text{nylon}} \times 0.22 \quad (2.17)$$

Then the output signal of wool fiber tension can be achieved by calibrating the

measured tension of nylon monofilament using DAOS. Figure 2.14 shows the tension force patterns of wool fiber in the spinning triangle at two different yarn twist levels. It is noted that the tension of fibers in spinning triangle is always changing with time.

This is an original and valuable measurement system developed for examining fiber tension forces. Nevertheless, the performance of monofilament is obviously different from that of wool fiber, and the devices worked on the long path of monofilament and the precision of measured fiber tensions using this direct measurement method were unverified.

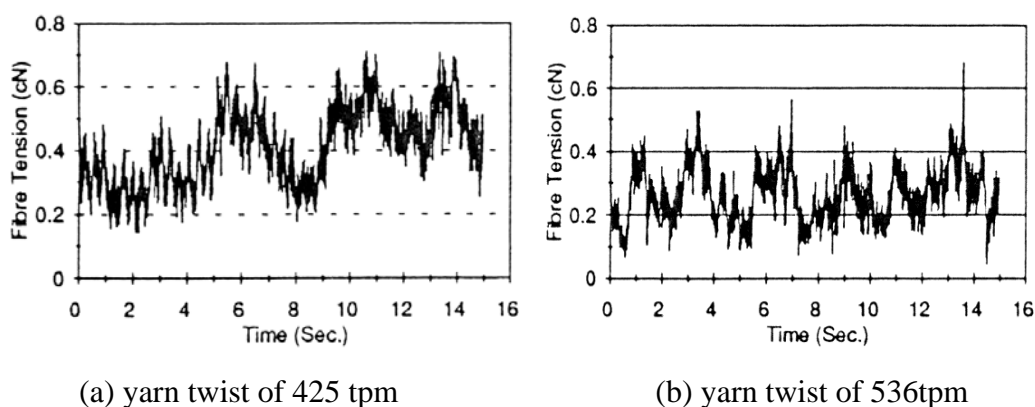
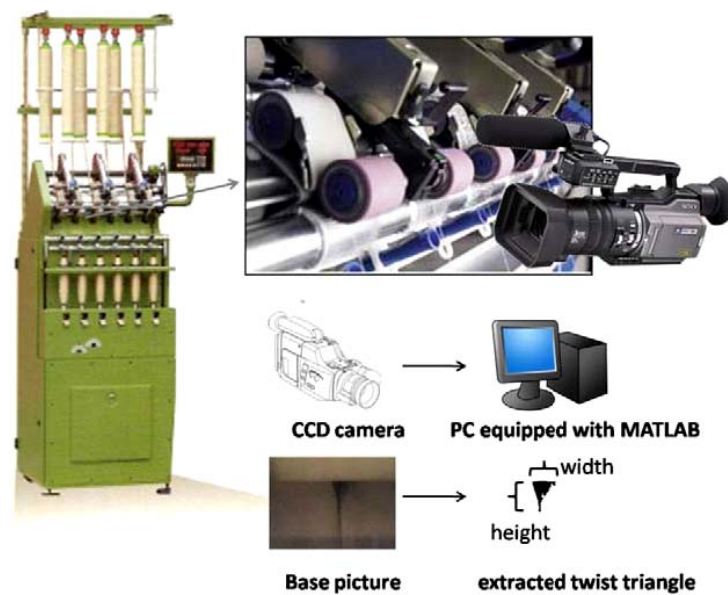


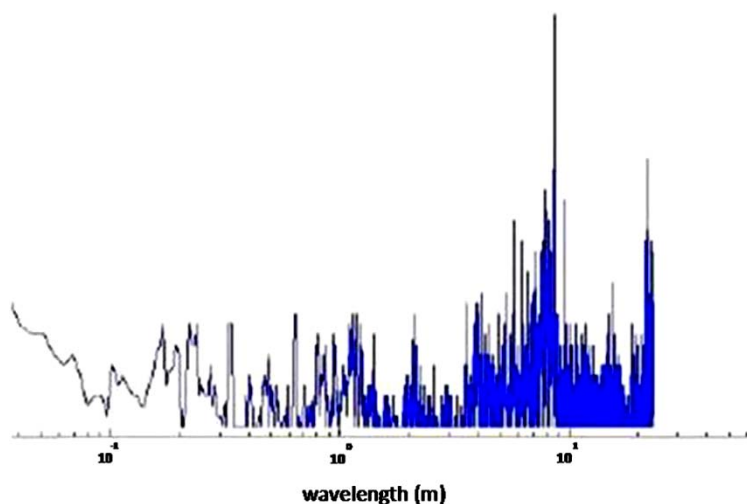
Figure 2.14 Tension force patterns of wool fiber in the spinning triangle [20]

Badehnoush and Yazdi [28] presented a non-contact approach for the online measurement of spinning triangle dimensions (width and height) by using machine vision and image-processing techniques for examining the relationship between

changes of spinning triangle and evenness of the finally produced yarn. Figure 2.15(a) shows the experimental set-up for capturing the spinning triangle by CCD camera. Three spinning triangle parameters, including width, height and area, can be measured. Figure 2.15(b) shows an example of the spectrogram of measured triangle area, demonstrating a variation of spinning triangle during yarn formation. The correlation between yarn irregularity and change in the triangle dimensions has been investigated and the acceptable correlation indicated that this image-processing approach could be implemented for measuring yarn irregularities during the spinning process. The drawback of this system is the low frequency rate (25fps) of the CCD camera employed, and if a high-speed camera was applied in the system, high-frequent change of spinning triangle could be obtained.



(a) experimental set-up to capture the triangle behaviour during yarn production



(b) spectrogram of triangle area

Figure 2.15 CCD system to capture spinning triangle and the relevant result [28].

2.2. Analysis of yarn internal structure

Generally, the physical properties and arrangement of fibers inside the yarn determine the geometric and physical performance of yarn. The investigation of yarn internal structure can be broadly divided into two categories [29]: cross section technique for yarn packing density and tracer fiber technique for fiber migration behavior.

2.2.1. Cross section technique

In the cross section method, fibers in a yarn are locked in their original positions by means of a suitable embedding medium, and then the yarn is cut into a series of thin sections for systematic study under microscope. [Figure 2.16](#) shows an example of a

cross-sectional image captured by microscope.



Figure 2.16 Cross-sectional image of a high-twist ring spun yarn (Tencel) [32].

With the assumption of fiber concentric helical configuration, the yarn cross-section can be divided into several annular zones by drawing the concentric circles of equal width or equal area for the calculation of fiber packing density. With the advances of image processing method, besides the study of fiber distribution in yarn cross section for fiber packing density [32, 81-82], this method can also be used for fiber recognition [83-85] and evaluation of fiber fineness and maturity [86].

2.2.2. Tracer fiber technique

Tracer fiber measurement developed by Morton and Yen in 1952 [31] is a popular method to study yarn internal structure by tracing the path of individual colored fibers in a yarn. In this method, an extremely small percentage (less than 1%) of dyed tracer fibers is introduced and adequately blended with the undyed fibers before

yarn spinning. The yarn containing the tracer fibers will be immersed in a transparent liquid whose refractive index is very close to that of the undyed fibers so that they can be optically dissolved. The yarn becomes almost transparent and the path of a colored fiber can be clearly followed. Figure 2.17 shows an example of the path projection of a fiber migrating over the yarn cross section. This method has been widely used for investigating the migration behavior of fibers inside staple yarns produced by different spinning methods [30-50].

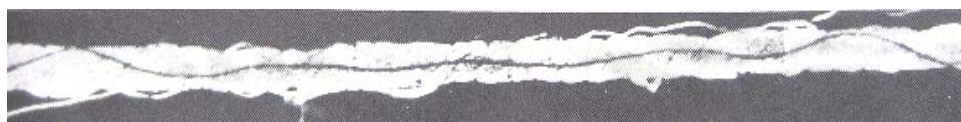


Figure 2.17 A section of a spun yarn with tracer fiber by Hearle and Gupta [38].

Based on this principle, researchers further extended the tracer fiber method by employing fiber of different colors in the same segment of yarn so as to observe yarn rupture occurred in a mixed mode of fiber breakage and slippage [37], proportion of broken fibers in failure zone [37], and yarn structure during extension [41-43]. Using more different colors of tracer fiber can provide a more accurate analysis of yarn internal structure and migration behavior while, of course, the computational complexity for automatic identification of these fibers will be substantially increased.

Further to two-dimensional (2D) investigation of tracer fiber and yarn, researchers have also developed valuable devices and methods for investigating fiber three-dimensional (3D) configurations based on the tracer fiber technique. The devices can be mainly classified into three categories: (1) Hi-scope video microscope system [48-49], (2) measurement system based on depth from focus [50], and (3) measurement system for two views of yarn by using a mirror [38-46].

2.2.2.1. Hi-scope video microscope system

Zhang et al. [48] and Fu et al. [49] employed a Questar Hi-scope video microscope system (as shown in Figure 2.18) to measure the 3D trajectory of a tracer fiber inside rotor spun yarn and compact spun yarn, respectively. The Questar Hi-scope video microscope system consists of an optical head, CCD camera, fiber-optic cable, and corresponding interfaces. The optical head, including an illuminating device, fixed focus lens, zoom lens and optional 3D rotating-head, is held to capture an image freely at any angle. The 3D rotating-head contains two synchronously rotating reflectors. Reflector 1 is placed in the center and inclined at 45° to the visual axis while reflector 2 is mounted on a rotating hoop. The optical head can be adjusted to capture two orthogonal profiles of the yarn and then the spatial trajectory of tracer fiber can be obtained by measuring the relevant coordinate values.

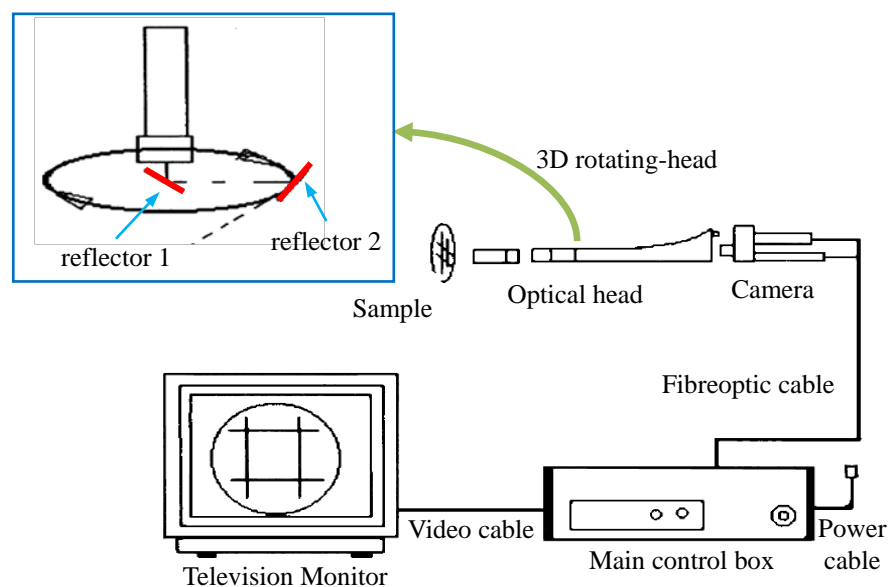
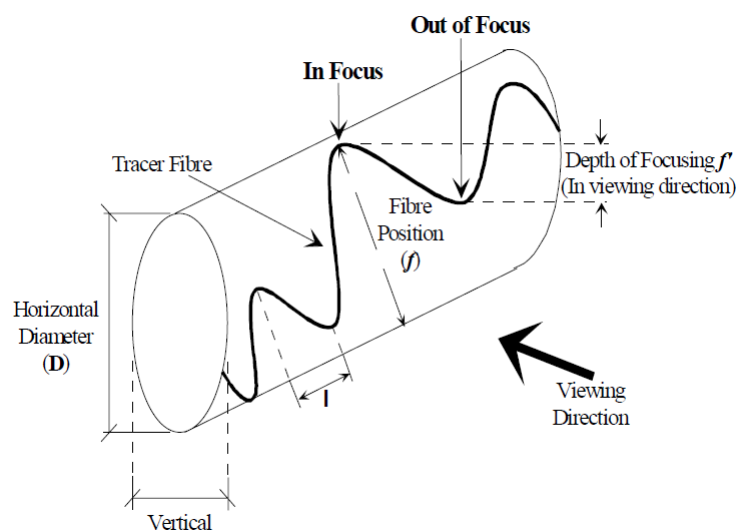


Figure 2.18 Standard Hi-scope video microscope system [48].

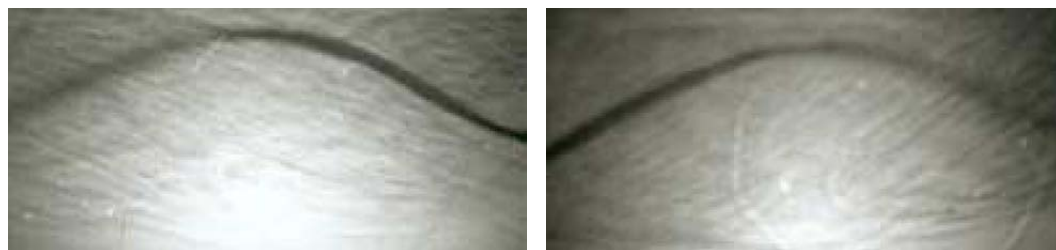
2.2.2.2. Measurement system based on depth from focus

Primentas and Iype [50] utilized the focusing depth of a microscope as a measure for accurately tracing the fiber position inside yarn body. Figure 2.19 shows a small length of yarn (around 1mm) which is viewed at a high magnification ($\times 40$), and the focus is highly dependent on the relative position of tracer fiber with respect to yarn body. The position of tracer fiber is obtained by the screen co-ordinate and the rotary position of focusing knob. The angles of focusing depth can be measured by a protractor fixed on the focusing device and their differences can be converted to rotary position. Therefore, the length of yarn l , the horizontal diameter D of yarn, and two distances f and f' of tracer fiber in two orthogonal views can be obtained for the 3D fiber configuration. This method for 3D observation of tracer fiber is just in

the embryonic stage of development [50].



(a)



(b)

(c)

Figure 2.19 Measurement principle and images based on depth from focus [50].

(a) Graphic presentation of yarn; (b) image of a focused and an unfocused parts of a tracer fiber (an indication of 149°); (c) image of a focused part which is unfocused in [Figure 2.19\(b\)](#) (an indication of 193°).

2.2.2.3. Measurement system for two views of yarn by using a mirror

Riding [46] experimentally observed fiber migration inside a spun yarn by using a

new measurement method in which the yarn was simultaneously viewed from two perpendicular directions. As shown in Figure 2.20(a), the apparatus mainly consists of a light source, a mirror, a microscope, liquid and a transparent trough. The plane mirror near the yarn is placed in liquid at 45° to the direction of light source and the light source is arranged perpendicular to the microscope. Therefore, the projection of yarn and its image in the mirror, which represents two perpendicular views of the yarn, can be simultaneously obtained by the microscope, as shown in Figure 2.20(b).

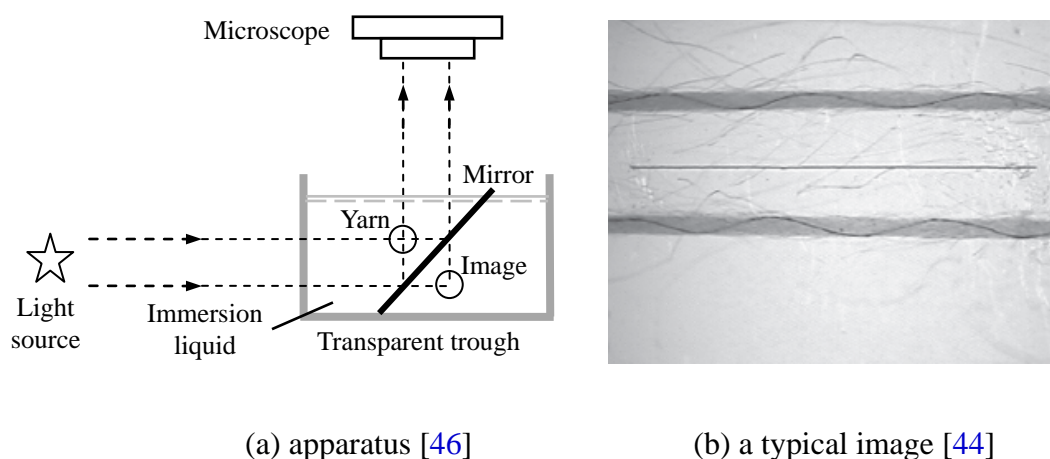


Figure 2.20 Apparatus for observing the yarn and its image in mirror.

Based on the obtained images, the positions of a tracer fiber trajectory can be measured in pixels, as shown in Figure 2.21 [45]. The positions of each tracer fiber are determined by the points (x_i, y_i, z_i) referring to the position of yarn surface (UB_{1i}, LB_{1i}) and (UB_{2i}, LB_{2i}) at the yarn axis z_i , where i represents the number of data sample along the yarn axis. To give a general view of the structural characteristics

of a staple yarn, trajectories of tracer fibers can be further reconstructed and visualized for a 3D analysis of fiber migration and yarn structure.

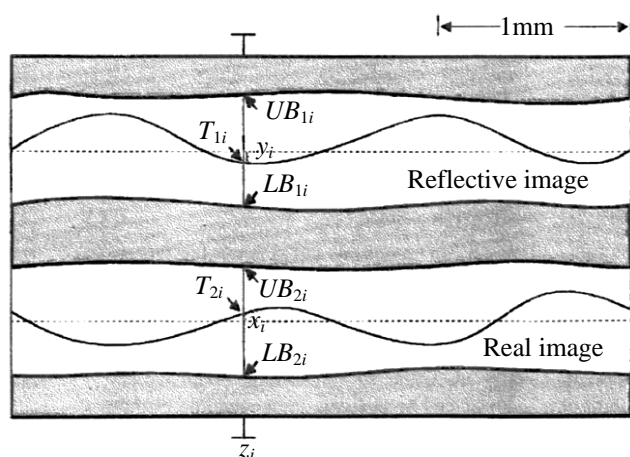


Figure 2.21 Measurement of tracer fiber and yarn surface [45].

This method has been widely adopted in later studies [38-45] and it currently becomes more popular for 3D analysis of fiber migration in the yarn. Because of the high magnification employed in the image acquisition process, a series of yarn images will be captured and each image contains only a part of the tracer fiber. In order to get the information of a whole tracer fiber in the yarn, many individual images have to be stitched into a composite image (panorama) for further processing.

2.2.3. Image mosaic

Image mosaic (or called image stitching) is a global transformation process, which combines several individual images having overlap into a composite image [87]. It

can be used for the creation of panoramic images by integrating a continuous sequence of overlapped images. [Figure 2.22](#) shows an example of panoramic photo stitched by a pair of overlapped photos.



(a) photo 1 of Honolulu (b) photo 2 of Honolulu (c) creation of image mosaic

Figure 2.22 An example of image mosaic [88].

The automatic image stitching has received substantial attentions in computer science and many matching methods have been proposed to mosaic the images into a panorama, such as scale invariant feature transform (SIFT) [89], speeded up robust feature (SURF) [90], RANdom SAmple Consensus (RANSAC) and phase correlation [91]. They are generally based on two principles: (1) direct (pixel-based) alignment for pixel-to-pixel matching; and (2) feature-based alignment. Besides SIFT and SURF, corners, blobs, harris corners and difference of gaussian of harris corners (DoG) are distinct and repeatable features for image stitching.

There are also several panorama commercial software systems available for stitching images into seamless panoramas, such as Hugin [92], MergeMagic [47], Spin

Panorama [30] and Panorama Maker [93-94]. Some of them have been employed for stitching tracer fiber images. Basal and Oxenham [30] applied Spin Panorama to stitch the tracer fiber images with a single view of vortex yarn and the panoramic image is shown in Figure 2.23. The tracer fiber image in Figure 2.23 shows distinct yarn hairs but the tracer fiber is not clear enough to be automatically detected in image segmentation. Zou et al [47] used the software MergeMagic to seamlessly stitch the partially overlapped single-viewed tracer fiber images into a large image with a whole fiber trajectory inside the vortex spun yarn, as shown in Figure 2.24.

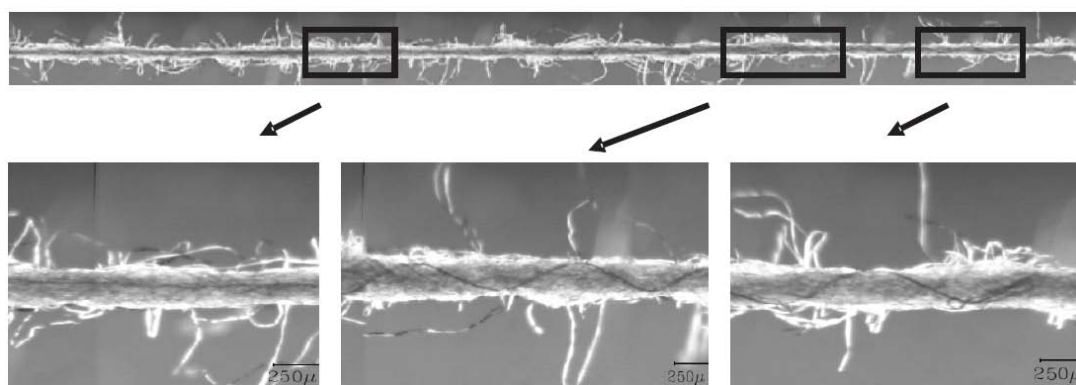


Figure 2.23 Stitched tracer fiber image of vortex yarns using Spin Panorama [30]

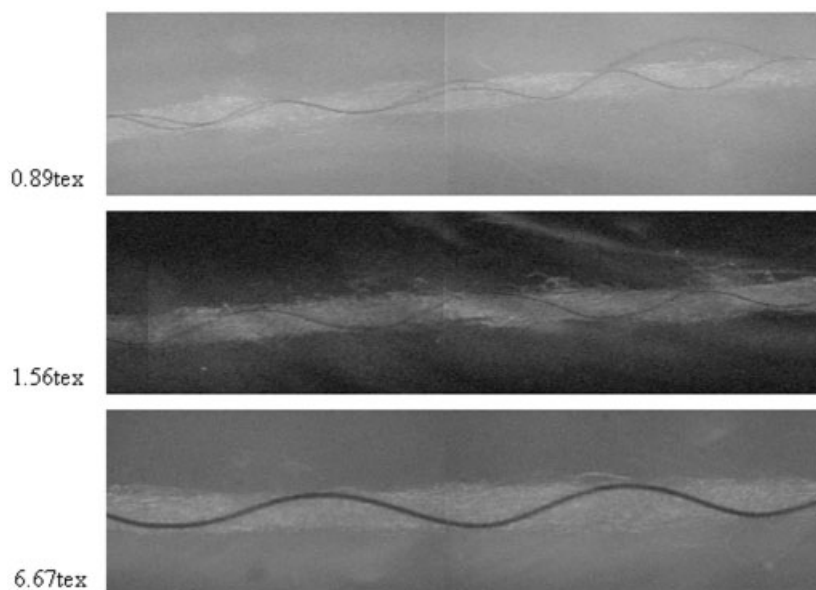


Figure 2.24 A part of panoramas by MergeMagic with different fineness yarn [47].

In the above two studies, however, the tracer fiber image just contains a single view of yarn. For the tracer fiber images involved in this study, the general methods or software are not suitable in most cases because: 1) the images contain two views of yarn observed from two perpendicular directions, and the yarn position and the distance between the two views of yarn are always changing due to yarn movement during image acquisition; and 2) the images have a highly repetitive pattern and are extremely similar to each other.

2.2.4. Yarn segmentation

In order to extract the appropriate information from a yarn image (e.g. separation of tracer fiber from the body of yarn, or yarn boundary from background), it is

necessary to process the image by image segmentation. In the past, various segmentation algorithms have been developed to extract yarn body and hairiness from the yarn image [95-108].

2.2.4.1. Optical method

Carvalho et al. [109-111] developed an automatic yarn characterization system by using optical sensors to measure yarn hairiness and diameter directly. Figure 2.25 shows the hardware of this system. In this system, laser diode is the illumination source, L1, L2, L3 are plano-convex lenses, O is an objective plane where yarn sample is placed, F is a spatial filter and I/PD is a photo detector. This optical setup can be used to conduct the hairiness measurement (see Figure 2.26(a)) with a high-pass spatial filter. A coherent light from the laser diode is incident on a collimating lens (L1) and then directed to the yarn placed in the object holder (O). A spatial filter with 1 mm of opaque target (F) placed in the Fourier plane of L2 blocks all spatial frequencies below 10mm^{-1} . The size of the final image detected by the photodiode array (I/PD) is controlled by the lenses L2 and L3. For the yarn diameter measurement (see Figure 2.26(b)), the same optical hardware is used except that the high-pass spatial filter is replaced by a low-pass spatial filter, blocking all spatial frequencies above 10mm^{-1} .

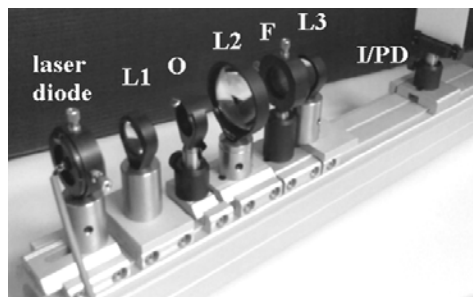


Figure 2.25 Developed optical yarn measurement hardware [109]

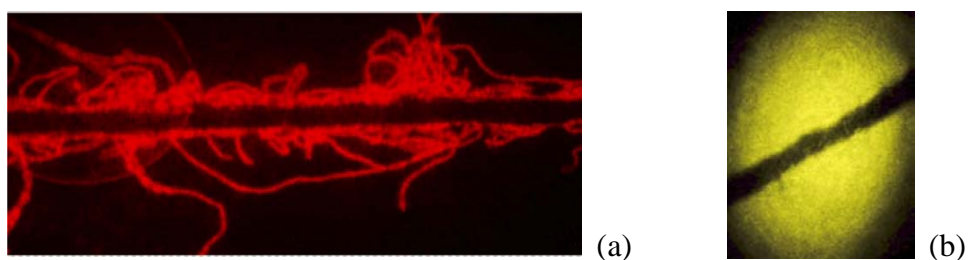


Figure 2.26 Example of an image resulting from the application of a (a) high-pass spatial filter [109], (b) low-pass spatial filter [111].

2.2.4.2. Image processing method

A yarn image generally includes background, yarn body and hairs. The main task of image segmentation is to separate yarn body and yarn hairs from the background.

As a rough segmentation, Guha et al. [107] and Chimeh et al. [105] used straight lines to approximate the yarn body from image with the assumption of a constant yarn diameter. For more accurate segmentation, thresholding method can be used for yarn body detection. Figure 2.27 shows the comparison of four histogram-based methods for yarn image segmentation. For the selection of

threshold algorithms on yarn images, Fabijańska [101] compared four kinds of histogram-based methods: (1) Otsu's method (minimizing inter-class variance), (2) ISODATA (Iterative Self-Organizing Data Analysis Technique), (3) maximum entropy method (maximizing inter-class entropy) and (4) mixture modeling (separating two Gaussian functions), and found that thresholding with the mixture modeling method provided the best image segmentation results, as shown in Figure 2.27. Besides thresholding method, Cybulska [102] proposed a method to identify yarn boundary by detecting the greatest connected intervals in each column (perpendicular to the yarn axis) of image.

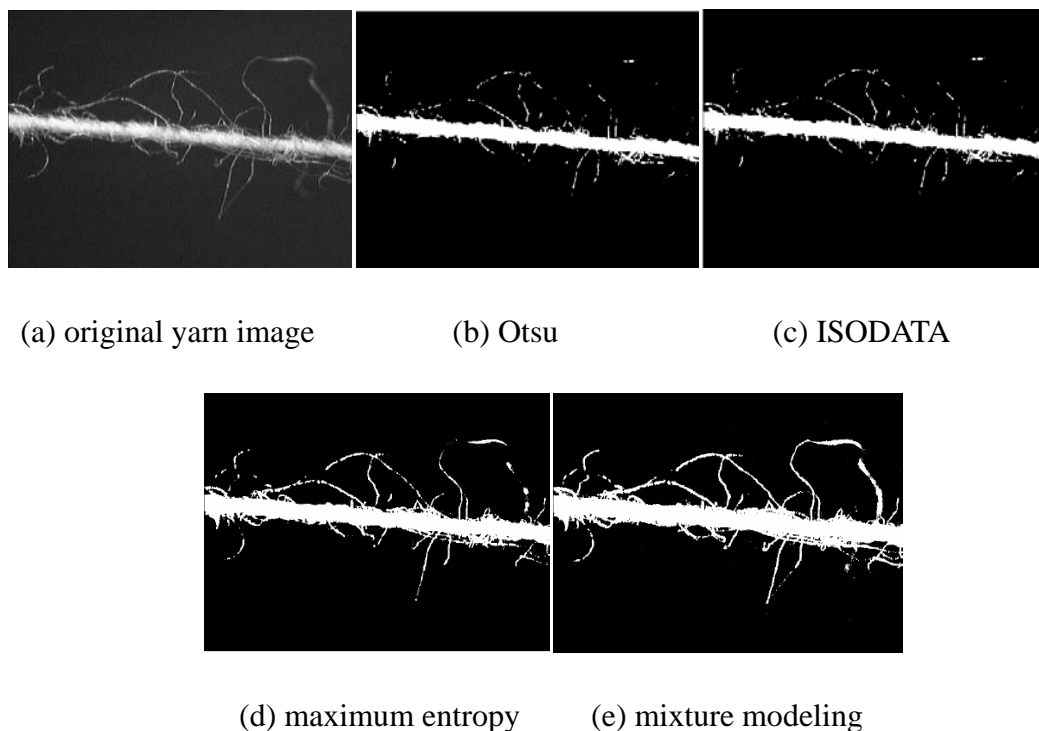


Figure 2.27 Comparison of four histogram-based methods for yarn image

For yarn hair detection, Fabijańska [99] proposed an algorithm of a region growing-based approach, where the growth of the region is guided and constrained by a coherence enhancing diffusion filter, for extracting yarn hairs from the yarn body. Figure 2.28 shows an example for segmentation of yarn body and yarn hairs by using the region growing-based approach. Fabijańska [100] also employed a graph cuts method [112] to identify yarn body, and used high-pass filtering based method for yarn hairiness extraction.

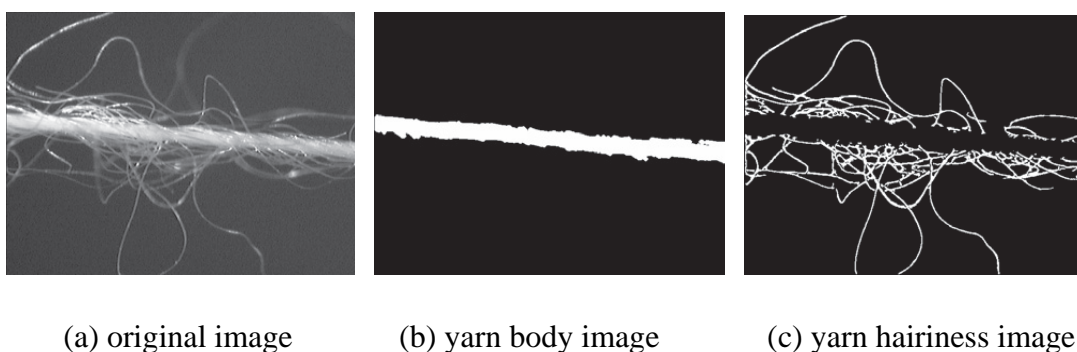


Figure 2.28 Yarn segmentation by a region growing-based approach [100]

2.2.4.3. Segmentation of tracer fiber image

For the tracer fiber images involved in this study, image segmentation becomes much more complicated because, besides the yarn body and background, tracer fiber is involved. For tracer fiber images with only a single view of measurement, Alagha et al. [113] adopted an image processing method for the detection of yarn boundary and tracer fiber. In this method, it was suggested to define a threshold

manually for yarn boundary detection. With the defined threshold, the yarn boundary can be extracted column by column. Firstly, in each column, the point, whose next ten consecutive pixels have gray level above the defined threshold, is detected as the suspended upper yarn boundary. And then the upper boundary will be confirmed by comparing these suspected points using a scanning window of adjacent pixels (15×15 pixels). The detection procedure for lower yarn boundary is similar to that of upper boundary. With detected upper and lower yarn boundaries, the tracer fiber is detected between them. In this detection, the yarn body is considered as background, the consecutive pixel with lower gray level than the threshold is identified as tracer fiber. Though Alagha et al. [113] used a simple thresholding method to separate yarn body and tracer fiber from background, it is not an automatic detection method because the thresholds have to be manually selected. Moreover, the threshold is sensitive to uneven background illumination and image quality (e.g. yarn hairs) may greatly influence the accuracy of image segmentation by using this algorithm.

For the tracer fiber images concened in this study, the image segmentation becomes more complicated because two perpendicular views of yarn are included in the image. Due to the complexity of images and presence of optical noises, in the early studies, the yarn boundary and tracer fiber had to be manually marked [30, 39, 44], and then,

the marked points were extracted from the image by using photoshop [30] or other image processing method [39, 44]. In order to analyze the structure of a spun yarn, hundreds of or even thousands of yarn images have to be processed. It is extremely time-consuming and becomes a bottleneck problem in yarn structure analysis.

2.3. Analysis of yarn surface appearance

The assessment of yarn surface quality, or so called yarn surface grading, is one of the important testing procedures in the textile industry. According to the standard testing method presented in ASTM D 2255 [51], a yarn sample is wound on a blackboard by using a yarn board winder and then compared with a series of photographic standards representing the grades A (best), B, C and D (worst), with consideration of the unevenness, fuzziness, neppiness and visible foreign matters. Traditionally it is carried out by the visual inspection of yarn sample appearance on a standard blackboard. A skilled specialist visually compares the wound yarn sample with the grade-labelled photographic standards and then judges the quality of the yarn sample according to the similarity between yarn sample and standard photograph, as shown in [Figure 2.29](#).

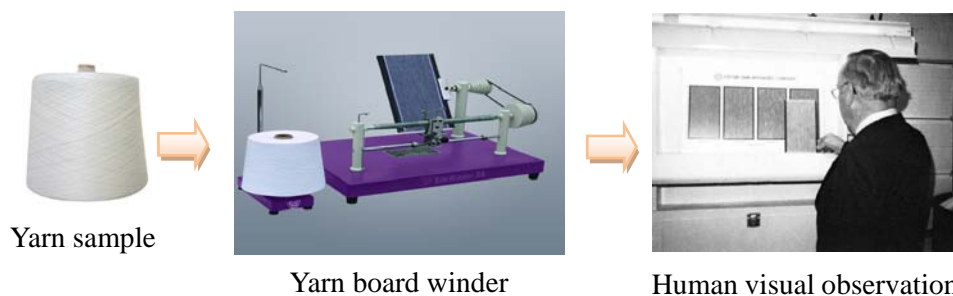


Figure 2.29 Traditional method for yarn surface evaluation

However, the traditional method is subjective, time-consuming, and sometimes inconsistent. During the past decades, the investigation on yarn analysis using image processing and artificial intelligence technologies has attracted an increasing interest of researchers [52-121]. Various image processing and analysis algorithms have been applied in the textile industry in order to measure the important parameters of yarn quality, including yarn evenness [102, 121], yarn hairiness [102-105], yarn twist [102, 106-108], yarn snarling features [96-97] and surface defects [114-116]. Some researchers also developed image processing methods for detection of yarn diameter [118] and the parameters of slub yarn [119-120].

2.3.1. Digital yarn grading methods

2.3.1.1. Yarn grading based on 1D continuous measurement

1D continuous measurement refers to the continuous measurement of yarn geometrical and physical properties when it is on moving. There are two kinds of

method for yarn classification. One is mainly based on the testing data of yarn physical properties, such as yarn strength, mass variation, yarn evenness, and neps. The other one is based on measurement data of yarn irregularity sampled from a moving yarn, such as evenness, hairiness and neps, by using different sensors, such as capacitance sensor, photoelectric sensor.

(1) Yarn property-based method

Rong et al [60] and Lien et al [57, 117] have extracted the experimental data of six yarn properties, including the coefficient of variation of yarn strength, the coefficient of variation of mass, the coefficient of variation of yarn evenness, the neps, the single yarn break strength and 100-meter mass variation tolerance, as analytical features for yarn classification. With these features, Rong et al. [60] presented a technique using splitting cluster analysis to classify polyester-fiber/cotton blended yarns into different grades. Lien and Lee [57] have graded yarns through feature selection and dimensional reduction using Karhunen-Loeve (K-L) expansion coupled with the Bayes classifier, and K-L expansion coupled with the minimum distance (MD) method. Furthermore, Lien and Lee [117] proposed an approach for feature selection by using the effective distance between clusters (EDC) for textile yarn appearance grading.

Besides, Amin [58] developed a classification model composed of a hybrid model of Artificial Neural Network (ANN) and genetic algorithm (GA) for cotton yarn quality classification. In this method, the problem of yarn quality is described in terms of eight characteristics and one target class as shown in Table 2.1. 26 input nodes and 5 output nodes were used for training the artificial neural network to obtain the weights. Then GA was applied to get the optimal values of input attributes for maximizing the output function.

Table 2.1 The attributes and their values of yarn quality of Amin [58]

Characteristics (attributes)	Nominal values
Yarn type	Carded, combed
Yarn count	Very fine, fine, medium, coarse
Yarn package	Cones, bobbin
Yarn twist	Woven, knitting
CVm %	Low, medium, high
Thin (-50%)	Low, medium, high
Thick (+50%)	Very low, low, medium, high, very high
Neps (+200%)	Very low, low, medium, high, very high
Levels (target class)	Very bad, bad, good, very good, excellent

(2) Yarn irregularity-based method

Based on yarn irregularity, there are two systems developed for yarn quality

evaluation, including Uster[®] Classimat (developed by Uster Technologies) [59] and Yarn Analysis System (developed by Lawson-Hemphill, Inc.) [65]. Both methods are based on the statistical analysis of yarn irregularity. In these methods, the capacitive or optical sensors are applied to detect the irregularity of yarn mass or absolute yarn diameter by measuring a moving yarn in a certain sampling interval.

In Uster[®] classimat, various sensors and hardware are used to detect and classify yarn defects: the capacitive sensor for the identification of thick, thin places and neps, and a novel sensor combination for the detection and classification polypropylene content. Yarn defects are classified into 23 classes based on their sizes (four thickness classes, at various levels between 100 and 400% of normal yarn linear density) and lengths (four length classifications, ranging from 1mm to 40mm). In this system, besides the fault classification based on the analysis of thick and thin places, some critical parameters, such as count variation, periodic faults, unevenness and hairiness, can also be obtained.

Lawson-Hemphill Inc has developed the Yarn Analysis System (YAS) for yarn surface grading and virtual fabric simulation [61-65]. [Figure 2.30](#) shows the optical measuring principle of the YAS grading system. A CCD camera is first used to measure the diameter of a moving yarn. Then various statistical measures of yarn

diameter, such as mean value, standard deviation, coefficient of variation, evenness, hairiness, neps, thick and thin places, can be obtained. With these features, a neural network is used for automatically grading yarn (fabric) quality. In addition, YAS can also virtually simulate yarn and fabric appearance for observation.

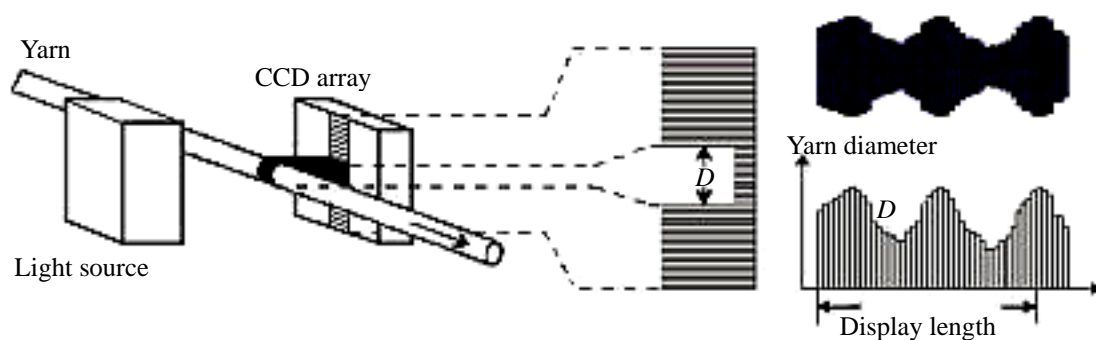


Figure 2.30 Optical measuring principle of YAS [65]. D is yarn diameter.

In all above-mentioned methods, although it was possible to define a classification for yarn appearance, a grading method based on a standard image of yarn board is found to be impossible. Most importantly, they are all based on the mechanism similar to the Uster Tester and depart from the originality of the visual grading method carried out on black boards as proposed in ASTM D2255, namely the comparison among adjacent yarn segments and the identification of other important yarn appearance features, such as yarn color variation, foreign matters and hairiness, being ignored.

2.3.1.2. Yarn grading based on 2D yarn black board

Semnani et al. [52-54] originally developed a computer vision method for evaluating and classifying yarn surface appearance on yarn black boards. In this method, a yarn fault image is obtained by eliminating yarn body and background from binary image of standard yarn board. Figure 2.31(b) shows the yarn fault image generated from yarn board image in Figure 2.31(a).

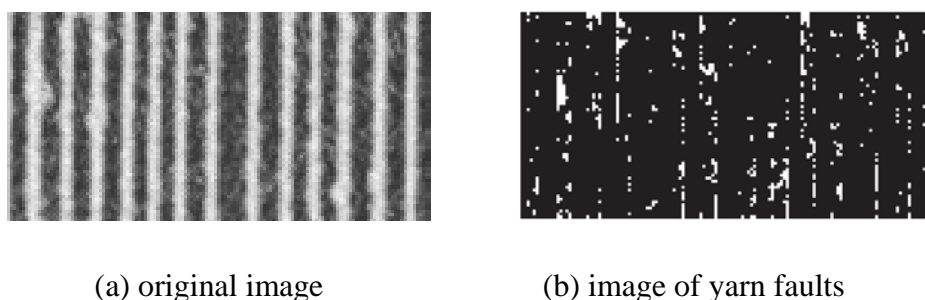


Figure 2.31 A sample for elimination of yarn body from yarn board [52]

According to fault size and the distribution of faults, yarn faults are defined into four classes. Then, four digital fault factors, PFF, PHF, PLF and PLF, were calculated from the yarn fault image, to represent the percentages of the four fault classes. With the extracted fault factors, an artificial neural network with a two-layer structure [52] was then employed to classify the grade of yarn surface appearance, as shown in Figure 2.32. Therefore, the index of yarn appearance I_D could be calculated by Equation (2.18) with consideration of the fault factor vector P and the

weight vector W :

$$I_D = W \cdot P \quad (2.18)$$

where P is a vector of fault factors [PFF, PHF, PLF, PLF]^T and W is a one-by-four vector of weights of the faults.

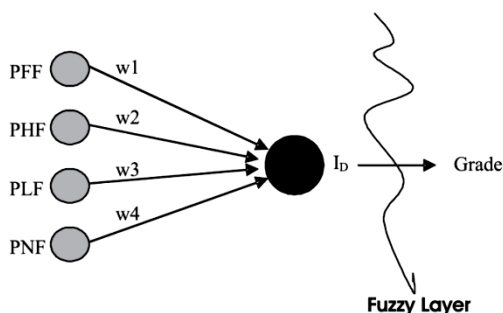


Figure 2.32 Perceptron artificial neural network with a fuzzy layer [57].

Although this method somehow enables the identification of thick places and the classification of yarn appearance from a standard yarn board image, the local thin places cannot be recognized because the feature has to be removed from thick places together with yarn body in the algorithm. In addition, yarn color variation, foreign matters and hairiness were neither identified.

Liang et al. [55] proposed an integrated computer method for digital characterization and evaluation of yarn surface appearance by using saliency map, wavelet transform and fuzzy ARTMAP neural network. In this method, a total of eighteen digital features, including three attention-driven fault features, four wavelet texture features

and eleven yarn statistical features, were extracted and used for characterization of yarn surface appearance in terms of unevenness and fuzziness. The digital features were extracted from yarn body image, hairiness image and the attention-driven fault image, respectively. Figure 2.33 shows the process of attention-driven fault detection. As shown in Figure 2.33, the saliency map is generated from a width map solely composed of yarn diameters and the attention-driven fault features include fault number F_N , fault grade F_{value} and fault size F_{size} , representing visual differences. The wavelet texture features are also formulated to represent the fuzziness of hairiness by calculating wavelet energies under four different mother wavelets.

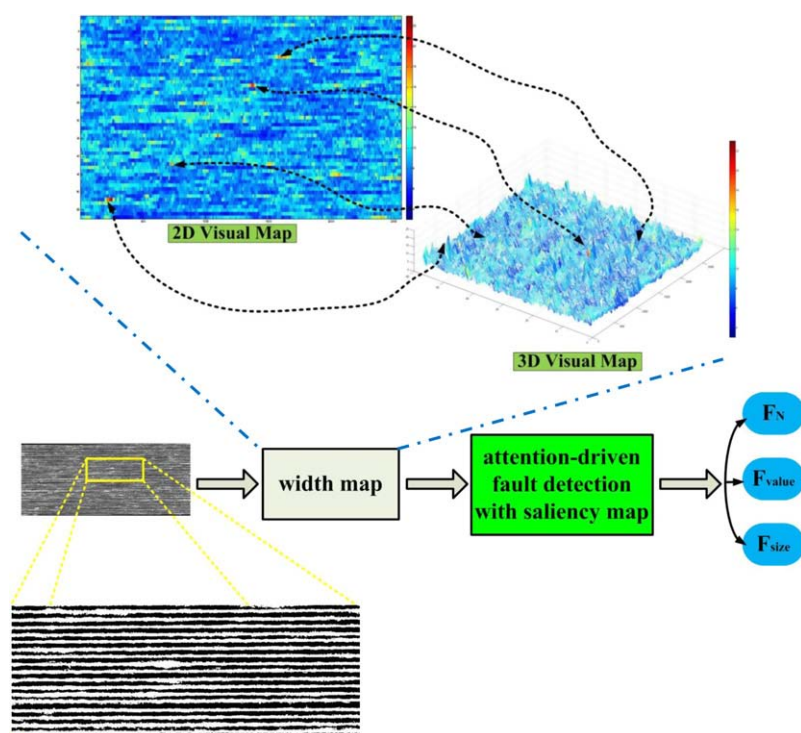


Figure 2.33 The process of attention-driven fault features detection [55].

With the above eighteen digital features, a fuzzy ARTMAP (FAM) neural network was employed to classify and grade yarn board images using supervised learning technique and multidimensional map. As shown in Figure 2.34, the FAM neural network consists of two ART_a and ART_b modules which are linked by a map field F^{ab} [122]. During the learning process, ART_a module receives input patterns while ART_b module receives target patterns which are the correct predictions of the input. Functions of the two modules can be treated as clusters in the input domain and output domain, respectively. On the other hand, the map field ensures autonomous system operation in real time and enables the efficient and accurate learning of FAM neural network and thus minimizes predictive error and maximizes predictive generalization.

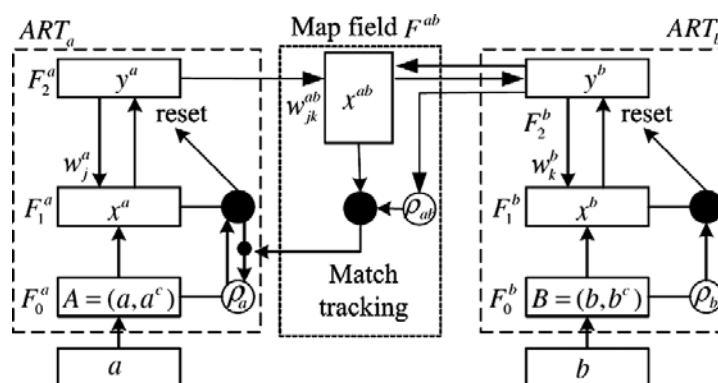


Figure 2.34 Fuzzy ARTMAP architecture [122]

Since the saliency obtained by traditional model [123] is only workable in a single image and cannot be used for a comparison between or among different images (e.g.

different grades of yarn), Liang et al. [56] further developed a visual attention model for evaluation of the saliency of different yarn board images by using an integration of bottom-up and top-down attention mechanisms. By this way, relative saliency can be compared for the cases where other image contents are involved. In the model, two levels of feature (high-level, low-level) and three types of feature (global, local-local, local-global) are extracted to characterize the differences among multiple images. In order to differentiate different yarn qualities, a mapping method is used to associate features with the ideally given saliency value. Figure 2.35 shows an example for fitting curve of one feature. Based on the discrimination among different grades, a simple classifier, K-means, is used to classify yarn grades.

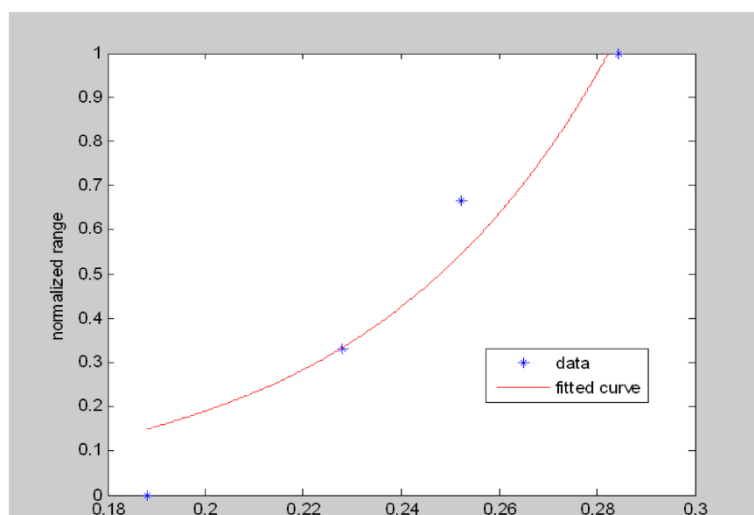


Figure 2.35 Example of fitting curve for one feature [56].

The above methods [55-56] accords with the evaluation mechanisms by enabling the comparison among adjacent yarn segments on the black board. However, as the

most important algorithm of these methods, saliency map of attention model, was only generated from yarn diameters [55] or binary image of yarn body [56], and therefore, other important characteristics of yarn surface appearance such as yarn hairs, color variation and foreign matter cannot be considered. They cannot fully imitate human visual behavior in the inspection and appraisal of yarn surface quality on black boards according to the standard ASTM D2255.

2.3.2. Attention model

Human visual fixation behavior is driven both by sensorial bottom-up mechanisms and by high order task-specific or goal-directed top-down mechanisms [124].

Visual saliency refers to the physical, bottom-up distinctness of image details, which depends on the degree to which a detail is visually distinct from its background [124].

The model of visual attention based saliency map is designed for identifying something different from its surroundings.

The saliency based attention model has received substantial attentions in computer science and various attention models have been developed for different applications.

These models can be generally divided into two categories of static attention model [123, 125-133] for image detection and dynamic attention model [134-137] for video detection.

2.3.2.1. Static attention model

The static attention model can be further divided into three categories [128] with local [123,129-132], global [133] and normality contexts [125-127]. In the model of local context, the salient objects are contrasted and compared to their surroundings, such as Itti model [123], attention based on information maximization (AIM model) [130], graph-based visual saliency (GBVS) [131]. For the model with global context, salient objects are different from all the others in the image. While in model of normal context, salient objects imply differences to what the normal image would be, such as spectral residual approach (SR model) [125] and saliency using natural statistics (SUN) [127].

(1) Itti model

Itti et al. [123] originally proposed a famous attention model by analyzing the image by different channels: colors, intensity and orientation, to identify the conspicuity region in the image called saliency map. [Figure 2.36](#) shows the general architecture of the Itti mode.

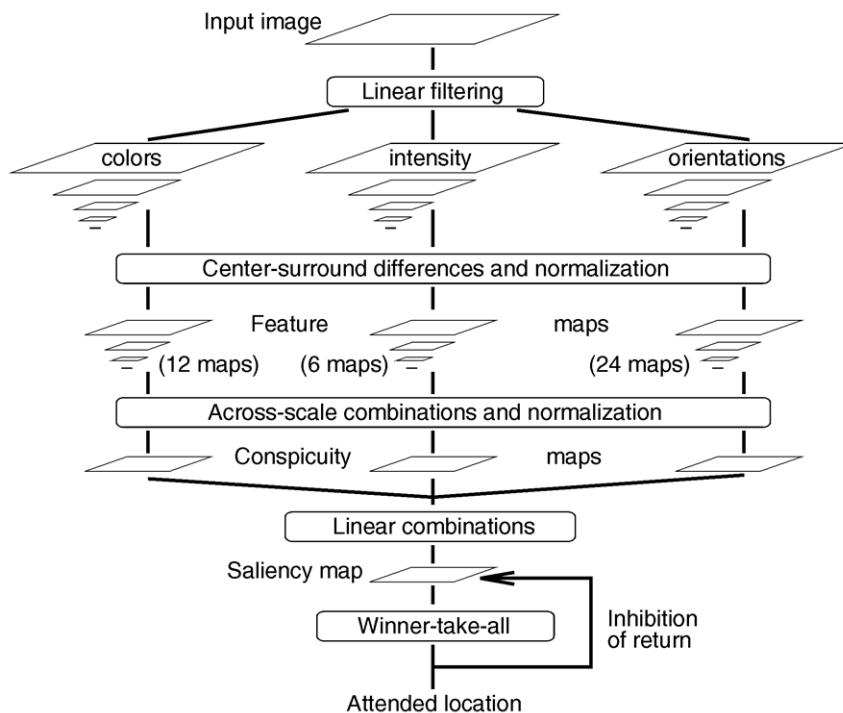


Figure 2.36 General architecture of the Itti model [123].

Figure 2.37 shows an example of processing of Itti model with a natural image, according to the general architecture in Figure 2.36. In Figure 2.37, a visual input image is first decomposed into three conspicuity maps for color contrasts \bar{C} , intensity contrasts \bar{I} and orientation contrasts \bar{O} . Different spatial locations compete for saliency within each map, and then these maps are combined into a single topographical saliency map S . It is noted that two attentive objects, i.e. the orange telephone box and the white sign, are detected as salient locations by Itti model, which accords with our visual attention.

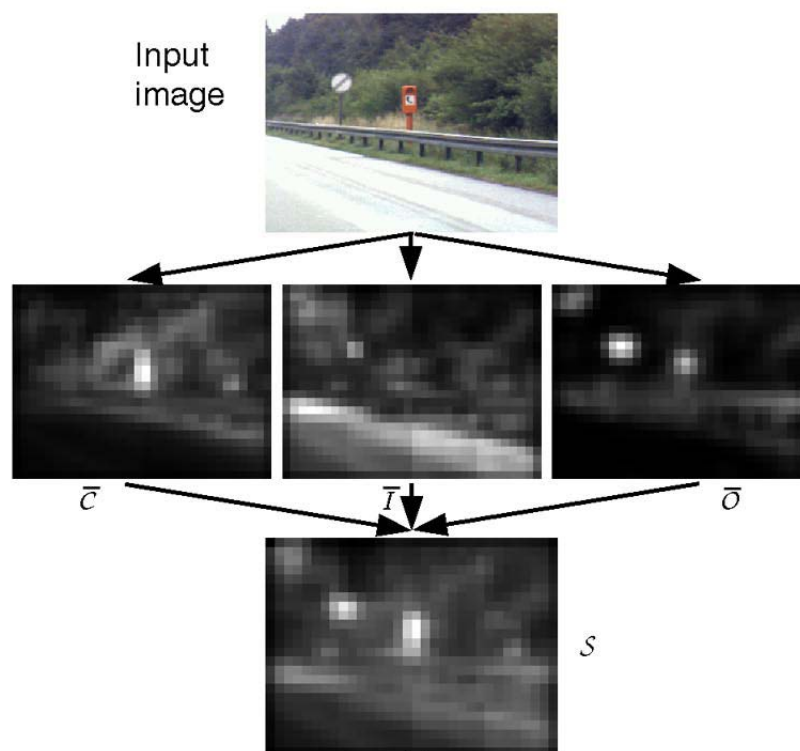


Figure 2.37 Saliency map generation by using Itti model. [123]

(2) Spectral residual approach (SR model)

Hou and Zhang [125] have developed a spectral residual approach (SR model) for generating saliency map by using the Fourier analysis. They believed that an image information is composed of a novelty part and redundant information. The redundant information can be represented by the log spectrum of each image. In the study of Hou and Zhang [125], a local average filter was adopted to approximate the general shape of log spectra, which is given as prior information.

Strategy of the spectral residual model can be described by Equations (2.19) ~ (2.22).

They analyzed the log spectrum $L(f)$ of input image $I(x)$ and obtain the spectral

residual $R(f)$ by removing the smoothed log spectrum $h_n(f) \times L(f)$ from the original log spectrum $L(f)$. Then the spectral residual $R(f)$ was transformed to spatial domain to obtain the saliency map $S(x)$.

Amplitude of image in Fourier transform is:

$$A(f) = R(F[I(x)]) \quad (2.19)$$

where $I(x)$ is an image, F denotes the Fourier transform and $R(F[I(x)])$ is the amplitude of $I(x)$.

And the phase spectrum $P(f)$ of image $I(x)$ is:

$$P(f) = \Im(F[I(x)]) \quad (2.20)$$

where \Im is the operation for phase spectrum.

Log spectrum $L(f)$ can be obtained by:

$$L(f) = \log(A(f)) \quad (2.21)$$

where \log denotes the natural logarithm of $A(f)$.

Therefore, spectral residual $R(f)$ of image $I(x)$ can be expressed as:

$$R(f) = L(f) - h_n(f) \times L(f) \tag{2.22}$$

where $h_n(f)$ is an average filter with a $n \times n$ matrix.

Finally, saliency map $S(x)$ of image $I(x)$ can be obtained by:

$$S(x) = g(x) \times F^{-1}[\exp(R(f) + P(f))]^2 \tag{2.23}$$

where F^{-1} denotes the Inverse Fourier Transform and $g(x)$ is a Gaussian filter.

Figure 2.38 shows the strategy of spectral residual model described by Equations (2.19) ~ (2.22) with an input nature image. The spectral residual contains the innovation of an image and the output saliency map denotes primarily nontrivial part of the scene. The higher saliency values (i.e. the brighter color) in the saliency map represent a more attractive part, which is a house in the scene.

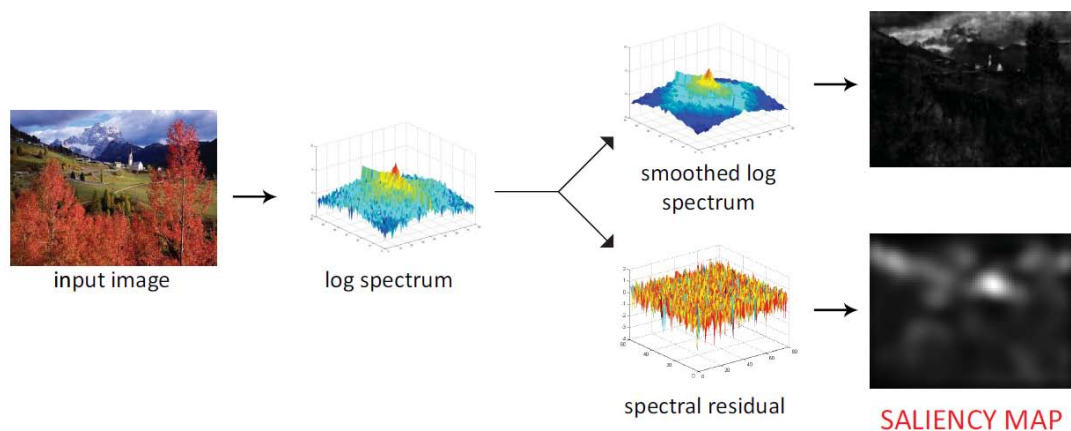


Figure 2.38 Spectral residual approach [125].

(3) Attention based on information maximization (AIM model)

The AIM model proposed by Bruce and Tsotsos [129-130] is a kind of attention model based on the principle of maximizing information sampled from the scene. The framework of AIM is illustrated in [Figure 2.39](#), which can achieve an estimate of the likelihood of contents within the central patch C_k on the basis of its surround S_k . In this method, firstly, the independent features, i.e. independent component analysis (ICA) coefficients, are extracted from each local neighborhood of the image. Then ICA can be performed on a large sample of color image patches drawn from natural images to determine a suitable basis. Afterwards, an estimate of a coefficient distribution of each single basis across the entire image can be produced by a probability density estimation. Any given coefficient may be readily converted to a probability by looking up its likelihood from the corresponding coefficient probability distribution derived from the surround. The product of all the individual likelihoods corresponding to a particular local region yields the joint likelihood. Then the joint likelihood can be translated into Shannon's measure of self-information. Finally, the resulting information map could depict the saliency attributed to each spatial location based on the aforementioned computation. Referring to the input image of [Figure 2.39](#), attention objects, such as desk lamp and bottle, are well identified and shown in the output saliency map by AIM.

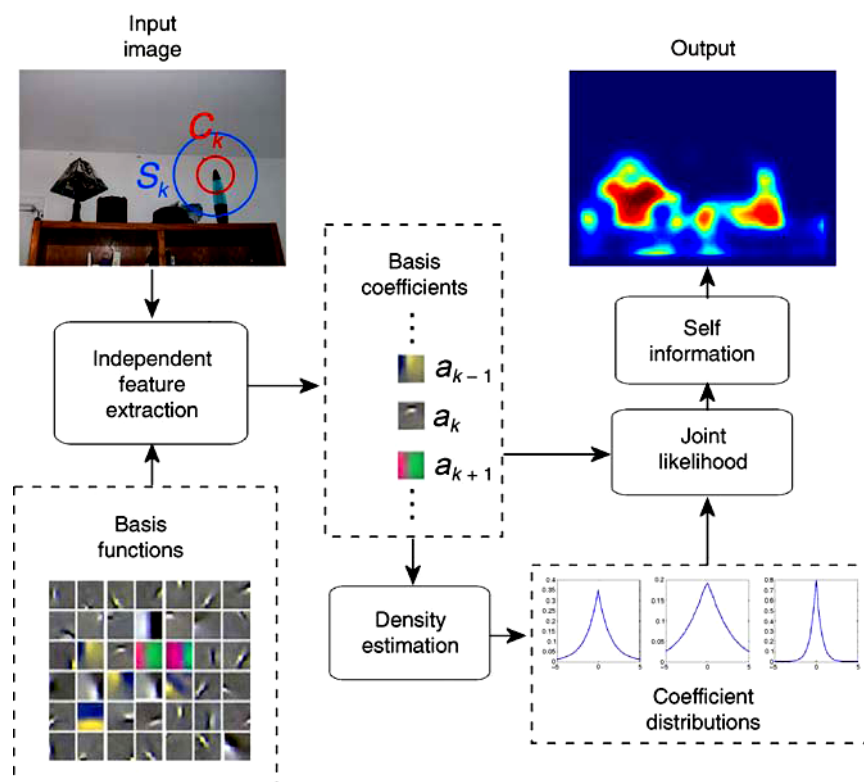


Figure 2.39 The framework of AIM [130].

Most of the attention models present a better performance when the saliency maps are generated from the image with lower-level resolution (typically 64×64 pixels), such as Itti model [123], graph-based visual saliency (GBVS) [131], spectral residual approach [125] and image signature [126]. While some attention models can be applied to high-resolution images, such as information maximization (AIM model) [129-130] and saliency using natural statistics (SUN) [127]. In this study, the attention models will be employed to detect the saliency of yarn board image for yarn surface appearance evaluation. Based on different image resolutions, two attention models, i.e. spectral residual (SR) model and attention model based on

information maximization (AIM), will be used in this study to imitate human visual attention on yarn surface grading with consideration of both a whole and a detailed yarn information.

2.3.2.2. Dynamic attention model

For the above-mentioned static attention models, they mainly work on single image and the generated saliency map can reflect the conspicuity within its own image [56].

On the contrary, dynamic attention model has been developed for analyzing dynamic saliency of scenes (or video). The dynamic saliency models, such as Coding Length Increment method [134], SUNDAY [135], Self-Resemblance model [136] and Bayesian Surprise model [137], are generally developed for dynamic visual search in video saliency generation, which largely depends on the difference of context between two neighboring frames in the same location. They are suitable to detect novel contents in the video with the same background. For the yarn board images involved in this study, they are separate and independent images. If considering the yarn faults as innovation information and the normal yarn as background, they do not have the same background because the locations of yarn body will be different from each other. Therefore, the dynamic attention models are not suitable for the saliency detection of yarn board image.

2.4. Summary

In this chapter, prior work on the spinning triangle, structure analysis and surface evaluation of spun yarns has been broadly reviewed. For spinning triangle, most theoretical models currently in use were based on the energy method. Due to the limitations of these models, some important mechanical properties of spinning triangle were not considered, such as inclined angle of yarn spinning tension, fiber torsion strains and fiber frictional contact with bottom roller. In addition, experimental measurements showed that yarn formation in spinning triangle is a real dynamic process. Particularly, with some recent developments in staple yarn spinning, working condition of spinning triangle becomes more complicated and thus it requires a more generalized dynamic model to analyze the physical properties of constituent fibers in the spinning triangle.

In yarn structure analysis, most of the existing methods or softwares for image mosaic are used for stitching nature images or images with significant features. For the two-viewed tracer fiber images concerned in this study, they are not suitable in most cases because: 1) the images contain two views of yarn observed from two perpendicular directions, and the yarn position and the distance between the two views of yarn are always changing due to yarn movement during image acquisition;

and 2) the images have a highly repetitive pattern and are extremely similar to each other. Besides, image segmentation for yarn structure analysis becomes more complicated because of three components of yarn body, background and tracer fiber involved. Therefore, the mosaic and segmentation methods currently in use largely involve manual operations. In order to analyze the structure of a spun yarn, hundreds of or even thousands of yarn images have to be processed. It is extremely time-consuming and becomes a bottleneck problem in the yarn structure analysis. Therefore, it is necessary to develop an automatic and efficient digital method and system for mosaic and segmentation of the two-viewed tracer fiber images for yarn structure analysis.

According to the standard of ASTM D2255, human visual inspection is adopted for the evaluation of yarn surface appearance with the consideration of various influential factors, such as yarn unevenness, fuzziness, neppiness and visible foreign matter. It is subjective, time consuming and sometimes inconsistent. There are currently two methods for digital evaluation of yarn surface appearance. One is based on 1D continuous measurement of yarn geometrical and physical properties. However, it is not performed on black board and departs from the originality of the visual grading method carried out on black boards as proposed in ASTM D2255, namely the comparison among adjacent yarn segments and the identification of other

important yarn appearance features, such as yarn color variation, foreign matters and hairiness, being ignored.. The other method is based on 2D black board. Nevertheless, existing methods can not take the important characteristics of yarn surface appearance, such as yarn hairs, color variation and foreign matter, into consideration, and thus can not fully imitate human visual behavior in the inspection and appraisal of yarn surface quality on black boards according to the standard ASTM D2255. Therefore, an objective and intelligent method and system are highly required for yarn surface evaluation, which can fully imitate human behavior according to the standard ASTM.

Chapter 3 Theoretical and Numerical Analysis of Mechanical Performance of Fibers in Spinning Triangle using Finite Element Method

3.1. Introduction

In yarn formation process, yarns are eventually formed in the spinning triangle (an area between the front roller nip line and the yarn twisting point) by twisting an assembly of short or long staple fibers. Therefore the geometric and mechanical performances of spinning triangle play an important role in determining the physical performance of these yarns, such as the strength, internal torque and regularity.

In the past, the investigations on the mechanical characteristics of spinning triangle were mainly based on the force method [15-19] and energy method [20-27]. The advantage of the latter lies that the full description of geometry is not required beforehand. Based on the energy method, the numerical simulations of fiber tension distribution in a symmetric spinning triangle under different yarn counts, twist angles and spinning tensions have been conducted by Najjar [20]. Then, Hua [21] and Hua et al. [22, 23] numerically analyzed the fiber tension distribution under an asymmetric spinning triangle with and without the consideration of fiber buckling. Feng et al. [25] further introduced a relationship of the shape of spinning triangle and an imaginary

(specifically defined) inclined angle of yarn spinning tension to quantitatively study the fiber tension distribution and its relationships with the spinning parameters. However, with energy method, due to the problem of dissipated friction energy and the mathematical complexities in formulating fiber bending and torsional strains, some important mechanical properties of spinning triangle are hardly to be considered, such as the inclined angle of yarn spinning tension, fiber torsion distribution and the fiber frictional contact with bottom roller.

Therefore, in this study, a new theoretical model of ring spinning triangle will be developed using finite element method (FEM) by taking account of the above-mentioned factors ignored previously. The initial conditions of the height of spinning triangle and the fiber initial strains are developed and the algorithms of element death are employed for handling fiber buckling. Then, a series of numerical simulations are carried out to fully examine the quantitative relationships between the spinning triangle and various spinning parameters, including the spinning tension, spinning tension angle, yarn twist, yarn count and the frictional contact of fibers with bottom roller, and their influences on fiber tension and torsion distributions of spinning triangle. Moreover, simulation results of the proposed model such as fiber tension distribution under different spinning tensions and yarn twists and their influences on yarn torque are also compared with those of earlier models [20-23] and

experimental data [14].

In most existing models, the performance of constituent fibers in spinning triangle was considered as a steady-state process. However, the experimental results [20, 28] showed that it is a real dynamic process. With the high speed photography, yarn formation in spinning triangle can be clearly observed as a real dynamic process. Particularly, with some recent developments in staple yarn spinning [8-11], the working condition for spinning triangle becomes more complex, and thus requires a more generalized dynamic model to analyze the properties of yarn and its constituent fibers. Therefore, a new generalized dynamic model of spinning triangle is further developed by extending the above proposed FEM model (static) with consideration of the dynamic characteristics such as the inertia and damping of constituent fibers for a more complete and accurate description. The dynamic behavior of fibers in spinning triangle, such as the natural frequency, mode shape, resonant response, harmonic analysis and response under a dynamic tension, has been numerically studied. The results show that dynamic parameters have a great influence on the amplitude and attenuation of the response of constituent fibers in spinning triangle.

3.2. Initial height of spinning triangle

The sketched view and geometry model of a symmetric spinning triangle are shown

in Figure 3.1, in which all fibers are uniformly and continuously distributed in the spinning triangle. The yarn diameter is ignored for model simplification and the fiber ends are assumed to be twisted together at a twisting point O (or called convergence point). In Figure 3.1, F_o is the spinning tension, H is the height of spinning triangle, d is the width of spinning triangle, α is the spinning angle and β is the helix angle of fibers distributed on the surface of yarn. It is assumed the yarn has an idealized helical structure as shown in Figure 3.2. The fiber can be treated as a cylindrical body and the yarn has an open-packing of circular fibers [138].

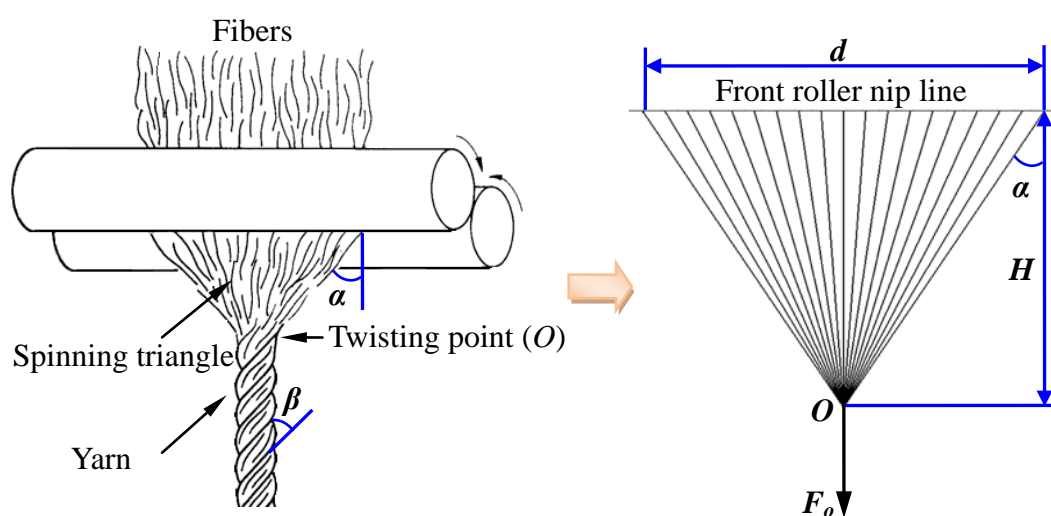
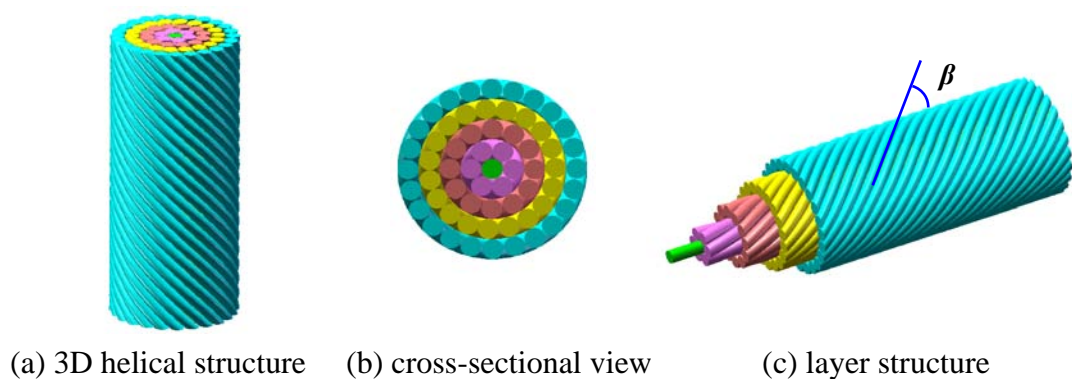


Figure 3.1 A sketched view and geometry model of a symmetric spinning triangle.



(a) 3D helical structure (b) cross-sectional view (c) layer structure

Figure 3.2 An ideal structure of a yarn (5 layers).

For the geometrical relationship shown in Figure 3.1, the initial height H of spinning triangle can be expressed in terms of its width d and the spinning angle α :

$$H = \frac{d}{2} \times \frac{1}{\tan \alpha} \quad (3.1)$$

In Equation (3.1), the width of spinning triangle d is considered as a constant and the spinning angle α can be formulated by the following analysis. Figure 3.3 shows a schematic view of fiber bending due to its flexural rigidity. Owing to the finite flexural rigidity of the fiber, it has an angle ψ between the line of fiber in spinning triangle and the tangent of the helical fiber in the yarn at the contact point. In Figure 3.3, R is the yarn radius, ρ_f is the curvature radius of the i^{th} fiber, f_i is the fiber tension of the i^{th} fiber in spinning triangle and f_i' is the tangent direction of the i^{th} helical fiber in the yarn.

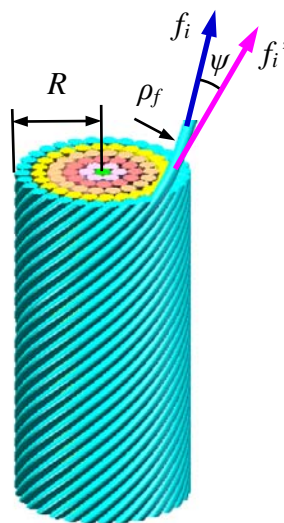


Figure 3.3 Fiber bending due to flexural rigidity of fiber.

The relationship between the spinning angle α and the helix angle β (see [Figure 3.1](#) and [Figure 3.3](#)) of the fiber distributed on the surface of the yarn can be expressed as:

$$\beta = \alpha + \psi \quad (3.2)$$

As shown in [Figure 3.3](#), for an elastic body, the curvature radius ρ_f of the i^{th} fiber is [139]:

$$\frac{1}{\rho_f} = \frac{d\psi}{d\gamma} = 2\sqrt{\frac{f_i}{B}} \sin\left(\frac{\psi}{2}\right) \quad (3.3)$$

where γ is the distance measured along the line of the fiber, and B is the flexural rigidity of the fiber.

Because the radius ρ_f at the contact point equals the radius of curvature of the helical path of the fiber at this point [140], so we have:

$$\rho_f = \frac{R}{\sin^2 \alpha} \quad (3.4)$$

And the flexural rigidity of the fiber can be obtained by [141]

$$B = R_f c_l^2 \quad (3.5)$$

where R_f is the specific flexural rigidity and c_l is yarn count.

Substituting Equations (3.4) and (3.5) into the Equation (3.3), we will have:

$$\cos\psi = 1 - \frac{R_f c_l^2 \sin^4 \alpha}{2 f_i R^2} \quad (3.6)$$

In the second term $\frac{R_f c_l^2 \sin^4 \alpha}{2 f_i R^2}$ of Equation (3.6), R_f , c_l and R are constants, so the term varies with α and f_i . In the analysis of low-twist yarns, the bending of fiber can be ignored. Hence, it is reasonably assumed that the helical angle β of the fibers distributed on the surface of the yarn is equal to the spinning angle α in the initial conditions of this model [20, 142], as shown in Equation (3.7):

$$\psi = 0, \text{ or } \alpha = \beta \quad (3.7)$$

As shown in Figure 3.4, opening the helical yarn out flat, the helix angle β can be expressed as:

$$\tan \beta = \frac{2\pi R}{h} = 2\pi RT \quad (3.8)$$

where h is the length of one turn of twist and T is yarn twist.

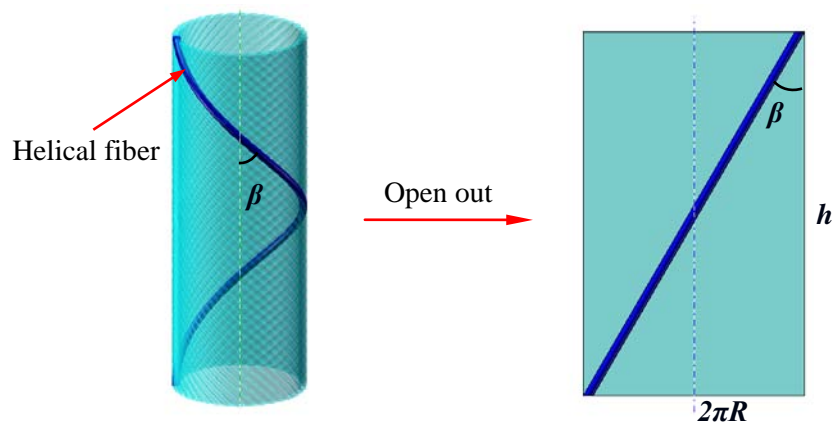


Figure 3.4 An idealized helical fiber on the surface of yarn.

Yarn count c_l can be represented by:

$$c_l = \rho \pi R^2 \quad (3.9)$$

where ρ is yarn density.

According to [Equations \(3.9\)](#), [Equation \(3.8\)](#) can be re-formulated as:

$$\tan \beta = 2T \times \sqrt{\frac{c_l \pi}{\rho}} \quad (3.10)$$

Substituting [Equations \(3.10\)](#) and [\(3.7\)](#) into [Equation \(3.1\)](#), the height of spinning triangle can be expressed:

$$H = \frac{d}{4T} \times \sqrt{\frac{\rho}{c_l \pi}} \quad (3.11)$$

Hence the initial height of spinning triangle is largely dependent on the yarn count c_l and yarn twist level of T .

3.3. Initial strain of constituent fibers

If all the fibers are twisted into the yarn and there is no fiber loss during spinning, the equation of mass conservation can be employed for the spinning triangle:

$$\pi r_1^2 \rho_1 v_1 + \pi r_2^2 \rho_2 v_2 + \cdots + \pi r_i^2 \rho_i v_i + \cdots + \pi r_n^2 \rho_n v_n = \pi R^2 \rho v_{yarn} \quad (3.12)$$

where r_i , ρ_i and v_i are the radius, density and velocity of the i^{th} fiber, respectively, n is the total number of fibers, and v_{yarn} is the velocity of the yarn.

The physical meaning shown in Equation (3.12) is that the total mass of fibers entering the spinning triangle per unit time is equal to that of fibers leaving the spinning triangle in the form of yarn per unit time. With the same type of materials, it can be reasonably assumed that, at the entering line (front roller nip line), all the fibers have the same circular cross section with ideal radius and density, and the fibers are delivered at the same speed:

$$r_1 = r_2 = \cdots = r_n = r, \quad \rho_1 = \rho_2 = \cdots = \rho_n = \rho_0, \quad v_1 = v_2 = \cdots = v_n = v_0 \quad (3.13)$$

where r , ρ_0 and v_0 are the radius, density and velocity of the fibers, respectively,

Substituting Equation (3.13) into Equation (3.12), we can obtain:

$$n \pi r^2 \rho_0 v_0 = \pi R^2 \rho v_{yarn} \quad (3.14)$$

In view of the delivery speed, Equation (3.14) can be further written as:

$$\frac{v_0}{v_{yam}} = \frac{\pi R^2 \rho}{n \pi r^2 \rho_0} = \frac{c_i}{nc_0} \quad (3.15)$$

where c_0 is linear density of a single fiber.

In formulation of the initial conditions, fiber initial strain can be considered as a sum of two components. The first component can be understood as a “drafting” result of spinning triangle because of pulling action and it is solely generated by the difference of delivery velocity between fibers and yarn:

$$\varepsilon_o = \frac{H-L}{L} = 1 - \frac{v_0}{v_{yam}} \quad (3.16)$$

where L is the initial length of fibers inside the spinning triangle.

According to Equation (3.16), all fibers are equally extended, regardless of their positions in the spinning triangle and the triangle profile of spinning triangle. Then the second component ε_i is purely resulted from the triangle profile of spinning triangle:

$$\varepsilon_i = \frac{L_i - H}{H} \quad (3.17)$$

where L_i is the length of the i^{th} fiber inside the spinning triangle

Therefore the total initial strain ε_i^* of i^{th} fiber in the spinning triangle can be obtained by considering the two components:

$$\varepsilon_i^* = \frac{L_i - L}{L} = \varepsilon_i + \varepsilon_i \varepsilon_0 + \varepsilon_o \cong \varepsilon_i + \varepsilon_o = \frac{L_i - H}{H} + \left(1 - \frac{v_0}{v_{\text{yarn}}}\right) \quad (3.18)$$

In practice, the strain ε_0 in Equation (3.18) can be considered as a correction factor and obtained by measuring the total number of fibers, the linear densities of a single fiber and yarn with Equation (3.16). To implement the total fiber initial strains formulated in Equation (3.18), an initial spinning tension force will be exerted on the twisting point, so that the central fiber is straight at zero extension and the other fibers are extended. Under the initial fiber strains, if the actual spinning tension is larger than the initial force, fibers in the spinning triangle will be further elongated, otherwise, they will be contracted or remain unchanged.

Some examples of fiber initial strain distribution are shown in Figure 3.5. Figure 3.5(a) illustrates a contour plot of fiber initial strain for a yarn of 58tex with a twist level of 398tpm. The fiber initial strain curves under different yarn twists (398tpm, 436tpm, 486tpm and 523tpm) for the same yarn count of 58tex are also shown in Figure 3.5(b). As shown in Figure 3.5(b), the position of fibers along the front roller nip line (or the width of spinning triangle) is normalized from -0.5 to 0.5 with

the central point as zero.

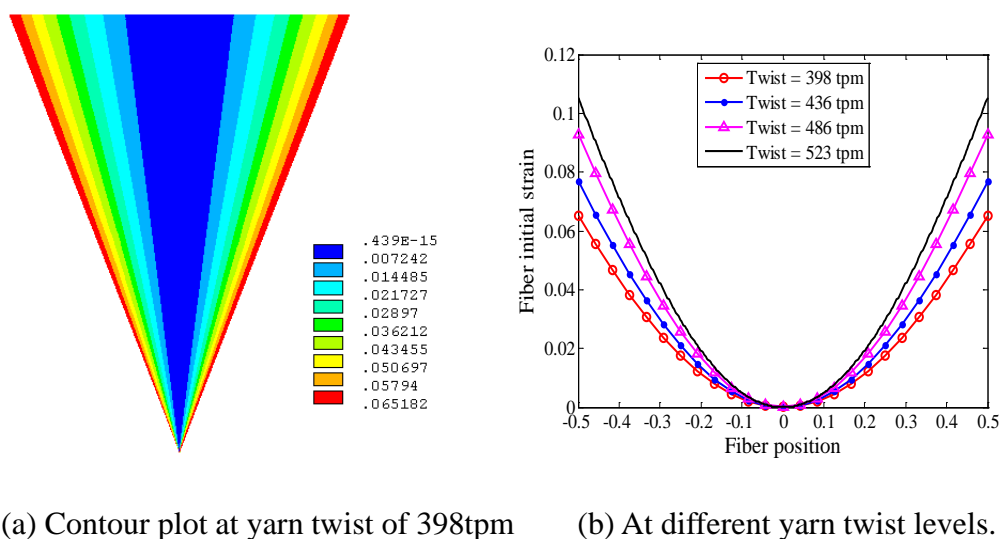


Figure 3.5 Examples of fiber initial strain for 58tex yarn.

3.4. Static analysis of spinning triangle

In this section, stationary finite element model of spinning triangle will be developed and a series of numerical simulations will be carried out to analyze the effects of spinning parameters on the fiber structural and mechanical behavior.

3.4.1. Static modelling using finite element method

3.4.1.1. Governing equations

Figure 3.6 shows a geometric model of the spinning triangle. In Figure 3.6, f_i is the tension force of i^{th} fiber, m_i is the elastic torque of i^{th} fiber, α_i is the angle between the

i^{th} fiber and the vertical axis of front roller nip line, L_i is the length of i^{th} fiber inside the spinning triangle, M is spinning torque, θ is the angle between the spinning tension of yarn and the vertical axis of front roller nip line, n is the number of fibers in spinning triangle, and X, Y, Z are the global coordinates.

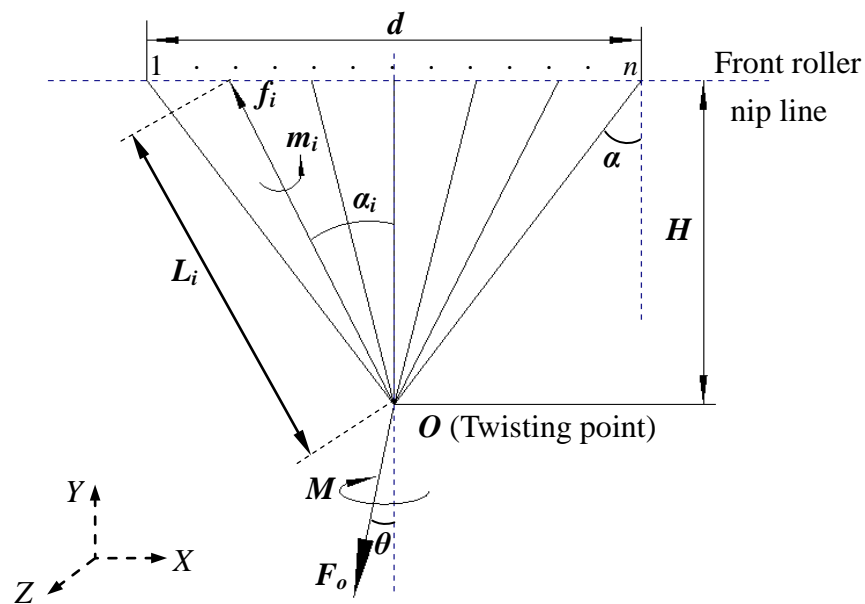


Figure 3.6 A geometric model of spinning triangle.

The constituent fibers in the spinning triangle are considered as 3-D beams with the tensile, compressive, torsional and bending capabilities. It is further assumed that the stress-strain behavior of fibers in ring spinning triangle follows Hooke's law as it is generally agreed [20-23] that it is not beyond the linear region of initial modulus. In addition, the effect of fiber migration, inter-fiber forces and fiber-to-fiber friction are ignored and the fiber ends are twisted together at an imaginary twisting point (O).

In this section, it focuses on analyzing the effects of spinning parameters on the fiber structural and mechanical behavior, therefore the stationary model of spinning triangle will be developed. As shown in [Figure 3.6](#), the governing equations of the fibers in the spinning triangle can be written as:

$$\left\{ \begin{array}{l} \sum_{i=1}^n f_i \cos \alpha_i - F_o \cos \theta = 0 \\ - \sum_{i=1}^{\frac{n-1}{2}} f_i \sin \alpha_i + \sum_{i=\frac{n+1}{2}}^n f_i \sin \alpha_i - F_o \sin \theta = 0 \\ \sum_{i=1}^n m_i \cos \alpha_i - M \cos \theta = 0 \\ - \sum_{i=1}^{\frac{n-1}{2}} m_i \sin \alpha_i + \sum_{i=\frac{n+1}{2}}^n m_i \sin \alpha_i - M \sin \theta = 0 \\ EA \frac{d\omega_i}{dt_i} - f_i(t_i) = 0 \\ GI_p \frac{d\varphi_i}{dt_i} - m_i(t_i) = 0 \end{array} \right. \quad (3.19)$$

where E is the modulus of elasticity, A is the cross-section area of fiber, GI_p is the torsional rigidity of fiber, ω_i , φ_i and t_i are the variables of axial deformation, torsion angle and axial direction of the i^{th} fiber, respectively.

3.4.1.2. Generation of yarn torque

The yarn torque discussed here is composed of three components, namely the torques generated by fiber tension, fiber bending and fiber torsion [[13](#)]:

$$M = M_T + M_B + M_E \quad (3.20)$$

where M_T is the yarn torque generated by fiber torsional stresses, M_B is the yarn torque generated by fiber bending stresses, and M_E is the yarn torque generated by fiber tensile stresses.

The yarn torque solely generated by the fiber tension can be calculated by considering a discrete distribution of fibers inside yarn [23]:

$$M_E = \sum_{i=1}^n M_{Ei} = \sum_{i=1}^n f_i R_i \sin \beta_i \quad (3.21)$$

where M_{Ei} is the component of yarn torque due to i^{th} fiber tension, R_i is the distance of the i^{th} fiber from the yarn-axis in the yarn cross-section, β_i is the helical angle of the i^{th} fiber within the yarn.

With the assumption of ideal yarn open-packing structure, the arrangement of fibers in the yarn can be made as shown in Figure 3.2. According to Figure 3.4 and Equation (3.8), the helical angle β_i of the i^{th} fiber within the yarn can be calculated as:

$$\tan \beta_i = \frac{2\pi R_i}{h} = 2\pi R_i T \quad (3.22)$$

And the distance R_i of the i^{th} fiber from the yarn-axis in the yarn cross-section can be obtained as:

$$R_i = 2r(j-1) \quad (3.23)$$

where r is the fiber radius and j is the layer number of i^{th} fiber located in.

Therefore, the tensional component M_{Ei} of yarn torque generated by the i^{th} fiber can be obtained:

$$M_{Ei} = 2rf_i(j-1) \times \sin\{\arctan[4\pi rT(j-1)]\} \quad (3.24)$$

Previous study [143] showed that the yarn torques generated by fiber bending (M_B) and fiber torsion (M_T) are significantly smaller than the torque by fiber tension (M_E) and thus are ignorable in most cases.

3.4.1.3. Element selection

The fibers in spinning triangle are divided into a set of 3-D beam elements based on Timoshenko beam theory and each end node has six degrees of freedom, as shown in [Figure 3.7](#).

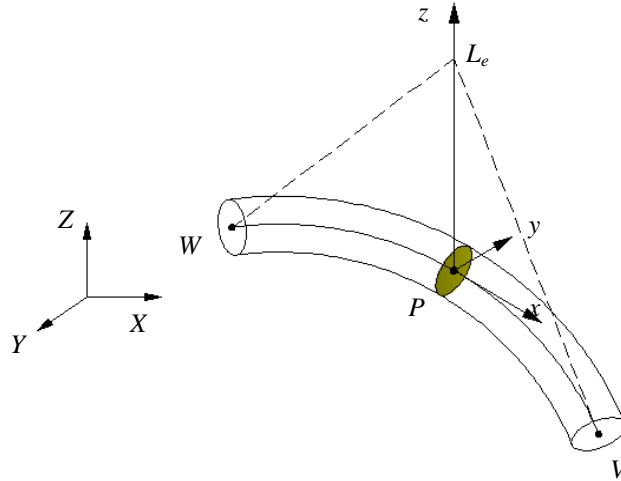


Figure 3.7 The adopted beam element. W , V , and P are the nodes of the element, L_e is the orientation node, x , y and z are the directions of element coordinate system.

The shape functions for the selected 3-D beam element are [144]:

$$\left\{ \begin{array}{l} \delta = \frac{1}{2}[\delta_w(-s + s^2) + \delta_v(s + s^2) + \delta_p(1 - s^2)] \\ \zeta = \frac{1}{2}[\zeta_w(-s + s^2) + \zeta_v(s + s^2) + \zeta_p(1 - s^2)] \\ \eta = \frac{1}{2}[\eta_w(-s + s^2) + \eta_v(s + s^2) + \eta_p(1 - s^2)] \\ \lambda_x = \frac{1}{2}[\lambda_{xw}(-s + s^2) + \lambda_{xv}(s + s^2) + \lambda_{xp}(1 - s^2)] \\ \lambda_y = \frac{1}{2}[\lambda_{yw}(-s + s^2) + \lambda_{yv}(s + s^2) + \lambda_{yp}(1 - s^2)] \\ \lambda_z = \frac{1}{2}[\lambda_{zw}(-s + s^2) + \lambda_{zv}(s + s^2) + \lambda_{zp}(1 - s^2)] \end{array} \right. \quad (3.25)$$

where δ , ζ and η are the translations in the x , y , z directions under the element coordinate system, respectively, λ_x , λ_y or λ_z is the rotational angle about its corresponding direction, and s is a normalized coordinate, starting from -1.0 on one side of the element to +1.0 on the other.

3.4.1.4. Boundary conditions

The degrees of freedom (DOFs) of the nodes which are on the front roller nip line are all equal to zero, so the displacement boundary condition of the model can be given by:

$$\{u^k\} = \{0\} \quad (3.26)$$

where k is the node on the front roller nip line.

The spinning tension F_o and spinning torque M are applied on the twisting point O , and thus the force boundary conditions of the model are as follows:

$$\begin{Bmatrix} f_x^j \\ f_y^j \\ f_z^j \\ m_x^j \\ m_y^j \\ m_z^j \end{Bmatrix} = \begin{Bmatrix} F_o \sin \theta \\ F_o \cos \theta \\ 0 \\ M \sin \theta \\ M \cos \theta \\ 0 \end{Bmatrix} \quad (3.27)$$

where j is the node on the convergence point.

The overall stiffness matrix $[K]$ can be obtained by:

$$[K] = \sum_{e=1}^{n_e} [K]^e \quad (3.28)$$

where n_e is the number of elements, $[K]^e$ is the element stiffness matrix in the global coordinate system.

Therefore the static analysis of the FEM model will be a solution of the following equations:

$$[K]\{u\} = \{F\} \quad (3.29)$$

where $\{u\}$ and $\{F\}$ are assembled nodal displacement and loading vectors, respectively.

The solution of Equation (3.29) gives the nodal displacements. Strains and stresses can be deduced by the nodal displacements.

Generally, the higher level of mesh, the higher precision will be obtained. In this study, because of the characteristics of employed beam element and the spinning triangle structure, the number of divided elements has little impact on the estimation result. Considering the precision and efficiency of the computation, every fiber in spinning triangle is divided into 10 3-D beam elements uniformly. With the above assumptions and deductions, the theoretical model of a symmetric ring spinning triangle using FEM can be developed, as shown in Figure 3.8. In Figure 3.8, F_X , F_Y are the spinning tensions in X and Y directions, and M_X , M_Y are the spinning torques in X and Y directions, respectively.

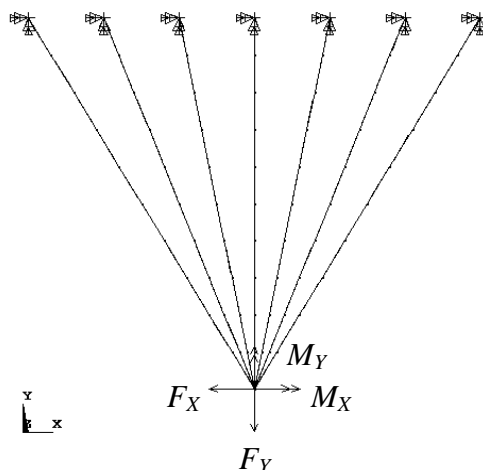


Figure 3.8 The finite element model of spinning triangle.

When the fibers have a considerable frictional contact area with the bottom roller, as a result of the spinning torque (e.g. Z twist for single yarn) acted on the twisting point, fibers on the right side of spinning triangle will be lifted up and leaving the contact area whereas fibers on the left side will be in a more tight contact with the bottom roller, leading to an enhanced normal reaction force in between. [Figure 3.9](#) shows a simplified finite element model of spinning triangle considering such frictional contact. In this model, it is assumed that the contact area of fiber with bottom roller is flat and the contact lengths for all contact fibers are same. In [Figure 3.9](#), the fibers in the shaded part contact with the bottom roller and h_c is the contact length of fibers with bottom roller in spinning triangle. In order to simulate the effect of frictional contact of fibers with bottom roller, the translation in Z axis of the contact fibers is restrained, and the frictions caused by the contact are applied on all nodes in the direction opposite to the movement of fibers.

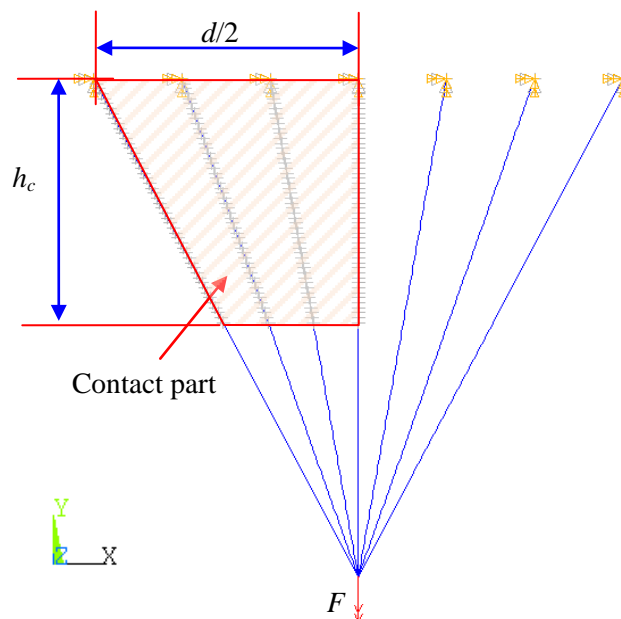


Figure 3.9 Finite element model of spinning triangle considering fiber-roller contact.

3.4.1.5. Algorithms for fiber buckling

The system of simultaneous linear equations generated by the finite element procedure is solved either using a direct elimination process or an iterative method.

In this study, the Sparse Direct Solver is employed. In the actual spinning process, fiber buckling is a very common phenomenon that occurs in center fibers of spinning triangle, as shown in [Figure 3.10](#). As the critical fiber strain for fiber buckling is approximately 10^{-6} [23], the element birth and death condition of the FEM can be employed to deactivate certain elements whose compressive strains are beyond the critical fiber strain. In the algorithm, a deactivated element physically remains in the model but contributes a near-zero stiffness value $[K]^e$ to the overall matrix of $[K]$.

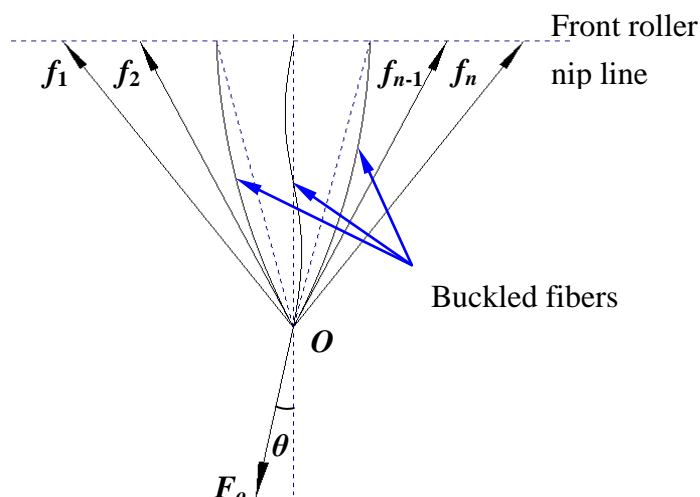


Figure 3.10 Fiber buckling in spinning triangle

3.4.2. Simulation results for fiber tension distributions

In order to fully study the mechanical performance of ring spinning triangle, including the fiber tension distribution and fiber torsion distribution of spinning triangle, a series of numerical simulations are carried out in this section. Cotton fibers and yarns are employed for the simulation. Material properties of cotton include the fiber elastic modulus (E) of 6.8Gpa [20], fiber shear modulus (G) of $E/3.7$ [141], fiber linear density of 1.5dtex and fiber density of 1.35Mg/m³ [20].

The influential factors considered in the following analysis are the spinning tension, spinning tension angle, yarn twist, yarn count and the frictional contact length of fibers with the bottom roller. The details of various simulation cases are listed in [Table 3.1](#). For each case, both fiber without and with buckling are considered.

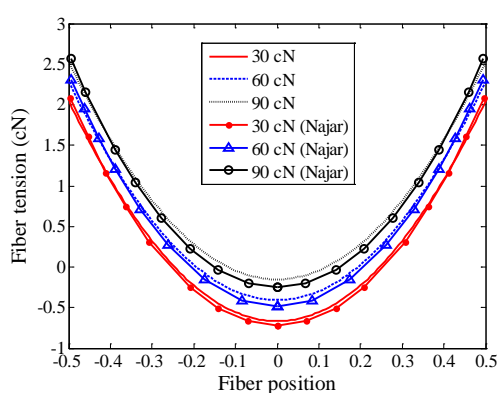
Table 3.1 Parameters adopted for the simulation of spinning triangle

Case No.	Yarn Count (tex)	Number of Fibers	Yarn Twist (tpm)	Spinning Tension (cN)	Inclined Angle of Spinning Tension θ (degree)	Contact length of fibers with bottom roller
1	25	121	418	30	0	0
				60		
				90		
2	58	385	523	30	0	0
				60		
				90		
3	25	121	418	30	0	0
					5	
					10	
					12	
4	58	385	398	30	0	0
			436			
			486			
			523			
5	15	101	523	30	0	0
	32	211				
	40	265				
	58	385				
6	58	385	523	30	0	H/4
						H/2
						3H/4

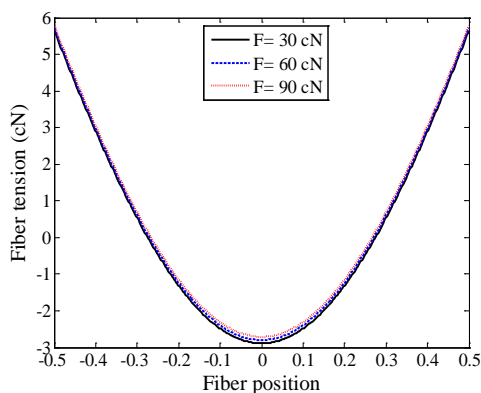
3.4.2.1. Effect of spinning tension

Figure 3.11 and Figure 3.12 show the fiber tension distribution for 25tex and 58tex cotton yarns at different spinning tensions of 30cN, 60cN and 90cN. The input parameters are shown in Case 1 and Case 2 in Table 3.1. Considering without fiber

buckling, Figure 3.11(a) shows a comparison of the fiber tension distribution calculated by the proposed FEM model and the energy model by Najar [20] in Case 1 in Table 3.1. It is noted that the FEM results are generally slightly larger than the results by energy method and both the trend of curves and the numerical values of fiber tension distribution are in a good agreement.

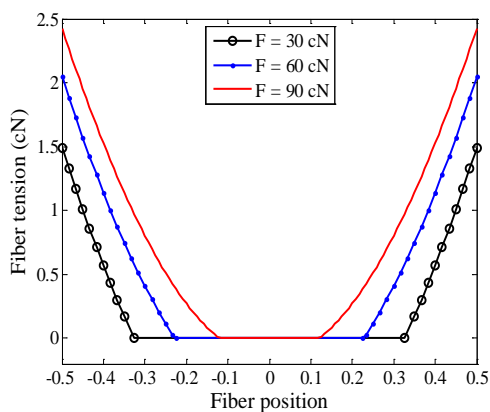


(a) Case 1 (25tex yarn)

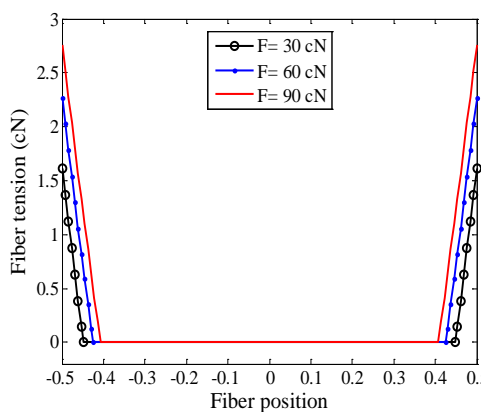


(b) Case 2 (58tex yarn)

Figure 3.11 Fiber tensions under different spinning tensions without fiber buckling.



(a) Case 1 (25tex yarn)



(b) Case 2 (58tex yarn)

Figure 3.12 Fiber tensions under different spinning tensions with fiber buckling.

In both [Figure 3.11](#) and [Figure 3.12](#), as the spinning tension is increased, the fiber tension at each position of spinning triangle is constantly increased. Hence the maximum value of spinning tension in the actual spinning should be well controlled so as to avoid any fiber breakage in the spinning triangle. Compared with the case where fiber buckling is not considered (see [Figure 3.11](#)), fiber tensile forces are considerably reduced in the case with fiber buckling considered (see [Figure 3.12](#)), particularly for the coarse yarn count of 58tex. This is because when fiber buckling is considered, most compressive loadings acted on the central fibers are released, leading to the reduced tensile forces of other fibers.

If fiber buckling is not considered, it is noted that the central fibers are always in a compressive loading, even for the spinning tension of 90cN (see [Figure 3.11](#)). Comparing [Figure 3.11\(a\)](#) (25tex yarn) with [Figure 3.11\(b\)](#) (58tex yarn), the influence of spinning tension on fiber tension is noticeably reduced as yarn count is increased. For the same yarn count of 58tex, compared with the case without fiber buckling (see [Figure 3.11\(b\)](#)), the effect of spinning tension value on fiber tension shown in [Figure 3.12\(b\)](#) is enhanced.

In the case where fiber buckling is considered (see [Figure 3.12](#)), the effect of yarn count on the fiber tension value becomes less evident, which is different from the

case where fiber buckling is not considered (see [Figure 3.11](#)). In addition, for both yarn counts in the case considering fiber buckling, with the increase of spinning tension, more fibers are under tensile loading or elongated (see [Figure 3.12](#)) and the number of those elongated fibers (i.e. under tensile loadings) can be calculated and are listed in [Table 3.2](#). In [Table 3.2](#), it is noted that the number of elongated fiber for 25tex yarn is more than that for 58tex yarn, and with higher spinning tension, such difference is enlarged.

Table 3.2 The number of elongated fibers under different spinning tensions with fiber buckling

Yarn Counts (tex)	Number of Fibers	Spinning Tensions		
		30cN	60cN	90cN
25	121	21×2	33×2	46×2
58	385	20×2	29×2	36×2

3.4.2.2. Effect of spinning tension angle

In practice, the spinning tension of yarn always has a large or small angle with the vertical axis of the front roller nip line, particularly for some recent developments in staple yarn spinning [[8-9](#), [25](#), [32](#)]. The magnitude of inclined angle is dynamically and slightly changed with time because of the movement of feeding roving and ring

rail. The magnitude of inclined angle is determined by several spinning parameters, such as traveler weight, spindle speed, yarn count and so on. In this study, several values of inclined angle are selected to predict the effect of inclined angle on the shape and mechanical performance of spinning triangle. In this simulation, the angles (θ) between yarn spinning tension and the vertical axis of the nip line are shown in Case 3 with various values of 0° , 5° , 10° and 12° . The effect of spinning tension angle on fiber tension distribution for the 25tex yarn is shown in [Figure 3.13](#).

In [Figure 3.13](#), when the direction of spinning tension is coincident with the vertical axis of the nip line (i.e. $\theta=0$), the curve of fiber tension distribution is perfectly symmetric. As expected, with the increase of angle θ , the curve of fiber tension is more asymmetric and the fiber tension distribution becomes more imbalanced. The fibers that are located on the right side of spinning triangle (i.e. the side opposite to the direction of spinning tension) are subject to larger tensile loadings than the fibers on the other side, especially in the case where fiber buckling is considered (see [Figure 3.13\(b\)](#)). As the distribution profile of fiber tensions is quite sensitive to the inclined angle of spinning tension, its value should be well controlled in order to keep a stable spinning condition of spun yarns. In the case of fiber buckling (see [Figure 3.13\(b\)](#)), the number of elongated fibers on the left side of spinning triangle (i.e. the side positive to the direction of spinning tension) is less than that on the

other side and this phenomenon becomes more serious with the increase of spinning tension angle.

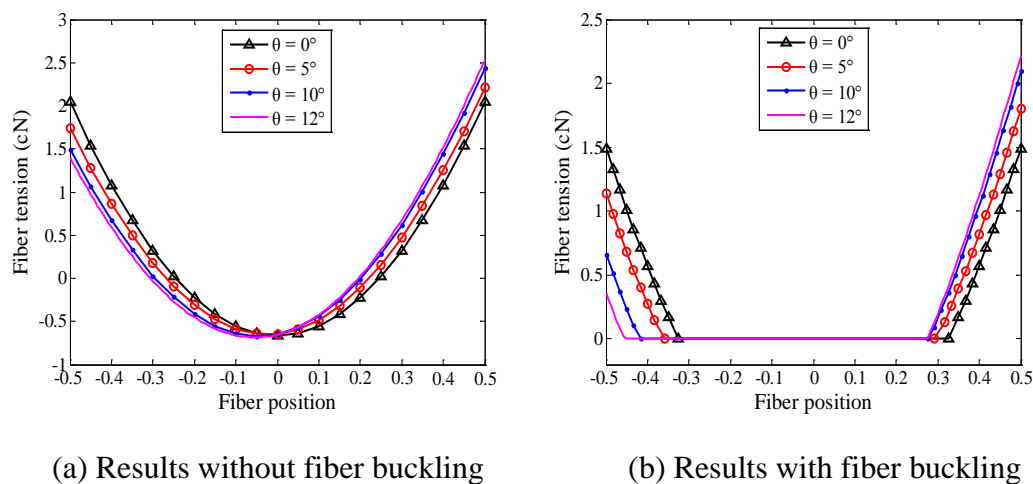


Figure 3.13 Fiber tensions under different spinning tension angles in Case 3.

3.4.2.3. Effect of yarn twist

The parameters shown in Case 4 are used to study the effect of yarn twist on fiber tension distribution in the spinning triangle. Figure 3.14 shows the fiber tensions under different yarn twist levels for the 58tex yarn. As shown in Figure 3.14(a), yarn twist has a significant influence on fiber tension distribution when fiber buckling is not considered. With an increase in yarn twist, the gradient of fiber tension curve becomes steeper and the maximum fiber tension is constantly increased. It is also noted that all the curves approximately have two intersection points around the dimensionless locations of ± 0.3 in the spinning triangle. Beyond

these two locations, fiber tensile forces are constantly increased with the increase of yarn twist, whereas within these two locations, fiber compressive loadings are enhanced. Compared with Figure 3.14(a) where fiber buckling is not considered, yarn twist does not have such a significant influence on the profile of fiber tension distribution when fiber buckling is considered (see Figure 3.14(b)). Similar to that shown in Figure 3.14(a), the gradient of fiber tension curve in Figure 3.14(b) becomes steeper and the maximum fiber tension is increased with the increase of yarn twist. However it is also noted that with an increase in yarn twist, less number of fibers will be under tensile loading or elongated.

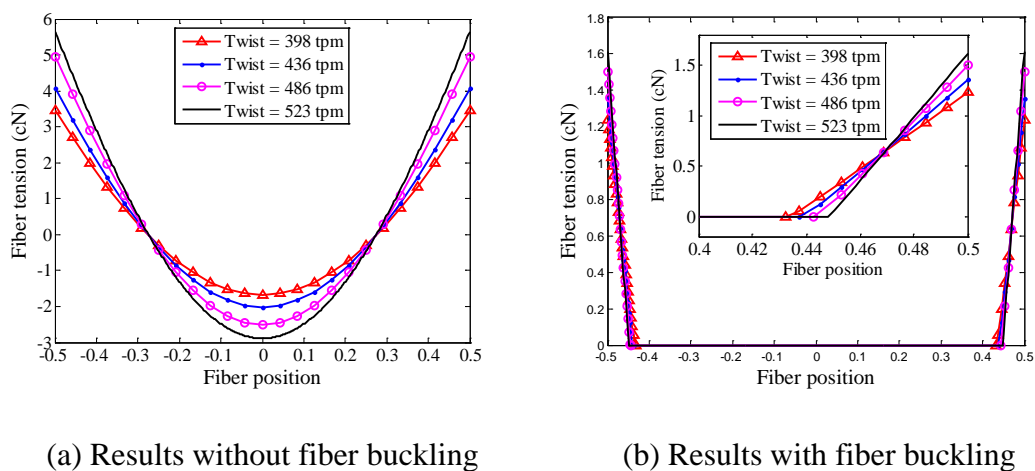
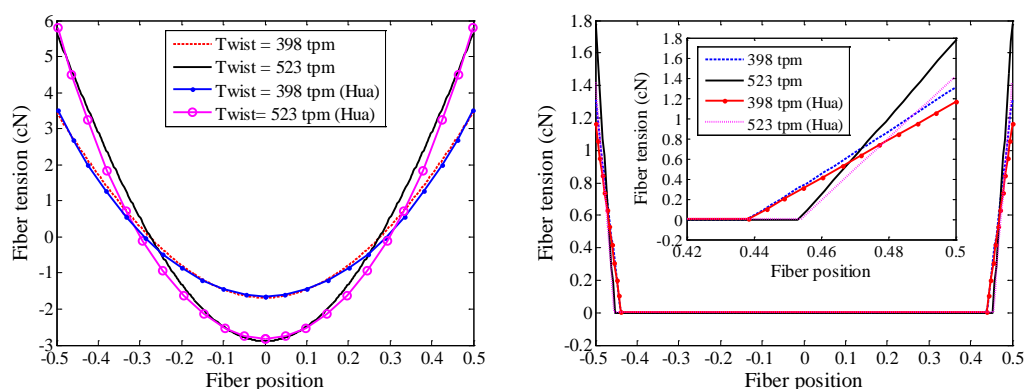


Figure 3.14 Fiber tensions under different yarn twists in Case 4.

For comparison, the simulation results of yarn twists 398tpm and 523tpm in Case 4 in Table 3.1 can also be obtained from the work by Hua [22] and Hua et al. [23] using the energy method both with and without consideration of fiber buckling, as

shown in Figure 3.15. In order to obtain more details of the comparison with fiber buckling, Figure 3.15(b) also displays the enlarged partial curves. It is noted that in the case without fiber buckling (see Figure 3.15(a)), the results obtained by the FEM in this study is in a good agreement with the results by Hua [22], and in the case with fiber buckling (see Figure 3.15(b)), the fiber tensions by the FEM are slightly larger than the results by Hua et al. [23] and the gap between the curves of FEM results and Hua's results gets widening with the increase of yarn twist.



(a) Results without fiber buckling [22]

(b) Results with fiber buckling [23]

Figure 3.15 Comparison of fiber tensions under different yarn twists with [22, 23].

3.4.2.4. Effect of yarn count

The parameters shown in Case 5 are used to evaluate the effect of yarn count on fiber tension distribution. The simulation results are shown in Figure 3.16. Generally the effect of yarn count on fiber tension distribution shown in Figure 3.16(a) is

similar to that of yarn twist in Figure 3.14(a). With an increase in yarn count, the gradient of fiber tension curve becomes steeper and the maximum fiber tension is constantly increased. However when fiber buckling is considered (see Figure 3.16(b)), though the gradient of fiber tension curves becomes steeper with the increase of yarn count, their maximum fiber tensions are approximately the same (around 1.6cN).

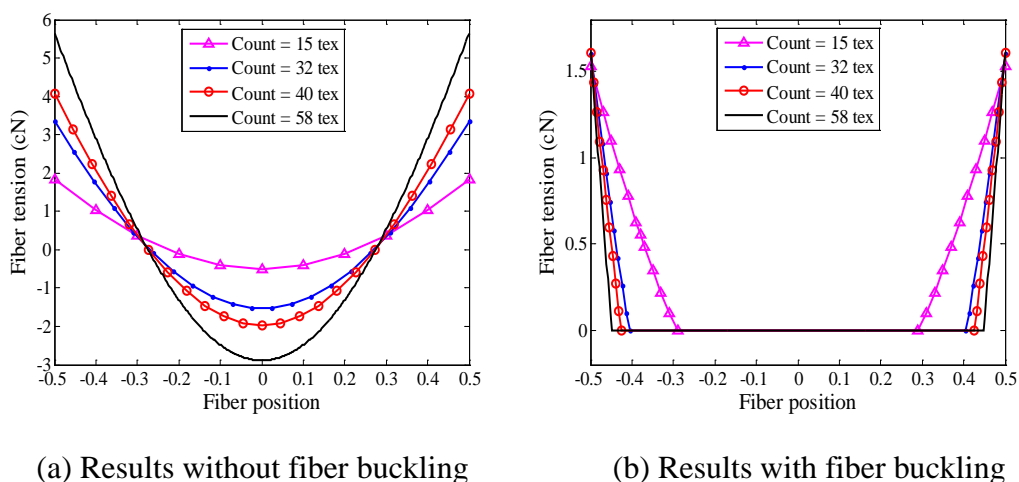
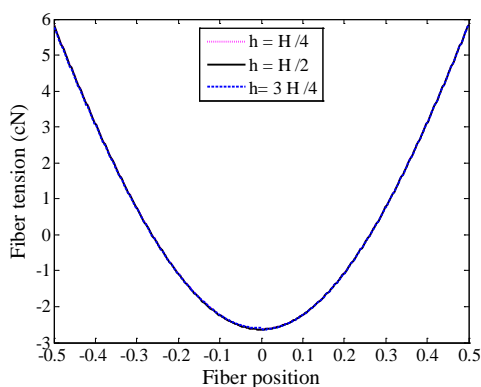


Figure 3.16 Fiber tensions at different yarn counts in Case 5 (yarn twist: 523tpm)

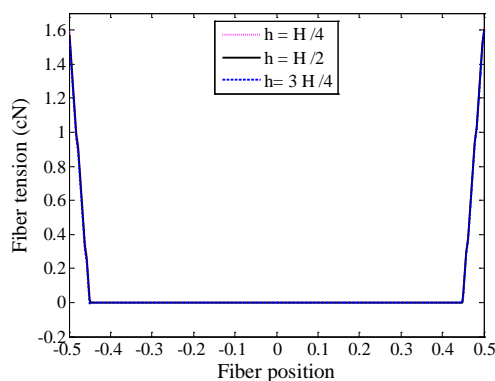
3.4.2.5. Effect of the frictional contact with bottom roller

In this section, the effect of fiber frictional contact with bottom roller on the fiber tension is evaluated. In Case 6, three levels of contacting length (h) of fibers with the bottom roller are adopted for simulation: $H/4$, $H/2$ and $3H/4$ (H is the height of spinning triangle). The effect of such contact length on fiber tension is shown in

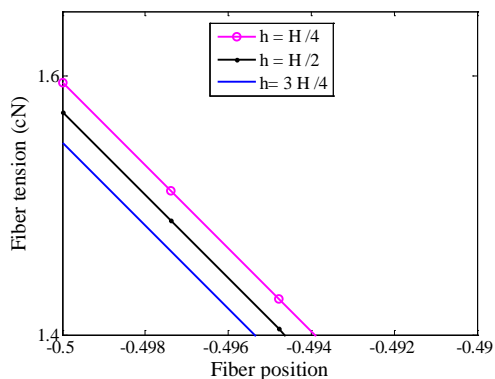
Figure 3.17 where Figure 3.17(c) and Figure 3.17(d) are the enlarged views of partial curves shown in Figure 3.17(b). Generally the frictional contact does not have a significant influence on fiber tension distribution as compared to its influence on the fiber torsional distribution (see Figure 3.19 and Figure 3.21). With the increase of the contact lengths with bottom roller, the contact tension results both without and with fiber buckling become slightly reduced. In the case of fiber buckling, the fiber tensions on the side of tight contact (i.e. the left side of spinning triangle) are smaller than those on the other side together with a larger variation.



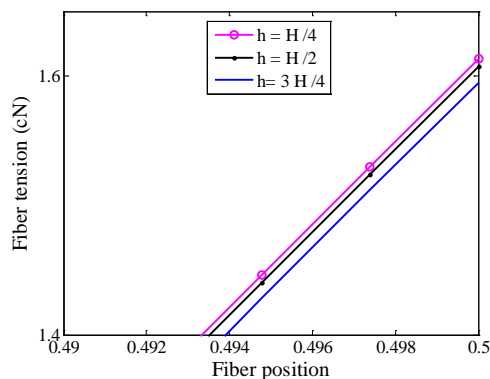
(a) Results without fiber buckling



(b) Results with fiber buckling



(c) Partial curves of Figure 3.17(b)

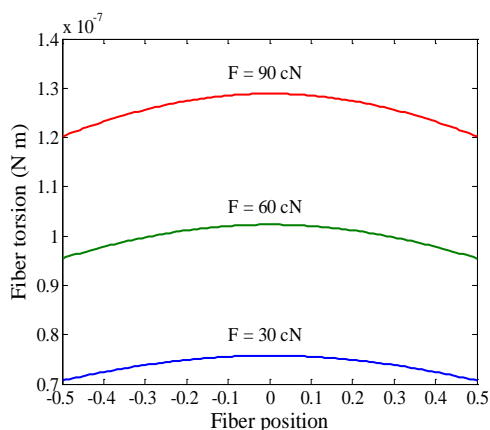


(d) Partial curves of Figure 3.17(b)

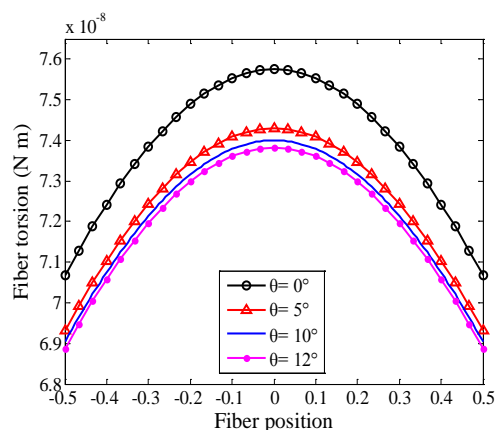
Figure 3.17 Fiber tensions at different contact lengths with roller in Case 6.

3.4.3. Simulation results for fiber torsion distributions

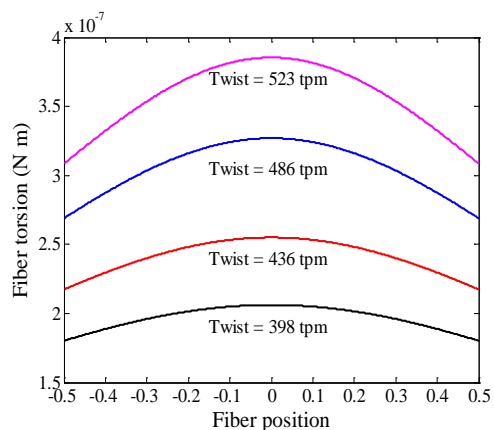
In this section, the effects of various influential parameters on the fiber torsion distribution will be evaluated. For simplicity, fiber buckling is not considered and the input parameters are shown in Cases 1, 3, 4, 5 and 6 in Table 3.1. Figure 3.18 and Figure 3.19 illustrate fiber torsion distributions of spinning triangle under various influencing parameters of spinning tension, spinning tension angle, yarn twist, yarn count and the frictional contact of fibers with bottom roller. Figure 3.20 and Figure 3.21 show two examples of the contour plots of fiber torsion distribution at the spinning triangle to demonstrate the effect of the frictional contact of fibers with bottom roller. As shown in Figure 3.18, it is apparently noted that with the increase of spinning tension, yarn twist and yarn count or the decrease of inclined spinning angle, fiber torsion is increased constantly and the gradient of curves becomes steeper.



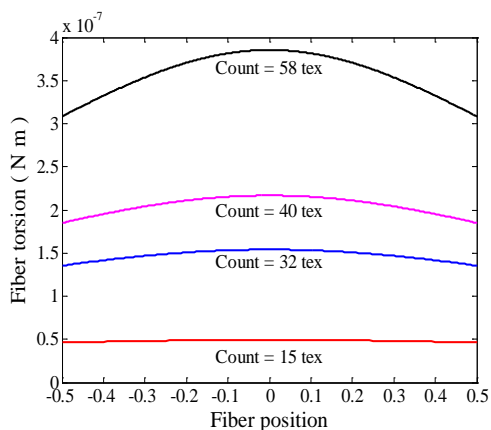
(a) spinning tensions in Case 1



(b) spinning tension angles in Case 3.

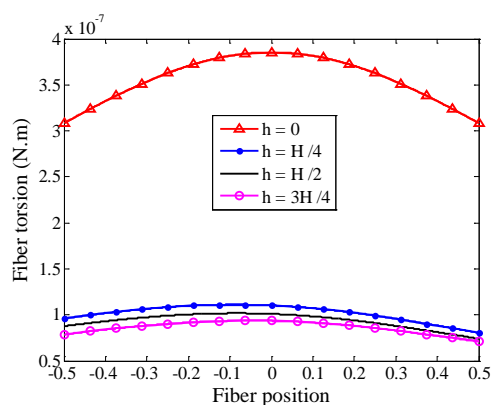


(c) yarn twists in Case 4

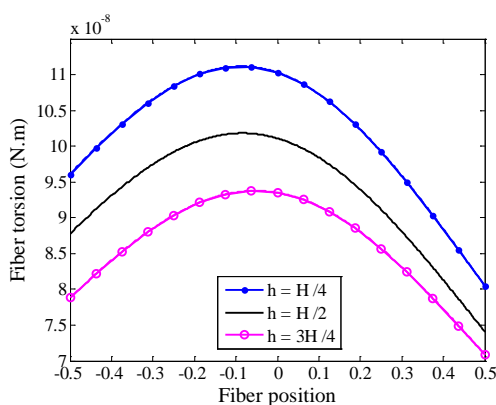


(d) yarn counts in Case 5

Figure 3.18. Effect of spinning parameters on fiber torsion distribution.



(a) Comparison with non-contact



(b) Contact curves only

Figure 3.19 Effect of the fiber contact lengths with bottom roller in Case 6.

Figure 3.19 illustrates the fiber torsional distribution under different fiber contact lengths with bottom roller. As shown in Figure 3.19(a), compared with the case of non-contact with bottom roller ($h=0$), the curves of fiber torsion with roller contact (i.e. $h=H/4$, $H/2$ and $3H/4$) become asymmetric and the values are noticeably reduced. However there is no significant difference of fiber torsion among the three curves of roller contact. Figure 3.19(b) is an enlarged view of fiber torsion

distributions with roller contact shown in Figure 3.19(a). It is noted that with the increase of contact length with bottom roller, the value of fiber torsion is gradually decreased.

Figure 3.20 and Figure 3.21 illustrate the contour plots of fiber torsion without and with roller contact, providing for a more intuitionistic picture of fiber torsion distribution and deformation at the spinning triangle. Figure 3.20 shows the fiber torsion and deformation of Case 6 without the frictional contact (i.e. $h=0$) and Figure 3.21 shows the fiber torsion and deformation of Case 6 with a contact length of $h=H/2$. It can be seen that both fiber torsion distribution and deformation become asymmetric because of the consideration of fiber contact with bottom roller.

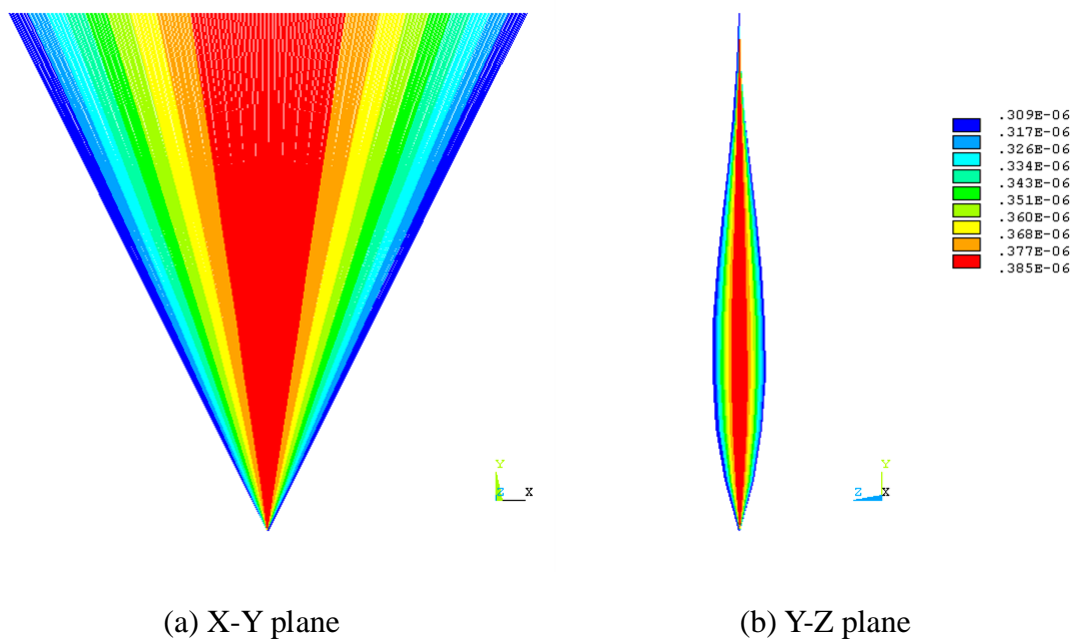


Figure 3.20 Contour plots of fiber torsion without roller contact
(30cN spinning tension, 58tex yarn)

The mechanical status of the fibers in tension, torsion and bending can give rise to radial stress components in the twisted yarn, which in turn will affect the yarn torque. Because fiber torsion and fiber bending are largely based on the yarn configuration, the two components of yarn torque generated by fiber torsion and fiber bending are considered to be the same as calculated by Bennett & Postle [14] since an ideal helical yarn structure is adopted by all the models. For the other component of yarn torque, it can be assumed [23] that the fiber tension created in the spinning triangle will be kept when the fibers are transferred from spinning triangle to the yarn, so the fiber tensions in spinning triangle by the proposed FEM model and energy model [23] can be used for calculating the component of yarn torque due to fiber tension respectively. All the components of yarn torque obtained by Bennett and Postle [14], Hua et al. [23] and the current FEM model are listed in Table 3.3.

Table 3.3 The spinning parameters and calculated components of yarn torque

Yarn Twist (tpm)	M_T ($\times 10^{-7}$ N m)	M_B ($\times 10^{-7}$ N m)	M_E ($\times 10^{-7}$ N m)		
			by Bennett & Postle [14]	by Hua et al. [23]	by FEM
200	31	2	50	57	30
400	43	9	76	103	61
600	46	21	99	123	93
800	47	39	125	124	127
1,000	48	59	154	115	162

As shown in Figure 3.22, considering fiber buckling, the yarn torques calculated by the proposed FEM model and earlier models (Hua et al. [23] and Bennett & Postle [13-14]) are obtained for the comparison with experimental results [14]. It is noted that the obtained results by different methods have the similar trend which initials from zero point and increases with the increase of the yarn twist. The yarn torque obtained by the FEM model is generally in a better agreement with experimental measurements than the other two models in the range of low twist. And in high level of yarn twist (e.g. over 800tpm), all the theoretical models create large deviations to the experimental data of yarn torque.

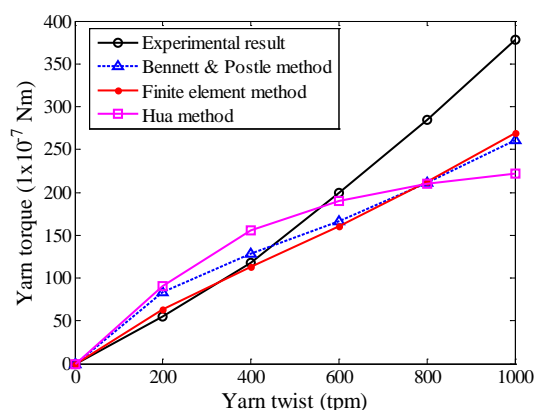


Figure 3.22 Comparison of the total yarn torque obtained by the theoretical models [14, 23] with experimental results [14].

3.5. Dynamic analysis of spinning triangle

Section 3.4 provides a new theoretical model of ring spinning triangle and numerical analysis of the relationship between the fiber tension and torsion distributions and some important spinning parameters, such as the spinning tension, spinning tension

angle, yarn twist, yarn count and the frictional contact of fibers with bottom roller.

Actually, the magnitude of spinning tension used to draw out the yarn is usually variable, leading to a spinning instability [145]. The experimental measurements [20] showed that the fibers in spinning triangle are subject to dynamic loads and impacts. And with the high speed photography, yarn formation in spinning triangle can be clearly observed to be a real complex dynamic process. In this section, in order to obtain a more complete estimation of the fiber mechanical behavior in spinning triangle, a new theoretical model with the consideration of the dynamic characteristics, such as the inertia and damping of the fibers, will be developed. Figure 3.23 shows a geometric model of spinning triangle. In Figure 3.23, F is spinning tension, H is the height of spinning triangle, θ is the angle between the spinning tension of yarn and the vertical axis of nip line and α is the half of spinning angle.

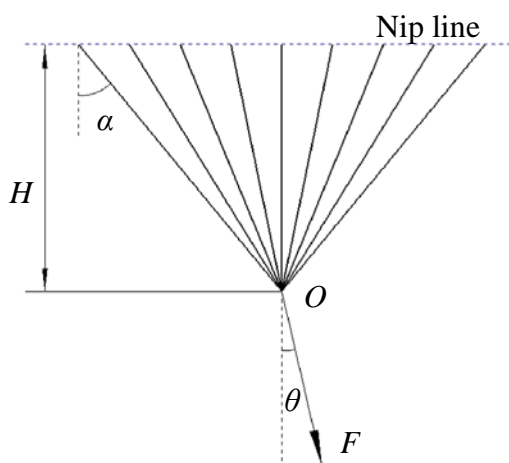


Figure 3.23 A geometric model of the spinning triangle

3.5.1. Dynamic modelling using finite element method

Most fibers like natural and polymeric fibers show viscoelastic behavior, which exhibits a combined feature of both elastic materials and viscous fluids. The viscoelastic mechanical properties of materials have been examined by many researchers [146-151]. They have applied the classical viscoelasticity theory to analyze the theoretical dynamic properties based on combinations of elastic and viscous elements, ranging from basic discrete systems such as the Maxwell and Voigt models, to distributions of infinite numbers of such elements. As illustrated in Figure 3.24, a Voigt model, a simple and effective type of elastoviscous behavior postulated by Voigt (Kelvin), is physically represented by an ideal (Hookean) spring, with stress proportional to strain, in parallel with an ideal (Newtonian) dashpot, with stress proportional to rate of strain [141]. The stress σ is given additively as:

$$\sigma = E\varepsilon + \eta \frac{d\varepsilon}{dt} = E\varepsilon + \eta \dot{\varepsilon} \quad (3.30)$$

where E is the elastic modulus of the spring, η is the viscous coefficient of the dashpot and ε is a component of strain and varies with time t .

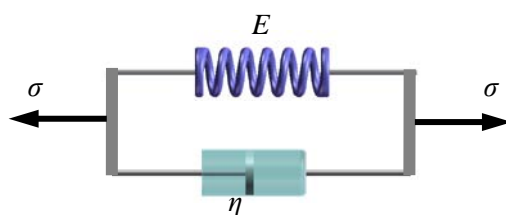


Figure 3.24 The Voigt model.

For the characteristics of viscoelastic material, the dynamic properties can be experimentally examined by considering two types of dynamic modulus: storage modulus E and loss modulus E' , or E and the tangent of loss angle $\tan \gamma = E'/E$. Considering the Voigt model is subject to a sinusoidal force with frequency f , the complex stiffness k^* of the Voigt model is equal to the sum of two effective stiffness (a real part k and an imaginary contribution k') in parallel [152]:

$$k^* = k + jk' \quad (3.31)$$

The loss-angle tangent $\tan \gamma$ can be also formulated as:

$$\tan \gamma = \frac{E'}{E} = \frac{k'}{k} \quad (3.32)$$

According to Equation (3.32), Equation (3.31) can be rewritten as:

$$k^* = k(1 + j \tan \gamma) \quad (3.33)$$

And the relation between structure damping ratio ζ and viscous damping ratio τ can be obtained by:

$$\zeta = \frac{\tau}{\pi f} \quad (3.34)$$

Therefore, the mechanical damping of fiber c can be calculated by the elastic

stiffness k and the loss-angle tangent $\tan \gamma$ as:

$$c = k \cdot \tan \gamma / \pi f \quad (3.35)$$

Considering the influences of mass and viscous damping, the mechanical model of spinning triangle can be developed, as shown in Figure 3.25. In Figure 3.25, m is the mass of individual fiber; m_y is the mass of yarn between the convergence point (O) and the yarn guide which is the additional mass in the spinning triangle.

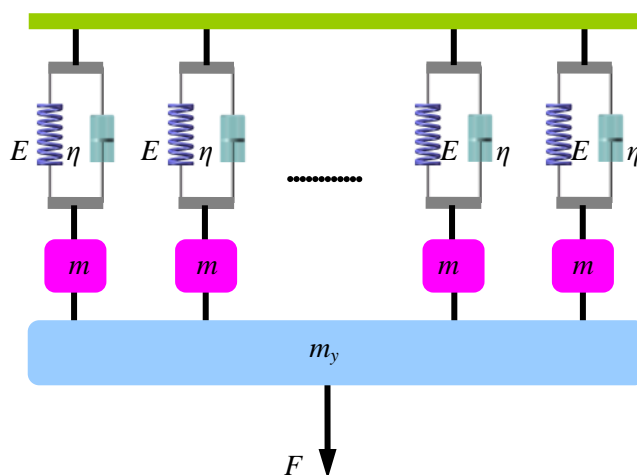


Figure 3.25 Mass-spring-damper system of spinning triangle.

With the above developed fiber mechanical damping, the equation of motion for the dynamic system can be written as:

$$[M]\{\ddot{u}\} + [C]\{\dot{u}\} + [K]\{u\} = [F] \quad (3.36)$$

where $[M]$ is the mass matrix which is influenced by the number of fibers in spinning

triangle, $\{\ddot{u}\}$ is the second time derivative of the displacement $\{u\}$ (i.e. the acceleration), $[C]$ is the damping matrix, $\{\dot{u}\}$ is the velocity, $[K]$ is the elastic stiffness matrix and $[F]$ is the force vector.

According to Equation (3.35), the damping matrix in Equation (3.36) can be expressed by elastic stiffness matrix with the experimental results of storage modulus E and loss modulus E' . Considering the influences of mass and viscous damping, the mechanical model of spinning triangle can be developed. With finite element meshing, finite element model of spinning triangle can be obtained. Figure 3.26 shows a finite element model of spinning triangle with 9 fibers, and each fiber is divided into 20 elements. In Figure 3.26, F_X , F_Y are the spinning tensions in X and Y directions.

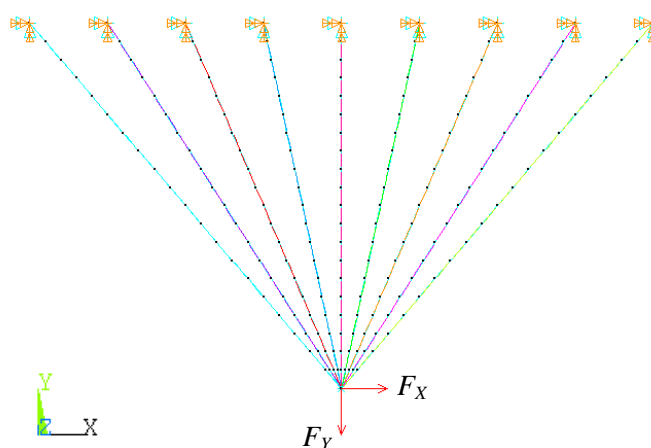


Figure 3.26 The finite element model of spinning triangle.

3.5.2. Modal analysis

The modal analysis is conducted to analyze mode shapes and natural frequencies of spinning triangle. Figure 3.27 indicates an example of its first 6 mode shapes. It is noted that the first six modes include three types of mode shape: swing in X-direction (1st mode and 3rd mode), Y-direction (2nd mode, 4th mode and 5th mode) and Z-direction (6th mode). For the relatively low natural frequency of 1st mode (swing in X-direction), if the frequency of impact force has the chance to be close to the first natural frequency of spinning triangle, the resonant response in X-direction may cause the damage to yarn formation, leading to a potential yarn end-breakage.

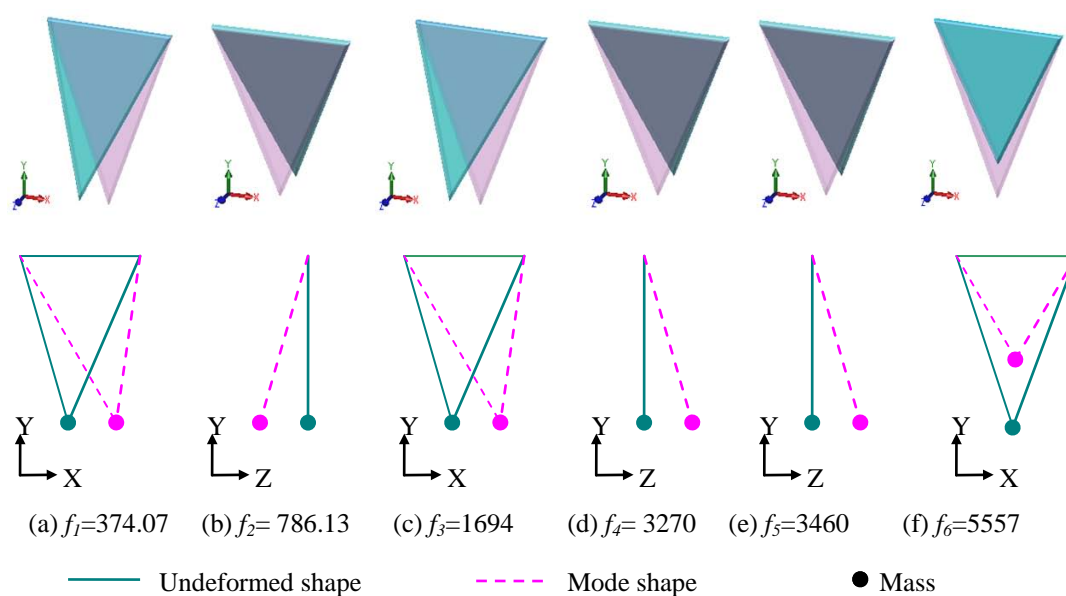


Figure 3.27 Mode shapes and natural frequencies (Hz) for the first 6 modes.

(wool yarn: yarn count of 68tex, twist of 100tpm and spinning tension of 11.5cN).

Two Cases are proposed to estimate the effects of two parameters: yarn twist (Case 1: wool yarn of 68tex with different twist levels of 100tpm, 200tpm, 300tpm and 400tpm, at spinning tension of 11.5cN) and yarn count (Case 2: wool yarn of 25tex, 33tex, 68tex and 145tex, with twist of 100tpm at spinning tension of 11.5cN), on natural frequencies and corresponding mode shapes of the structure. Figure 3.28 shows the effects of yarn twist and yarn count on natural frequency of first three modes.

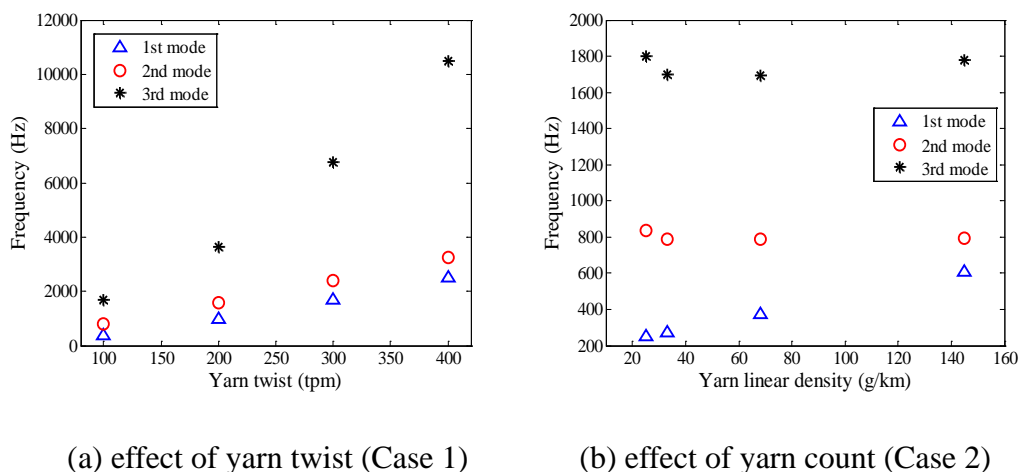


Figure 3.28 Effects of spinning parameters on natural frequency of first 3 modes.

In Figure 3.28 (a), the frequency curves of the 1st mode and 2nd mode show linear upward trends in parallel, while that of the 3rd mode goes up nonlinearly. It is noted that with the increase of yarn twist, all natural frequencies of spinning triangle are obviously increasing. In Figure 3.28 (b), compared with the rising up frequency curve of the 1st mode, the curves of the 2nd and 3rd modes almost remain stable

except for a slight decrease between 25tex and 33tex, which indicates that the effects of yarn count on the 2nd and 3rd mode frequencies are not significant. In addition, with the increase of yarn twist and yarn count, the most important frequency of structure (i.e. the first natural frequency) will increase.

3.5.3. Harmonic analysis

The harmonic analysis is employed to examine the response of spinning triangle in different frequencies in order to find out the relationship between the response and frequency. The effect of fiber damping on the response of displacement on convergence point and the fiber tension on the left side of the spinning triangle will be evaluated by Case 3 and Case 4, which are considered without and with fiber damping (damping ratio $\zeta = 10^{-4}$ [153]) in the wool yarn of 68tex and 100tpm at spinning tension of 11.5cN with 10° inclined angle.

Figure 3.29 and Figure 3.30 show the simulation results of the response in harmonic analysis without and with consideration of fiber damping, respectively. It is noticeable that in both of Figure 3.29 and Figure 3.30, the response of fiber tension and displacement in X-direction all have an extraordinary peak (around 370Hz) corresponding to the first natural frequency. Compared with the curve similar to an impulse signal in Figure 3.29, the delay and attenuation of the response in Figure

3.30 are noticeable due to the fiber damping. For example, the peak of X-direction displacement on convergence point falls from around 40mm to only around 1.4mm and the peak of fiber tension falls from around 43cN to around 1.7cN. In addition, there is another very small peak at around 1680Hz (3rd mode) in the insert of Figure 3.29, but it is not presented in Figure 3.30. It indicates the effect of the fiber damping is significant and cannot be ignored in dynamic condition.

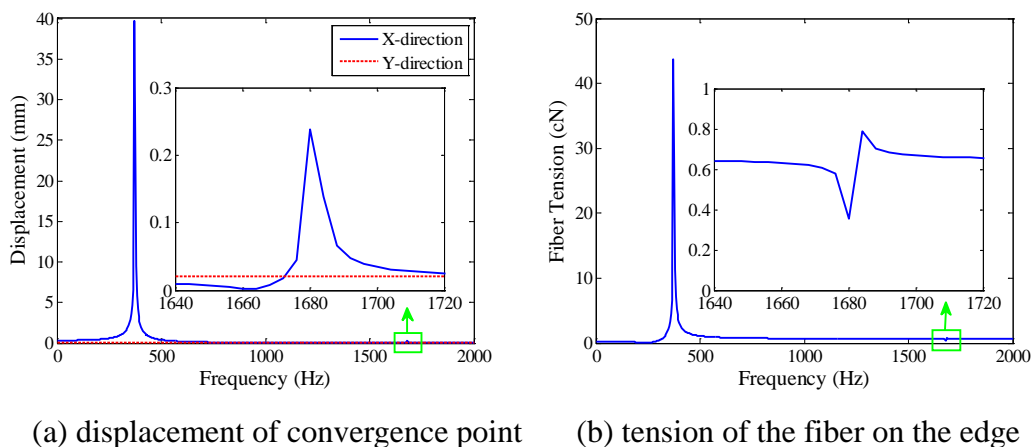


Figure 3.29 Harmonic responses without consideration of fiber damping (Case 3)

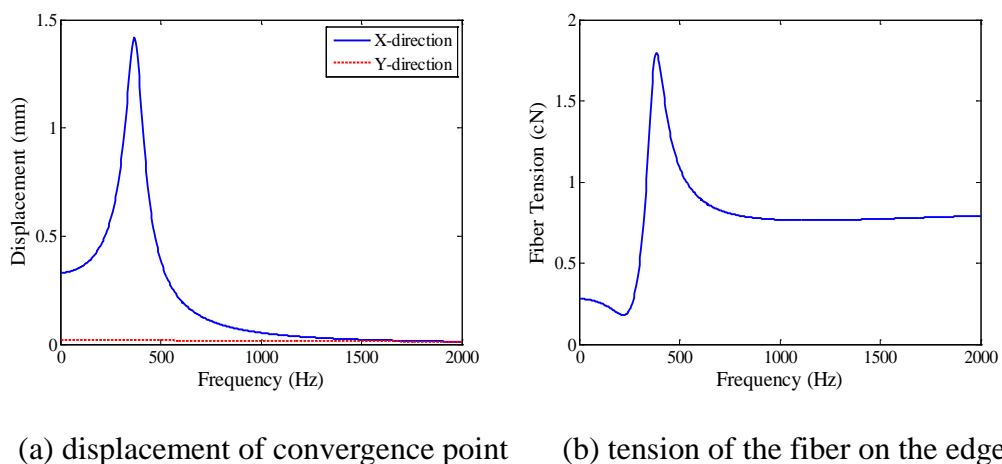
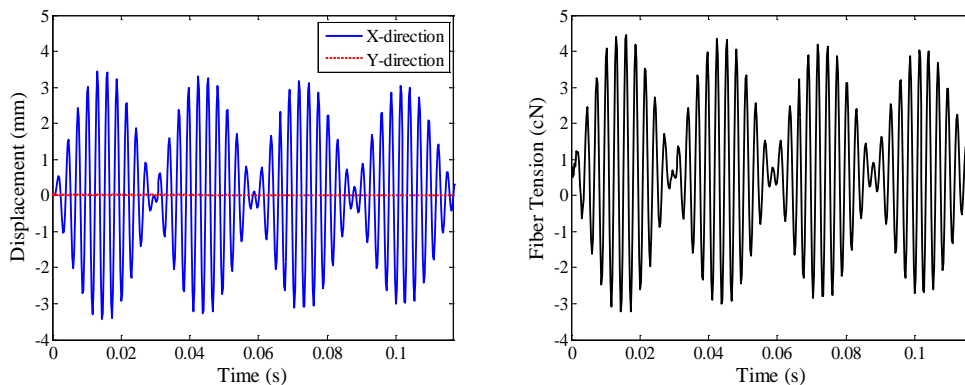


Figure 3.30 Harmonic responses with consideration of fiber damping (Case 4)

3.5.4. Resonant response

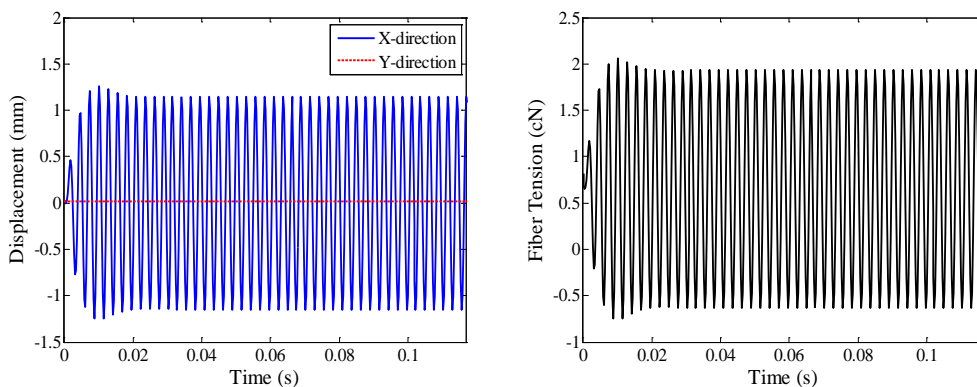
According to the results of above modal and harmonic analysis, if the frequency of impact loads in X-direction is close to the first natural frequency, the response in X-direction will be in a resonant state. Therefore, the previous Case 3 and Case 4 are further used to evaluate the effect of fiber damping on the response of spinning triangle in the resonant state.

With the negligence of fiber damping (Case 3), the responses of X-direction displacement and fiber tension show the obvious beats with the frequency of about 34Hz in [Figure 3.31](#). [Figure 3.32](#) (Case 4) shows that, after a very short shake (about 0.02s), the response of X-direction displacement and fiber tension fall into a stable oscillation in the range of $\pm 1.15\text{mm}$ and $-0.6\text{cN}\sim 1.9\text{cN}$, respectively. The maximum response of X-direction displacement and fiber tension in [Figure 3.31](#) are much larger than that in [Figure 3.32](#). It is, therefore, noted that with considering the fiber damping of structure, the response is faster to become stable with a much lower amplitude.



(a) displacement of convergence point (b) tension of the fiber on the edge

Figure 3.31 Resonant responses without consideration of fiber damping (Case 3)



(a) displacement of convergence point (b) tension of the fiber on the edge

Figure 3.32 Resonant responses with consideration of fiber damping (Case 4)

3.5.5. Transient analysis

3.5.5.1. Dynamic spinning tension

In spinning process, spinning tension used to draw out the yarn from spinning triangle is a dynamic force which is influenced by many factors. For example, in

the ring spinning process, the ascending and descending of the ring rail will obviously cause a low-frequency fluctuation of spinning tension. In addition, rotation of spinning balloon or yarn winding is another major factor to generate a change of spinning tension and a periodical change of inclined angle of spinning tension. Moreover, there are also other factors, such as mechanical defaults of spinning machine (e.g. misalignment of ring spindle to ring rail) and random impacts, which may lead to a variation of spinning tension.

Figure 3.33 shows a perfect ideal force analysis of yarn formation in ring spinning system [154]. In Figure 3.33, T_s is the spinning tension acted on spinning triangle; θ is the enveloped angle of yarn guide; C is the centripetal force needed to keep the traveler circulating around the ring; and σ is the angle between the force of ring towards traveller and horizontal axis. The spinning tension T_s of spinning triangle (in the absence of air drag) can be expressed by [154]:

$$T_s = \left(\frac{\chi\mu C}{\sqrt{\sin^2 \phi - \chi^2 \mu^2} + \mu \cos \phi} + \frac{1}{2} mR^2 \omega^2 \right) e^{-\eta\theta} \quad (3.37)$$

where $\chi = e^{-v\sigma}$; v is friction coefficient between yarn and traveler; μ is friction coefficient between ring and traveler; ϕ is the angle between winding tension and horizontal normals of ring; m is the mass per unit length of the yarn, R is ring radius; ω is rotational speed of traveler and η is friction coefficient of yarn with yarn guide.

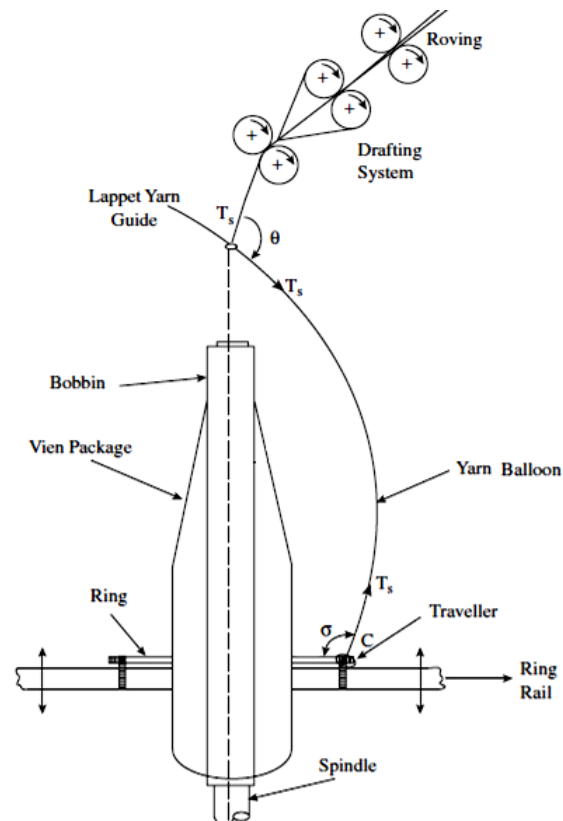


Figure 3.33 Force analysis in yarn formation of ring spinning [154].

According to Equation (3.37), spinning tension is indeed influenced by many factors in the spinning process and thus presents a complex dynamic behavior. Here, a complex dynamic force F , consisting of a series of periodic sinusoid loads with different frequencies and a random noise, will be employed to simulate the dynamic loading force:

$$F = \sum_i a_i \sin(2\pi b_i t + \varphi_i) + \text{noise} \quad (3.38)$$

where a_i , b_i , and φ_i are the amplitude, frequency and phase of the i^{th} sinusoidal component of the load, respectively.

According to measurement results [155], the dynamic spinning tension with a mean value of 26cN in a range of 20cN-34cN is employed to estimate the fiber tension in spinning triangle:

$$F(t) = 23 + 5 \sin(0.1\pi t + 10^\circ) + 3 \sin(2\pi t + 10^\circ) + 1.5 \cos(20\pi t + 5^\circ) + 0.1 \cos(200\pi t + 1^\circ) + 2 \times \text{random (Normal)} \quad (3.39)$$

According to Equation (3.39), Figure 3.34 illustrates a dynamic spinning tension (from 0s to 0.4s), which will be used as an example in the following simulation for the response of fiber tension under time-varying spinning tension.

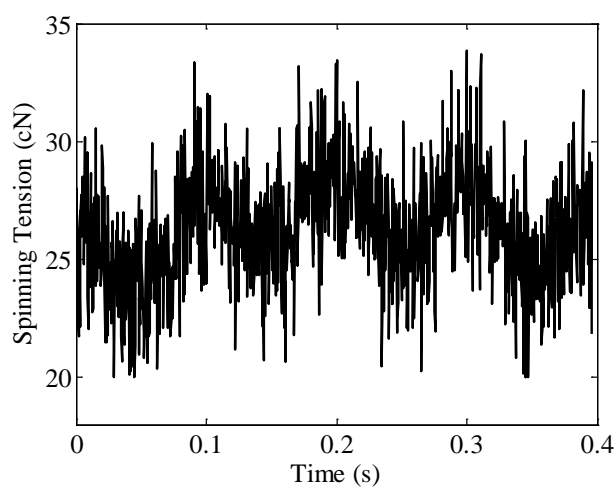


Figure 3.34 Simulated dynamic spinning tension according to Equation (3.39).

As shown in Figure 3.35, during yarn spinning, the spinning triangle is always subject to an inclined spinning tension with a periodical oscillation, where θ is the inclined angle of spinning tension. Generally, the periodical oscillation is caused by yarn winding, so the oscillation frequency f can be calculated from ring rotational

speed. Thus, the components of spinning tension in X- and Y- directions can be obtained as

$$\begin{cases} F_x(t) = F(t) \times \sin(\theta \times \sin 2\pi ft) \\ F_y(t) = F(t) \times \cos(\theta \times \sin 2\pi ft) \end{cases} \quad (3.40)$$

where θ is the inclined angle and f is the oscillation frequency.

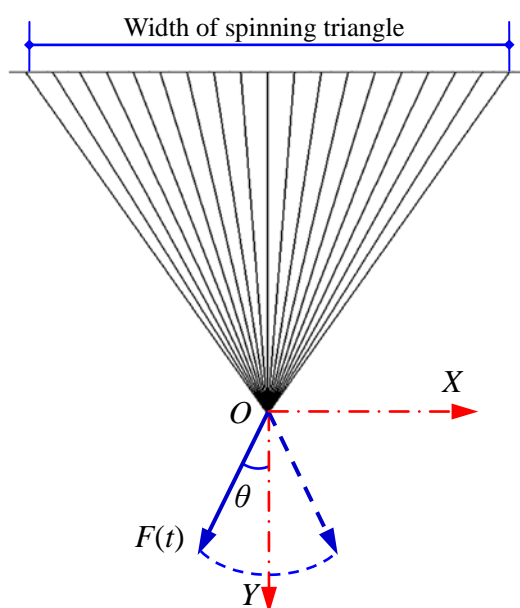


Figure 3.35 Dynamic inclined spinning tension with a periodical oscillation.

Assume the inclined angle θ of spinning tension is 10 degrees and the spinning speed is 12,000rpm (the oscillation frequency f is 200Hz). According to Equations (3.39) and (3.40), the X-direction component and Y-direction component of spinning tension (as shown in Figure 3.34) from 0 to 0.4s can be calculated and illustrated in Figure 3.36. The X-direction component of spinning tension inclined to right is defined as a positive value, otherwise it is negative.

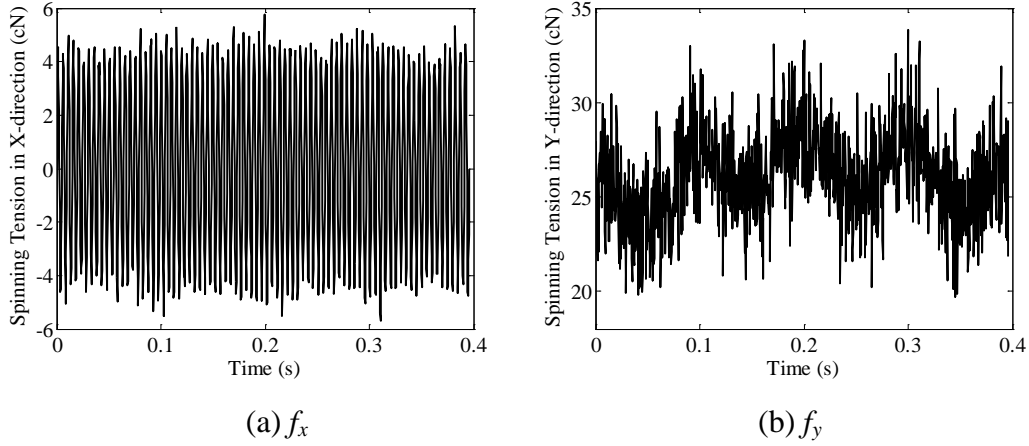


Figure 3.36 Simulated spinning tension on twisting point of spinning triangle

3.5.5.2. Solution methodology

A transient analysis is used to determine the response of spinning triangle under a time-varying spinning tension. The Newmark time integration method HHT [156] is used for solving the implicit transient dynamic analyses in this study. The Newmark method uses finite difference expansions in the time interval Δt [144]:

$$\{\dot{u}_{n+1}\} = \{\dot{u}_n\} + [(1-\delta)\{\ddot{u}_n\} + \delta\{\ddot{u}_{n+1}\}]\Delta t \quad (3.41)$$

$$\{u_{n+1}\} = \{u_n\} + \{\dot{u}_n\}\Delta t + \left[\left(\frac{1}{2} - \lambda \right) \{\ddot{u}_n\} + \lambda \{\ddot{u}_{n+1}\} \right] \Delta t^2 \quad (3.42)$$

where λ, δ is Newmark integration parameters, and $\Delta t = t_{n+1} - t_n$.

In the full transient analysis, the HHT time integration method has the desired property for the numerical damping. The basic form of the HHT method is given

by [144]:

$$[M]\{\ddot{u}_{n+1-\alpha_m}\} + [C]\{\dot{u}_{n+1-\alpha_f}\} + [K]\{u_{n+1-\alpha_f}\} = \{F_{n+1-\alpha_f}\} \quad (3.43)$$

where α_m and α_f are two extra integration parameters for the interpolation of acceleration, displacement, velocity and loads, and

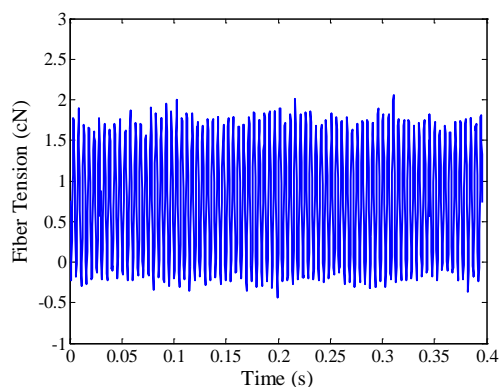
$$\begin{cases} \{\ddot{u}_{n+1-\alpha_m}\} = (1-\alpha_m)\{\ddot{u}_{n+1}\} + \alpha_m\{\ddot{u}_n\} \\ \{\dot{u}_{n+1-\alpha_f}\} = (1-\alpha_f)\{\dot{u}_{n+1}\} + \alpha_f\{\dot{u}_n\} \\ \{u_{n+1-\alpha_f}\} = (1-\alpha_f)\{u_{n+1}\} + \alpha_f\{u_n\} \\ \{F_{n+1-\alpha_f}\} = (1-\alpha_f)\{F_{n+1}\} + \alpha_f\{F_n\} \end{cases}.$$

Because of the initial strain involved in the proposed model, nonzero initial conditions are input by performing a pre-load step prior to the start of the transient itself.

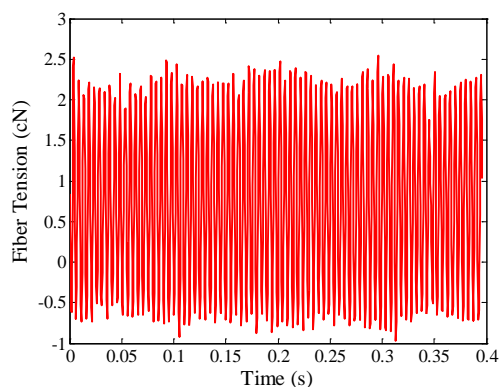
3.5.5.3. Simulation results

Wool yarn with count of 68tex and twist of 100tpm is employed to estimate the fiber tension in spinning triangle. According to the loaded spinning tension in [Figure 3.36](#), the static and dynamic responses of fiber tension on the left edge of spinning triangle are shown in [Figure 3.37\(a\)](#) and [\(b\)](#), respectively. The curves shown in

Figure 3.36(a) and Figure 3.37 are changed with a similar frequency. It may give one explanation to the rapid shape change of the spinning triangle in spinning process: the X-direction component of spinning tension takes a significant influence on the geometrical profile and performance of spinning triangle. In addition, the magnitude range of dynamic response is much larger than that of static response, and there is a little delay in the dynamic result. It is noted that the actual fiber tension in the spinning triangle may be much different from the static result because of the effect of dynamic parameters (fiber mass and damping). Therefore, it is necessary to develop a dynamic model of spinning triangle for the estimation of the fiber mechanical behavior in the spinning triangle.



(a) by static model



(b) by dynamic model

Figure 3.37 Response of fiber tension (on left edge) to spinning tension in Figure 3.36.

3.5.6. Fiber tension comparison

In this section, fiber tension calculated by the proposed model will be compared with

those theoretical and experimental results obtained by Najjar [20].

First, the static model can be considered as a special case of the dynamic model proposed in this study if the fiber mass and damping are ignored. Hence, the simulation of our proposed model can be compared with theoretical predictions of Najjar [20] by energy method, as shown in Figure 3.38. A series of 25g/km wool yarn with various twist angle (α) of 8° , 15° and 30° at 30cN spinning tension are used for analyzing the effect of twist angle (or yarn twist) on fiber tension distribution. It is noted that the results of our proposed model and the earlier model [20] are well agreed, though there is a slight difference in the case with 30° twist angle. Besides, it is clear that all the fibers in spinning triangle are elongated when the twist angle is 8° . With the increase of twist angle (or yarn twist), the fibers in the center of spinning triangle tend to be compressed and the fibers in the edge of spinning triangle are subject to larger tension.

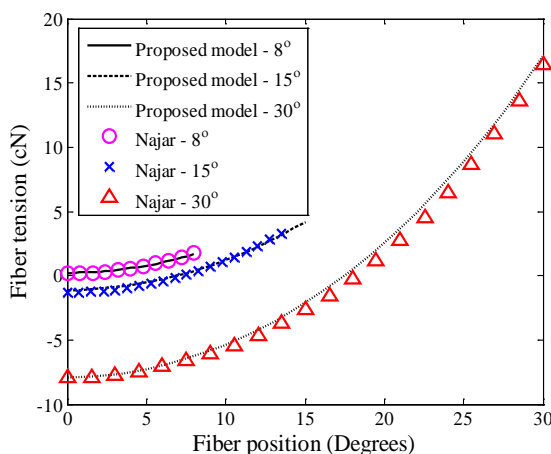


Figure 3.38 Comparison of fiber tensions under different twist angles with Najjar[20].

In order to visualize the effect of yarn twist on spinning triangle, [Figure 3.39](#) shows the geometric shapes of the spinning triangles with the twist angles of 8° , 15° and 30° used in the above comparison, respectively. For different twist angles (or yarn twists), the shape and height of spinning triangles are quite different and the larger the twist angle (or the higher yarn twist), the smaller height of spinning triangle.

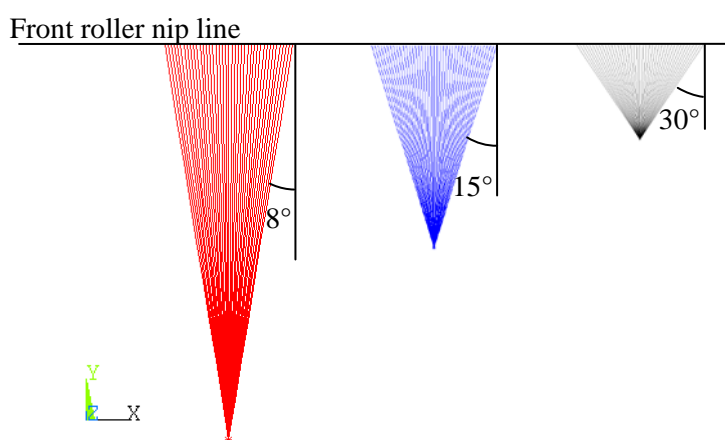


Figure 3.39 Geometric shapes of spinning triangle with different twist angles.

[Figure 3.40](#) gives three examples of the spinning triangle for different shape and fiber tension distributions under the spinning tension with different inclined angles. The asymmetric spinning triangles inclined to the left (see [Figure 3.40\(a\)](#)) or right ([Figure 3.40\(c\)](#)) show that the fibers in one edge are compressed while the other edge is elongated. [Figure 3.40\(b\)](#) illustrates a symmetric spinning triangle where the fibers in the center of spinning triangle are compressed while the fibers in the two edges are elongated. It shows that the inclined spinning angle takes a great influence

on the shape of spinning triangle, which may cause a variation for yarn quality.

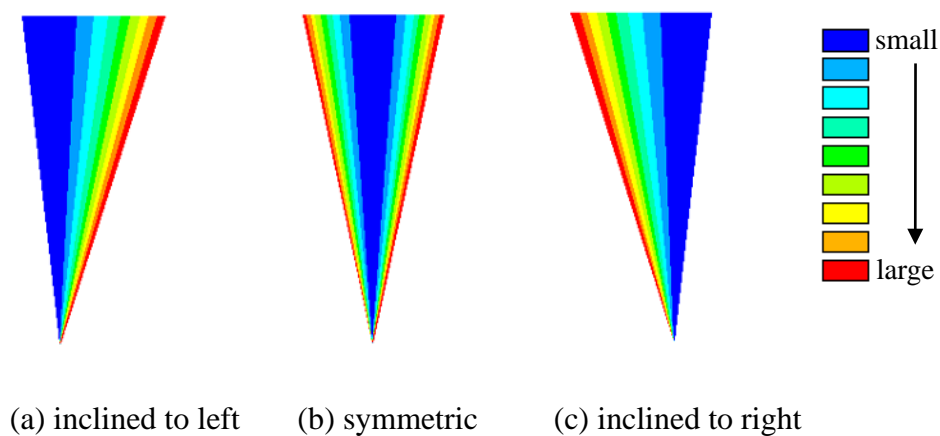


Figure 3.40 The fiber tension distribution of spinning triangle in different shape.

Secondly, simulation results of the proposed model will also be compared with measurement data of Najjar [20]. According to the measurement parameters [20], 22.3tex and 632tpm wool yarn under the average spinning tension of 11.77cN, 17.66cN, 19.62cN and 24.52cN are used for analyzing the effect of spinning tension on fiber tension. The dynamic spinning tension is assumed to load as a periodical oscillation force around the symmetric vertical line within inclined angle (θ) of 10° . And the solution of the proposed model is obtained both with and without fiber buckling consideration.

Figure 3.41 shows the results of fiber tension at (a) left side and (b) right side of the spinning triangle under different spinning tensions as compared to the experimental results by Najjar [20]. In Figure 3.41(a), compared with the linear upward trend

given by the results of the proposed model without fiber buckling, the results of the proposed model with fiber buckling agree more well with the measurement data. Similarly, in Figure 3.41(b), the results of the proposed model with fiber buckling and measurement data show similar upward trends, while the results of the proposed model without fiber buckling keep stable at a high level of about 1.55cN. Figure 3.41 illustrates that the results of the proposed model with fiber buckling are much closer to the measurement data and the agreement on right side is slightly better than that on the left side of spinning triangle.

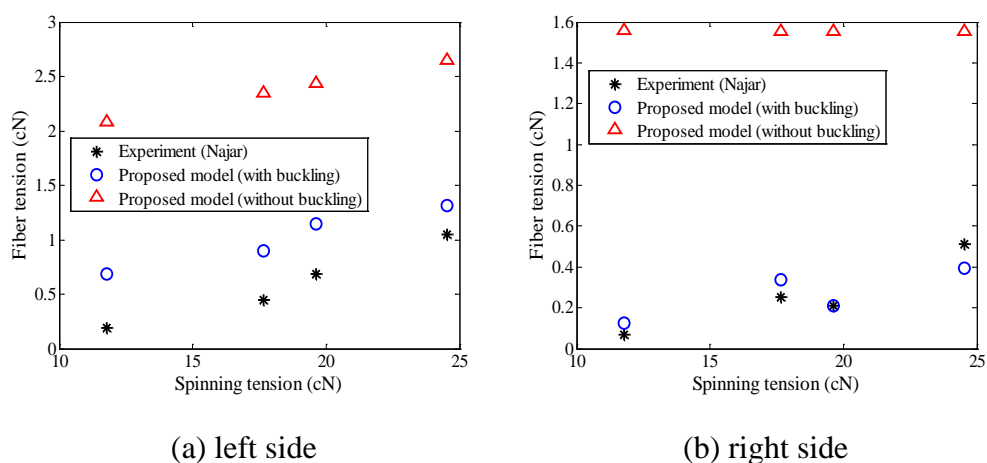


Figure 3.41 Comparison of the proposed model with experimental measurements of Najjar [20] under different spinning tensions

3.6. Conclusions

In this chapter, the Finite Element Method (FEM) has been applied in the theoretical modeling of the spinning triangle in order to develop a more generalized static model

and address more complicated yarn formation process. The initial strain of fibers and the algorithm of element birth and death were employed with a consideration of the inclined spinning tension and fiber torsional strains. Numerical simulations were carried out to quantitatively study the relationship between the mechanical performance of the spinning triangle and various operational parameters. Three potential factors ignored previously, i.e. the inclined angle of spinning tension, the fiber torsional strain and the frictional contact of fibers with the bottom roller, were taken into consideration in the proposed model.

The simulation results showed that some spinning parameters, such as yarn count, yarn twist, spinning tension and its inclined angle, all have the important influences on the fiber tension distribution and fiber torsion distribution. With the consideration of fiber bulking, the fiber tensions are greatly influenced by the spinning tension and its inclined angle, resulting an asymmetric geometry of the spinning triangle. The effect of yarn count on the fiber tension distribution is obvious but it presents a less influence on the maximum value of fiber tension. Besides, the effect of fiber frictional contact with bottom roller on fiber tension distribution is not as significant as that on fiber torsion distribution.

The obtained numerical results of fiber tension in the spinning triangle by the static

FEM model were also compared with the theoretical and experimental results by earlier studies [14, 20, 22-23]. The comparative studies showed that the predictions by the developed finite element model were in good agreements with those by Najjar [20] and Hua [22-23] using the energy method. And the yarn torques obtained by the FEM model were generally closer to the experimental measurements as compared to those by Bennett and Postle [14] and Hua [23].

Based on the above developed static model, a new dynamic model of spinning triangle was further developed in this study with a consideration of the fiber mass and damping by using Finite Element Method. This study originally provided studies on the dynamic properties of spinning triangle, such as natural modes, natural frequency, mode shapes, harmonic analysis, resonant responses as well as effects of spinning parameters. The results of fiber tension in the spinning triangle were also compared with theoretical and experimental results by Najjar [20]. Results showed that the simulation results by the proposed model agree well with the earlier theoretical model and qualitatively agree with experimental measurements. Besides, the response of fiber tension was also investigated under a time-varying spinning tension. The consideration of dynamic parameters of fiber mass and damping has a notable influence on the amplitude and attenuation of the response in dynamic processing.

Chapter 4 Intelligent Computer Method and System for Automatic Mosaic and Segmentation of Tracer Fiber Images in Yarn Structure Analysis

4.1. Introduction

In tracer fiber measurement, a series of consecutive tracer fiber images, simultaneously viewed from two perpendicular directions [44], are obtained and each of them only contains a part of tracer fiber. It is, therefore, required to stitch them into a panorama with a whole complete tracer fiber and then extract yarn boundaries and tracer fiber for further analysis of yarn internal structure. However, the mosaic and segmentation methods currently in use largely involve manual operation. This is mainly because most of the existing mosaic methods or software are only suitable for stitching nature images or the images with distinctive features. For tracer fiber images concerned in this study, the general mosaic methods or software fail in most cases because (1) the images contain two views of yarn, and the yarn position and the distance between the two views of yarn are always changing due to yarn movement during image acquisition; and (2) the images have a highly repetitive pattern and are extremely similar to each other. Meanwhile, although image segmentation algorithms have been developed to extract yarn body and

hairiness from the yarn image, the segmentation of tracer fiber images becomes much more complicated because of the involvement of three components of yarn body, background and tracer fiber. In order to analyze the structure of a spun yarn, hundreds of or even thousands of yarn images have to be processed. It is extremely time-consuming and becomes a bottleneck problem in the yarn structure analysis.

Therefore, in this chapter, an intelligent computer method is proposed and developed for automatically stitching a series of consecutive trace fiber images into a panorama and identifying the yarn boundaries and tracer fiber from the panorama. [Figure 4.1](#) shows the framework of the proposed computer method. It is composed of four components, including image acquisition, image mosaics, image segmentation and three-dimensional (3D) tracer fiber construction. In [Figure 4.1](#), yarn images are firstly acquired with a microscope from yarn samples containing tracer fibers, followed by the creation of panorama with a complete tracer fiber using an automatic mosaic method, and then the yarn body and tracer fiber are extracted by using an automatic segmentation method. Finally the 3D configuration of tracer fiber in the yarn can be reconstructed and various parameters related to fiber migration can be calculated.

In order to evaluate the qualities of image mosaic and segmentation by proposed

method, an objective method is proposed to measure the difference of results by the proposed computer method and manual method. Furthermore, a yarn image database is constructed and a series of experimental work is carried out for a full evaluation of the proposed method by using various yarn samples at different counts (linear density) under different acquisition conditions. Finally, based on the proposed method, an integrated system is designed and developed to visualize and implement the whole progress of the image processing and analysis with an interactive and user-friendly interface.

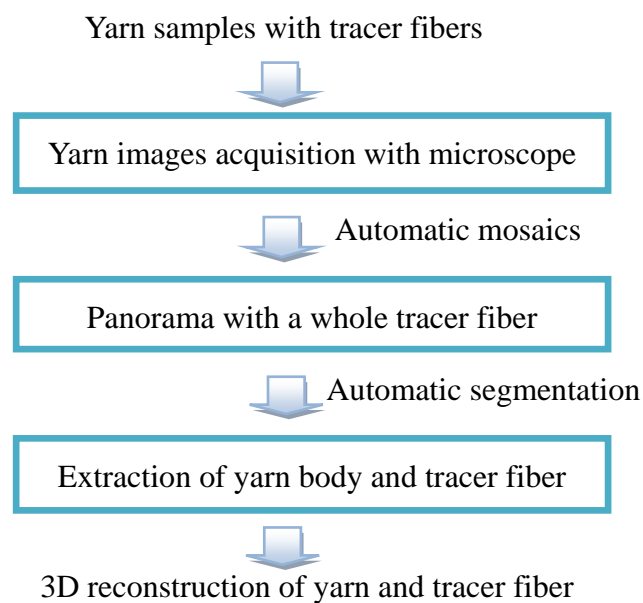


Figure 4.1 Framework of the proposed computer method for tracer fiber analysis.

4.2. Image acquisition

Figure 4.2 shows the measurement system developed by Guo et al. [44] employed for image acquisition. The system is composed of a microscope, a light source, two

mirrors, a metal container and a unit for yarn delivery. Tencel yarn with about 0.4% black-dyed Tencel fibers (a linear density of 1.5 denier, 38 mm in length and 12.08 μm in diameter) is immersed in the mixture of turpentine oil (refractive index: 1.460-1.480) and 1-bromonaphthalene (refractive index: 1.657-1.659) at a proportion of round 1:1, which has a refractive index close to that of Tencel fiber. In order to simplify the problem, the light condition and mixing ratio of solutions are adjusted to make the intensities of background, yarn body and tracer fiber follow the sequence from light to dark. Figure 4.3 shows a series of typical consecutive tracer fiber images (20Ne) obtained by the measurement system and each of them only contains a part of tracer fiber.

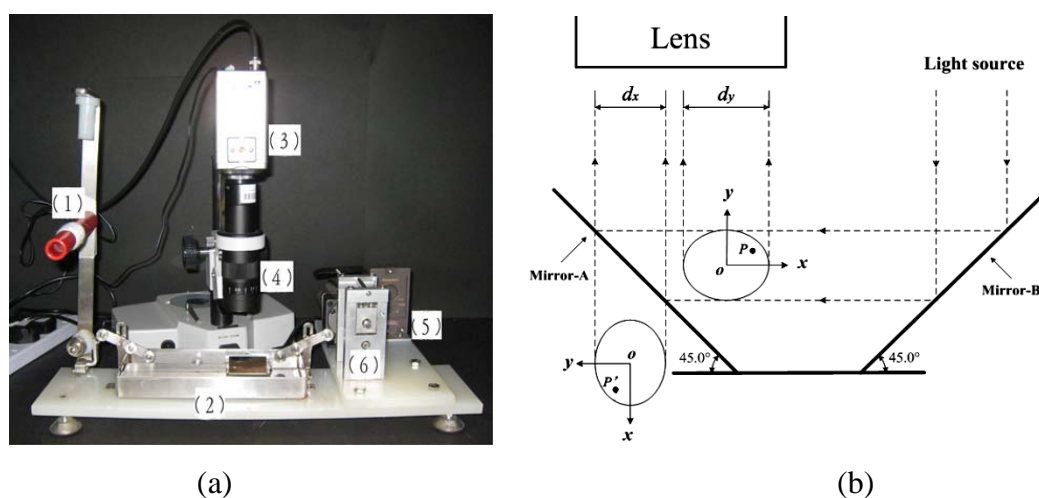
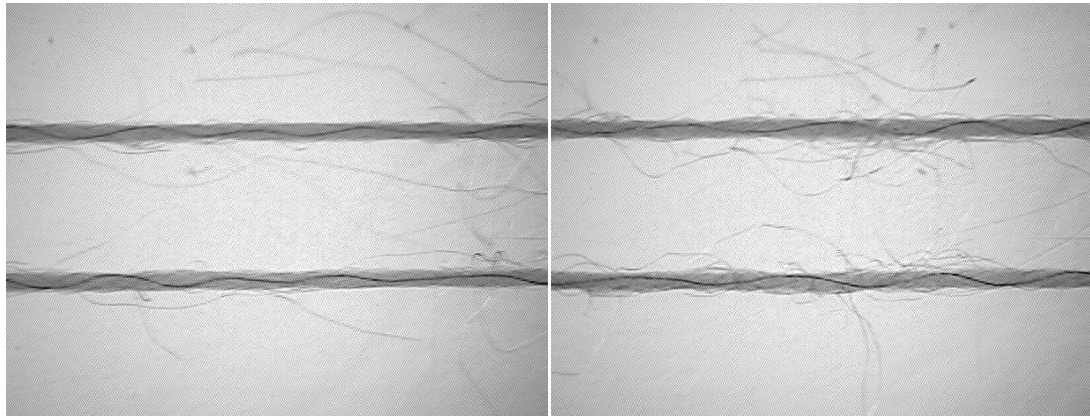
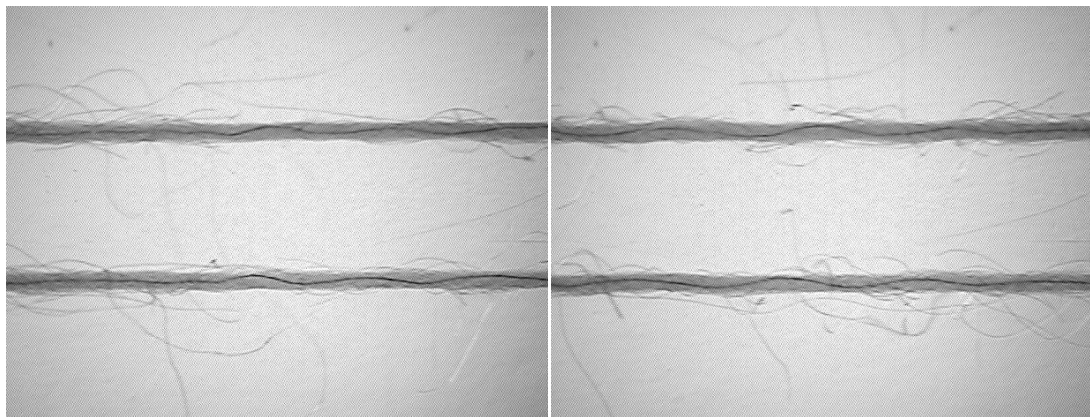


Figure 4.2 Configuration of the measurement system developed by Guo et al. [44].
 (a) Major components: (1) yarn tube holder; (2) metal container; (3) CCD camera; (4) lens; (5) motor and (6) delivery rollers. (b) Optical path: O is yarn center; x and y are coordinate axes in the plane of the yarn-cross section; d_x and d_y are yarn diameters in the x - and y - axes; P is a point of tracer fiber and P' is its image in mirror-A.



(a) 1st image

(b) 2nd image



(c) 3rd image

(d) 4th image



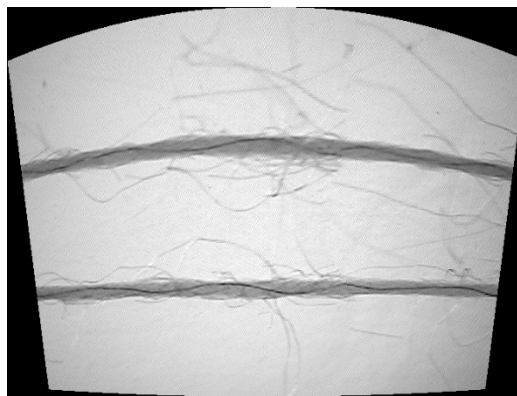
(e) 5th image

(f) 6th image

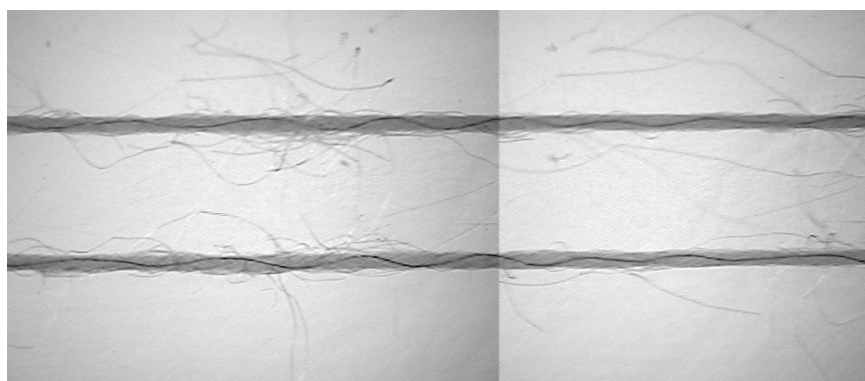
Figure 4.3. A series of consecutive 20Ne yarn images (twist multiplier of 3.3).

4.3. Image mosaic

In order to stitch the images into a panorama, the neighboring images should contain a certain level (e.g. 20%~30%) of overlap area during acquisition. In the following sections, the first two neighboring images of 20Ne yarn shown in [Figure 4.3](#) will be used as an example pair of input images to describe the working principle of the proposed method. As mentioned before, for tracer fiber images concerned in this study, the general methods or software are not capable in most cases because of the highly repetitive pattern of tracer fibers and the change of distance between two views of the tracer fiber image. Here, we employed the existing panorama software (ArcSoft Panorama Maker) to stitch this example pair of tracer fiber images and the mosaic result is shown in [Figure 4.4 \(a\)](#). Compared with the panorama by manual stitching in [Figure 4.4 \(b\)](#), [Figure 4.4 \(a\)](#) shows an image distortion and a false mosaic result. Besides, the line scan camera also failed for image acquisition of tracer fiber images. The main reason is that the delivery speed of yarn in the liquid is not consistent, and there is a serious distortion of signal obtained by the line scan camera at a fixed sampling frequency. It shows that the mosaic of tracer fiber images is quite special, and so proposing a suitable automatic mosaic method is highly significant.



(a)



(b)

Figure 4.4 Panorama created by (a) ArcSoft Panorama Maker and (b) manual stitching.

Figure 4.5 shows the working principle of the proposed computer method for an automatic image mosaic. In Figure 4.5, image 1 and image 2 are the 1st and 2nd images in Figure 4.3 respectively; O - xyz is a coordinate system of the yarn; the upper yarn/tracer fiber captured from the mirror is in yz plane and named yz yarn/tracer fiber; the lower yarn/tracer fiber captured from the real sample is in xz plane and named xz yarn/tracer fiber; u and v are the coordinate axes in horizontal and vertical directions of the image, respectively; A_1 and A_2 are the overlap areas in image 1 and image 2 respectively; P_{y1} and P_{y2} , and P_{x1} and P_{x2} are the matching points of tracer

fiber in image 1 and image 2 respectively; M_1 and M_2 are the points on the top-right corner of A_1 and A_2 , respectively; B_1 and B_2 are two separated regions of image 1 in the middle.

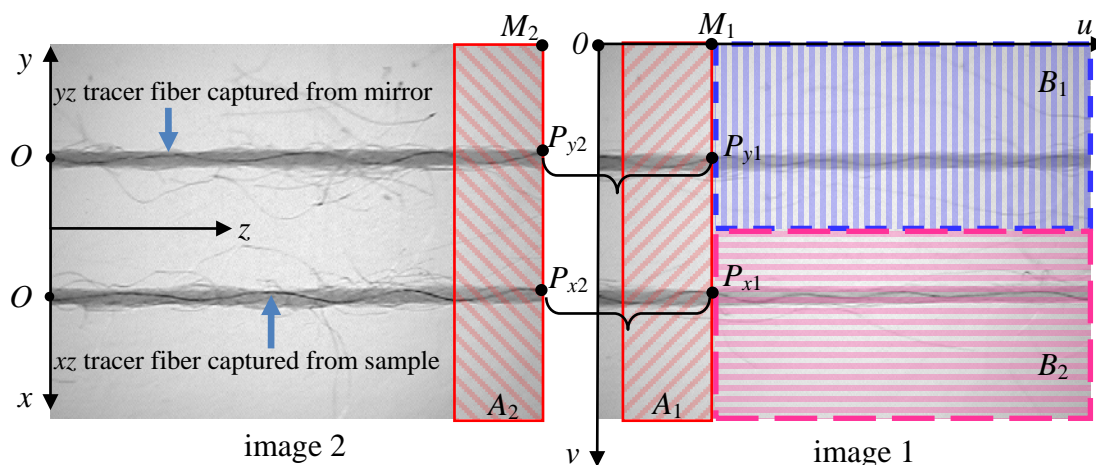


Figure 4.5 Principle of the proposed computer method for automatic image mosaic

Figure 4.6 shows the procedure of the proposed computer method for an automatic image mosaic. As shown in Figure 4.6, the proposed method for image mosaic can be divided into the following two main steps.

(1) Mosaic in the horizontal direction

Yarn images have a highly repetitive pattern and are highly similar to each other, so it is difficult to detect the correct matching position (i.e. M_1 and M_2 in Figure 4.5) in the horizontal direction (u axis). Therefore, in order for an accurate image stitching, a decision function $H(u)$ (see Figure 4.6) is proposed to identify the optimal

matching position for horizontal mosaic of a pair of images (image 1 and image 2) by incorporating four matching functions ($H_1(u)$, $H_2(u)$, $H_3(u)$ and $H_4(u)$) extracted from tracer fiber and gradient images:

$$H(u) = \sum_{i=1}^k w_i H_i(u) \quad (4.1)$$

where $H_i(u)$ is i^{th} normalized matching function, w_i is the weight for $H_i(u)$ and k is the number of matching functions ($k = 4$ in this study).

As shown in [Figure 4.6](#), among the four matching functions, three of them ($H_1(u)$, $H_2(u)$ and $H_3(u)$) are extracted from the tracer fiber and the other one ($H_4(u)$) is extracted from the gradient image, which will be fully discussed in the following two [Sections 4.3.1](#) and [4.3.2](#). Based on the decision function $H(u)$, the optimal stitching position for M_1 - M_2 in u -axis can be identified and thus a mosaic line ($u = M_1$) can be obtained.

(2) Mosaic in the vertical direction

The yarn image contains two views of yarn and the distance between them is always changing due to yarn movement during image acquisition. So the existing methods and software may cause unreasonable image deformation in image mosaic. Hence, as shown in [Figure 4.5](#) and [Figure 4.6](#), we will separate image 1 into two individual

regions (B_1 and B_2) from the middle of image and each region contains a single view of the yarn. The two regions are then moved in the vertical direction (v axis) to stitch the matching points of the tracer fiber (P_{y1} with P_{y2} and P_{x1} with P_{x2}) according to the continuity of the tracer fiber.

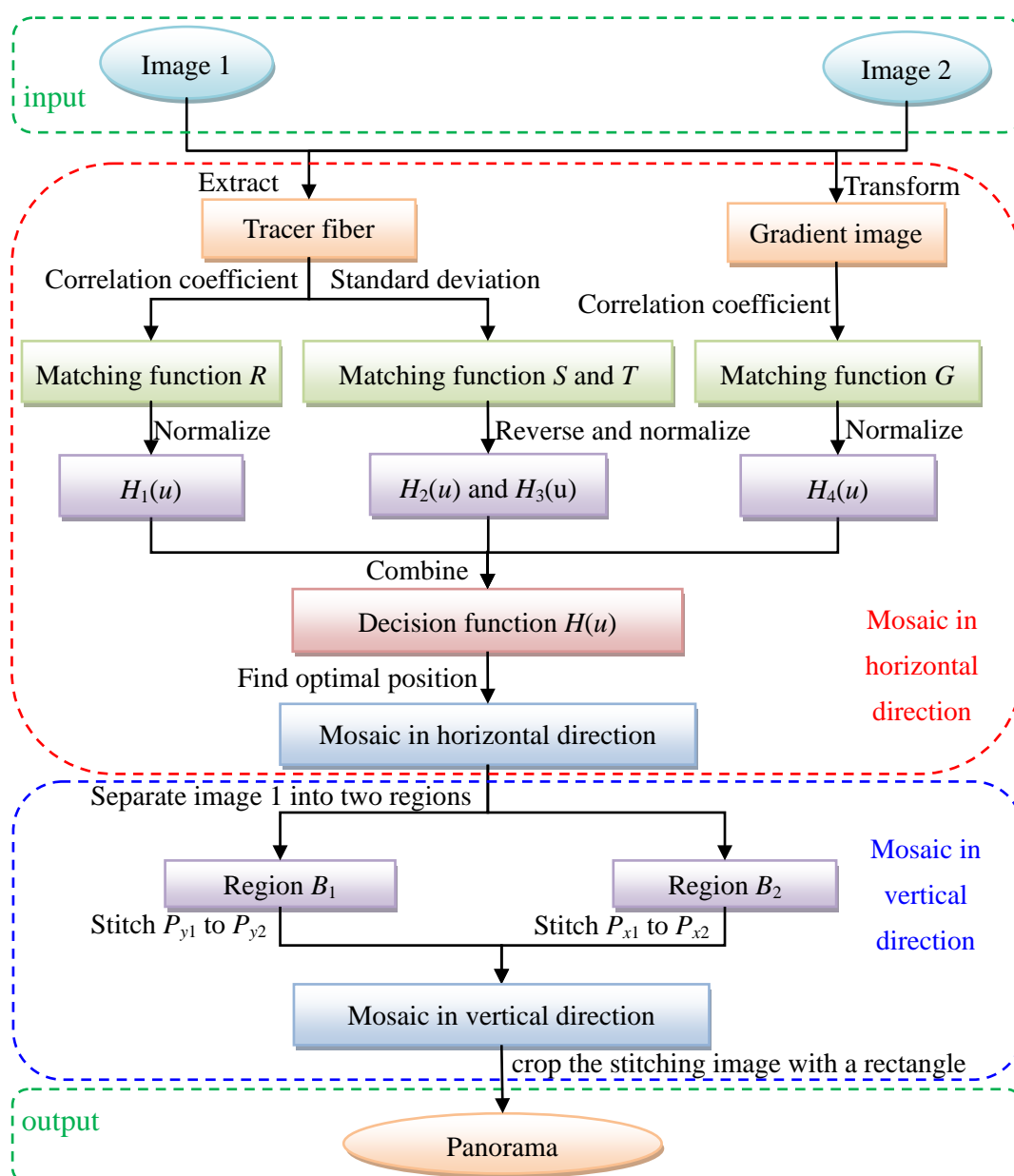


Figure 4.6 Procedure of the proposed computer algorithms for image mosaics

4.3.1. Matching function related to the tracer fiber

In image acquisition, the yarn is moving in the liquid with a high viscosity, so the fluctuation of yarn sample cannot be avoided. As the most stable feature, tracer fiber will be extracted and used for building up the decision function for the image mosaic. A digital yarn image with a size of $M \times N$ can be denoted by $f(u, v)$, which presents the intensity of the pixel at coordinate (u, v) . Figure 4.7(a) illustrates the intensity profile $f(i, v)$ of the i^{th} column of the tracer fiber image with size of $M \times 1$. It is noted that it is a signal featured with two obvious narrow valleys (in ellipses) that contain the information of the yarn body and tracer fiber. As the colored tracer fiber is normally darker than other yarn fibers and background, the minimum point (marked by "b") in each valley should be a pixel of the tracer fiber. Then, the problem of tracer fiber detection is equivalent to identifying the minimum point in each valley. However, the two minimum points in the valleys could not be identified by simply sorting $f(i, v)$. Besides, there might be some extreme points caused by yarn hairiness or foreign fiber, which further increases the complexity of problem. For example, in Figure 4.7(a), an obvious noise point marked by "*" is a pixel of yarn hairs whose value is even smaller than one of the minimum points in the valley. Therefore, identification of the two valleys is practically challenging. In order to facilitate the analysis, the intensity profile $f(i, v)$ will be reversed and

normalized as an input signal $f_1(i,v)$, as shown in Figure 4.7(b):

$$f_1(i,v) = \frac{\max(f(i,v)) - f(i,v)}{\max(f(i,v)) - \min(f(i,v))} \quad (4.2)$$

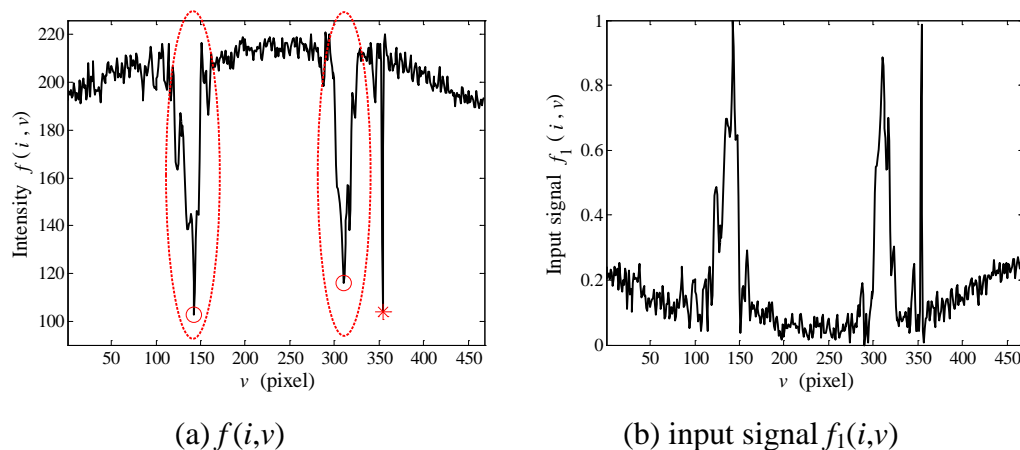


Figure 4.7 Intensity profile of the i^{th} column of the tracer fiber image.

The tracer fiber detection method developed in this study is similar to that for QRS complex from the electrocardiogram (ECG) signals [67, 157]. The QRS complex is a name for the combination of Q wave, R wave and S wave on an ECG (as shown in Figure 4.8), which reflects the rapid depolarization of the right and left ventricles.

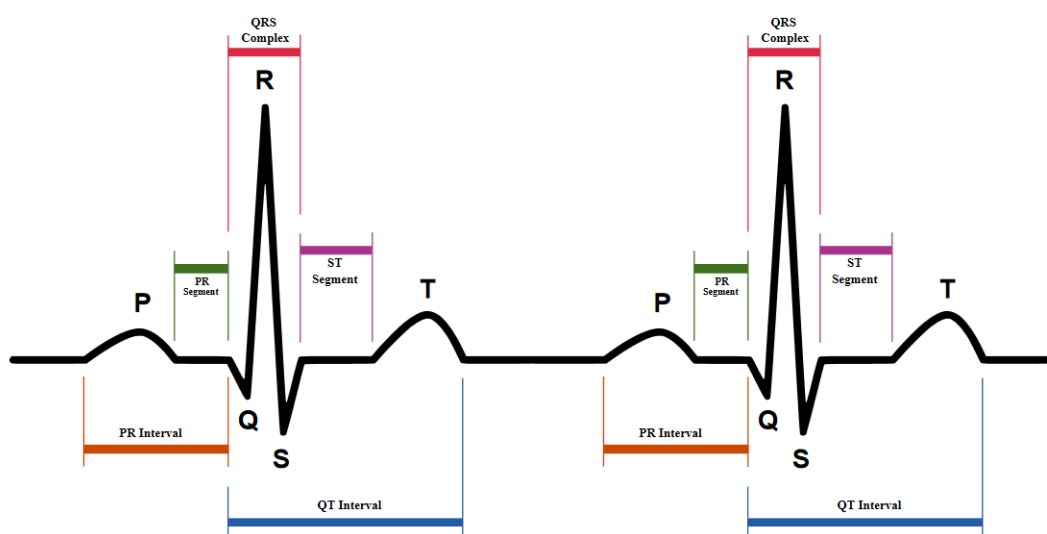


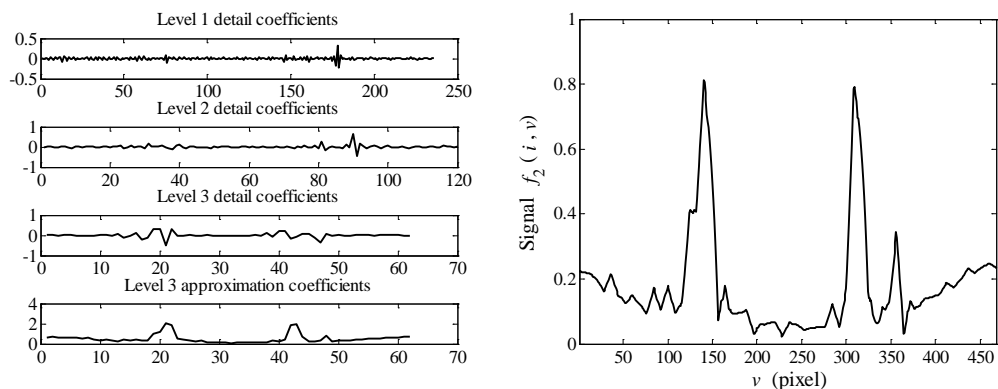
Figure 4.8 Schematic representation of normal ECG [158].

Pan and Tompkins [67] proposed a real-time QRS complex detection algorithm (as shown in Figure 4.9) that includes a series of filters and methods that perform low-pass, high-pass, derivative, squaring, integration, adaptive threshold and search procedures.



Figure 4.9 Block diagram of Pan-Tompkins algorithm for QRS complex detection.

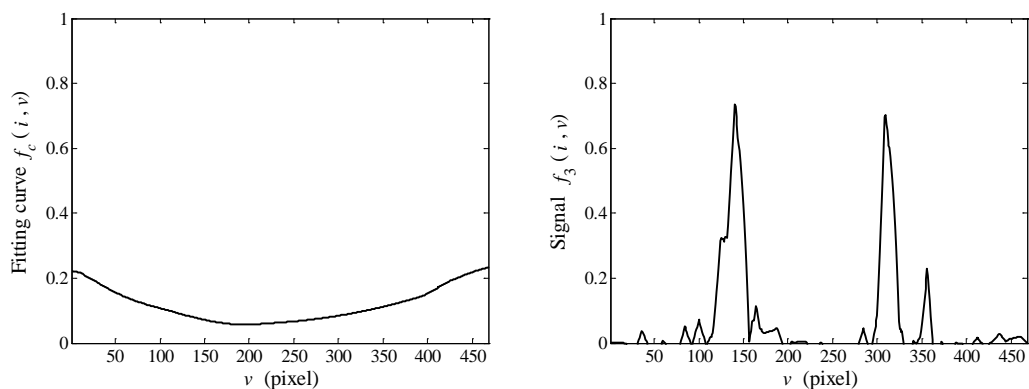
In this study, we will extend the Pan-Tompkins algorithm for detecting tracer fiber by developing more suitable filters. As shown in Figure 4.7(b), the profile of input signal $f_1(i,v)$ is apparently different from that of the ECG signal, so the discrete wavelet transform (DWT) is used as low-pass filter for noise reduction and the Daubechies-3 wavelet is employed in this study. Figure 4.10(a) shows the three-level decomposition of the signal $f_1(i,v)$ using Daubechies-3 wavelet. In each level, soft threshold based on BayesShrink by minimizing the Bayesian Risk is used for the detail coefficients, and then the approximation coefficients at level 3 and the three-level thresholded detail coefficients of signal $f_1(i,v)$ are reconstructed as the de-noised signal $f_2(i,v)$, as shown in Figure 4.10(b). However, signal $f_2(i,v)$ still contains a clear baseline drift due to the light condition.



(a) analyzing $f_1(i,v)$ with Daubechies-3

(b) de-noised signal $f_2(i,v)$

Figure 4.10 Signal de-noising.



(a) fitting curve $f_c(i,v)$

(b) de-baseline signal $f_3(i,v)$

Figure 4.11 Baseline fitting.

In order to remove the baseline, a fitting curve $f_c(i,v)$ (see Figure 4.11(a)) for the baseline is interpolated by several points automatically selected from the beginning, middle and end of the signal $f_2(i,v)$ by using the piecewise cubic Hermite interpolation method [68]. So, a new signal $f_3(i,v)$ without the baseline (see Figure 4.11(b)) can be obtained by:

$$f_3(i,v) = f_2(i,v) - f_c(i,v) \tag{4.3}$$

Then the first-order derivatives $f_4(i,v)$ (see [Figure 4.12\(a\)](#)) of $f_3(i,v)$ can be calculated between adjacent pixels:

$$f_4(i,v) = \frac{\partial f_3(i,v)}{\partial v} \quad (4.4)$$

As shown in [Figure 4.12\(b\)](#), it is squared point-by-point to make all points positive and enlarge higher frequencies:

$$f_5(i,v) = (f_4(i,v))^2 \quad (4.5)$$

Afterwards, an integrator [67] is employed to sum the area under the squared waveform over a suitable interval and integrate the new interval to reduce the effect of noise:

$$f_6^*(i,v) = \left(\frac{1}{N_{iw}} \right) [f_5(i,v-N+1) + f_5(i,v-N+2) + \dots + f_5(i,v)] \quad (4.6)$$

where N_{iw} is the number of samples in the width of integration.

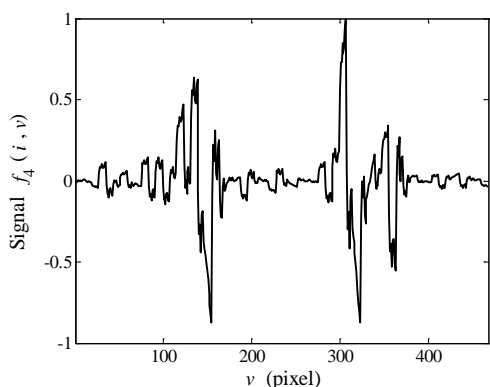
A new waveform $f_6(i,v)$ can be then obtained by normalizing $f_6^*(i,v)$. A threshold T_b is used for its segmentation:

$$T_b = 0.5 \times \text{mean}(f_6(i,v)) \times \max(f_6(i,v)) \quad (4.7)$$

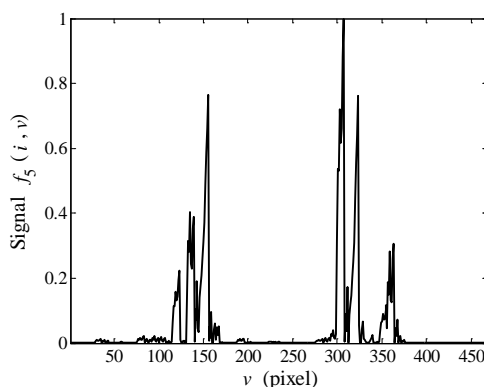
Finally, as shown in [Figure 4.12\(c\)](#), the regions can be identified by two pairs of boundary, which can be obtained by the first-order difference of $B_p(i,v)$:

$$B_p(i, v) = \begin{cases} 1 & f_6(i, v) > T_b \\ 0 & f_6(i, v) \leq T_b \end{cases} \quad (4.8)$$

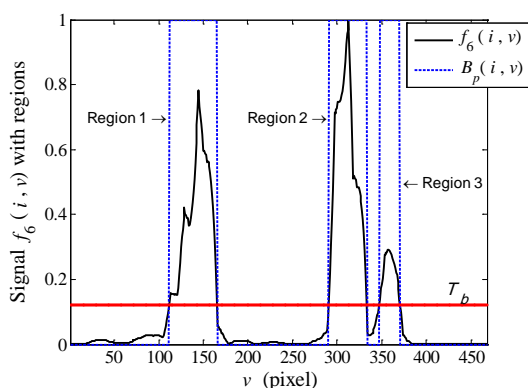
In this example, three regions are detected: regions 1 and 2 for tracer fiber, region 3 for yarn hairiness. It is reasonably believed that yarn body is much thicker than the hairiness or foreign fiber, so two widest regions will be considered as the real regions of valley. In each region, the maximum peak of the signal $f_1(i, v)$ could be detected as the position of the tracer fiber, as shown in Figure 4.12(d).



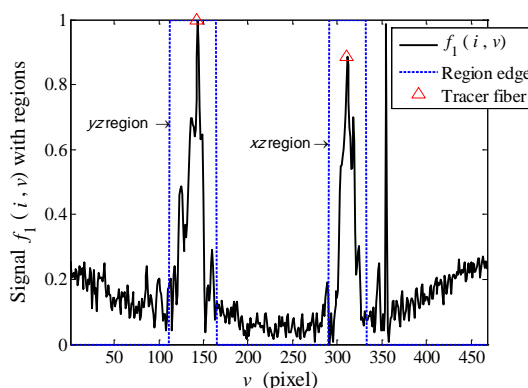
(a) signal $f_4(i, v)$



(b) signal $f_5(i, v)$



(c) signal $f_6(i, v)$ with regions, $N_{iw}=20$



(d) regions and tracer fibers in $f_1(i, v)$

Figure 4.12 Processing results of tracer fiber detection.

The connectivity will also be used in the tracer fiber identification to reduce the influence of noises. Then the proposed method can be further used for every column of the image and therefore the tracer fiber can be automatically identified. Based on the above, the tracer fibers in image 1 and the overlap area A_2 of image 2 can be detected, as shown in Figure 4.13.

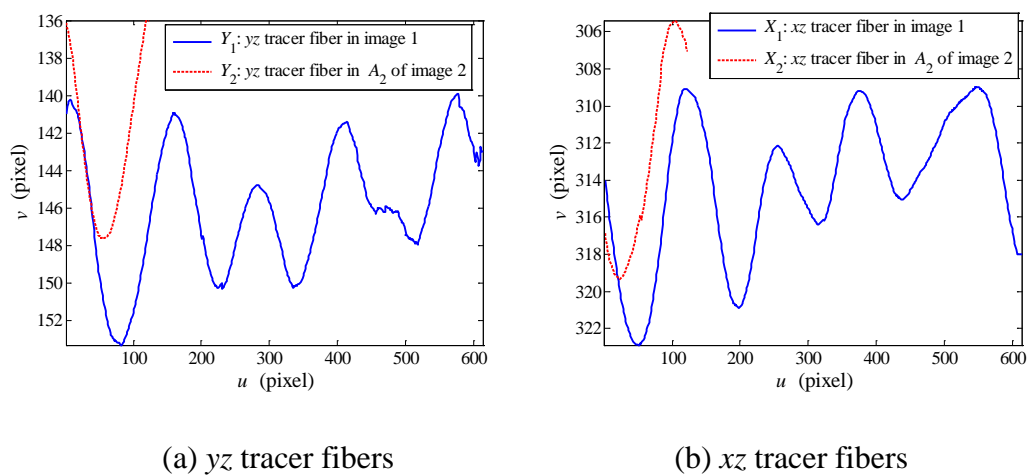


Figure 4.13 Tracer fibers in image 1 and A_2 of image 2.

The yz and xz tracer fibers in A_2 of image 2 are denoted as vectors Y_2 and X_2 of size $L \times 1$, respectively:

$$Y_2 = [y_2(1); y_2(2); \dots; y_2(L)], \quad X_2 = [x_2(1); x_2(2); \dots; x_2(L)] \quad (4.9)$$

where $y_2(i)$ and $x_2(i)$ are the v -axis location (pixel) of the i^{th} point of yz and xz tracer fibers in A_2 of image 2, and L is the width of A_2 .

In addition, y_z and x_z tracer fibers in image 1 are defined as vectors Y_1 and X_1 of size $N \times 1$, respectively:

$$Y_1 = [y_1(1); y_1(2); \dots; y_1(N)], \quad X_1 = [x_1(1); x_1(2); \dots; x_1(N)] \quad (4.10)$$

where $y_1(i)$ and $x_1(i)$ are the v -axis location (pixel) of the i^{th} point of y_z and x_z tracer fibers in image 1, and N is the width of image 1.

One of the statistical measures, the correlation coefficient, can be used to evaluate the similarity of the tracer fiber in A_2 of image 2 and the tracer fiber in image 1 of the same length for identifying the optimal location for image stitching. Accordingly, the correlation coefficients $R_y(u)$ for y_z tracer fiber and $R_x(u)$ for x_z tracer fiber in images 1 and 2 at point u can be defined as

$$R_y(u) = R_y(Y_2, Y_1(u)) = \frac{C(Y_2, Y_1(u))}{\sqrt{C(Y_2, Y_2) C(Y_1(u), Y_1(u))}} \quad (4.11)$$

$$R_x(u) = R_x(X_2, X_1(u)) = \frac{C(X_2, X_1(u))}{\sqrt{C(X_2, X_2) C(X_1(u), X_1(u))}} \quad (4.12)$$

where $Y_1(u) = [y_1(u); y_1(u+1); \dots; y_1(u+L-1)]$, $X_1(u) = [x_1(u); x_1(u+1); \dots; x_1(u+L-1)]$, $u = 1, 2, \dots, N-L, N-L+1$ and C is the covariance matrix.

Then the matching function related to correlation coefficients of the tracer fiber can

be obtained as

$$R(u) = R_y(u) + R_x(u) \quad (4.13)$$

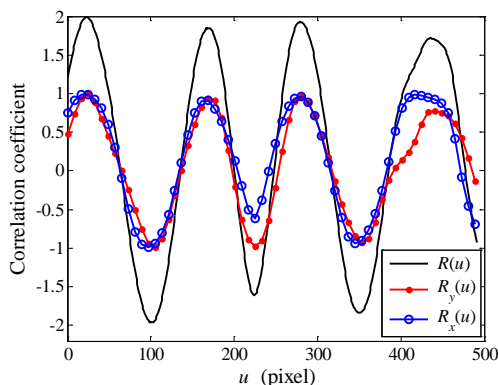


Figure 4.14 Matching function related to correlation coefficients of the tracer fiber.

Figure 4.14 shows the matching function $R(u)$ of the example images 1 and 2. It is noted that there are four peaks of $R(u)$ and they are the potential stitching points.

Although the first peak is largest, the differences among them may not be strong and stable enough to decide which is the correct stitching point. The matching function

$R(u)$ is normalized to form a component of the decision function $H(u)$ in Equation

(4.1):

$$H_1(u) = \frac{R(u) - \min(R(u))}{\max(R(u)) - \min(R(u))} \quad (4.14)$$

Besides the similarity of the tracer fiber, the standard deviation can be also employed to describe the relationship of tracer fibers in consecutive images. Therefore, one

more matching function $S(u)$ can be defined as

$$S(u) = S_y(u) + S_x(u) = \sigma(Y_1(u) - Y_2) + \sigma(X_1(u) - X_2) \quad (4.15)$$

where $S_y(u)$ and $S_x(u)$ are the variations of distance between two yz tracer fibers and two xz tracer fibers at point u , respectively, and σ is the standard deviation.

In addition, another matching function $T(u)$ related to standard deviation is also proposed to evaluate the absolute variation $T_y(u)$ between two yz tracer fibers and $T_x(u)$ between two xz tracer fibers:

$$T(u) = T_y(u) + T_x(u) = |\sigma(Y_1(u)) - \sigma(Y_2)| + |\sigma(X_1(u)) - \sigma(X_2)| \quad (4.16)$$

where $||$ presents the absolute value.

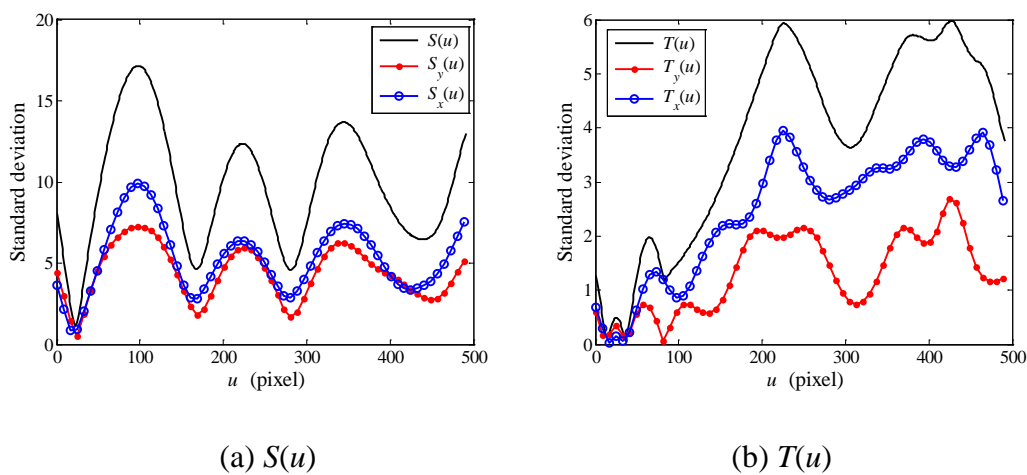


Figure 4.15 Matching functions related to standard deviation of the tracer fiber.

As $S(u)$ and $T(u)$ are related to the variation of tracer fibers, a lower value indicates a higher matching level. If the value is equal to zero, it means that the tracer fibers coincide with each other at this point. Therefore, the optimal stitching position should be the minimum point. Figure 4.15 shows $S(u)$ and $T(u)$ for the two example images. The minimum value in Figure 4.15(a) locates at around the 25th pixel, which is close to the maximum point in Figure 4.14. In Figure 4.15(b), a lower value also presents around the position. The matching functions $S(u)$ and $T(u)$ are then reversed and normalized to form two more components of the decision function $H(u)$ in Equation (4.1):

$$H_2(u) = \frac{\max(S(u)) - S(u)}{\max(S(u)) - \min(S(u))}, \quad H_3(u) = \frac{\max(T(u)) - T(u)}{\max(T(u)) - \min(T(u))} \quad (4.17)$$

Hence, three matching functions ($R(u)$, $S(u)$ and $T(u)$) related to statistical measures of tracer fibers were extracted and normalized to be the components ($H_1(u)$, $H_2(u)$ and $H_3(u)$) in decision function $H(u)$. They can be considered as local features of the yarn image. In order to identify the optimal results, one more matching function should be built up by global features of the yarn image to complete the decision function, as discussed in the following section.

4.3.2. Matching function related to gradient image

In this section, correlation coefficients of two neighboring yarn images will be extracted to form the global features of the decision function. However, uneven illumination in original images caused by light condition will negatively affect the results. In order to reduce the influence of the light condition, a gradient image is obtained by using a Sobel edge detector [50]. Figure 4.16 shows the gradient images of the example images 1 and 2. It is noted that compared with the original images, uneven illumination caused by light condition can be avoided and the edges in the image become clearer.

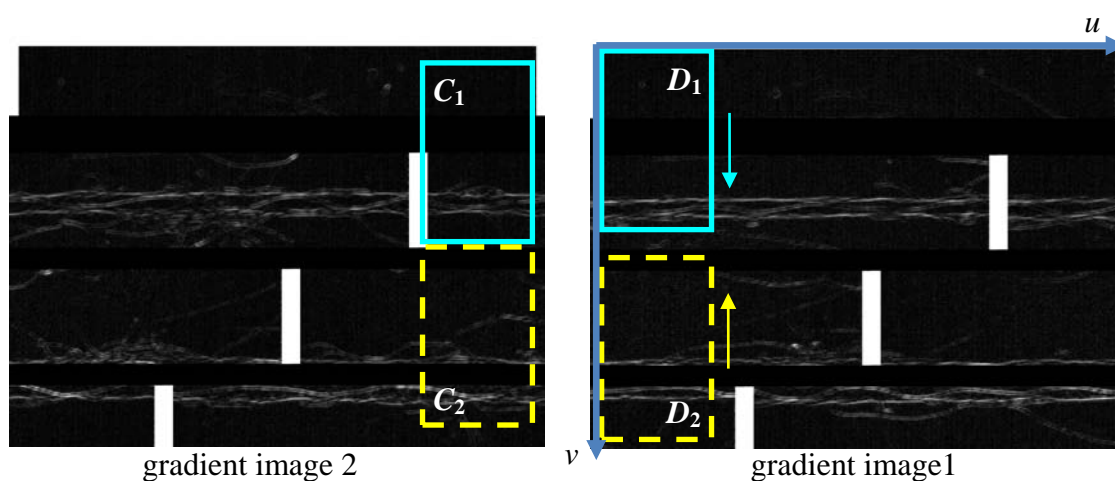


Figure 4.16 Gradient images of the example images 1 and 2.

As mentioned before, changes of yarn position and the distance between the yarn and the mirror cannot be avoided when the yarn is on moving. Therefore, as shown in

Figure 4.16, the overlap area in gradient image 2 will be divided into two parts, C_1 and C_2 , and they will be compared with the moving windows D_1 and D_2 along both horizontal and vertical directions in gradient image 1 to identify the stitching position by using the two-dimensional (2D) correlation coefficients. Figure 4.17 illustrates the 2D correlation coefficients $G_y(u,v)$ and $G_x(u,v)$ of region C_1-D_1 and region C_2-D_2 , respectively. The coefficient C_{AB} can be defined between matrices A and B as follows:

$$C_{AB} = \frac{\sum \sum (A - \bar{A})(B - \bar{B})}{\sqrt{(\sum \sum (A - \bar{A})^2)(\sum \sum (B - \bar{B})^2)}} \quad (4.18)$$

where A and B are two example matrices, and \bar{A} and \bar{B} are the means of A and B .

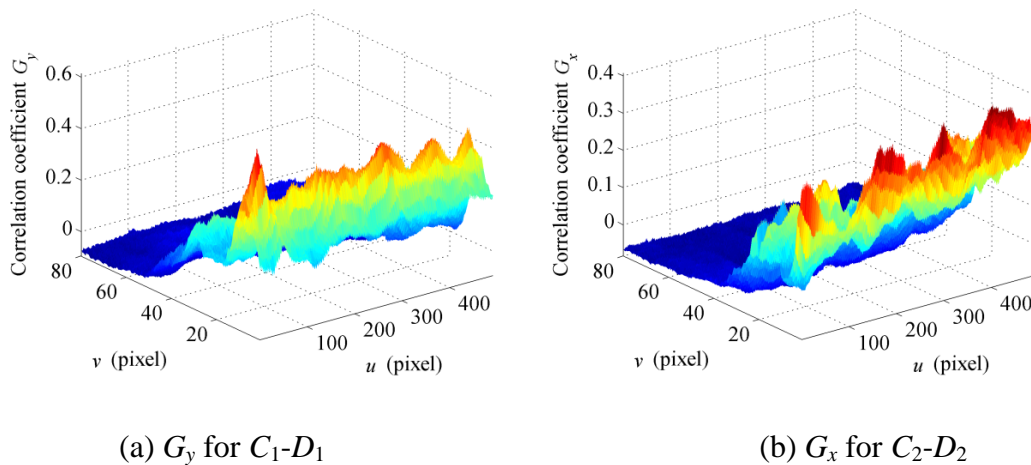


Figure 4.17 2D correlation coefficients of the gradient image.

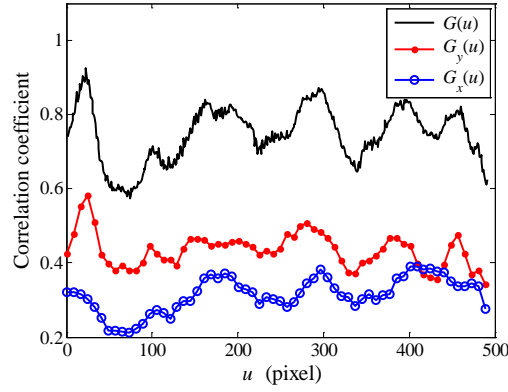


Figure 4.18 Matching function $G(u)$ from correlation coefficients of gradient image.

To evaluate the whole image, maximums $G_y(u)$ and $G_x(u)$ in each column of the u -axis are extracted to form a matching function related to the correlation coefficient of the gradient image:

$$G(u) = G_y(u) + G_x(u) \quad (4.19)$$

Figure 4.18 shows matching function $G(u)$ calculated from Figure 4.17. It is noted that there are several clear peaks that are potentially considered as the stitching position. Finally, the matching function $G(u)$ is normalized to be a component of the decision function $H(u)$ in Equation (4.1):

$$H_4(u) = \frac{G - \max(G)}{\max(G) - \min(G)} \quad (4.20)$$

4.3.3. Results of the image mosaic

Based on the above analysis and Equations (4.14), (4.17) and (4.20), the decision

function $H(u)$ for identifying the optimal matching position in the u -axis can be obtained as:

$$H(u) = \sum_{i=1}^k w_i H_i(u) = w_1 H_1(u) + w_2 H_2(u) + w_3 H_3(u) + w_4 H_4(u) \quad (4.21)$$

Figure 4.19 shows the decision function $H(u)$ and its components for the example images 1 and 2, holding all weights equal. The maximum point in $H(u)$ marked by " Δ " could be considered as the optimal position for image stitching in the u -axis. Although all components of $H(u)$ provide useful information of the optimal stitching position, each of them alone sometimes may not be strong and stable enough for an accurate detection. Therefore, as shown in Figure 4.19, the benefit of their combination lies in an enhanced and magnified feature for a stable and accurate image stitching.

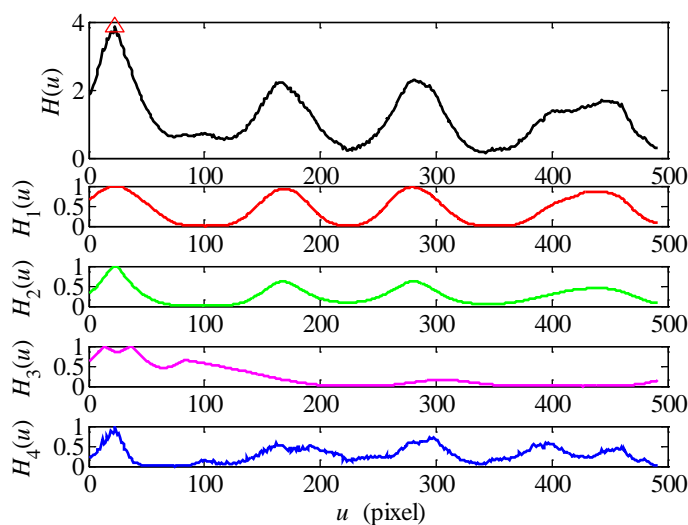


Figure 4.19 Decision function and its components.

Finally, image 1 is separated into two regions and they are moved in the v -axis according to the continuity of the tracer fiber to get the panoramic image, as shown in [Figure 4.20](#).

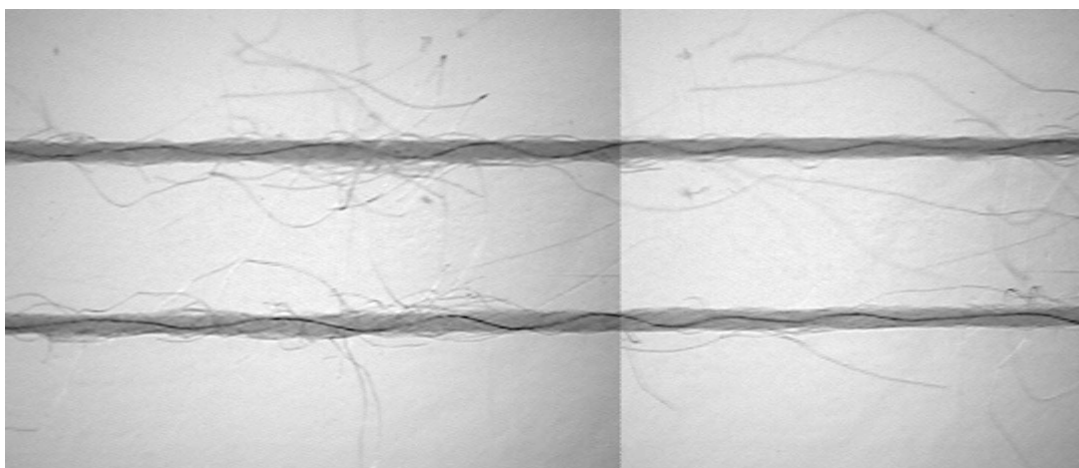
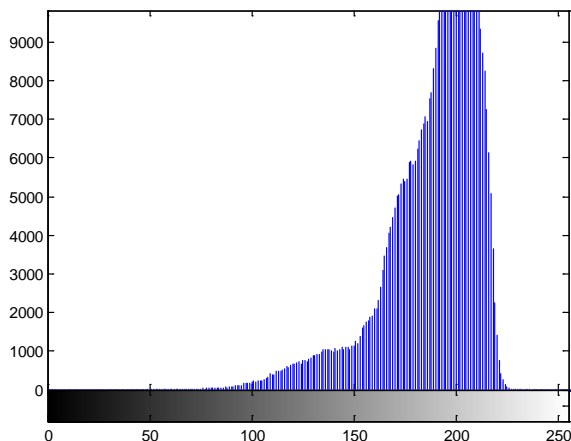


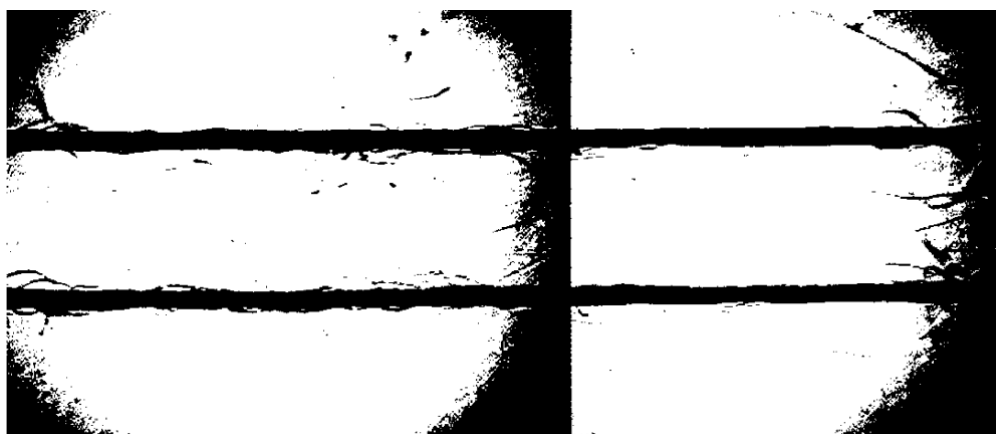
Figure 4.20 Panorama of images 1 and 2.

4.4. Image segmentation

After the panorama of yarn containing a whole tracer fiber is obtained, the yarn boundaries and tracer fiber can be extracted for further analysis. As the method for detection of tracer fiber has been proposed in the previous [Section 4.3.1](#), this section mainly focuses on the detection of yarn boundaries. [Figure 4.21\(a\)](#) shows a histogram of the panorama in [Figure 4.20](#).



(a) histogram



(b) binary image

Figure 4.21 Histogram and binary image of the panorama in [Figure 4.20](#).

Otsu's method, a method of minimizing the interclass variance of the black and white pixels, is used to select the threshold for image segmentation. [Figure 4.21\(b\)](#) shows the binary image obtained by the Otsu's method. It is noted that it is impossible to identify the yarn bodies by using a global threshold because of the partial dark background caused by the uneven light condition. So the image preprocessing should be employed to eliminate the effect of the uneven light condition. The main algorithms for boundary detection are described in [Figure 4.22](#).

Steps for detection of yarn boundaries:

- (1) Average the image using a moving window to reduce noise;
- (2) Delete the effect of uneven distribution of light;
- (3) Select threshold for binary image of yarn bodies;
- (4) Detect the edge of binary image as yarn boundaries.

Figure 4.22 The algorithms diagram for yarn boundary detection.

Besides the yarn body and tracer fiber, the yarn image also includes background, hairiness and other potential noises. In order to reduce the effect of image noise, as shown in Figure 4.23, a moving window with a certain width is used to average the intensities of pixels in the u -axis. The panoramic image of size $K \times M$ can be expressed by $f(u, v)$. Hence, a new average image \mathbf{Q} can be generated by $q(u, v)$:

$$q(u, v) = \frac{1}{L_m} \sum_{u=1}^{L_m} f(u, v), \quad u=1, \dots, K-L_m+1 \quad (4.22)$$

where L_m is the width of the moving average window.

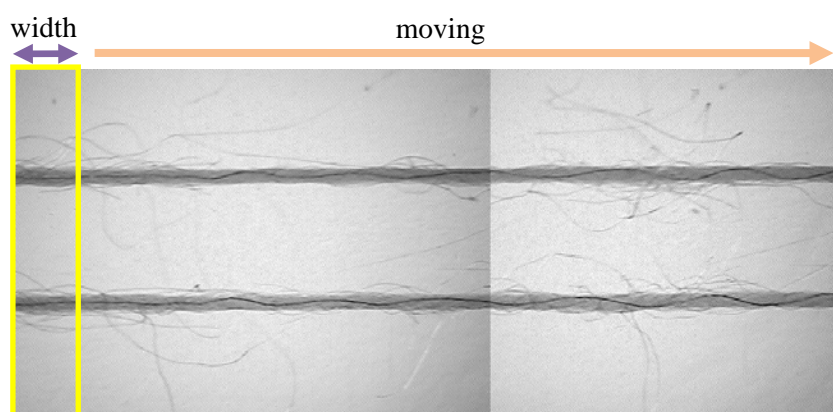
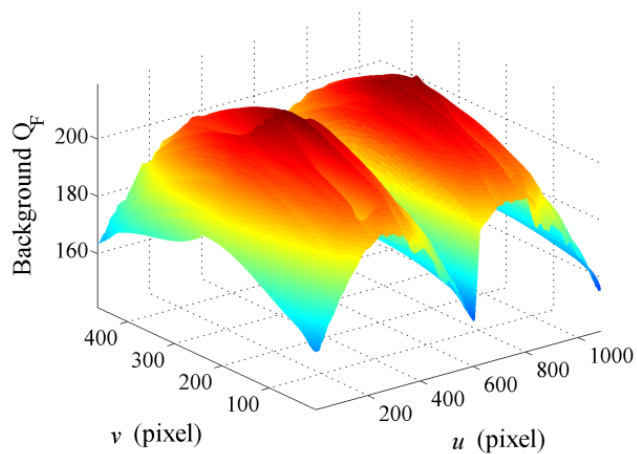
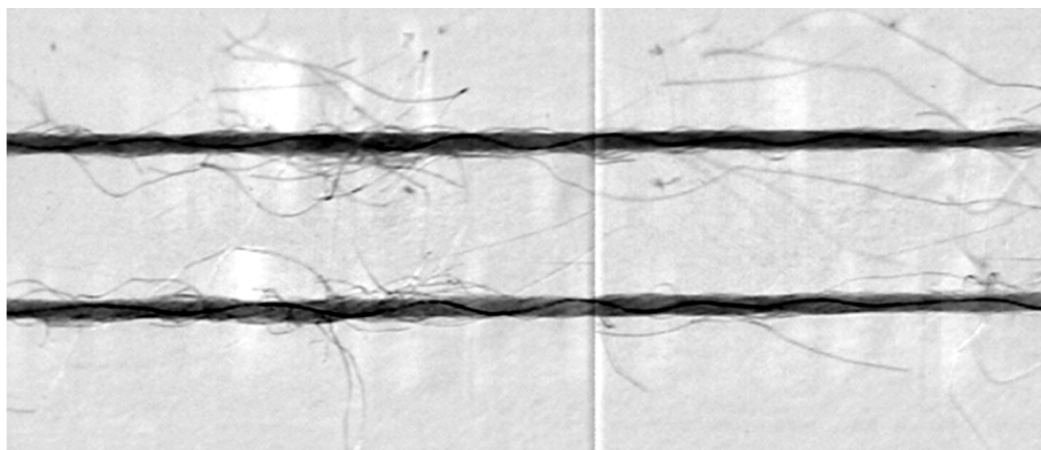


Figure 4.23 Average the image using a moving window.

Same as the baseline fitting method discussed in Section 4.3.1, the piecewise cubic Hermite method can also be used to identify the baseline of each column of average image \mathbf{Q} . The fitting results \mathbf{Q}_F of whole image \mathbf{Q} can be considered as the background of the image, as shown in Figure 4.24(a). Figure 4.24(b) shows the residual image \mathbf{Q}_R obtained by subtracting the background \mathbf{Q}_F from image \mathbf{Q} .



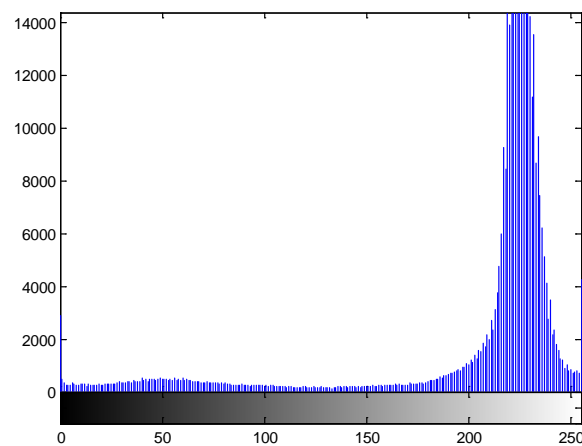
(a) background \mathbf{Q}_F of \mathbf{Q}



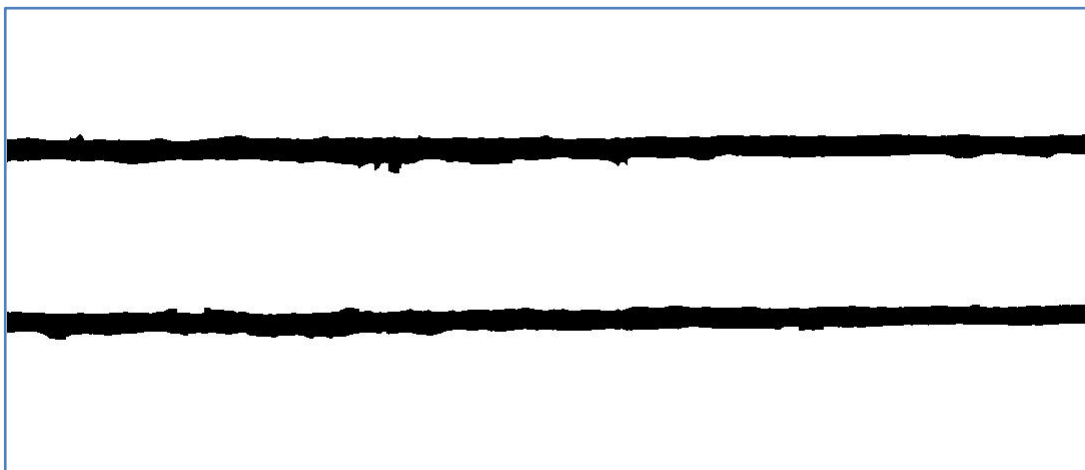
(b) residual image \mathbf{Q}_R

Figure 4.24 Image preprocessing results.

The histogram of the residual image Q_R is shown in Figure 4.25(a). It is clearly suitable now to use Otsu's method for thresholding yarn segmentation. After deleting the isolated small regions, the binary image of Q_R can be obtained, as shown in Figure 4.25(b). And the yarn boundaries and tracer fibers are finally identified as $l_1(u) \sim l_6(u)$, as shown in Figure 4.26.



(a) histogram of Q_R



(b) binary image of Q_R

Figure 4.25 Threshold segmentation.

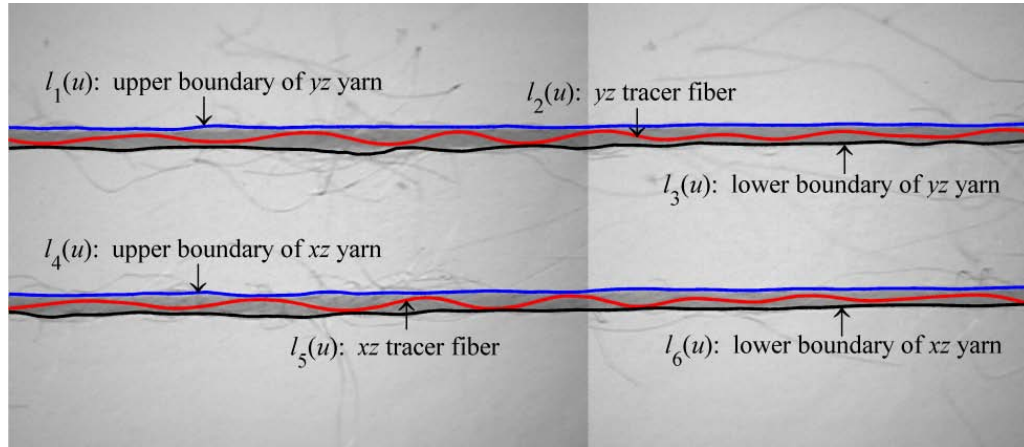


Figure 4.26 Panorama with identified yarn boundaries and tracer fibers.

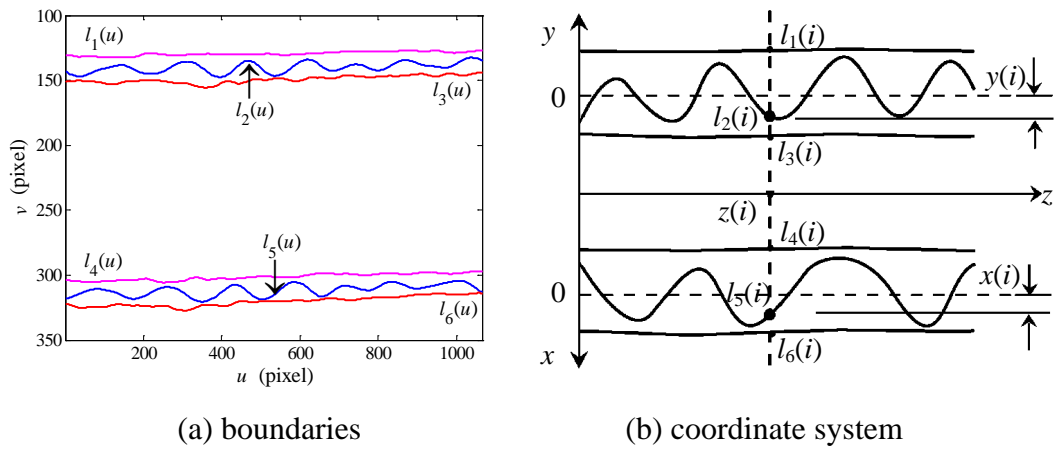


Figure 4.27 Segmentation signals and the coordinate system.

Thus yarn diameters at the i^{th} point in the x - and y - axes can be calculated by:

$$d_x(i) = l_6(i) - l_4(i), \quad d_y(i) = l_3(i) - l_1(i) \quad (4.23)$$

Figure 4.27(a) shows the identified signals and their coordinate systems in the image.

It should be transferred to the coordinate system of yarn, as shown in Figure 4.27(b).

Then the coordinates of the i^{th} tracer fiber in the x - and y - axes can be obtained by:

$$x(i) = l_5(i) - \frac{l_4(i) + l_6(i)}{2}, \quad y(i) = \frac{l_1(i) + l_3(i)}{2} - l_2(i) \quad (4.24)$$

Based on Equations (4.23) and (4.24) and the results of yarn boundaries and tracer fibers, three-dimensional (3D) configurations of the yarn and tracer fiber can be reconstructed, as shown in Figure 4.28. It visually shows a helical structure of a part of tracer fiber (i.e. from a panorama of a pair of yarn images) and its migration path in the yarn.

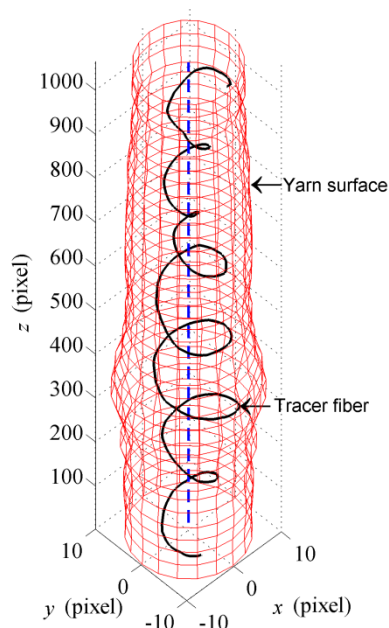


Figure 4.28 3D configurations of a pair of yarn images.

4.5. Quality evaluation of the image mosaic and segmentation

4.5.1. Application on a whole series of images

Besides the first two images, the panoramic image of the whole series of 20Ne yarn images in Figure 4.3 can be obtained by stitching the neighboring images using the proposed mosaic method, as shown in Figure 4.29. It is noted that the tracer fiber and yarn body look quite continuous and smooth at each stitching position.

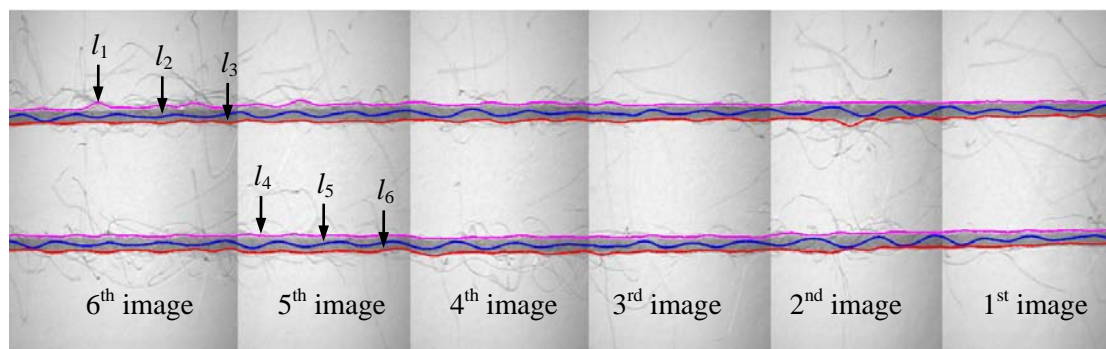


Figure 4.29. Results of image mosaic and segmentation for whole series.

Furthermore, [Figure 4.30](#) shows a panorama of these 20Ne consecutive yarn images created by an existing panorama software (ArcSoft Panorama Maker). Compared with the results by the proposed computer method (as shown in [Figure 4.29](#)), besides of image distortion in [Figure 4.4 \(a\)](#), the panorama created by the existing panorama software shows an obviously incredible short length, which is caused by the high repetition and similarity of the tracer fiber images. Therefore, because of the peculiarity of tracer fiber image (i.e. pattern repetition and similarity, change of distance between two views), the general mosaic method may fail in most cases.

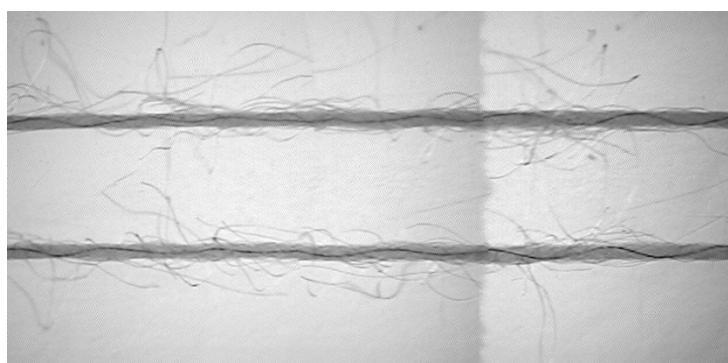


Figure 4.30. Panorama for whole series created by Panorama Maker.

With the proposed segmentation, the yarn boundaries and tracer fibers (l_1 to l_6) can be then identified from the panorama, as shown in Figure 4.29. It is visually noted that the detected yarn boundaries and tracer fibers coincide well with the real ones, especially the tracer fiber. Based on the above, 3D configuration of the 20Ne yarn sample containing a whole tracer fiber can be reconstructed, as shown in Figure 4.31. It is noted that the yarn diameter is slightly uneven and the tracer fiber also migrates from the center to the surface over the length.

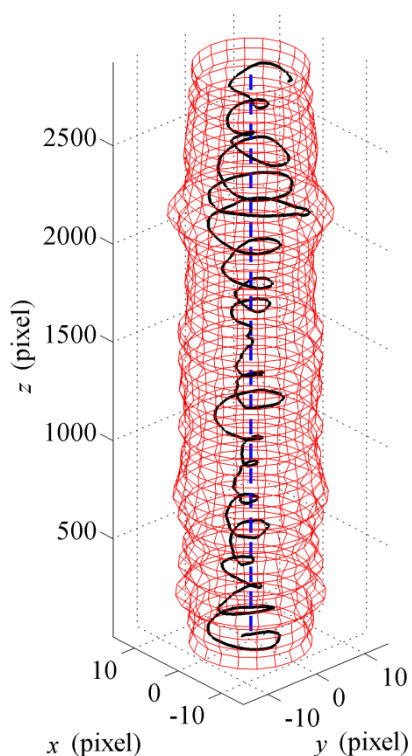


Figure 4.31. 3D configuration of the 20Ne yarn sample containing a whole complete tracer fiber.

From the above results, it is noted that the proposed method looks workable in the automatic image mosaic and segmentation for the 20Ne yarn sample. In the

following section, a method will be further proposed to objectively evaluate the qualities of image mosaic and segmentation by comparing the results of the proposed computer method with the manual method.

4.5.2. Evaluation of the image mosaic

In the processing of the image mosaic, yarn images are consecutively stitched by neighboring pairs. Hence the evaluation of the image mosaic should be based on the result of each pair. The stitching position of the tracer fiber for each neighboring pair of yarn images is employed to evaluate the quality of the image mosaic. As shown in Figure 4.32, the distances z_i , y_i and x_i are used to describe the stitching position of the tracer fiber for the i^{th} and $(i+1)^{\text{th}}$ images in the panorama.

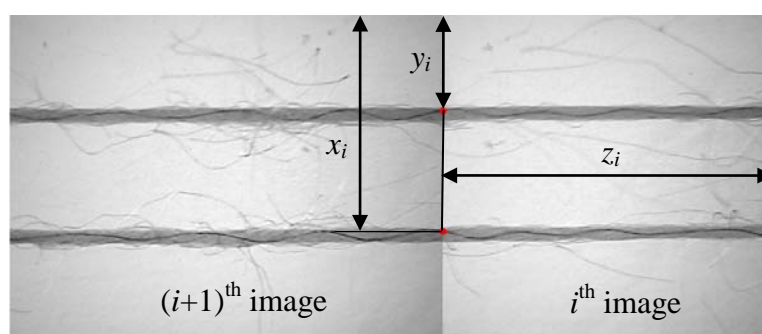


Figure 4.32. Parameters (z_i , y_i and x_i) for the stitching point of the tracer fiber.

In the manual method, the determination of the stitching position, yarn boundary and tracer fiber is mainly based on visual inspection, and the software Photoshop is utilized to stitch images and mark the positions according to the visual detections.

Suppose $(z_i^c, y_i^c$ and $x_i^c)$ and $(z_i^m, y_i^m$ and $x_i^m)$ are the stitching positions of the tracer fiber obtained by the proposed computer method and manual method, respectively.

In order to obtain a dimensionless measure to evaluate the error of image mosaic in the horizontal direction, a relative error Ez_i , which is defined as the absolute difference of z_i between these two methods relative to the image width N , can be defined as:

$$Ez_i = \left| \frac{z_i^c - z_i^m}{N} \right| \quad (4.25)$$

Compared with the horizontal direction, the image mosaic is more sensitive to error in the vertical direction. Therefore, a small value of yarn diameter instead of a large value of image height will be used to formulate the relative errors in the vertical direction:

$$Ey_i = \left| \frac{y_i^c - y_i^m}{D} \right|, \quad Ex_i = \left| \frac{x_i^c - x_i^m}{D} \right| \quad (4.26)$$

where D is the predicted diameter of yarn obtained using the manual method.

For the application case described in [Section 4.5.1](#), the evaluation results of image mosaic are listed in [Table 4.1](#). In this study, the image width N is 614 pixels, and the yarn diameter D obtained using the manual method is 21 pixels. It is noted that the result of the image mosaic using the proposed computer method is in good

agreement with that of the manual method. The differences between the two methods in the horizontal (z_i) and vertical directions (y_i, x_i) range from 1 to 13 and from 0 to 2 pixels, respectively. In particular, all differences of y_i are either 0 or 1 pixel and most of the x_i differences are less than 2 pixels. In addition, the relative errors in the horizontal direction (Ez_i) are generally smaller than those in the vertical direction (Ey_i and Ex_i), and Ex_i is generally larger than Ey_i . Relative errors (Ez_i, Ey_i and Ex_i) of most image pairs are less than 5%, except the third image pair that presents a large magnitude of 9.52% in Ex_i . The means of relative errors are smallest in z_i (1.11%), followed by y_i (2.86%) and x_i (4.76%). It indicates that the error in the vertical direction (Ey_i and Ex_i) is more sensitive than that in the horizontal direction (Ez_i). The relative error Ex_i is generally larger than Ey_i , and it is probably because the error Ex_i contains a cumulative error of Ey_i . As the mean of Ez_i for the 20Ne yarn is 1.11% and the length of the tracer fiber in this study is around 38mm, 0.42mm ($38\text{mm} \times 1.11\%$) yarn may be lost or added in the processing of the automatic image mosaic.

Moreover, a combined overall error E can be defined as

$$E = \frac{1}{n-1} \sum_i^{n-1} (Ez_i + Ey_i + Ex_i) \quad (4.27)$$

where n is the number of yarn images in one series of yarn sample.

Based on Table 4.1, the overall error E of mosaic quality can be calculated as 8.73%.

This shows that the error of the image mosaic is in a relatively low level.

Table 4.1. Mosaic results of the 20Ne yarn sample ($N=614$ pixels, $D=21$ pixels)

i^{th} image pair	z_i^c	y_i^c	x_i^c	z_i^m	y_i^m	x_i^m	Ez_i (%)	Ey_i (%)	Ex_i (%)
1	469	136	307	470	137	307	0.16	4.76	0
2	452	136	310	462	137	311	1.63	4.76	4.76
3	479	143	313	484	142	315	0.81	4.76	9.52
4	470	137	313	475	137	312	0.81	0	4.76
5	455	136	309	442	136	310	2.12	0	4.76
Mean							1.11	2.86	4.76
Standard deviation							0.77	2.61	3.37

unit of $z_i^c, y_i^c, x_i^c, z_i^m, y_i^m$ and x_i^m : pixel.

4.5.3. Evaluation of the image segmentation

In image segmentation, the identified yarn boundaries and tracer fibers (l_1 to l_6) can be considered as six signals. For the evaluation of segmentation quality, these six signals are also detected using the manual method for a comparison with the results of the proposed computer method. Figure 4.33 shows the comparison of segmentation results for the yarn panorama in Figure 4.29, where l_i^m (dotted line) and l_i (solid line) are the i^{th} signal obtained using the manual method and proposed computer method, respectively. It is noted that the segmentation results for the

tracer fiber (l_2 and l_2^m , l_5 and l_5^m) always coincide with each other. In image acquisition, as the yarn body is set as semi-transparent for capturing the tracer fiber, it is blurry and is not as clear as tracer fiber in yarn image. Therefore, the identified yarn boundaries using these two methods present a certain level of deviation. And the differences $l_i - l_i^m$ between the computer method and manual method are shown in

Figure 4.34 for a further comparison.

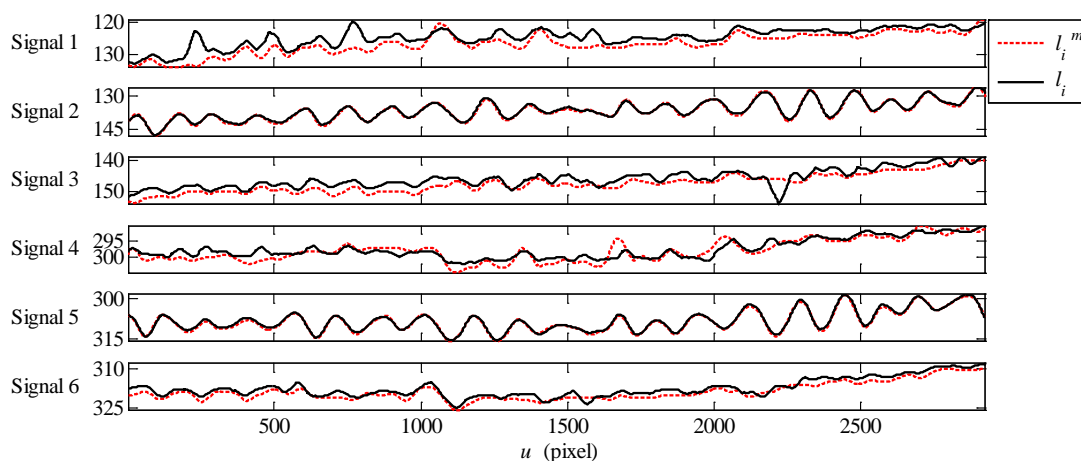


Figure 4.33 Comparison of segmentation results using the proposed computer method and manual method for the 20Ne yarn sample (unit: pixel).

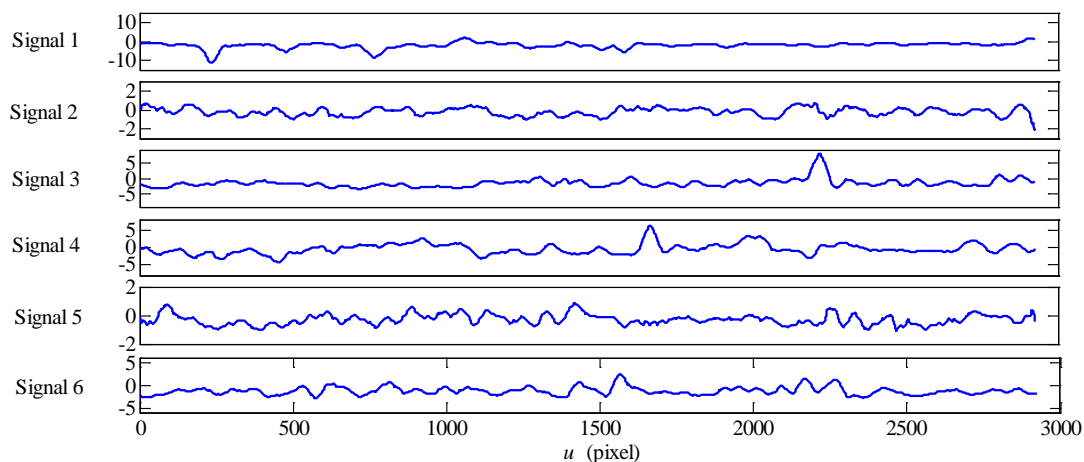


Figure 4.34 Differences $l_i - l_i^m$ (pixel) between the computer and manual method.

In order to quantitatively evaluate the quality of image segmentation, the statistical results of yarn diameter and relative difference between the proposed method and manual method will be extracted for further analysis. Based on Equation (4.23), the yarn diameters d_y and d_x , d_y^m and d_x^m in the y - and x - axes using the two methods can be obtained by:

$$d_y = l_3 - l_1, \quad d_x = l_6 - l_4 \quad (4.28)$$

$$d_y^m = l_3^m - l_1^m, \quad d_x^m = l_6^m - l_4^m \quad (4.29)$$

Relative measures Δd_y and Δd_x of yarn diameter in the y - and x - axes are defined as

$$\Delta d_y = \frac{|d_y - d_y^m|}{D} = \frac{|l_3 - l_1 - l_3^m + l_1^m|}{D}, \quad \Delta d_x = \frac{|d_x - d_x^m|}{D} = \frac{|l_6 - l_4 - l_6^m + l_4^m|}{D} \quad (4.30)$$

In addition, the relative difference Δl_i is defined as a dimensionless measure:

$$\Delta l_i = \frac{|l_i - l_i^m|}{D} \quad (4.31)$$

The statistical results of yarn diameter and relative differences are calculated and listed in Table 4.2. It is noted that both the mean and standard deviation of yarn diameter using the proposed method are slightly lower than those using the manual method in the x -direction, while in the y -direction this phenomenon is the opposite. This is probably because the threshold for the yarn boundary decided by the manual

method is slightly different from that by the proposed computer method and the threshold may not be consistent with the determination of hundreds of boundary positions in the manual method. The dimensionless measures Δd_y and Δd_x for the yarn sample are similar (mean of about 7%). It is also noted that the means of relative differences Δl_2 and Δl_5 (tracer fiber) is less than 2%, which is smaller than that of yarn boundaries (higher than 5%), and their standard deviations are also quite small. In addition, the mean of difference Δl_1 shows the largest magnitude (10.05%). These indicate that tracer fiber presents a higher detection accuracy than yarn boundaries.

Table 4.2. Evaluation of the yarn diameter and relative differences ($D=21$ pixels)

Item	Diameter		Item	Differences	
	Mean	SD		Mean	SD
d_y^m (pixel)	20.70	1.89	Δl_1 (%)	10.05	7.22
d_x^m (pixel)	20.85	1.87	Δl_2 (%)	1.79	1.31
d_y (pixel)	21.23	2.27	Δl_3 (%)	8.38	4.65
d_x (pixel)	19.97	1.68	Δl_4 (%)	5.91	4.45
Δd_y (%)	6.51	7.93	Δl_5 (%)	1.83	1.19
Δd_x (%)	7.38	5.98	Δl_6 (%)	6.69	3.23

SD: standard deviation.

Based on information of image segmentation, some structural parameters can be

used to statistically describe the migration behavior of fibers in the yarn, including mean fiber position, root-mean-square (RMS) deviation, mean migration intension and equivalent migration frequency [46, 113, 138], which can be calculated using Equations (4.32)-(4.36).

The radial position of tracer fiber at the i^{th} position along yarn can be expressed as:

$$Y(i) = 4\left[x(i)/d_x(i)\right]^2 + 4\left[y(i)/d_y(i)\right]^2 \quad (4.32)$$

Figure 4.35 shows the radial position of the tracer fiber in the 20Ne yarn sample obtained by using the proposed computer method and manual method (horizontal scale of the image is 93 pixels/mm). It is noted that the radial position obtained by the two methods looks generally similar and the difference is mainly caused by the slight difference of the obtained yarn diameter.

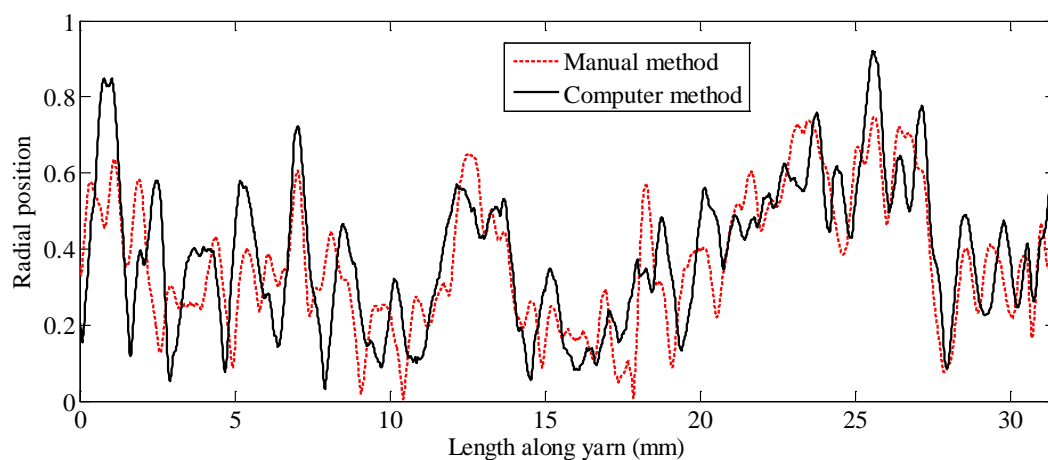


Figure 4.35 Radial position of the tracer fiber in the 20Ne yarn sample.

With the above $Y(i)$, the tendency of fiber to be near the yarn surface or yarn center can be represented by mean fiber position \bar{Y} :

$$\bar{Y} = \frac{1}{k_n} \sum_{i=1}^{k_n} Y(i) \quad (4.33)$$

where there are k_n observations of Y over the length of the yarn.

The magnitude of deviations from the mean fiber position can be represented by RMS deviation D_{RMS} :

$$D_{RMS} = \left[\frac{1}{k_n} \sum_{i=1}^{k_n} (Y(i) - \bar{Y})^2 \right]^{1/2} \quad (4.34)$$

The rate of radial change of fiber can be represented by mean migration intensity I_m :

$$I_m = \frac{1}{\Delta Z} \left[\frac{1}{k_n} \sum_{i=1}^{k_n-1} (Y(i+1) - Y(i))^2 \right]^{1/2} \quad (4.35)$$

where ΔZ is the difference of distance between two neighboring observations along the yarn axis.

Based on [Equations \(4.34\)](#) and [\(4.35\)](#), equivalent migration frequency f_m can be represented by:

$$f_m = \frac{I_m}{4\sqrt{3}D_{RMS}} \quad (4.36)$$

The results of fiber migration parameter for the 20Ne yarn sample using the proposed method and manual method are listed in [Table 4.3](#). The results using the proposed computer method are generally in good agreement with those using the manual method. In [Table 4.3](#), the migration parameters using the proposed computer method are greater than those using the manual method. This may be mainly caused by the slightly larger yarn diameter obtained by manual method. As calculated from [Table 4.2](#), the mean of yarn diameter (x - and y - directions) is 20.77 pixels for the manual method, which is larger than 20.6 pixels using the computer method.

Table 4.3. Comparison of migration parameters using computer and manual methods

Migration parameters	Computer method	Manual method
Mean fiber position	0.1899	0.1673
RMS deviation	0.1677	0.1448
Mean migration intensity (cm^{-1})	6.2663	5.2335
Equivalent migration frequency (cm^{-1})	5.3949	5.2179

4.5.4. Evaluation of efficiency

The comparison of time taken for the proposed computer method and manual method is also made, as shown in [Table 4.4](#). In the manual method, it takes about 6 minutes to stitch six images into a panorama and about 24 minutes to extract the

boundaries. The proposed computer method is implemented by MathWorks MATLAB on a notebook computer with a CPU of 1.9GHz and 6GB memory. It takes about 50 seconds for the image mosaic and about 20 seconds for the image segmentation. For the whole process, it takes about 30 minutes and about 70 seconds for the manual method and the proposed computer method respectively. The time taken for the manual method is about 25 times of that for the proposed method.

Table 4.4. Comparison of time taken by the proposed computer and manual methods

	Computer method	Manual method
Image mosaic (5 pairs of images)	49 seconds	6 minutes
Image segmentation (a panorama)	22 seconds	24 minutes

4.6. Experiments

4.6.1. Database construction of tracer fiber images

In this section, more yarn samples will be prepared and used for a full evaluation of the proposed computer method. A series of Tencel yarns (with black tracer fibers), ranging from coarse count (10Ne) to fine count (60Ne), were produced by using ring spinning machine (Zinser 351) with different yarn twists for the database construction, as listed in [Table 4.5](#). The specifications of tracer fiber are same as

those mentioned in Section 4.2. The measurement system [44], with a CCD camera (Samsung SCC-131BP) attaching a pair of zoom lens (0.5×, 0.7-4.5), was employed to acquire the tracer fiber images (see Section 4.2). As shown in Table 4.5, for each yarn count, ten complete tracer fibers were acquired for producing a total of fifty series of tracer fiber images (i.e. 50 complete tracer fibers).

Table 4.5. Database of yarn samples

Yarn count (Ne)	Yarn twist		Number of samples	Scale (pixels/mm)	
	Twist Multiplier	T_m (tpm)		Horizontal K_z	Vertical K_x
10	3.2	398	10	100.0	121.7
20	3.3	581	10	105.6	127.0
30	3.6	776	10	157.7	189.5
40	3.8	946	10	177.0	221.0
60	3.6	1098	10	205.5	242.0

Figure 4.36 (a)~(e) show some examples of images for different yarn counts. In order for a clear observation of the yarn body and tracer fiber, the magnification of the microscope was enlarged with the increase of yarn count. Therefore the diameter of fine yarn looks similar to that of coarse yarn in the image and the hairs of fine yarn become much thicker and clearer than those of coarse yarn. The horizontal scale K_z (pixels/mm) and vertical scale K_x (pixels/mm) of the tracer fiber

image are shown in Table 4.5. The two scales are different for different counts and they are significantly linearly related, as shown in Figure 4.36(f).

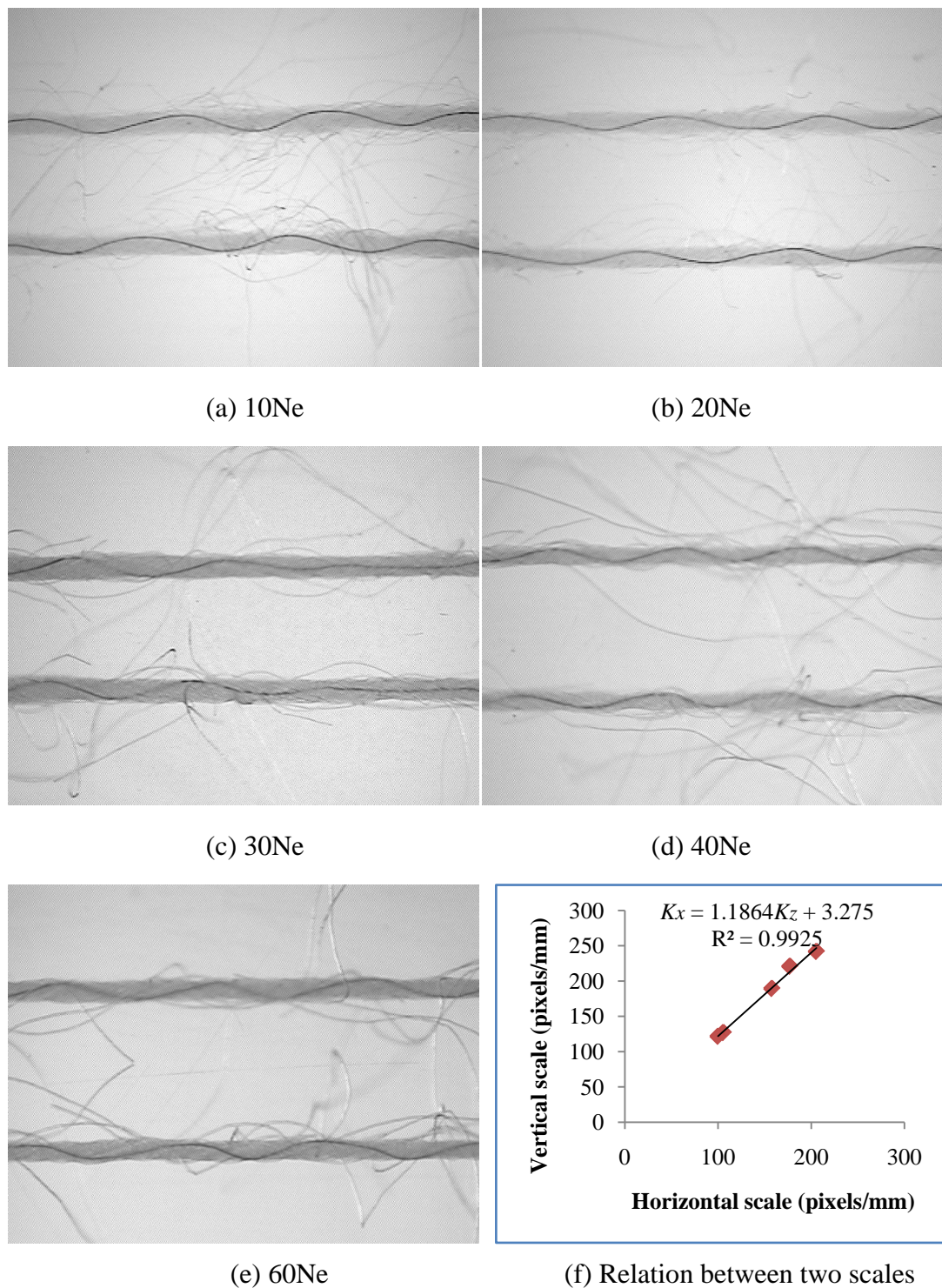


Figure 4.36 Examples of yarn images of different counts with different magnifications.

In the image acquisition, the yarn is moving slowly for a continuous measurement and the consecutive tracer fiber images are acquired in a certain time interval which depends on the magnification and delivery speed of yarn. In this experiment, an overlap of about 30% is obtained between two neighboring images in order for a higher accurate image mosaic. Each complete tracer fiber is composed of a number of individual tracer fiber images. Table 4.6 shows the number of images involved for a complete tracer fiber.

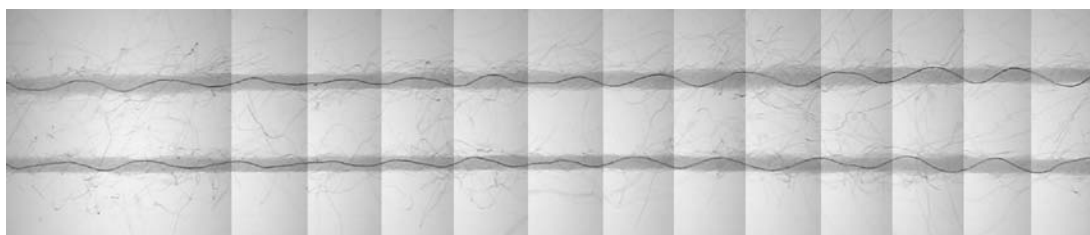
Table 4.6. Number of images for each complete tracer fiber in the database

Yarn count Sample No	10Ne	20Ne	30Ne	40Ne	60Ne
1	15	11	19	17	19
2	15	15	15	21	27
3	11	15	13	17	26
4	15	15	19	19	19
5	9	15	21	23	15
6	13	17	23	17	25
7	13	15	19	23	23
8	15	17	21	19	23
9	9	15	21	21	25
10	11	14	13	17	17
Mean	13	15	18	19	22
(CV%)	(19.51)	(11.16)	(19.21)	(12.67)	(18.82)
Sub-total	126	149	184	194	219
Total	872				

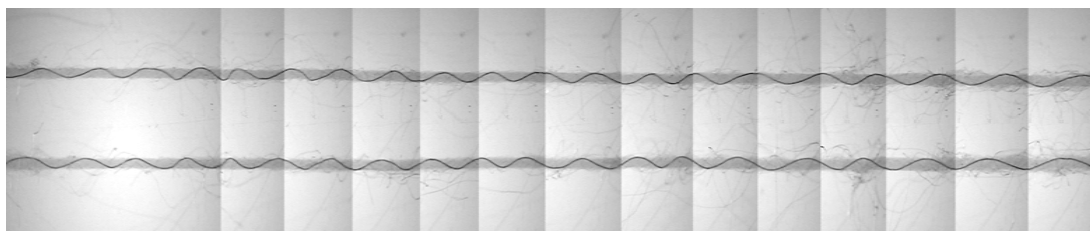
Taking Sample No.1 of 10Ne yarn in [Table 4.6](#) as example, there are 15 individual tracer fiber images involved for a whole complete image. It can be noted that the number of image for a complete tracer fiber is different for different yarn counts, and even for the same yarn count, the number varies. This is mainly attributed to the different microscope magnification, percentage of overlapping between neighboring images and fiber migration behavior. The average number of images for a single complete tracer fiber is 13, 15, 18, 19 and 22 for different counts, respectively, producing a total of 872 tracer fiber images for analysis. The more detailed information is listed in [Appendix B](#).

4.6.2. Results of the image mosaic

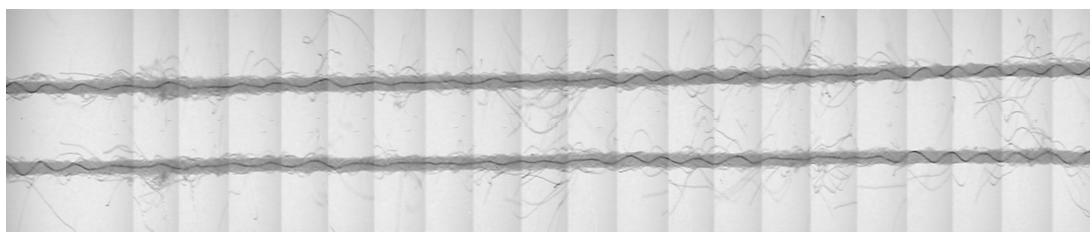
According to the algorithms introduced in [Section 4.3](#), a series of consecutive tracer fiber images with about 30% overlap can be automatically stitched one by one into a panorama containing a whole complete tracer fiber. Some examples of the panoramas are shown in [Figure 4.37](#) for different yarn counts. The obtained panoramas for all 50 complete tracer fibers of the database are shown in [Appendix A](#). From [Figure 4.37](#), it can be noted that the image mosaics are visually correct.



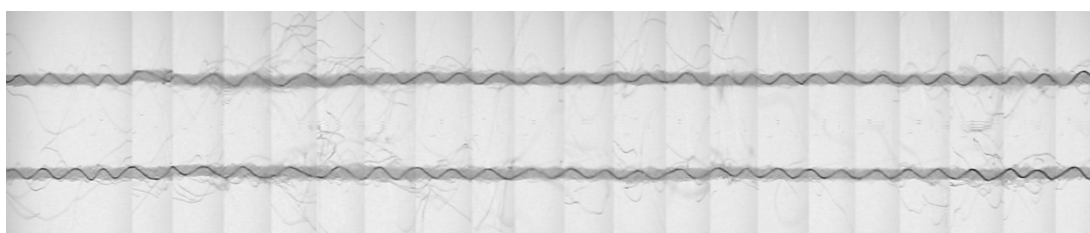
(a) 10Ne yarn-sample 6



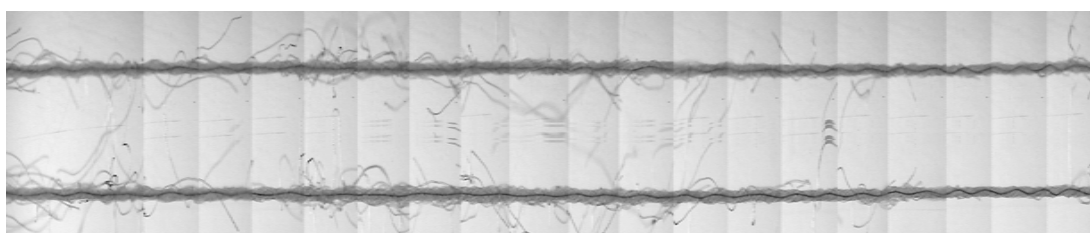
(b) 20Ne yarn-sample 10



(c) 30Ne yarn-sample 9



(d) 40Ne yarn-sample 2



(e) 60Ne yarn-sample 4

Figure 4.37 Examples of the panoramas for different yarn counts.

In order for a full objective evaluation, the method introduced in [Section 4.5.2](#) will be employed to evaluate the mosaic quality of these panoramas and the detailed evaluation results are listed in [Appendix B](#).

According to Equation (4.27), the overall errors of image mosaic for each yarn count can be written as

$$E = \frac{1}{m} \sum_{i=1}^m (Ez_i + Ey_i + Ex_i) = \overline{Ez} + \overline{Ey} + \overline{Ex} \quad (4.37)$$

where m is the number of mosaic pairs in each yarn count, Ez_i , Ey_i and Ex_i are relative errors of image mosaic in z , y and x axes, as shown in Equations (4.25) and

$$(4.26), \quad \overline{Ez} = \frac{1}{m} \sum_{i=1}^m Ez_i, \quad \overline{Ey} = \frac{1}{m} \sum_{i=1}^m Ey_i, \quad \text{and} \quad \overline{Ex} = \frac{1}{m} \sum_{i=1}^m Ex_i.$$

The statistical results of each relative errors and overall error for the image mosaic are calculated, as listed in Table 4.7. For these 50 series of tracer fiber images, 822 pairs of image mosaic, including 116 for 10Ne yarn, 139 for 20Ne yarn, 174 for 30Ne yarn, 184 for 40Ne yarn and 209 for 60Ne yarn, were carried out. It can be seen that the magnitudes of relative errors for all yarn counts are small with \overline{Ez} of 0.73% ~ 0.98%, \overline{Ey} of 2.71% ~ 3.87% and \overline{Ex} of 2.81% ~ 4.64%. The overall error E ranges from 6.24% to 9.49%, which is less than 10%. Both the overall and relative errors indicate that the error of the image mosaic for all 50 samples is at a relatively low level. Moreover, it can be noted that both the relative and overall errors are generally increased with the increase of yarn count, indicating mosaic error becomes larger for finer yarns. The relative errors (\overline{Ey} and \overline{Ex}) in the vertical direction are 2.71~4.64%, which is higher than that in horizontal direction (\overline{Ez} , <1%). And the relative error in x-direction (\overline{Ex}) is slightly larger than that in

y-direction (\overline{E}_y).

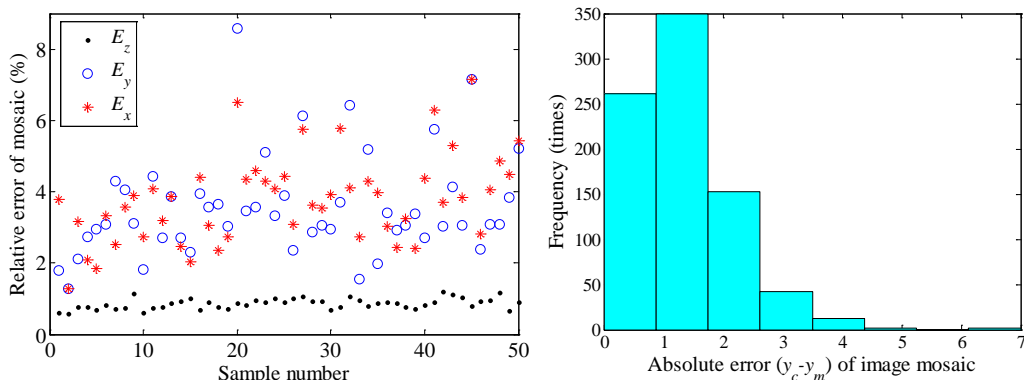
Table 4.7. Relative errors of image mosaic for each yarn count

Yarn count (Ne)	m	\overline{E}_z (%)	\overline{E}_y (%)	\overline{E}_x (%)	E (%)
10	116	0.73	2.71	2.81	6.24
20	139	0.83	3.83	3.43	8.09
30	174	0.93	3.63	4.13	8.67
40	184	0.86	3.45	3.60	7.91
60	209	0.98	3.87	4.64	9.49

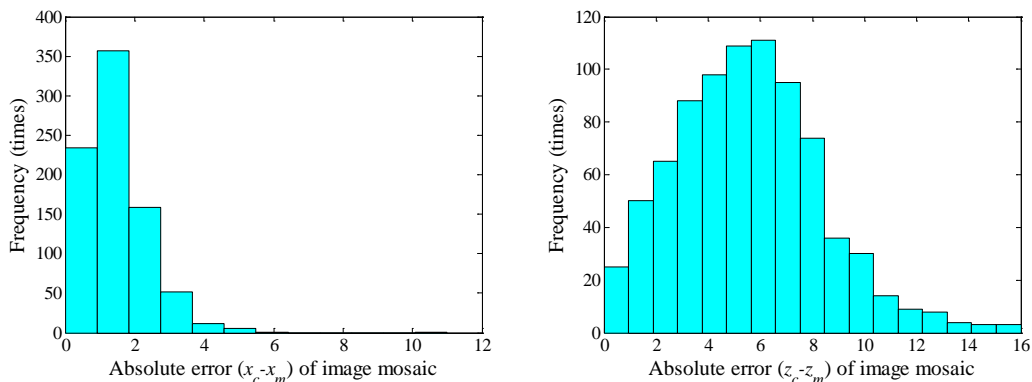
m is the number of mosaic pairs for each yarn count.

The relative errors E_z , E_y and E_x of image mosaic for each sample are also plotted in [Figure 4.38 \(a\)](#) for a further analysis. The horizontal axis is sample number (1~50) for different yarn counts as listed in [Appendix B](#). It is noted that the relative error E_z is quite stable at a relatively low magnitude (around 1%) while the relative errors E_y and E_x vary at a relatively high level (2 ~ 8%). There is generally an increasing trend for E_y and E_x with the increase of yarn count (finer yarns). Actually, most of the vertical differences are just a few pixels (1~4 pixels for y_c-y_m and 1~5 pixels for x_c-x_m), as shown in [Figure 4.38 \(b\)](#) and [\(c\)](#), respectively. However, because the yarn diameter is very small (20~40 pixels), the relative vertical errors of E_y and E_x are enlarged. As shown in [Figure 4.6](#), image mosaic is implemented in horizontal direction, followed by the vertical direction. Therefore, the vertical errors are

influenced by the precision of horizontal mosaic, or in other word, they are not independent parameters unless the horizontal error is zero. In order to further analyze the relative horizontal error E_z , a histogram of the absolute error z_c-z_m (in horizontal direction) is generated for all 822 stitching pairs in the database, as shown in Figure 4.38 (d). It is noted that it appears a skewed-right distribution, and in most cases, the absolute error z_c-z_m is less than 10 pixels. Actually, it is really hard for human to distinguish the difference of even 15 pixels in the horizontal direction of image mosaic.



(a) mean of relative errors for each sample (b) histogram of absolute error $y_c - y_m$

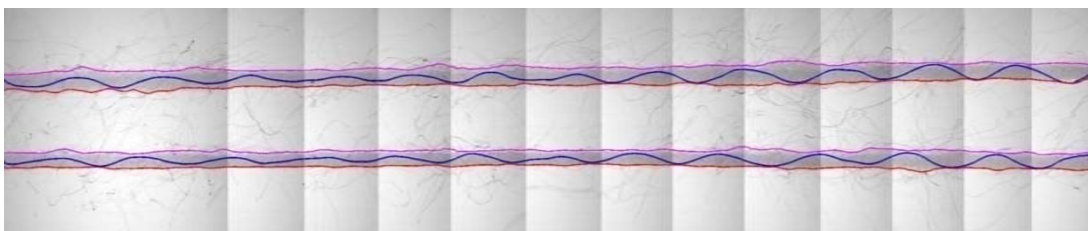


(c) histogram of absolute error $x_c - x_m$ (d) histogram of absolute error $z_c - z_m$

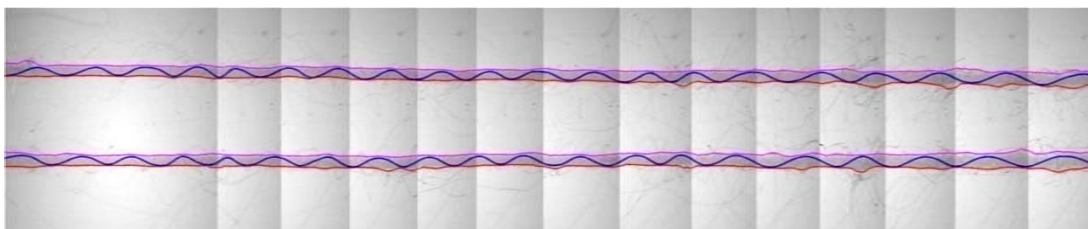
Figure 4.38 Errors of image mosaic in quality evaluation.

4.6.3. Results of the image segmentation

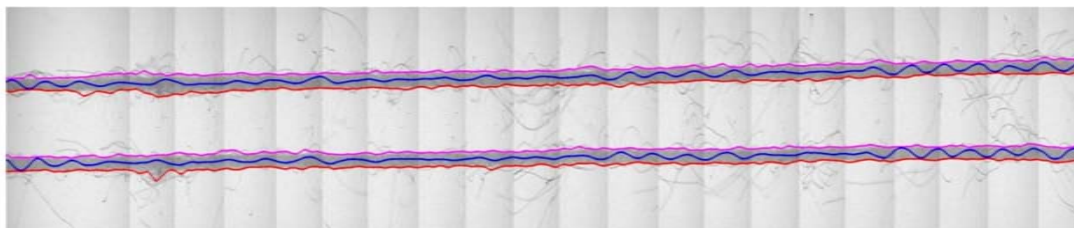
According to the algorithm introduced in [Section 4.4](#), the 50 panoramas created in [Section 4.6.2](#) can be automatically segmented. [Figure 4.39](#) shows the segmentation results of the panorama examples shown in [Figure 4.37](#), where the yarn boundaries and tracer fibers are labeled. The results of image segmentation for all 50 yarn samples are shown in [Appendix A](#).



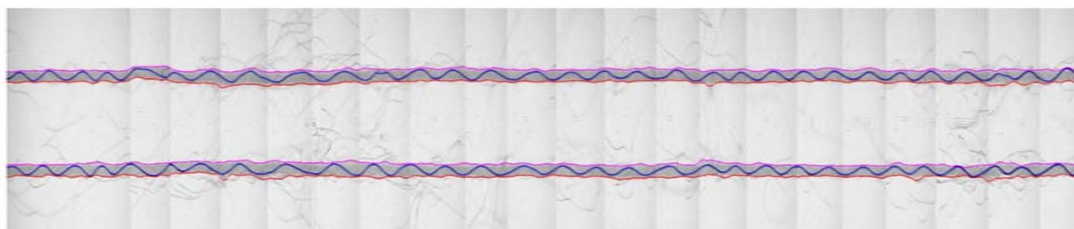
(a) 10Ne yarn-sample 6



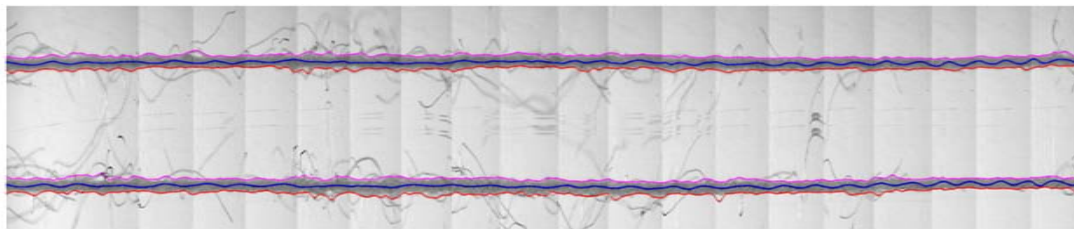
(b) 20Ne yarn-sample 10



(c) 30Ne yarn-sample 9



(d) 40Ne yarn-sample 2



(e) 60Ne yarn-sample 4

Figure 4.39 Identified yarn boundaries and tracer fiber on the panoramas.

The method introduced in [Section 4.5.3](#) is adopted for evaluation of the digital segmentations, and the full evaluation results of the image segmentation are listed in [Appendix C](#). The statistical results for each yarn count are calculated and shown in [Table 4.8](#). In [Table 4.8](#), D_e is an estimate of yarn diameter, which can be estimated by the following equation of cotton yarn [142]:

$$D_e = 0.03568 \sqrt{\frac{N_{\text{tex}}}{\gamma}} = 0.037 \sqrt{N_{\text{tex}}} \quad (\text{mm}) \quad (4.38)$$

where γ is yarn density and yarn count $N_{\text{tex}} = \frac{590.5}{N_e}$.

\bar{D} and \bar{d} are the mean values of yarn diameter calculated from the segmentation results of the tracer fiber images using the manual method and the proposed computer method, respectively. It can be noted that the three values of yarn diameter, namely D_e , \bar{D} and \bar{d} , are very close for all five yarn counts, demonstrating the proposed digital method produces a good segmentation and measure for yarn diameter. $\bar{\Delta d}$ and $\bar{\Delta l}$ are the mean relative errors of yarn

diameter and identified signals for each yarn count. The mean of relative error $\overline{\Delta l}$ ranges from 3.20% to 4.22% and it appears no linear relationship with yarn count. And the relative error of yarn diameter $\overline{\Delta d}$ (6.56~9.04%) is almost twice of $\overline{\Delta l}$ in magnitude. It is mainly because the error of yarn diameter is caused by the error of detected yarn boundaries. Table 4.8 shows the digital segmentation of tracer fiber image is generally acceptable with a low level of deviation from the manual method.

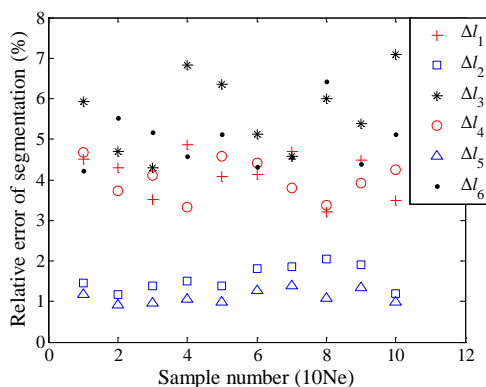
Table 4.8. Evaluation results of image segmentation for each count in the database

Yarn count (Ne)	D_e (mm)	\overline{D} (mm)	\overline{d} (mm)	$\overline{\Delta d}$ (%)	$\overline{\Delta l}$ (%)
10	0.2843	0.2769	0.2728	6.56	3.57
20	0.2010	0.2094	0.2008	7.79	4.22
30	0.1642	0.1599	0.1515	6.64	3.20
40	0.1422	0.1335	0.1226	9.04	4.15
60	0.1161	0.1136	0.1095	7.82	3.73

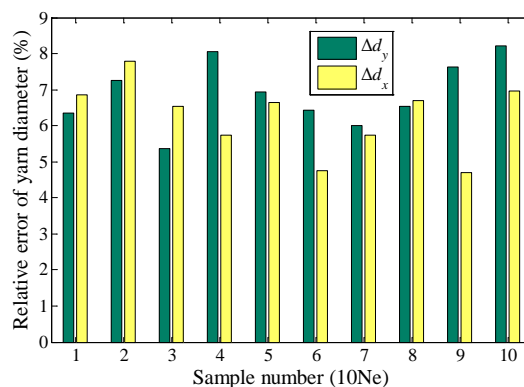
where, $\overline{D} = \frac{1}{n_c} \sum D$, $\overline{d} = \frac{1}{n_c} \sum d$, $\overline{\Delta d} = \frac{1}{n_c} \sum \frac{\Delta d_y + \Delta d_x}{2}$, $\overline{\Delta l} = \frac{1}{n_c} \sum \left(\frac{1}{6} \sum_i^6 \Delta l_i \right)$, Δd_y and Δd_x , Δl_i are formulated in Equations (4.30) and (4.31), n_c is the number of sample of complete tracer fiber in each yarn count ($n_c=10$).

In order to further analyze the quality of image segmentation, the relative errors of identified curves (Δl_i , $i=1\sim 6$) and yarn diameter (Δd_y and Δd_x) for each yarn count are plotted in Figure 4.40 for comparison. The relative error for the detection of tracer fiber (Δl_2 and Δl_5) mainly varies from 1% to 3%, which is smaller than those

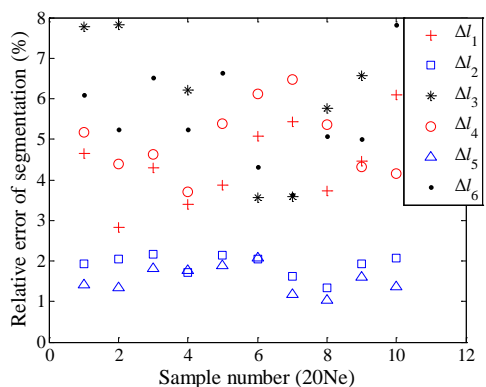
for yarn boundary (2%~8%). That indicates the detection error of yarn boundary contributes more to the mean error $\overline{\Delta l}$. In addition, the identification of upper boundary (Δl_1 and Δl_4) is generally better than that of the lower boundary (Δl_3 and Δl_6) for 10Ne and 20Ne yarns, while it is opposite for 30Ne and 40Ne yarns. For 60Ne yarn, there is no obvious difference. From Figure 4.40 (a2), (b2), (c2), (d2) and (e2), the relative error of yarn diameter (Δd_y and Δd_x) is between 4% and 14%. In most cases of finer yarn samples (30Ne~60Ne), Δd_x is larger than Δd_y in value.



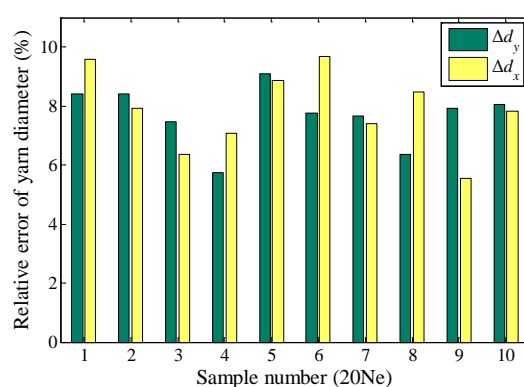
(a1) Δl for 10Ne yarn



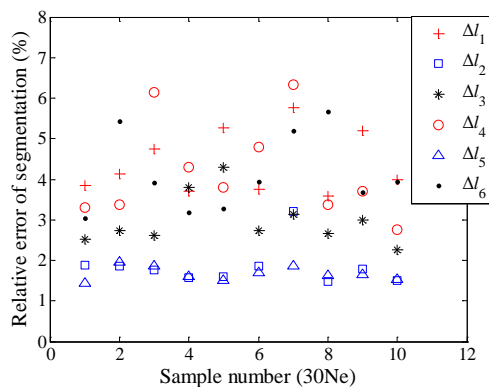
(a2) Δd for 10Ne yarn



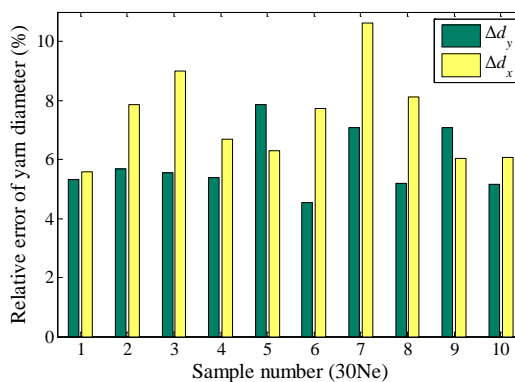
(b1) Δl for 20Ne yarn



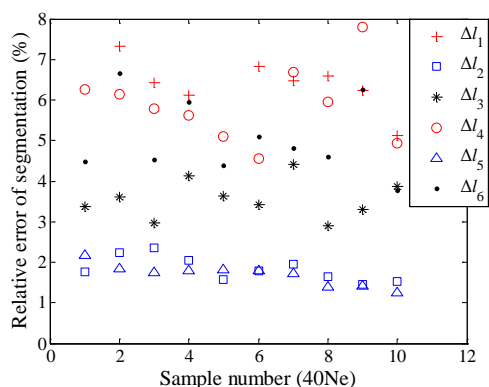
(b2) Δd for 20Ne yarn



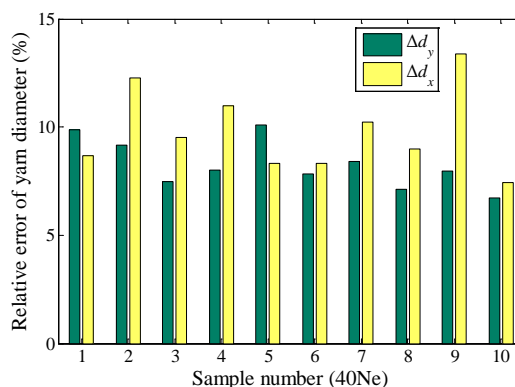
(c1) Δl for 30Ne yarn



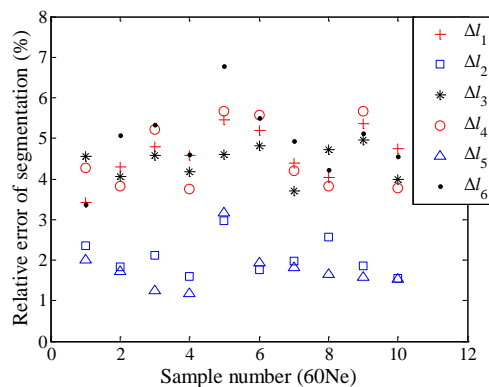
(c2) Δd for 30Ne yarn



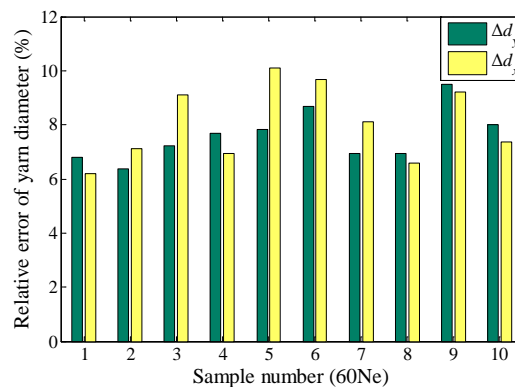
(d1) Δl for 40Ne yarn



(d2) Δd for 40Ne yarn



(e1) Δl for 60Ne yarn



(e2) Δd for 60Ne yarn

Figure 4.40 Relative errors for the image segmentation.

There are two potential factors affecting the relative errors. One is the subjective factor related to the inconsistent determination of threshold in manual method for

different tracer fiber images. The other one is the low image quality caused by improper focal distance. The microscope lens has a different distance to the yarn and its image in mirror A, as shown in [Figure 4.2\(b\)](#). In order to obtain a same intensity for yz yarn and xz yarn in the image, the best focus of the microscope should be exactly in the middle of the two. However, it is impossible to set the focus on the exact middle, and the difference of intensity cannot be avoided. As listed in [Table 4.8](#), the relative error $\overline{\Delta I}$ of 30Ne yarn is the lowest (3.2%) and this is probably attributed to the lower intensity difference of its yarn body. As shown in [Figure 4.36](#), 30Ne yarn image shows a slightly clearer yarn boundary than the other count images. It is noted that the image quality presents a great influence on the accuracy of digital segmentation.

4.6.4. 3D configuration and structural analysis

The digital image mosaics and segmentation by the proposed method are fully evaluated in the previous section. Based on the segmentation results, the 3D configuration of the tracer fiber in the yarn can be constructed and the yarn structural parameters (yarn diameter and fiber migration) can be calculated. The detailed results of 3D configuration and yarn structural parameters for all 50 tracer fibers are listed in [Appendix D](#) and [E](#), respectively. [Figure 4.41](#) shows some examples of the

3D configurations of panorama of different-count yarns in [Figure 4.37](#), based on their segmentation results in [Figure 4.39](#). Their statistical results of yarn diameter and fiber migration behavior are also calculated and shown in [Table 4.9](#). From [Figure 4.41](#) and [Table 4.9](#), tracer fibers present various geometrical paths and migration behavior, including cylindrical helix (20Ne-s10, 40Ne-s2), conical helical trajectory (10Ne-s6, 30Ne-s9 and 60Ne-s4), inner distribution (30Ne-s9 and 60Ne-s4), outer distribution (20Ne-s10), larger migration (10Ne-s6), and lower migration (40Ne-s2). The 3D configuration and migration parameters obtained provide an objective and useful measures for yarn internal structure analysis.

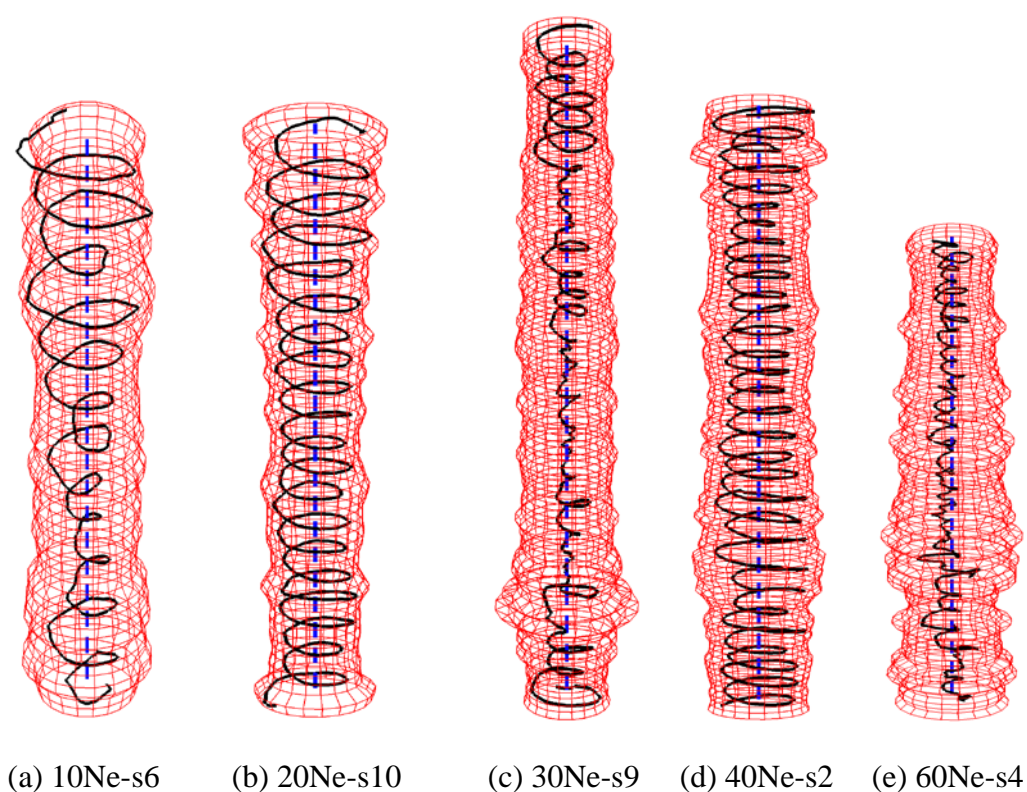


Figure 4.41 3D configuration of the examples shown in [Figure 4.37](#).

Table 4.9. Structural parameters of the yarn samples in [Figure 4.41](#)

Sample No	Yarn length (mm)	Yarn diameter		Fiber migration			
		Mean (mm)	CV (%)	MFP	RMSD	MMI (cm ⁻¹)	EMF (cm ⁻¹)
10Ne-s6	29.80	0.2794	11.18	0.4382	0.3004	8.7541	4.2061
20Ne-s10	29.60	0.1890	15.74	0.5820	0.1960	13.1493	9.6849
30Ne-s9	33.44	0.153	12.69	0.1739	0.1975	8.3535	6.1055
40Ne-s2	30.07	0.1131	11.5	0.4373	0.1656	17.4678	15.2293
60Ne-s4	23.86	0.1157	16.68	0.0792	0.0711	7.7399	15.7230

MFP: mean fiber position, RMSD: RMS deviation, MMI: mean migration intensity, EMF: equivalent migration frequency

In addition, the time taken for the image mosaic is longer than that mentioned in [Section 4.5](#). It is mainly because the overlap in this experiment is 30%, which is higher than 20% in [Section 4.5](#) and the number of images also increases. Under this situation, the time taken of image segmentation is still much shorter than the manual method. The detailed time taken for the proposed method is listed in [Appendix E](#). [Table 4.10](#) shows the average time taken for mosaic of a pair of images and segmentation for a panorama in [Appendix E](#). In [Table 4.10](#), the mosaic time for each pair of image using manual method is about twice of that of computer method, and the segmentation time by manual method is about 50 times of that by computer method.

Table 4.10. Time taken for image mosaic and segmentation

Yarn count	Computer method (mean of samples)		Manual method for 20Ne yarn	
	mosaic (a pair of images)	segmentation (a panorama)	mosaic (a pair of images)	segmentation (a panorama)
10Ne	32 seconds	18 seconds		
20Ne	32 seconds	21 seconds		
30Ne	37 seconds	28 seconds	72 seconds	24 minutes
40Ne	33 seconds	25 seconds		
60Ne	32 seconds	29 seconds		

4.7. System development for image processing of tracer fiber images

Besides the algorithms discussed in previous sections, a software system is also designed and developed for image analysis of tracer fiber images, using MATLAB Graphical User Interface (GUI). [Figure 4.42](#) shows the outline for the proposed image processing system. It contains five modules, including *Video Acquisition*, *Image Acquisition*, *Image Mosaic*, *Image Segmentation* and *Parameter Analysis*. In addition, two more modules, i.e. *Mosaic of Pair Images* and *Tracer Fiber Detection*, are developed to facilitate the parameter adjustment and optimization in image mosaic and segmentation. [Figure 4.43](#) shows the main interface of the developed digital system with five menus: video acquisition, image acquisition, image mosaic, image segmentation and yarn structural analysis.

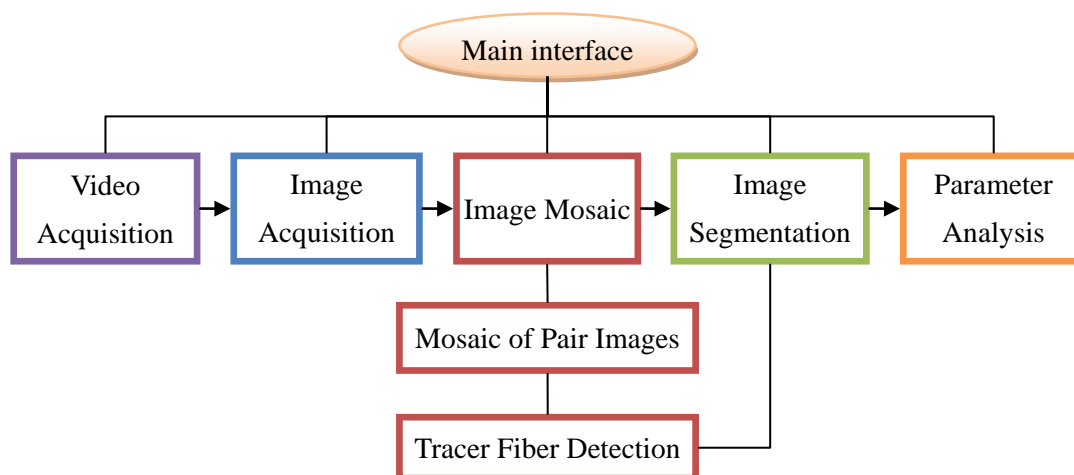


Figure 4.42 Interface outline of the proposed system for tracer fiber images.

Figure 4.44 shows the main steps involved in the image processing of tracer fiber images. Firstly, the *Video Acquisition* module is connected with the hardware of measurement system [44] to obtain a video of a moving yarn (containing tracer fibers). In the *Image Acquisition* module, a series of overlapped tracer fiber images can be extracted from the video. Then the overlapped images will be stitched into a panorama in module of *Image Mosaic*. Afterwards, the information of yarn boundaries and tracer fiber will be extracted in module of *Image Segmentation*. Finally, in the module of *Parameter Analysis*, the 3D configuration of the tracer fiber in the yarn will be constructed and visualized. Besides, various yarn structural and migration parameters, including yarn diameter and fiber migration, will be also statistically calculated and visualized in that module.

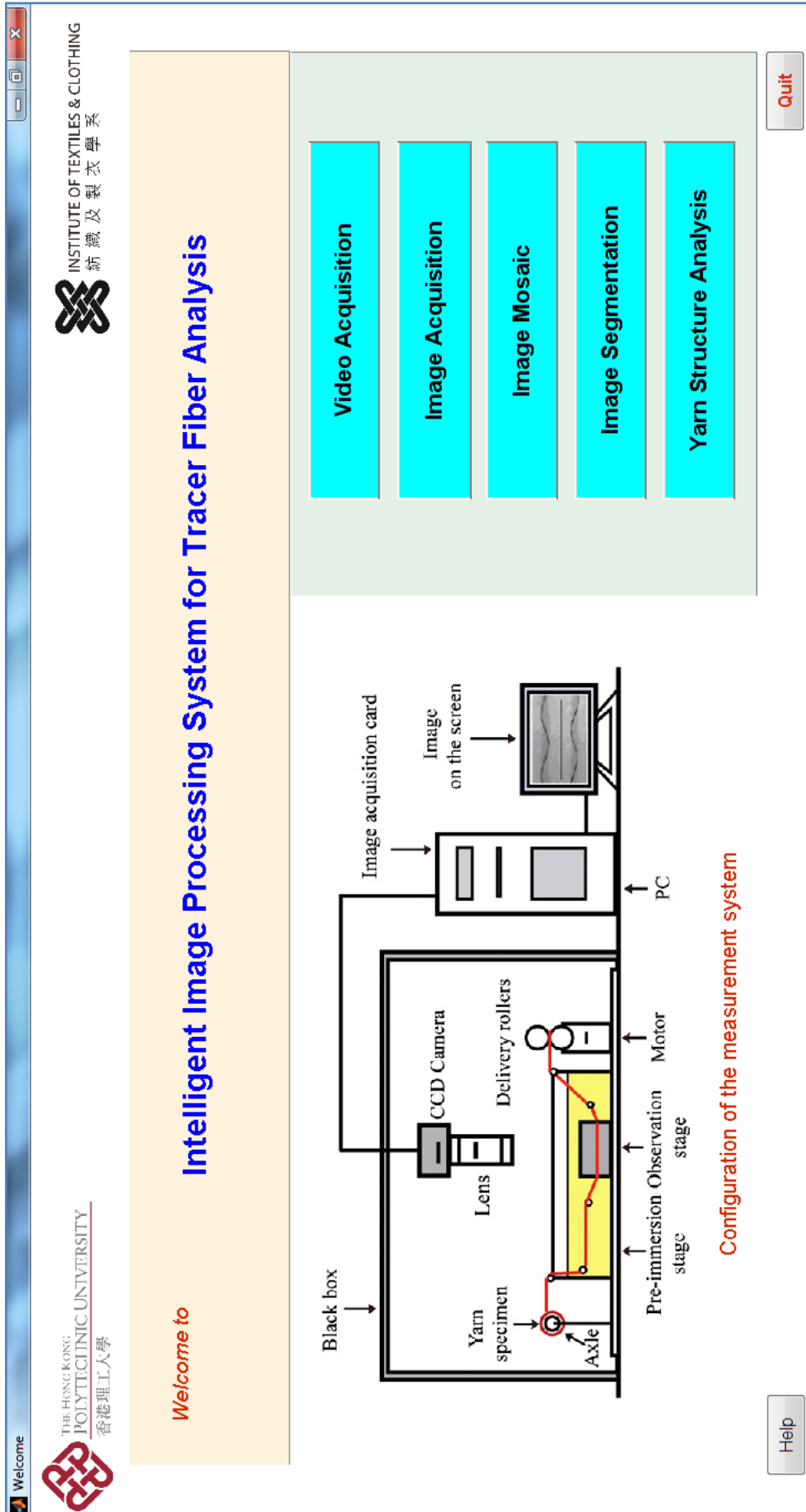


Figure 4.43 Main interface of the system

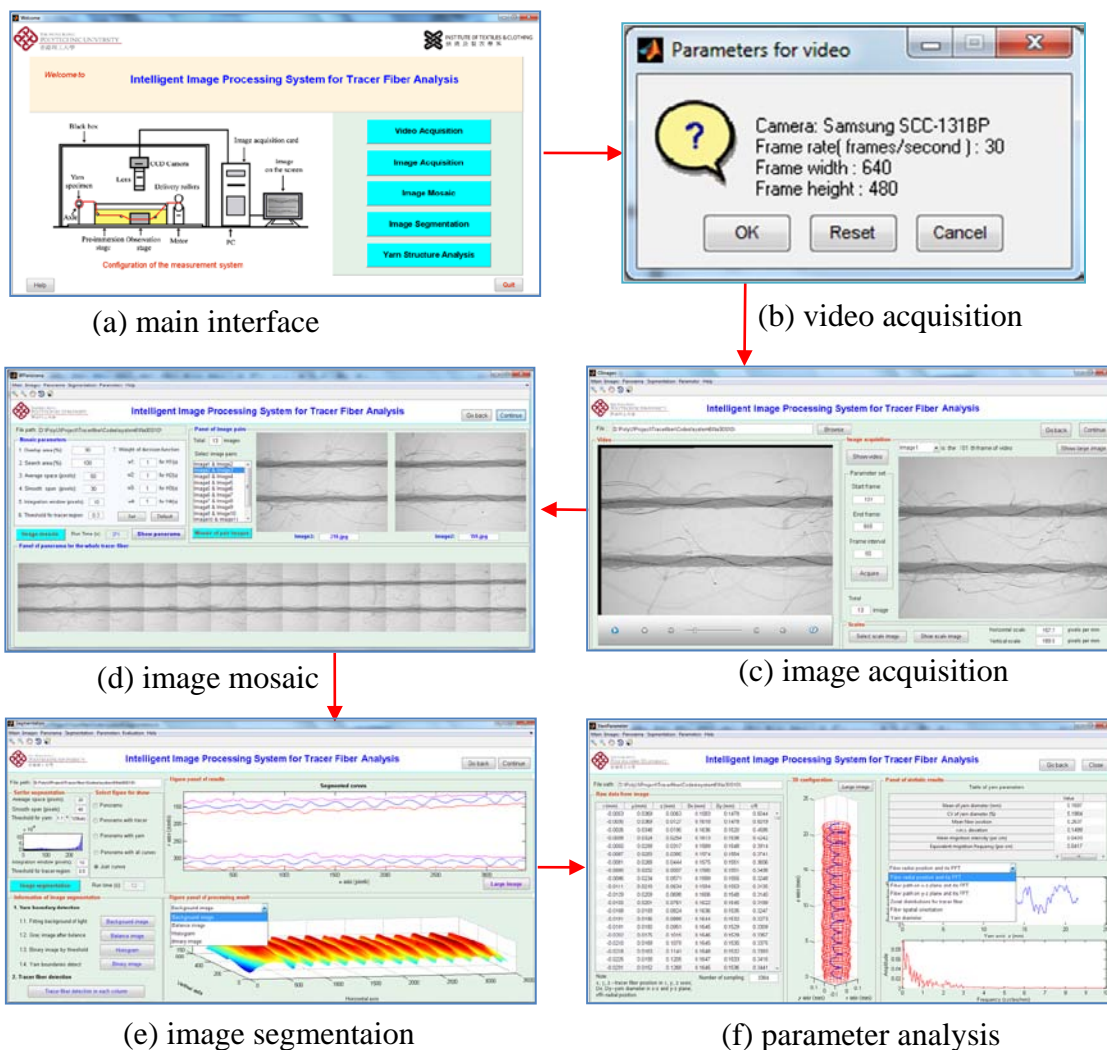


Figure 4.44 Main steps for the image processing in the system.

4.7.1. Video acquisition

The module of *Video Acquisition* in Figure 4.43 is used to connect and open the interface of measurement system for video capture. According to the hardware of measurement system developed by Guo et al. [44], Camera is Samsung SCC-131BP with 0.5× eyepiece adapter and 0.7-4.5× objective lens (total magnification is 0.35-2.25×). The parameters of video acquisition include frame rate (30 frames per

second), frame width (640 pixels) and frame height (480 pixels).

4.7.2. Image acquisition

After video acquisition, the module of *Image Acquisition* will be used to acquire a series of consecutive tracer fiber images from the video, as shown in [Figure 4.45](#).

The interface is mainly composed of two panels of video playing and image acquisition. First, a captured video of moving yarn can be loaded into the system.

In this study, the overlap of a pair of neighboring images is around 30% in order for an accurate image mosaic. For doing this, users can watch the video and then make a rough estimate of frame interval for image acquisition. With this frame interval, a series of consecutive tracer fiber images can be automatically extracted from the video. Afterwards, the acquired images are displayed and can also be compared with the video.

Besides, in the developed measurement system [44], the measurement scale of microscope is determined by an image containing a ruler, as shown in [Figure 4.46](#).

Each rectangle unit in the scale image presents the size of 1mm×1mm. The scale image can be loaded into the system and then the scales in horizontal and vertical directions can be calculated from the scale image for further analysis of yarn structural parameters.

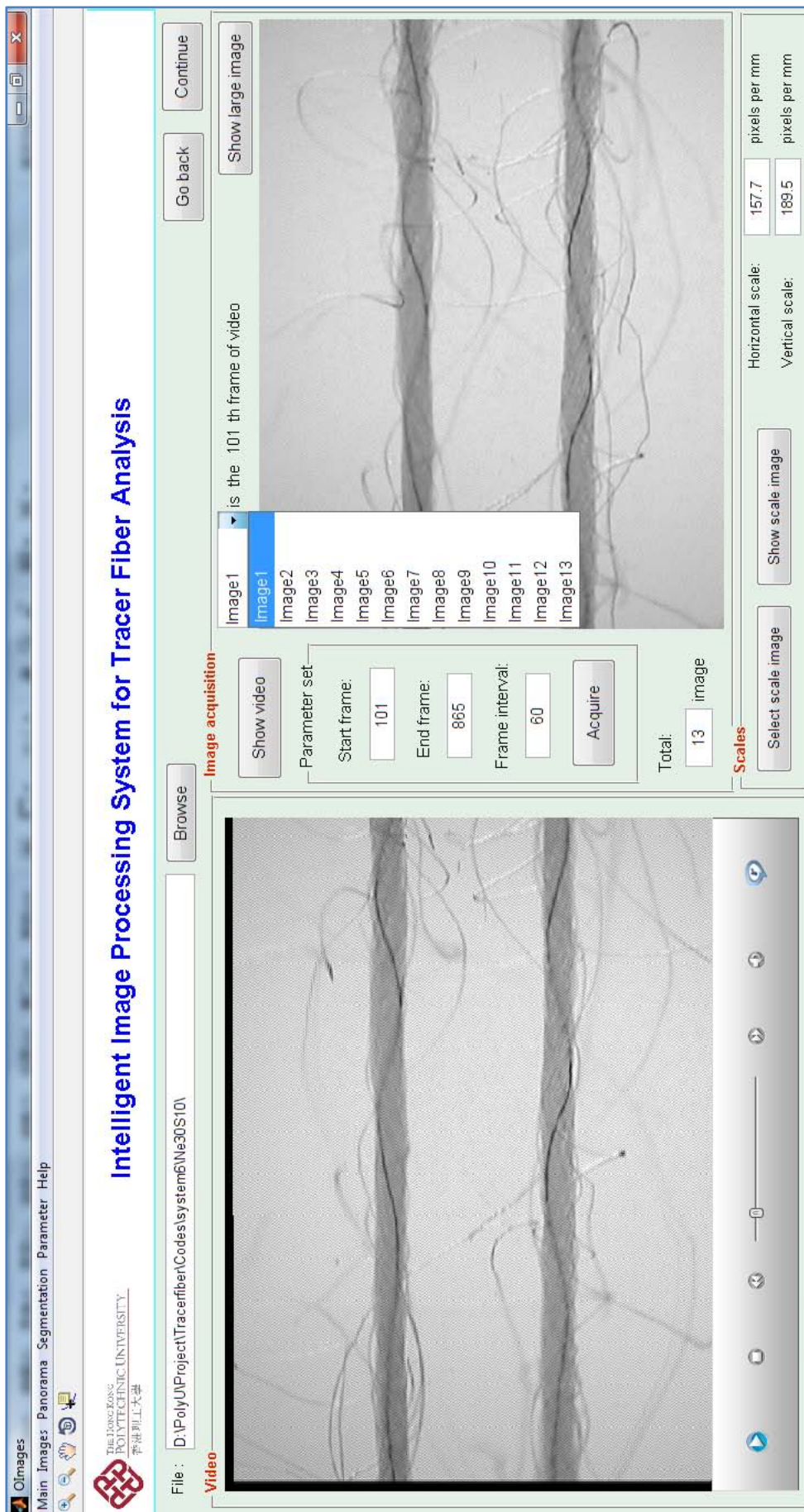


Figure 4.45 Interface of image acquisition

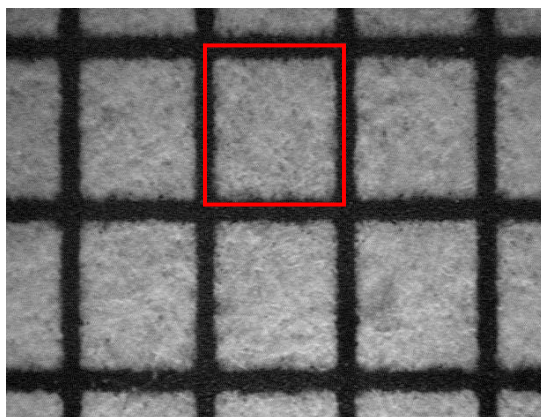


Figure 4.46 Scale image in image acquisition.

In [Figure 4.45](#), a 30Ne yarn sample, 30Ne-s10 in the experiment, is under processing. 13 individual tracer fiber images are acquired from a video with the interval of about 60 frames. The horizontal and vertical scales are 157.7 and 189.5 pixels per mm, respectively.

4.7.3. Image mosaic

With a series of consecutive tracer fiber images obtained in [Section 4.7.2](#), an interface is developed for image mosaic, as shown in [Figure 4.47](#). In this window, various parameters for image mosaic, including overlap area (% , percentage of overlap in neighboring images), search area (% , percentage of search area for matching the image), average space (pixels, width of average window for noise elimination), smooth span (pixels, span of smooth filter for detected signal of tracer fiber), and parameters for the tracer fiber detection (i.e. width of integration window (pixels) and the threshold for detection of tracer fiber region) as well as the weights (w_1, w_2, w_3 and w_4) assigned to each components in decision function, are considered.

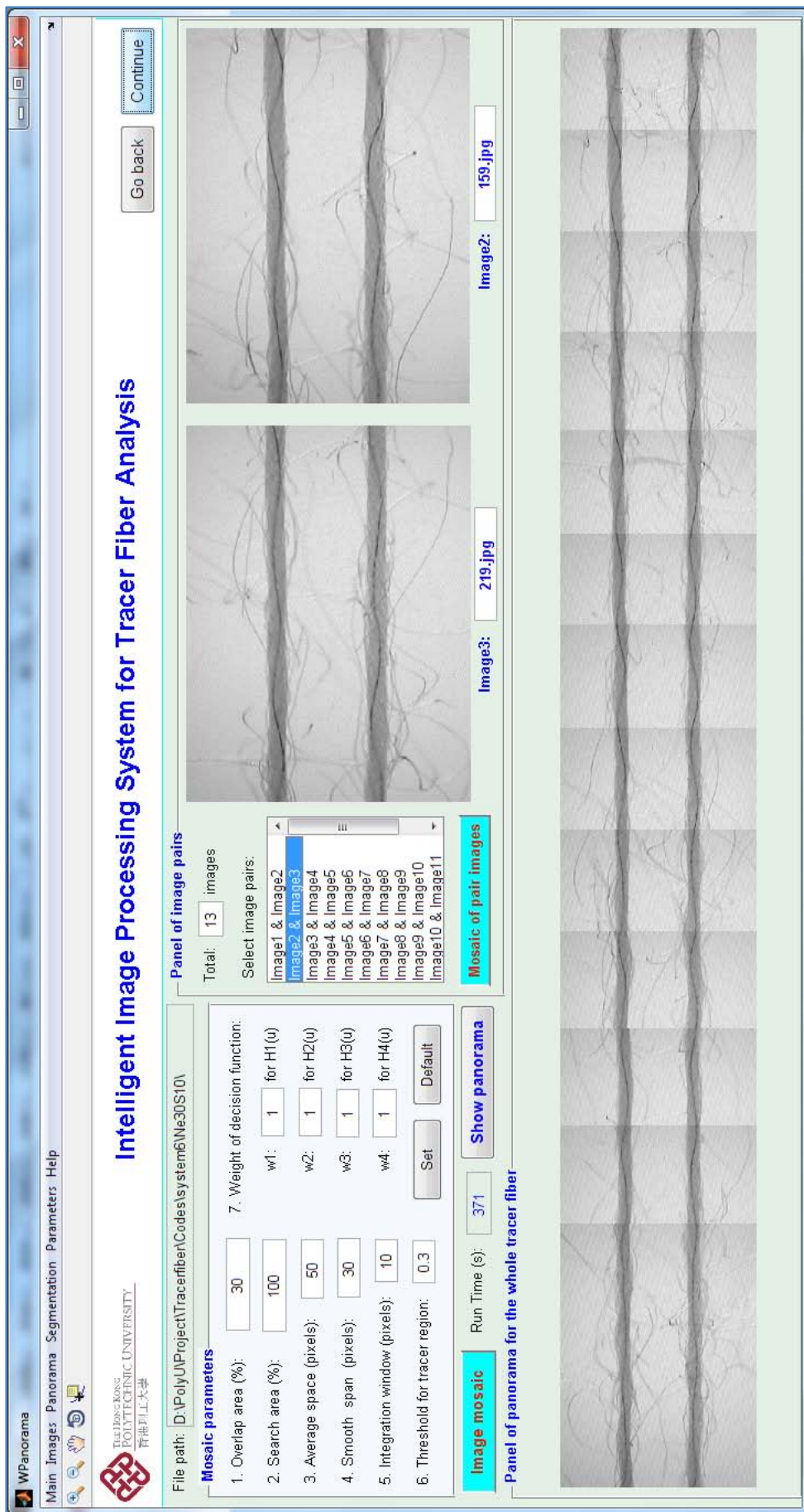


Figure 4.47 Interfaces of image mosaic

Figure 4.48 shows the parameter setting of image mosaic. The default parameters in the window are the optimized values obtained in Section 4.6. All pairs of neighboring images (13 pairs in Figure 4.47) can be individually displayed for a clear observation. Finally a panorama can be obtained and displayed by automatic stitching the consecutive tracer fiber images. In addition, the time taken will be also shown in the interface. It may take a few minutes for image mosaic, which depends on the number of tracer fiber images in the series.

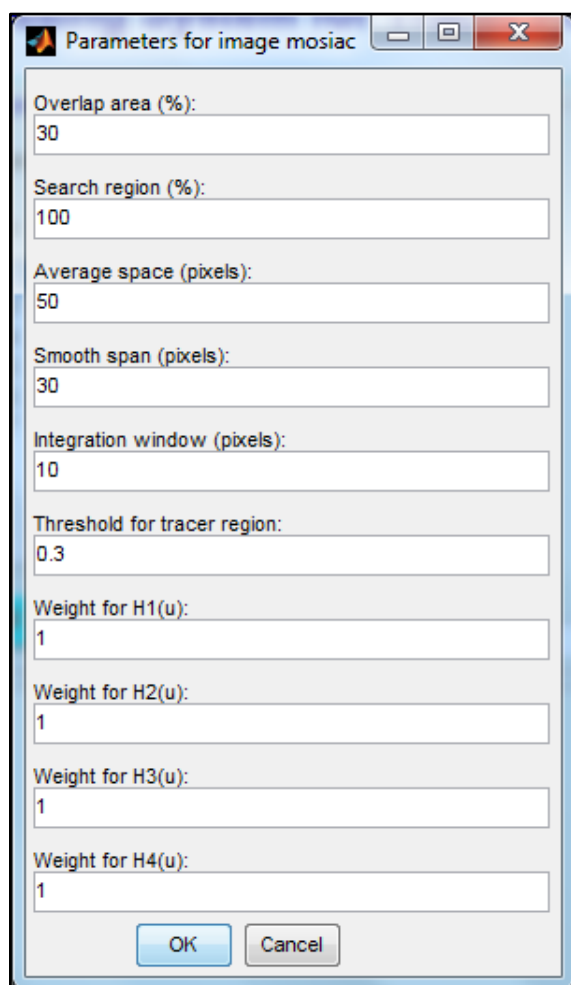


Figure 4.48 Parameter setting for image mosaic.

4.7.3.1. Mosaic of pair images

In [Figure 4.47](#), the neighbor images can be individually shown in pairs in the window. Since the panorama is stitched pair by pair of images, the processing details of each pair of image mosaic may be desirable by users for operating the process and adjusting the processing parameters. Hence, a module of *Mosaic of Pair Images* is designed to show the details of mosaic of designated pair images, as shown in [Figure 4.49](#). In this module, the accuracy of mosaic of each pair of images can be evaluated. For each pair of image mosaic, all progressing results as discussed in [Section 4.3](#), including the detected tracer fiber and gradient image for feature extraction, and the statistical measures extracted from tracer fiber and gradient image for the decision function, can be visualized and evaluated, as shown in [Figure 4.50](#) and [Figure 4.51](#), respectively. In additions, the details of tracer fiber detected in each column of image are also shown in the following module of *Tracer Fiber Detection*.

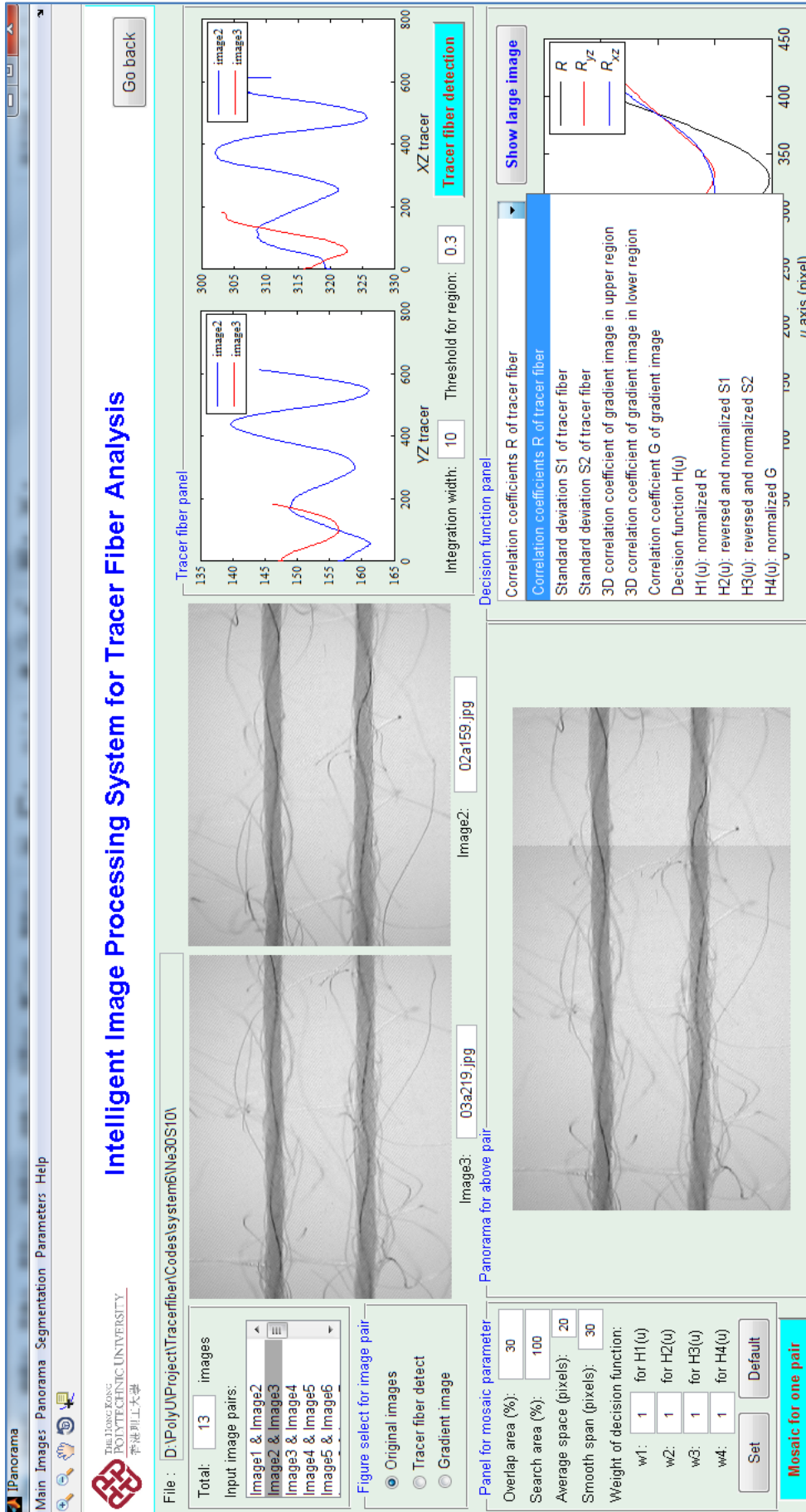
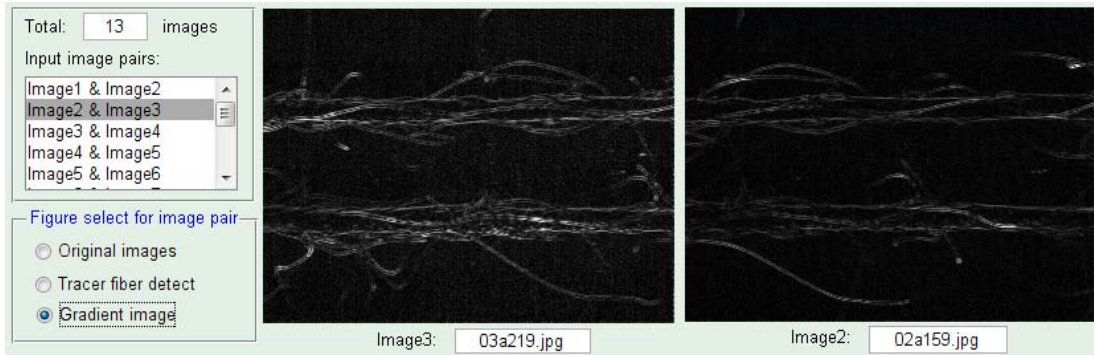
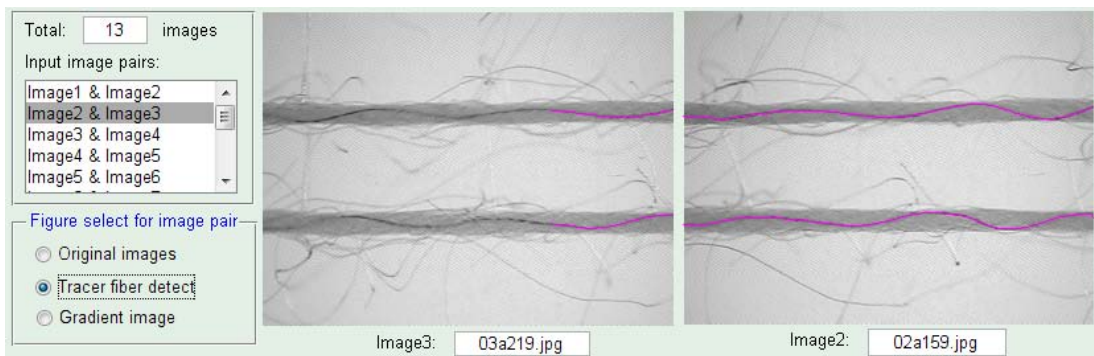


Figure 4.49 Interface for the details of pair image mosaic

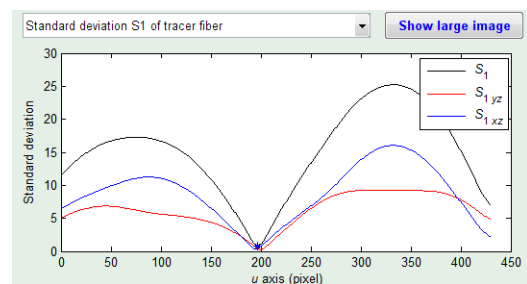
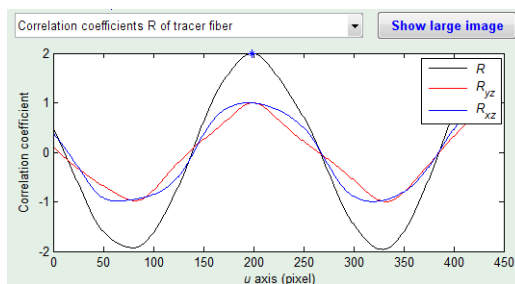


(a) gradient image

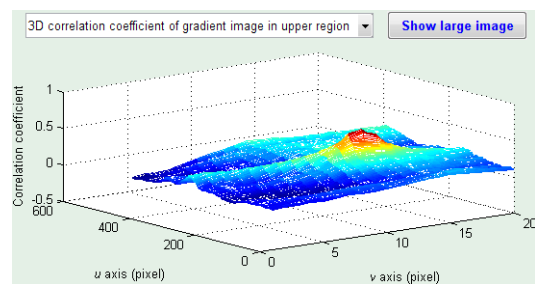
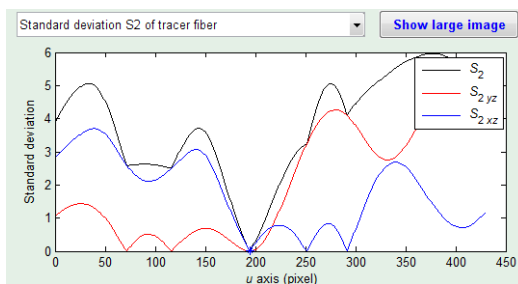


(b) tracer fibers

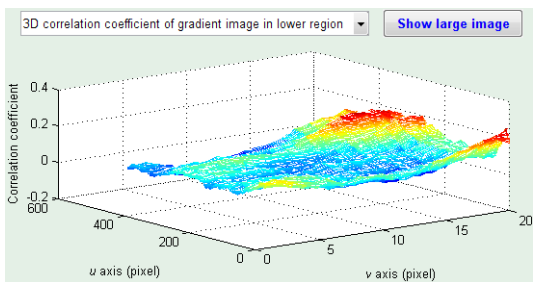
Figure 4.50 Processing results of gradient image and tracer fibers in the interface.



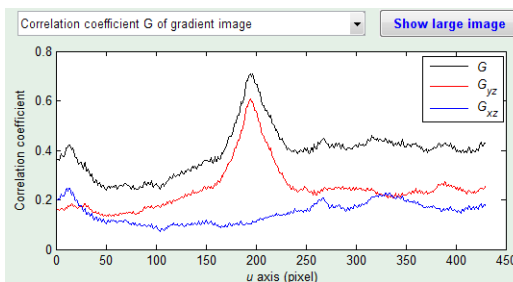
(a) correlation coefficient (CC) of tracer fiber (b) standard deviation S_1 of tracer fiber



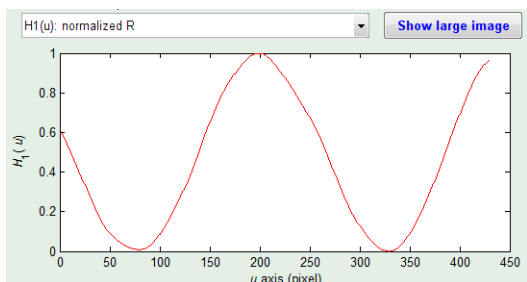
(c) standard deviation S_2 of tracer fiber (d) CC of gradient image in upper region



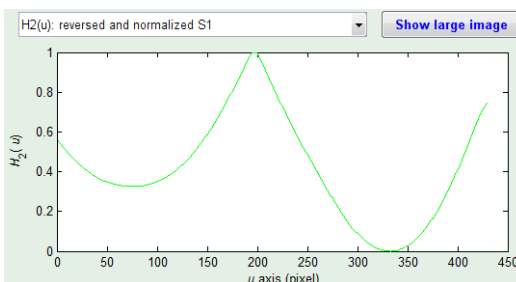
(e) CC of gradient image in lower region



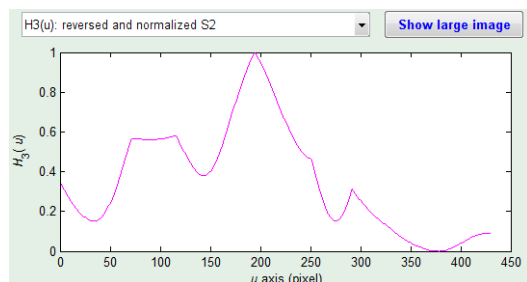
(f) maximum in v axis for (d)&(e)



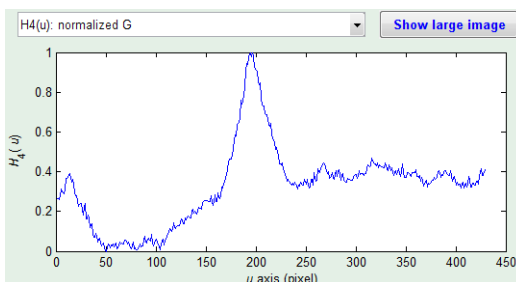
(g) component $H_1(u)$



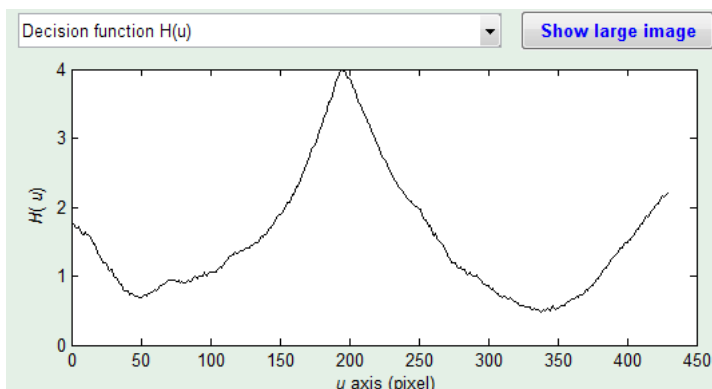
(h) component $H_2(u)$



(i) component $H_3(u)$



(j) component $H_4(u)$

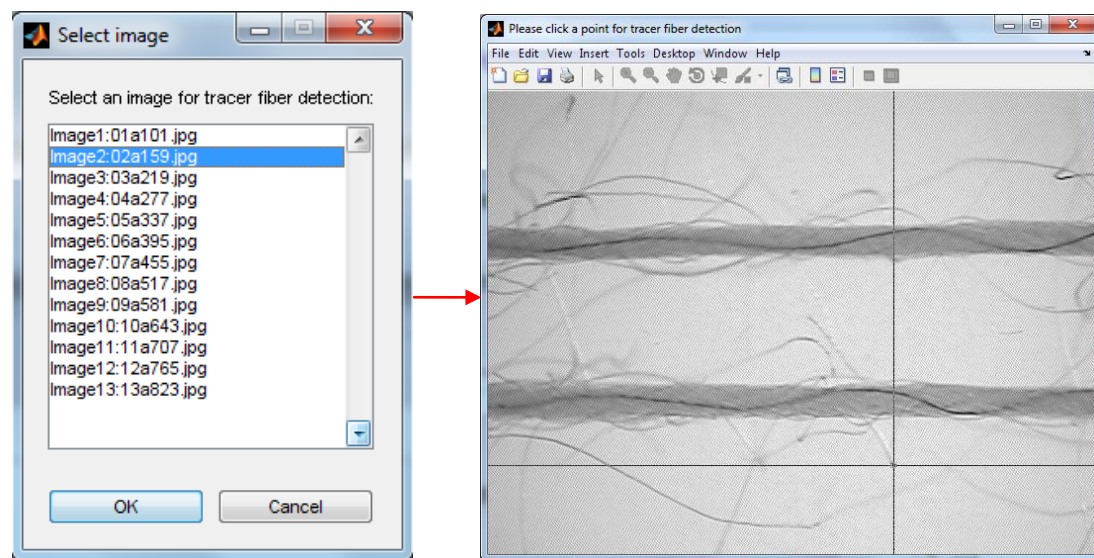


(k) decision function $H(u) = w_1H_1(u) + w_2H_2(u) + w_3H_3(u) + w_4H_4(u)$

Figure 4.51 Statistical measures for image mosaic shown in the interface.

4.7.3.2. Tracer fiber detection

A module of *Tracer Fiber Detection* is developed for the identification of tracer fiber at each column of image. Firstly, a window, as shown in [Figure 4.52\(a\)](#), will pop out for choosing an image from the series of consecutive tracer fiber images. Then the selected image will be displayed for selecting a point/column of interest for further analysis of tracer fiber, as shown in [Figure 4.52\(b\)](#).



(a) dialog for image selection

(b) column section for tracer fiber detection

Figure 4.52 Selection windows for tracer fiber detection.

After the selection of point/column in [Figure 4.52\(b\)](#), a window is developed to show the processing details of signal at the selected column of image for tracer fiber detection, as shown in [Figure 4.53](#).

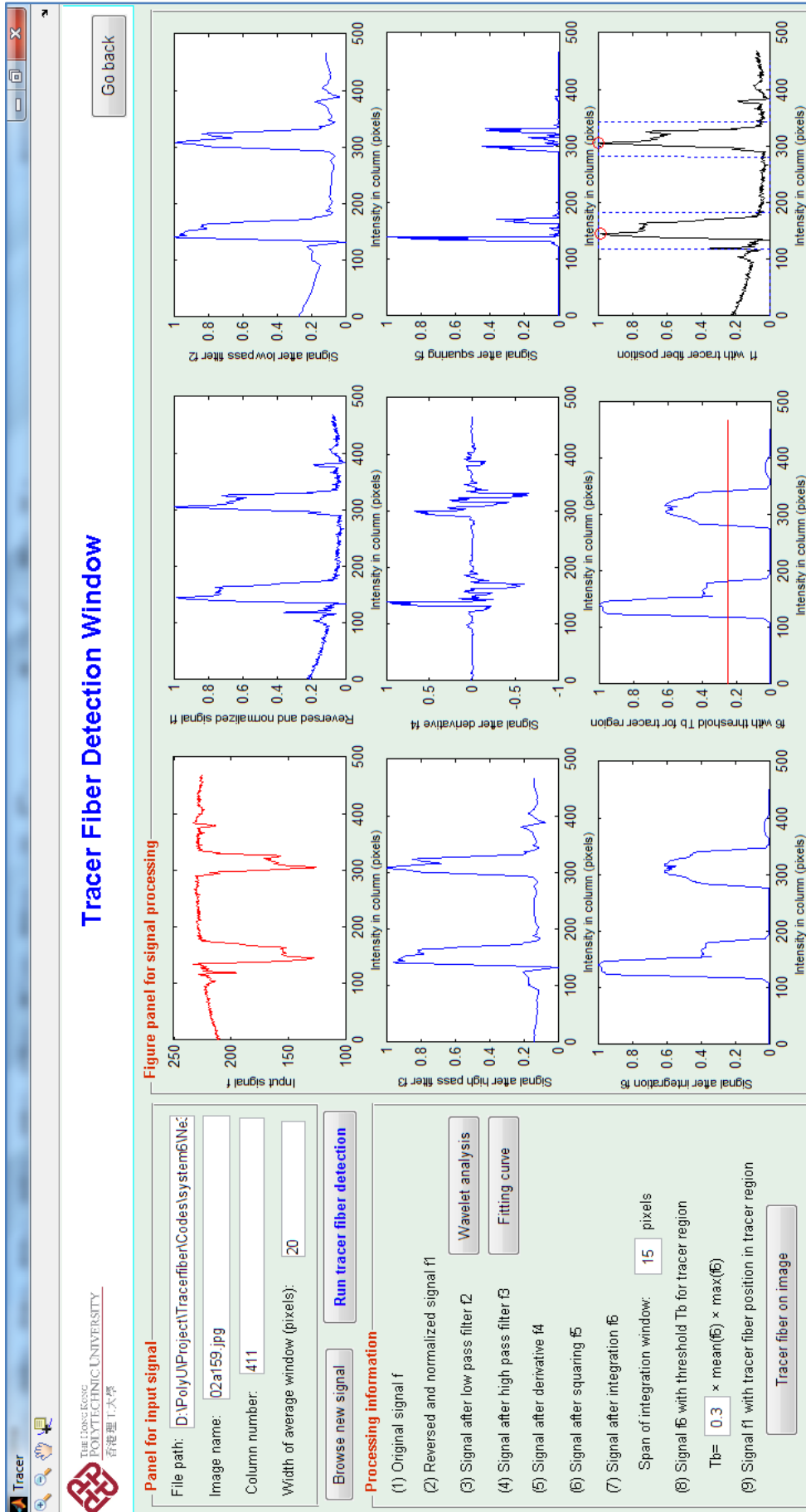
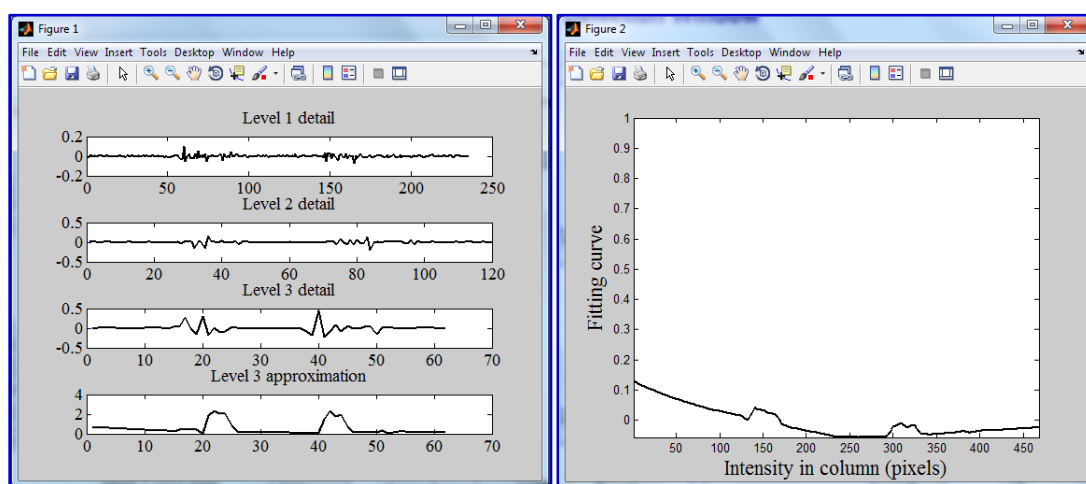


Figure 4.53 Tracer fiber detection window

In this window, all progressing results for tracer fiber detection as discussed in Section 4.3.1, including the original signal L_1 (one column of image), reversed and normalized signal L_2 , signal after low-pass filter L_3 , signal after high-pass filter L_4 , signal after derivative L_5 , signal after squaring L_6 , signal after integration L_7 , tracer fiber region detected by threshold and tracer fiber detected in tracer fiber region, can be displayed for evaluation. Besides, the wavelet analysis for low-pass filter and fitting curve for high-pass filter can also be obtained, as shown in Figure 4.54. Finally, the two locations of the tracer fiber on the selected column of image can be identified (see Figure 4.55). Moreover, various processing parameters, such as the width of average window, the span of integration window and the coefficient of threshold for the identification of tracer fiber regions, can be adjusted if necessary, as shown in Figure 4.53.



(a) wavelet analysis for low-pass filter

(b) fitting curve for high-pass filter

Figure 4.54 Windows for the results of high- and low-pass filter methods.

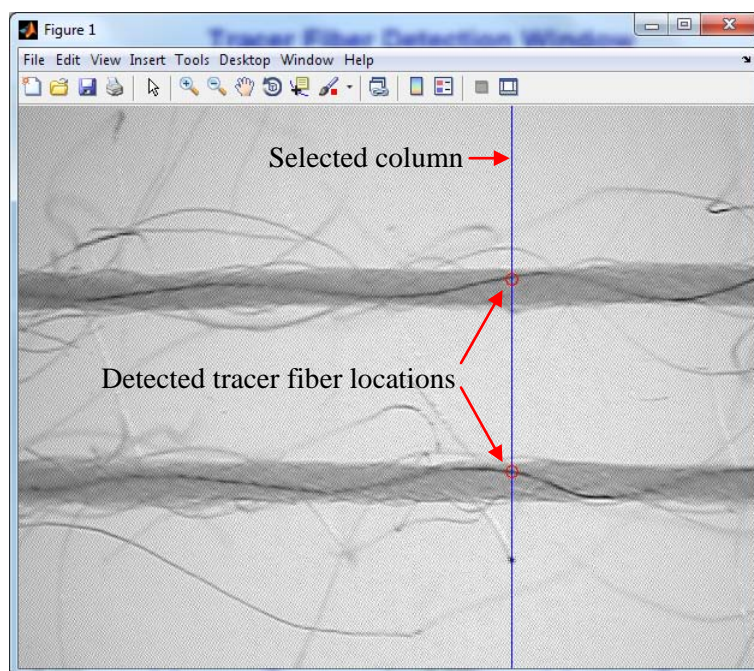


Figure 4.55 Tracer fiber locations detected in image.

4.7.4. Image segmentation

With the panorama obtained in [Section 4.7.3](#), the module of *Image Segmentation* is designed for identification of yarn boundaries and tracer fiber from the obtained panorama. Firstly, a dialog box, as shown in [Figure 4.56](#), will pop out for parameter setting in image segmentation. Five parameters, including average space (pixels, the width of average window for noise elimination), smooth span (pixels, span of smooth filter for detected signals of yarn boundaries and tracer fiber), threshold for binary image of yarn (% , ratio of the threshold using Otsu's method for binary image), integration window (pixels, the span of integration window in tracer fiber detection) and threshold for tracer region (the coefficient of threshold for

identifying tracer fiber regions in tracer fiber detection), can be adjusted if necessary.

The default parameters are the optimized values obtained in [Section 4.6](#).

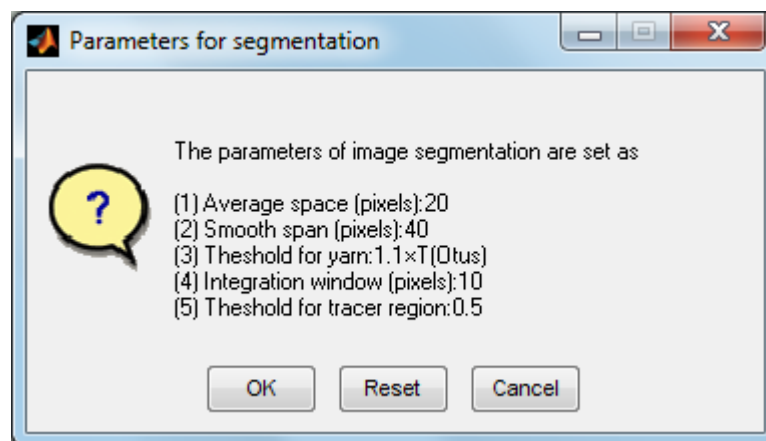


Figure 4.56 Dialog box for the panorama setting in image segmentation.

With the setting of parameter, the identification of the yarn boundary and tracer fiber will take place, as shown in [Figure 4.57](#). After image segmentation, the processing results, such as the identified tracer fiber, yarn boundaries and the their curves can be displayed, as shown in [Figure 4.57](#) and [Figure 4.58](#). In addition, larger image with higher resolution can be shown and saved for each segmentation results. Besides the final results of segmentation, the processing results for tracer fiber detection and yarn boundary detection can also be evaluated. As shown in [Figure 4.59](#), the processing results for yarn boundary detection, such as background of the pnorama (fitting background of light), residual image (gray image obtained by subtracting the background from the panorama), histogram of residual image and binary image of the panorama, can all be displayed.

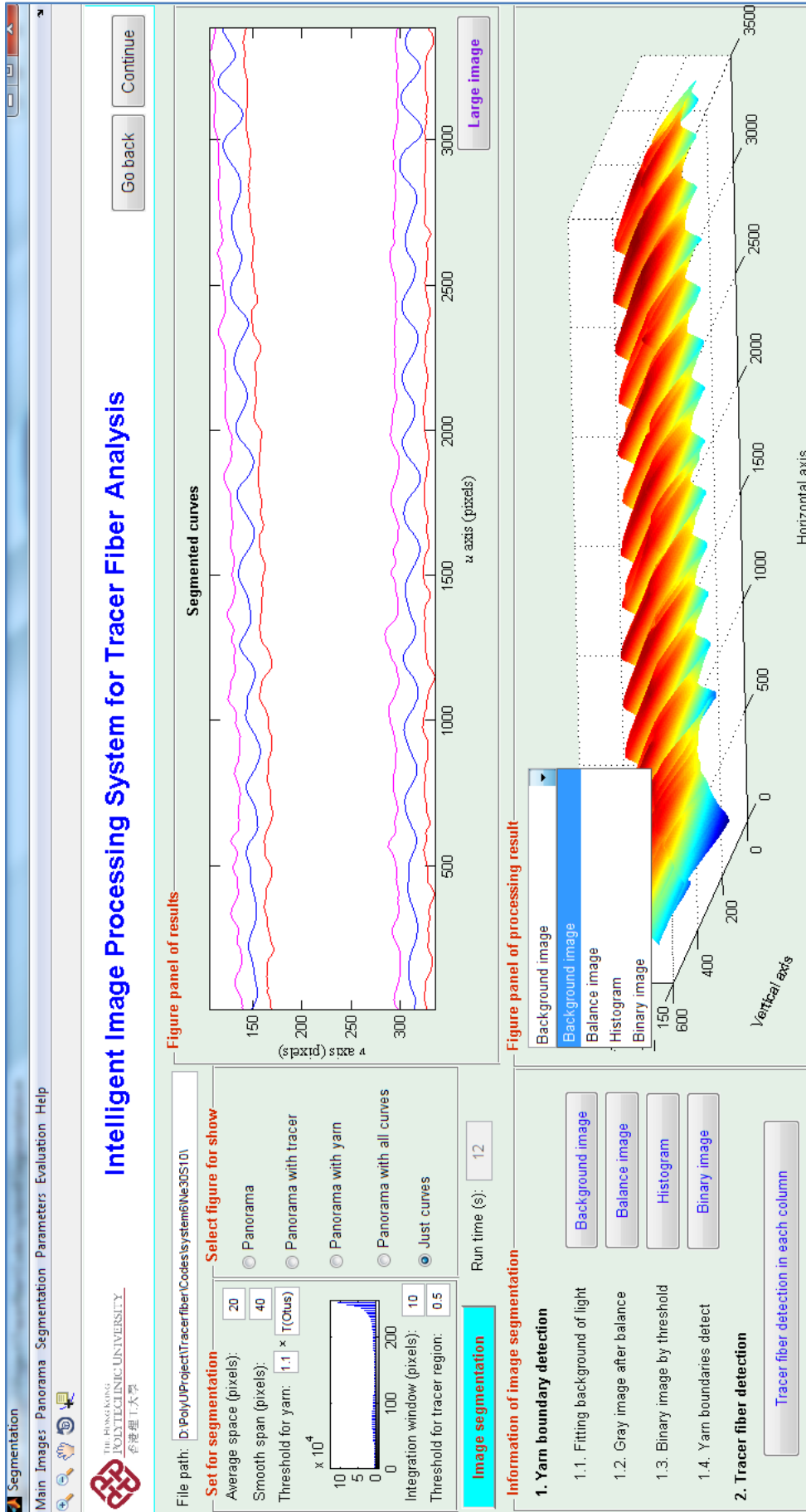
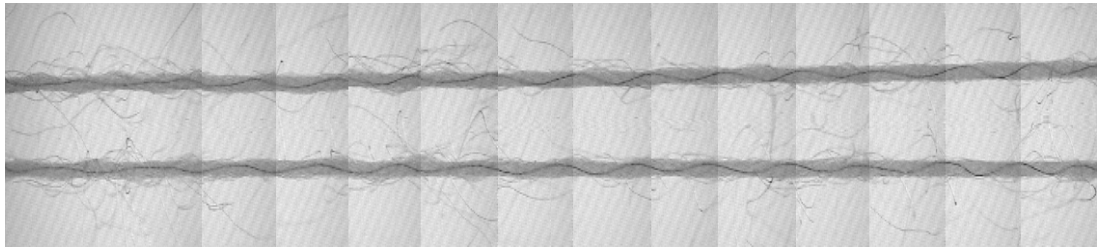
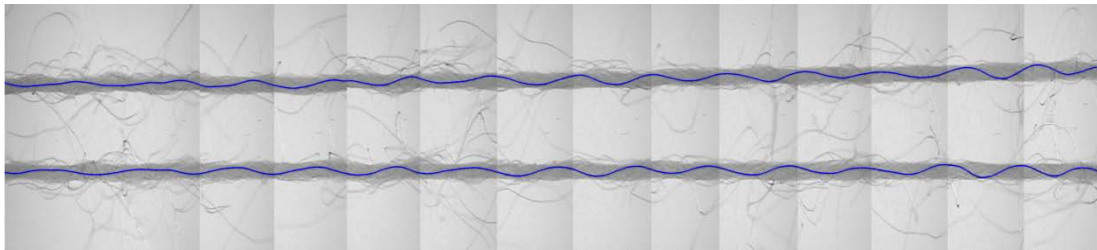


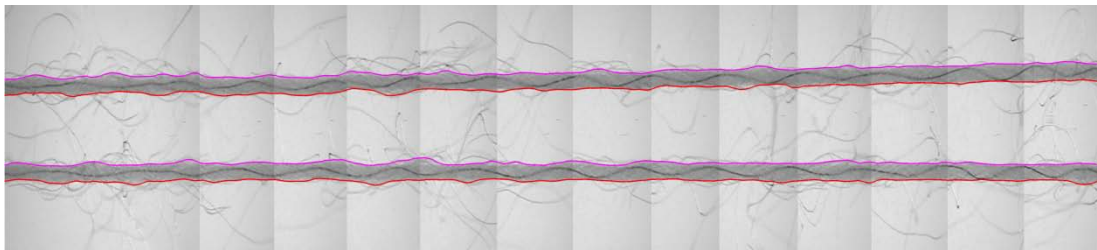
Figure 4.57 Interface for image segmentation



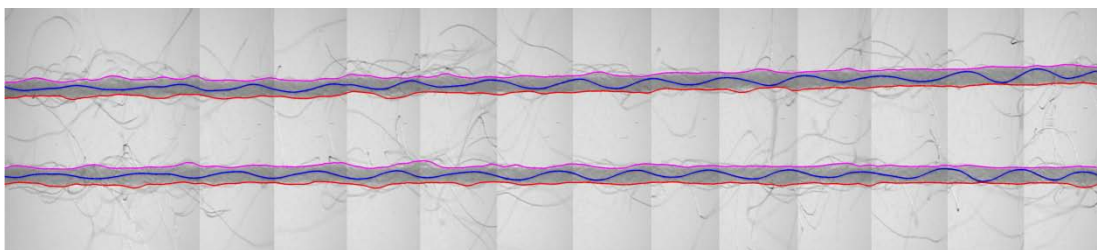
(a) panorama



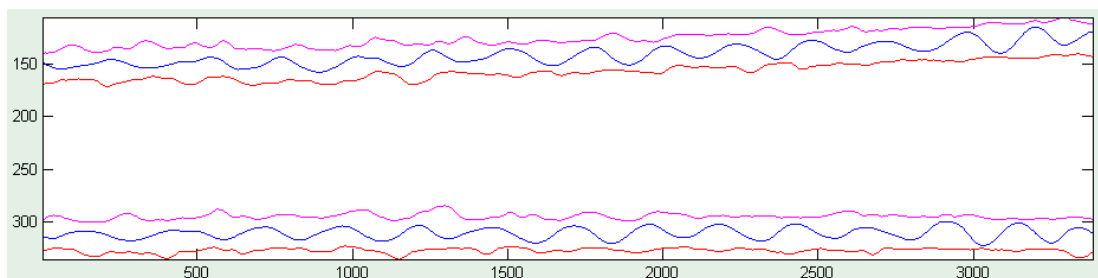
(b) panorama with identified tracer fiber



(c) panorama with identified yarn boundary

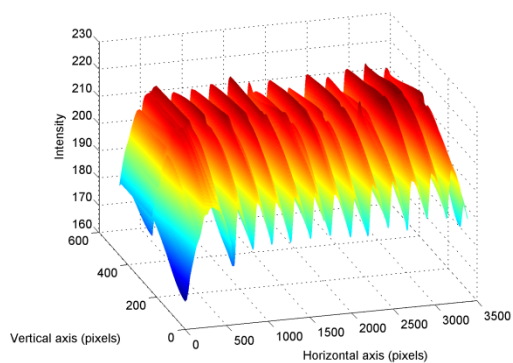


(d) panorama with identified tracer fiber and yarn boundary

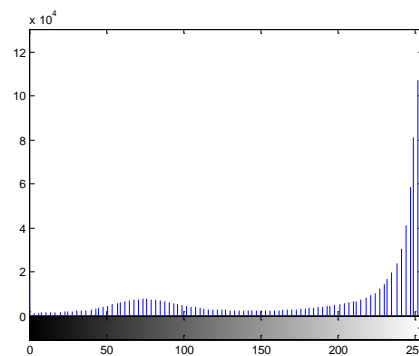


(e) identified curves of tracer fiber and yarn boundary

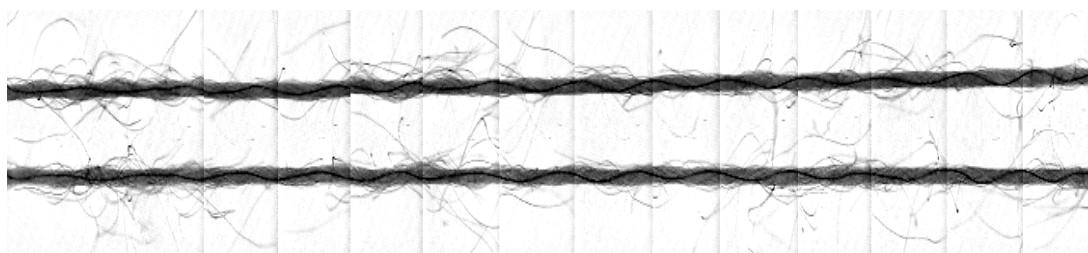
Figure 4.58 Results of image segmentation shown in the interface.



(a) background of image



(b) histogram of residual image



(c) residual image



(d) binary image

Figure 4.59 Preprocessing results of yarn boundary detection shown in the interface.

4.7.5. Parameter analysis

The yarn structural parameters, related to yarn diameter and fiber migration behavior, can be finally calculated from the segmentation results and displayed in the interface of *Parameter Analysis* module, as shown in [Figure 4.60](#).

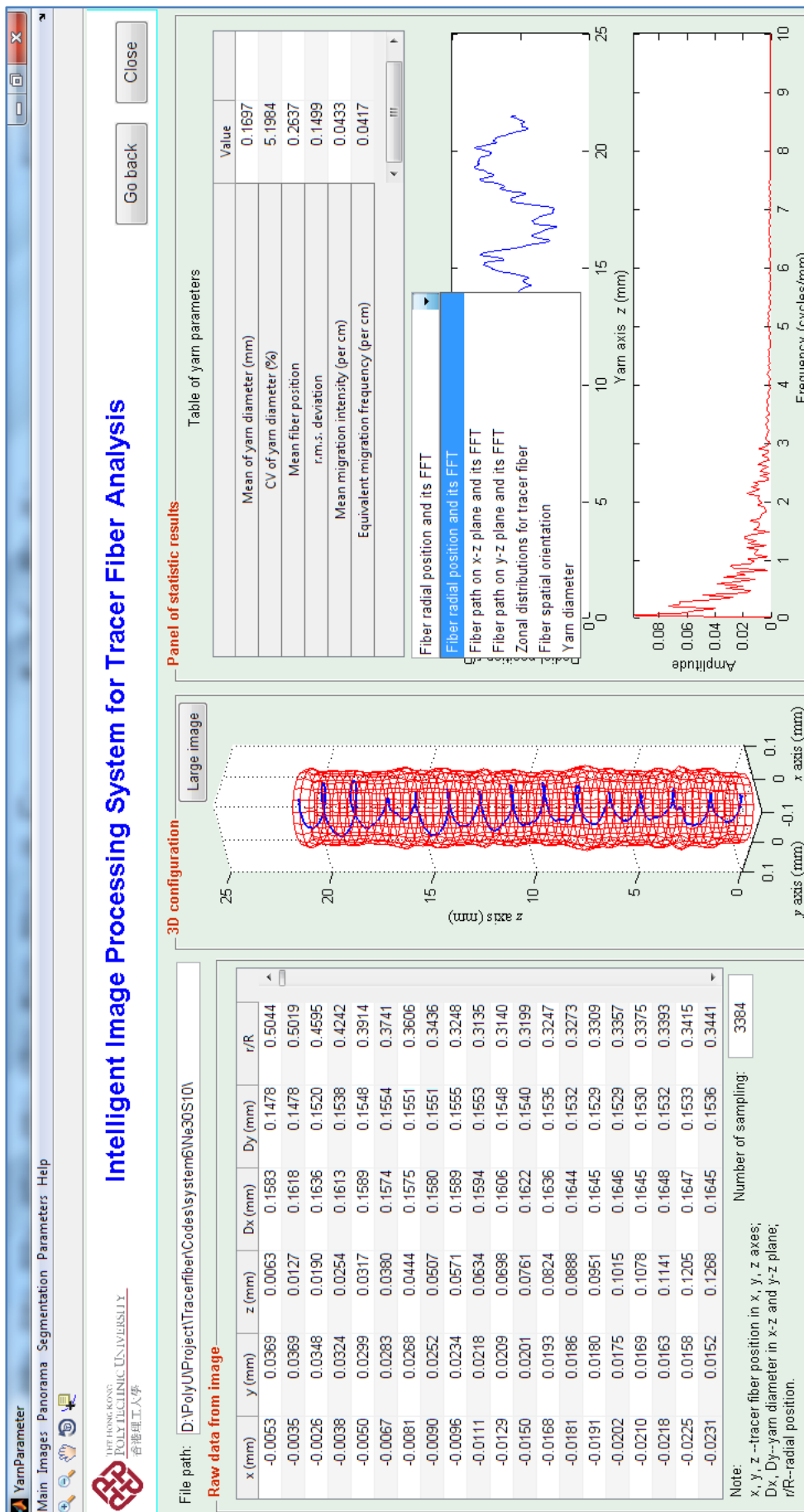


Figure 4.60 Interface for parameter analysis of yarn

In this window, raw data of segmentation results, such as tracer fiber position (x, y, z) , the yarn diameter in xz - and yz - plane (D_x and D_y) and radial position (r/R) , are all listed at each sampling point (pixel). Based on the data, the three-dimensional (3D) yarn and tracer fiber can be re-constructed and shown in the window. In addition, the statistical results of yarn structural parameters, such as the yarn diameter (mean and CV) and the fiber migration measures (mean fiber position, RMS deviation, mean migration intension and equivalent migration frequency), are summarized in a table. Moreover, some graphical results of yarn structure are also shown for a better evaluation, as discussed as follows.

(1) Radial position

As expressed by Equation (4.32), the fiber radial position can be calculated and displayed along the length of yarn axis. Besides, its frequency-amplitude curve can also be obtained by using Fast Fourier Transform (FFT) for reference. Figure 4.61 shows the radial position and frequency-amplitude curve of an example yarn (30Ne-s10) in which tracer fiber presents a complex path inside the yarn body. The tracer fiber fluctuates around the middle layer of yarn, showing a certain level of migration inside the yarn.

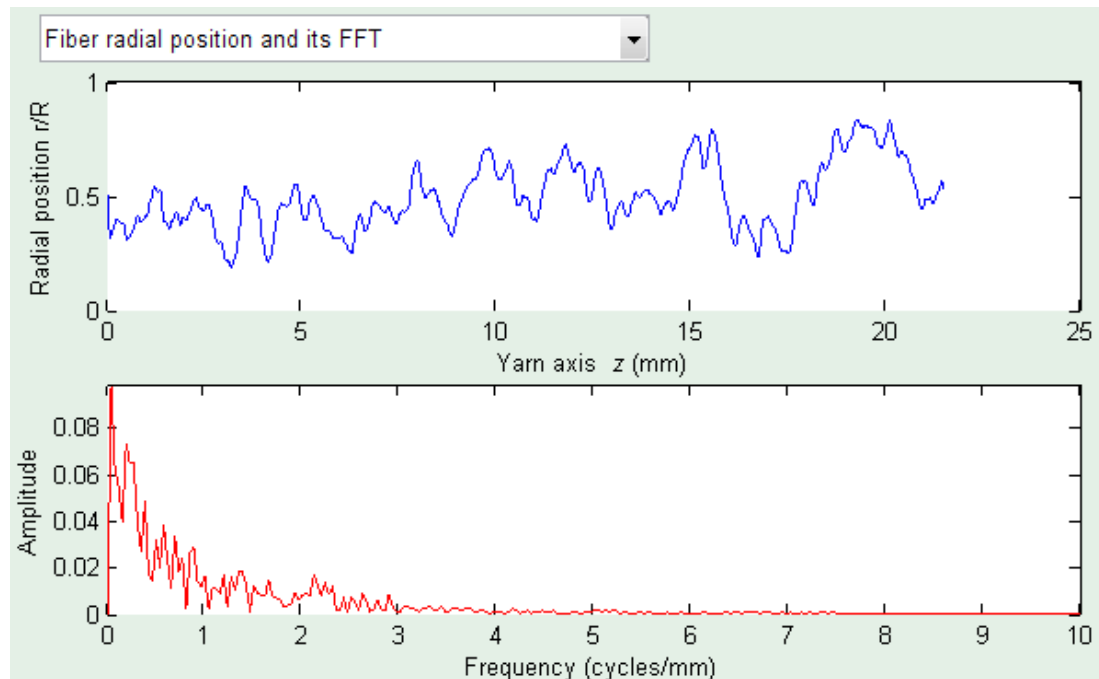
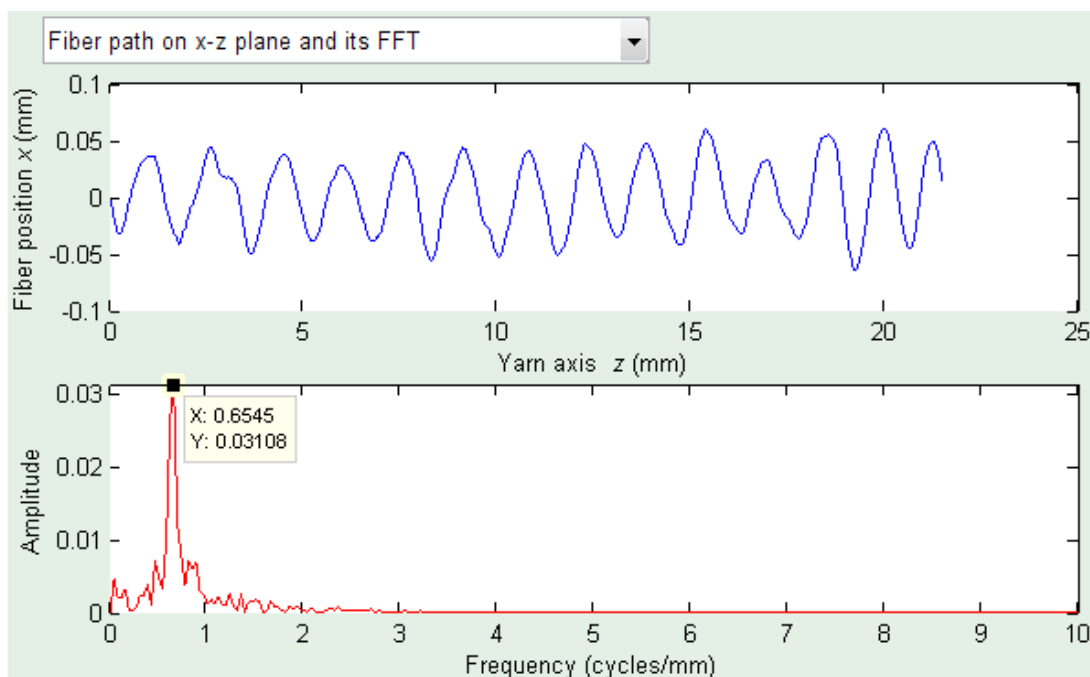


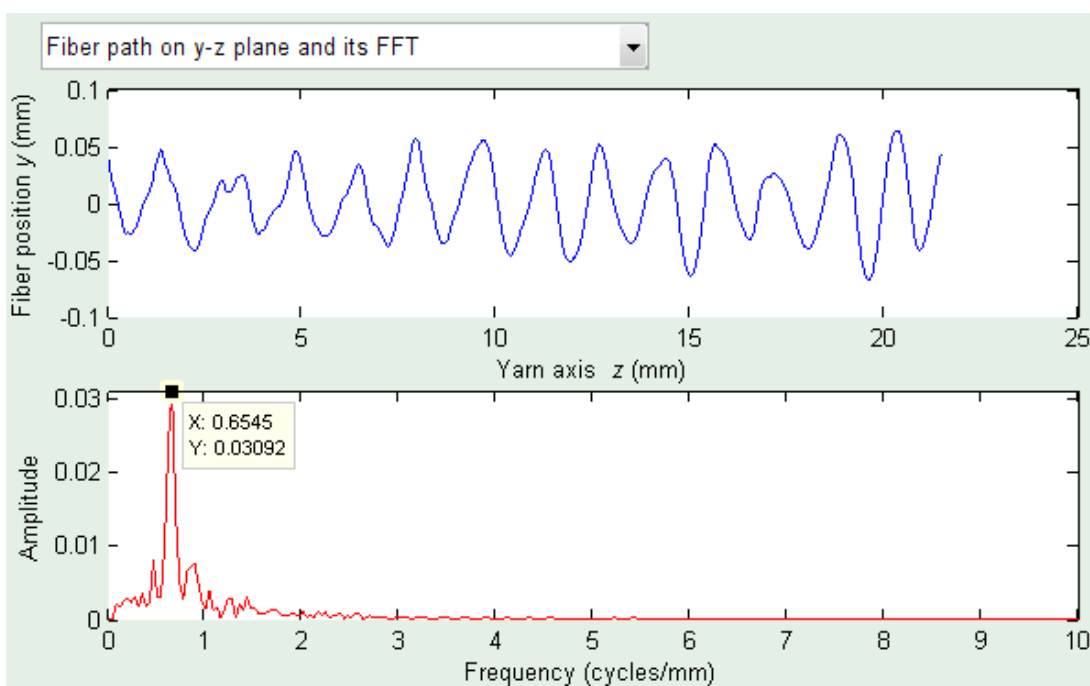
Figure 4.61 Fiber radial position and frequency-amplitude curve.

(2) Tracer fiber positions in xz and yz direction and their frequency analysis.

The results of tracer fiber position in xz and yz coordinates and their frequency results (FFT) can be calculated and shown in the [Figure 4.62](#). Fiber positions in $x-z$ and $y-z$ planes look similar, which is obviously different to the radial position in [Figure 4.61](#). As shown in the frequency-magnitude curves of $x-z$ and $y-z$ planes, they present a similar frequency distribution pattern with the largest peak at 0.6545 cycles/mm, which corresponds to the level of yarn twist. The obtained twist (654.5tpm) is close to the nominal twist (776tpm) and the difference is probably caused by fiber migrations inside the yarn.



(a) x-z plane



(b) y-z plane

Figure 4.62 2D fiber paths and their frequency-amplitude curve.

(3) Zonal distributions of individual fiber

Morton [159] proposed an analysis method of zonal distribution for individual fiber

to measure the irregularity of fiber migration by combining the effects of both frequency and amplitude. Figure 4.63(b) shows that the yarn is divided into five concentric zones with equal increments of radius. Figure 4.63(a) shows the projection of fiber trajectory in the x - y plane. It is noted that the movement of tracer fiber in this yarn sample is mainly between the second and fourth zone.

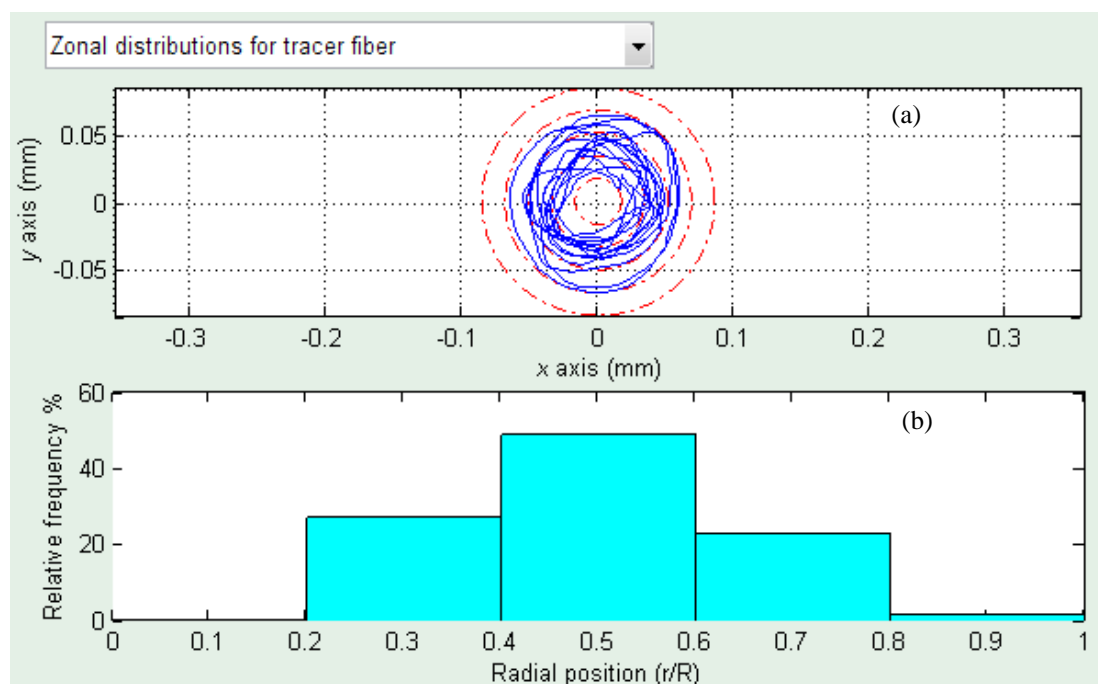


Figure 4.63 Zonal distribution of individual fiber

(4) Fiber spatial orientation angle

The orientation angle θ , which is the spatial angle between the yarn axis and the fiber segment, is defined as [44]:

$$\theta_i = \arccos \frac{z_{i+1} - z_i}{\sqrt{(x_{i+1} - x_i)^2 + (y_{i+1} - y_i)^2 + (z_{i+1} - z_i)^2}} \quad (4.39)$$

Figure 4.64(a) shows the fiber orientation angle of yarn sample. Figure 4.64(b) shows the relation of fiber orientation angle with radial position. For this yarn sample, the orientation angles are positive and they range from 0 and 25 degrees with a mean value of about 10 degrees.

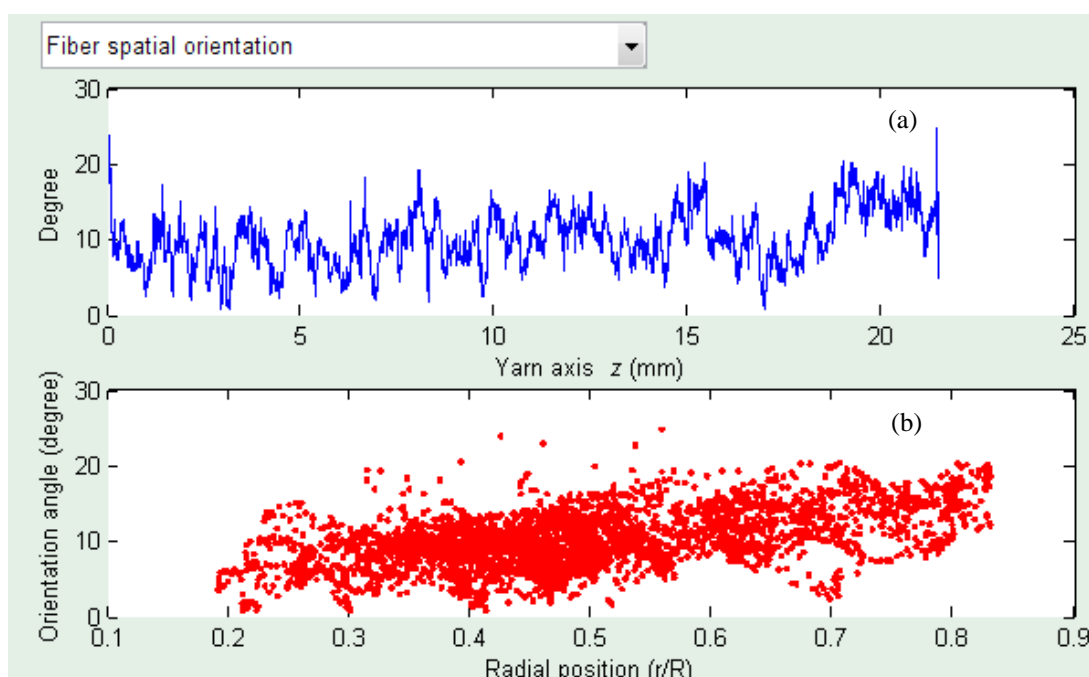


Figure 4.64 Fiber spatial orientation and the relation with radial position.

(5) Yarn diameter

Besides the previous migration results, the distribution of yarn diameter D (mean of D_x and D_y) along yarn axis and its histogram can be generated, as shown in Figure 4.65. The diameter of this sample ranges from 0.15mm to 0.2mm and concentrates between 0.15mm and 0.18mm, corresponding to the mean (0.1697mm) and CV of yarn diameter (5.1984%) shown in Figure 4.60.

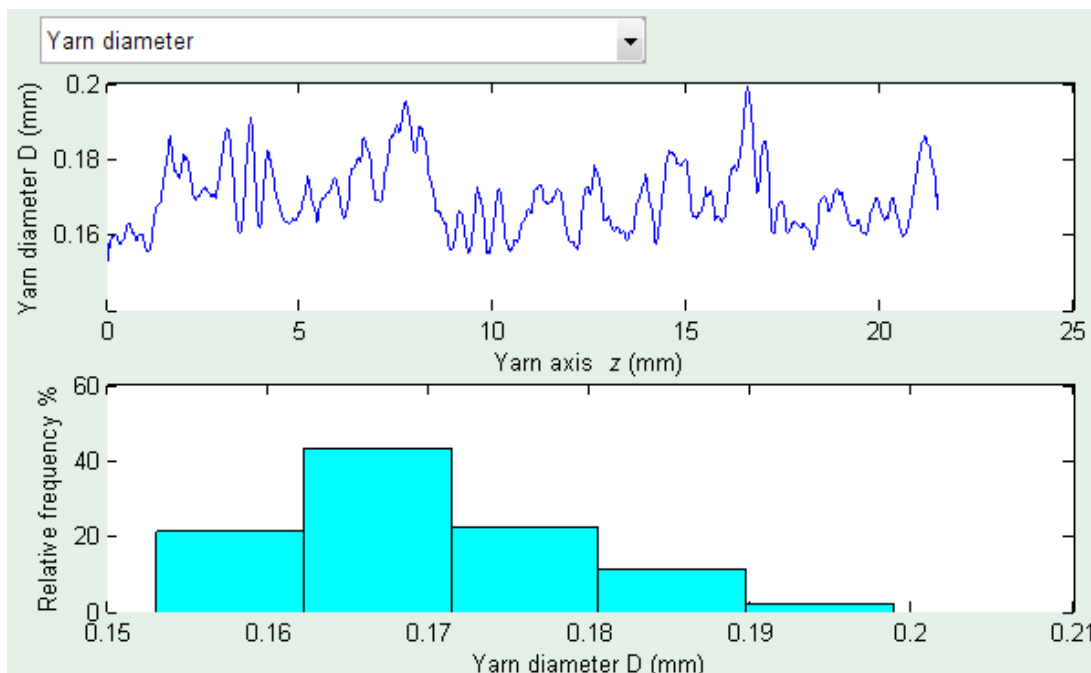


Figure 4.65 Yarn diameter and its histogram

Besides, as shown in Figure 4.66, menus are also designed on the top of interface to facilitate users' operation of the system, including (1) Main interface, (2) Images for module of *Image Acquisition*, (3) Panorama for module of *Image Mosaic*, (4) Segmentation for module of *Image Segmentation* and (5) Parameters for module of *Parameter Analysis*. In addition, various tools (see Figure 4.66) are also designed below the menu to zoom in, zoom out, pan and rotate the graph, as well as read data from the graph.

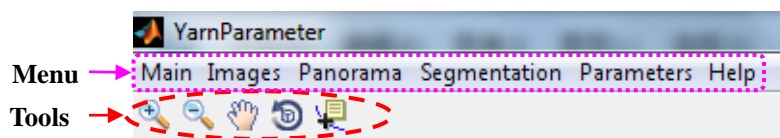


Figure 4.66 Manu and tools

4.8. Conclusions

This chapter presents an intelligent computer method and system for automatically stitching a series of consecutive images into a panoramic image and extracting yarn boundaries and tracer fiber for yarn structure and fiber migration studies. In the proposed computer method, a moving-window algorithm is proposed to reduce the noise in particular for eliminating the effect of yarn hairs. In image mosaic, various matching functions related to the tracer fiber and gradient image are extracted and combined into a decision function to identify the optimal stitching position in the horizontal direction. In tracer fiber detection, the 2D image is converted into a series of one-dimensional (1D) signal and the Pan-Tompkins algorithm is extended to detect the position points of the tracer fiber on these 1D signals. The image is then divided into two separate parts for stitching in the vertical direction to obtain the panorama by the continuity of the tracer fiber. In image segmentation, besides the proposed method for identification of tracer fiber, yarn boundaries are also extracted from binary image of the panorama. In this part, in order to eliminate the effect of the uneven light condition, the piecewise cubic Hermite interpolation method is employed to fit the background of image. Based on the results of yarn boundaries and tracer fibers detected from the panorama, 3D configurations of the yarn and tracer fiber can be reconstructed and various yarn structural parameters can be

further analyzed.

Moreover, an objective method is then proposed to evaluate the qualities of the image mosaic and segmentation of the proposed method. In this method, the qualities of the image mosaic and segmentation for a series of yarn images are evaluated by comparing the results with those obtained using the manual method. Furthermore, fifty series of tracer fiber images (total 872 images) at five different yarn counts (10Ne, 20ne, 30Ne, 40Ne and 60Ne) are prepared and used for a full evaluation of the proposed algorithms for the automatic image mosaic and image segmentation. The evaluation results show that the proposed computer method is generally in good agreement with the manual method. The mosaic and segmentation errors for all the fifty series of tracer fiber images are at a relatively low level. More specifically, the relative mosaic error in horizontal direction is smaller than that in vertical direction, and most vertical mosaic differences between the proposed method and manual method are just a few pixels. The relative segmentation error of detected tracer fiber (1%~3%) is smaller than that for yarn boundary (2%~8%). In addition, the comparison of time taken between the two methods demonstrates the high efficiency of the proposed computer method in the image mosaic and segmentation.

Finally, based on the proposed image processing method of image mosaic and segmentation, an intelligent image processing system has been developed to implement and control the whole process of tracer fiber measurement and analysis, including five modules of video acquisition, image acquisition, image mosaic, image segmentation and parameter analysis of yarn structure. In each corresponding module, important processing results can be visualized and the key parameters for image processing can be adjusted. The final results of yarn diameter and fiber migration behavior can be statistically analyzed and evaluated. The intelligent system developed in this study can be used for various textile researches, such as analysis of yarn structural characteristics developed by an innovative spinning method, investigation of effect of spinning parameters on yarn structures, and exploration of mechanism for the yarn structure-property relationship.

Chapter 5 Intelligent Method and System for Yarn Surface Grading based on Digital Blackboard Images

5.1. Introduction

According to ASTM D2255, with the consideration of yarn unevenness, fuzziness, neppiness and visible foreign matter, human visual inspection is adopted for the evaluation of yarn surface appearance, which is, however, subjective, time consuming and sometimes inconsistent. As revealed in the chapter of literature review, although some methods have been developed for objective evaluation of yarn surface quality, most of them are based on the mechanism similar to the Uster Tester and depart from the originality of the visual grading method carried out on black boards (ASTM D2255), namely the comparison among adjacent yarn segments and the identification of other important yarn appearance features, such as yarn color variation, foreign matters and hairiness, being ignored.

Therefore, in this chapter, a computerized evaluation method and system will be developed for the objective and intelligent evaluation of yarn surface appearance based on multi-scale attention model. The proposed method will fully imitate human visual behavior in the inspection and visual appraisal of yarn segments on a

blackboard. In the developed method, digital yarn images will be acquired from yarn board samples by scanning. Then yarn board image will be segmented into yarn body and yarn hairs by Fourier transform for extracting the features of yarn regularity and fuzziness. Moreover, the conspicuity and saliency map of yarn board image will be generated by a proposed multi-scale attention model. Finally, the yarn surface characteristic features extracted from yarn conspicuity, regularity and hairiness are incorporated as an input for a Probabilistic Neural Network (PNN) to classify and grade yarn surface qualities. Finally, based on the proposed method, an integrated system is designed and developed to visualize and control the whole progress of the image processing and yarn classification.

5.2. Methodology

Figure 5.1 shows the proposed computer method for yarn surface grading. It mainly consists of four modules, including image acquisition, image processing, feature extraction and yarn classification. In Figure 5.1, digital yarn image is acquired from the prepared yarn board sample by digital scanning. Then three digital and computational methods, including Fourier transform (FFT), attention model and multi-scale model, are used for image processing and feature extraction. More specifically, Fourier analysis is employed for extracting yarn body and hairs,

and the multi-scale attention models are used to detect saliency objects at different observation distances. All digital features will be finally extracted and used as input to Probabilistic Neural Network (PNN) for yarn surface classification.

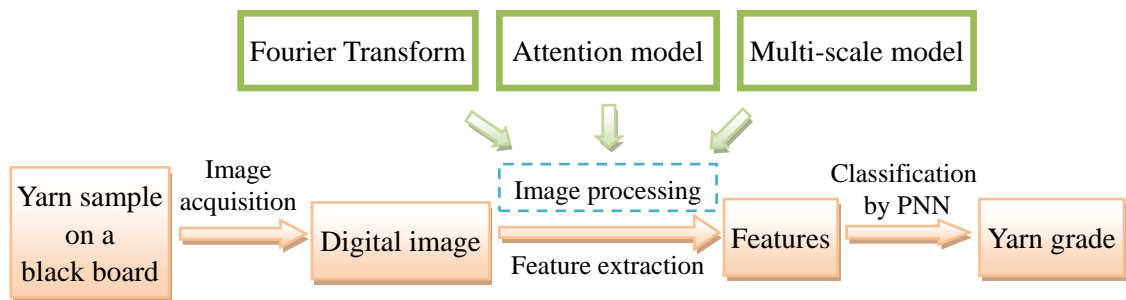


Figure 5.1 Proposed computer method for yarn grading.

5.2.1. Fourier analysis and filtering

Two-dimensional Fourier transform can be employed to transform images between spatial domain and frequency domain. Assuming an image has a size of $N \times N$, the two-dimensional discrete Fourier transform (2-D DFT) can be expressed by

$$F(u, v) = \frac{1}{N} \sum_{r=0}^{N-1} \sum_{c=0}^{N-1} I(r, c) e^{-j2\pi(ur+vc)/N} \quad (5.1)$$

where $I(r, c)$ is the projection of image, u and v are the frequency domain variables, and $F(u, v)$ is the corresponding transform coefficients.

In the frequency domain of FFT, high frequency corresponds to the rapidly changing brightness of an image, whereas low frequency information is related to the slowly

changing brightness. And the zero frequency (DC term) represents the average brightness of the image. Figure 5.2 shows an example of Fourier transform of two different periodic structures. In Figure 5.2, (a) and (b) show two objects with vertical and horizontal periodic patterns, and their corresponding amplitude spectrums of Fourier transform are shown in Figure 5.2(c) and (d), respectively. It can be noted that the two periodic patterns are well differentiated and recognized in the frequency domain of FFT by the horizontally and vertically distributed main frequency components in Figure 5.2(c) and (d), respectively.

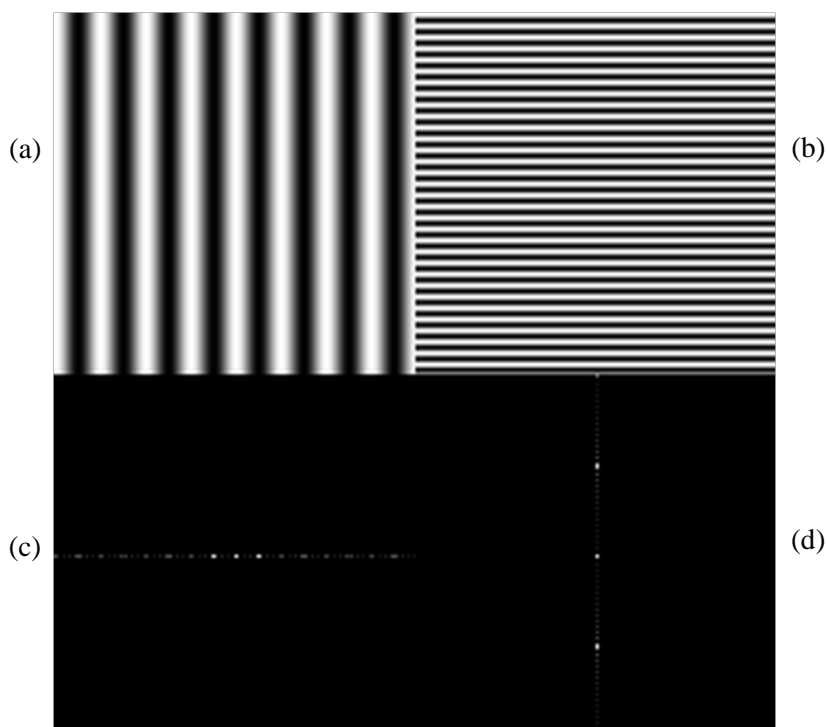
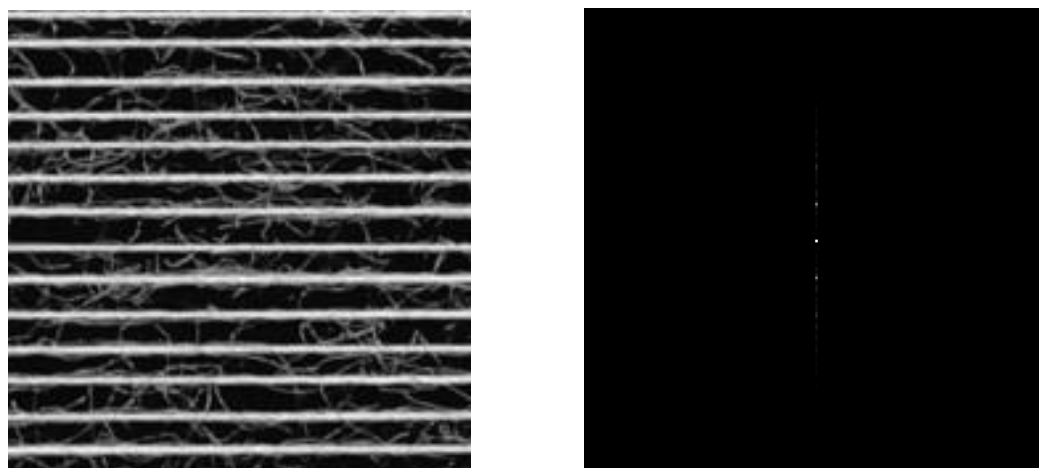


Figure 5.2 Fourier transform of vertical and horizontal periodic structures [160].

Top is the original object and bottom is corresponding Fourier transform (amplitude).

Figure 5.3 (a) shows a part of a yarn board image with a regular periodic pattern. It is similar to the object structure shown in Figure 5.2 (b), but presents a lot of the protruding yarn hairs. The amplitude of Fourier transform in the frequency domain is shown in Figure 5.3 (b). As expected, it shows a similar distribution pattern with Figure 5.2 (d). Therefore, FFT can reflect, to some extent, the periodic distribution pattern of yarn segments on the blackboard, and thus is potentially useful for analysis of yarn board image in this study.



(a) a part of yarn board image

(b) amplitude of Fourier transform of (a)

Figure 5.3 Amplitude of yarn board image in frequency domain.

As shown in Figure 5.3 (b), the main frequency components are distributed in the vertical direction. The maximum amplitude of Fourier transform in each row can be extracted to generate a one-dimensional distribution of frequency components. Figure 5.4 shows two examples of one-dimensional distribution of frequency domain for 60Ne yarn board images with two different grades (B+ and D+).

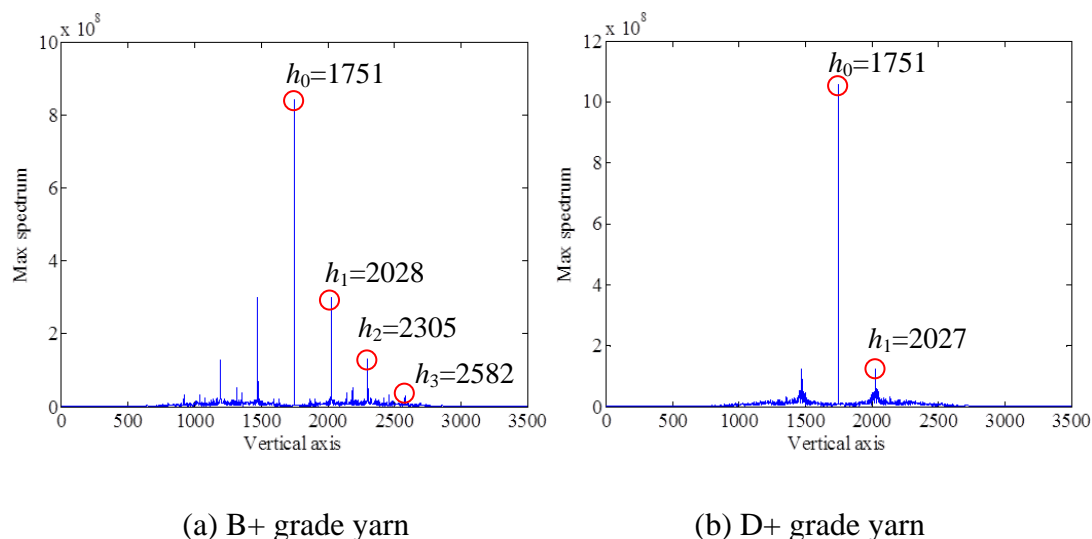


Figure 5.4 Maximum amplitude of yarn board image in frequency domain.

In Figure 5.4, the highest peak h_0 presents the mean brightness of the image and the second largest peak h_1 indicates the frequency of yarn wraps. Although their amplitudes are different (about 3×10^8 for B+, about 1×10^8 for D+), the frequencies of h_1 for these two images are similar (2028 for B+ grade yarn image and 2027 for D+ grade yarn image). With the frequency of h_1 , we can calculate:

$$\text{B+ yarn: } \frac{(h_1 - h_0) \times \text{image resolution}}{\text{image height}} = \frac{(2028 - 1751) \times 500}{3500} = 39.6 \text{ wraps per inch}$$

$$\text{D+ yarn: } \frac{(h_1 - h_0) \times \text{image resolution}}{\text{image height}} = \frac{(2027 - 1751) \times 500}{3500} = 39.4 \text{ wraps per inch}$$

where zero frequency h_0 is 1751 (pixel), image resolution is 500 (dpi) and image height is 3500 (pixel) in this study.

Wrapping frequency of the two yarn samples shown in [Figure 5.4](#) is 40 wraps per inch, so h_1 matches well with the real wrapping frequency of yarn. In [Figure 5.4 \(a\)](#), h_2 and h_3 of the B+ yarn image are the second and third harmonic of wrapping frequency h_1 , respectively. However, for the low-quality yarn in [Figure 5.4 \(b\)](#), there is no obvious harmonic of h_1 .

As shown in [Figure 5.3 \(a\)](#), yarn board image mainly contains three elements of yarn body, yarn hairs and blackboard. Yarn body possesses a low-frequency distribution while yarn hairs present high-frequency components in the FFT spectrum. In order to separate the yarn body from hairs, a Butterworth low-pass filter (BLPF) will be employed in this study, which can be defined:

$$H(u, v) = \frac{1}{1 + [D(u, v)/D_0]^{2n}} \quad (5.2)$$

where $D(u, v)$ is the distance of a point (u, v) from the origin in frequency domain, D_0 is a distance of the point of cut-off frequency from origin, and n is the order of a Butterworth low-pass filter (BLPF).

Moreover, the Fourier transform of an image can be inverted back to the spatial domain by [Equation \(5.3\)](#) for further processing of yarn image segmentation.

$$F^{-1}[F(u, v)] = I(r, c) = \frac{1}{N} \sum_{u=0}^{N-1} \sum_{v=0}^{N-1} F(u, v) e^{j2\pi(ur+vc)/N} \quad (5.3)$$

Based on the above processing of Fourier transform, low-pass filtering and inverse Fourier transform, the yarn board image can be separated into images of yarn body and hairiness, and then the statistical features can be extracted from yarn diameter and hairs for further analysis. The extraction strategy is shown in Figure 5.5. Seven features will be extracted from yarn body image and one feature is extracted from yarn hairiness image. The meanings of these features are listed in Table 5.1.

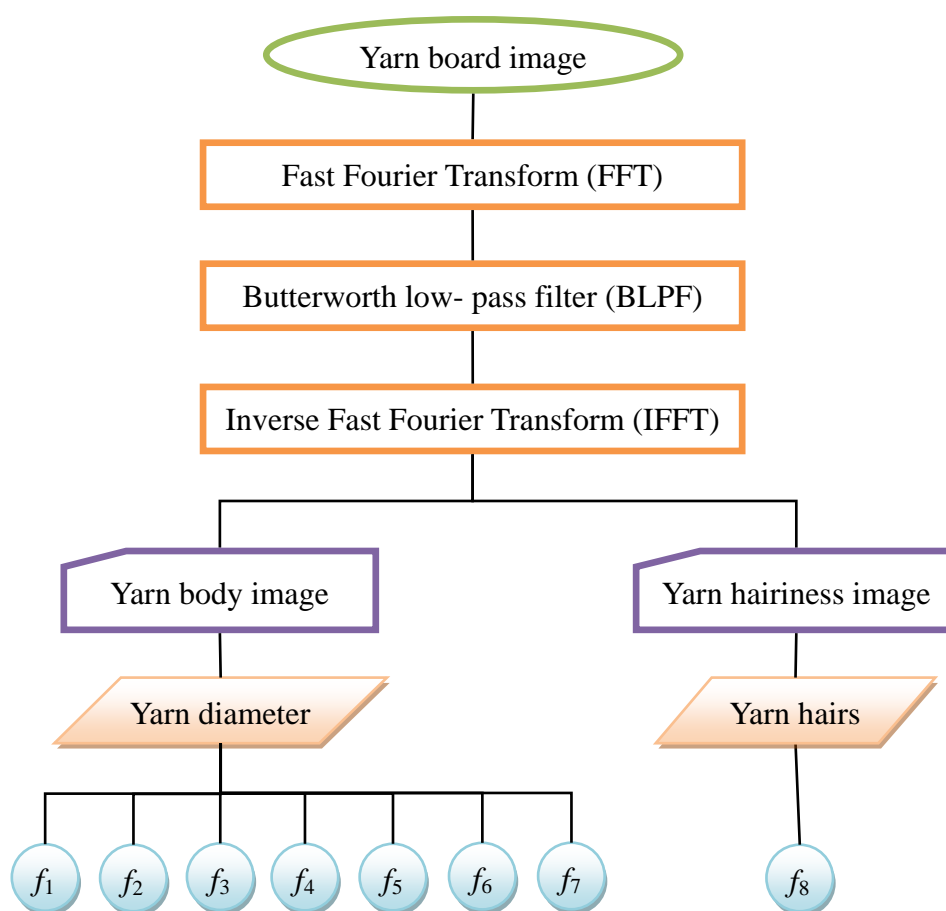


Figure 5.5 Proposed strategy for feature extractions of yarn diameter and hairs.

Table 5.1 Features and their meanings

Feature	Meaning
f_1 :	Mean of yarn diameter
f_2 :	CV of yarn diameter
f_3 :	Percentage of yarn diameter larger than 150% of mean (thick places)
f_4 :	Percentage of yarn diameter smaller than 50% of mean (thin places)
f_5 :	Percentage of yarn diameter larger than 300% of mean (neps)
f_6 :	Skewness of yarn diameter
f_7 :	Kurtosis of yarn diameter
f_8 :	Entropy of yarn hairiness image

5.2.2. Multi-scale information

It is a common knowledge that the view of an object appears to be different when observed at different observation distances. The details of the object will become clearer when observed at a closer distance. [Figure 5.6](#) shows the relation between the size of retinal image and the observation location. In [Figure 5.6](#), H is an object, l_1 and l_2 are its retinal images at different observation distances d_1 and d_2 , and f is the distance from the nodal point to the retina in a typical human eye, which is assumed to be a constant. According to trigonometry, the size of retinal image can be determined by:

$$\frac{l_1}{H} = \frac{f}{d_1} \quad \text{and} \quad \frac{l_2}{H} = \frac{f}{d_2} \quad (5.4)$$

So, the relationship of retinal images l_1 and l_2 of the object H observed at d_1 and d_2 can be obtained as

$$\frac{l_1}{l_2} = \frac{d_2}{d_1} \quad (5.5)$$

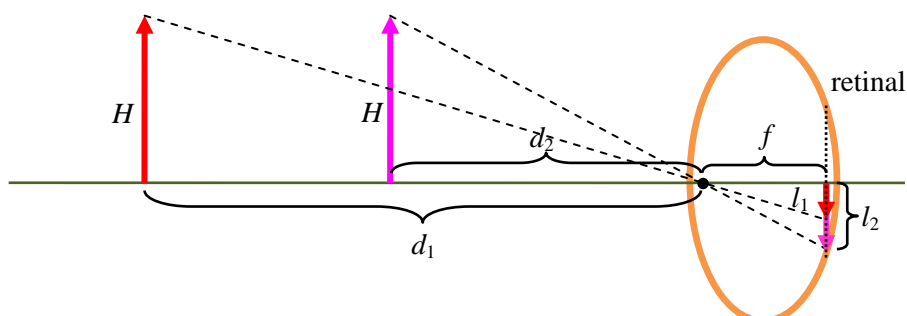


Figure 5.6. Retinal image of an object at different observation locations.

In order to imitate human visual behavior, we will use different resolutions (in DPI) of digital image to represent the retinal image observed at different distances. For constant neuron in the retina, a larger retinal image will indicate a clearer object or a higher image resolution. Assuming the size of retinal image l is proportional to the image resolution p , we can have:

$$\frac{l_1}{l_2} = \frac{p_1}{p_2} \quad (5.6)$$

Combining [Equations \(5.5\)](#) and [\(5.6\)](#), the relationship between the observation

distance and image resolution should be:

$$\frac{d_1}{d_2} = \frac{p_2}{p_1} \quad (5.7)$$

Hence, the distance of observation is in inverse proportion to the image resolution.

In other words, a shorter observation distance is corresponding to a higher resolution of the image, and vice versa. [Figure 5.7 \(a\)](#) shows a view of yarn board image with

high resolution, corresponding to a close observation distance. The details of yarn, such as yarn body, yarn hairs and foreign fiber, can be clearly observed. [Figure 5.7](#)

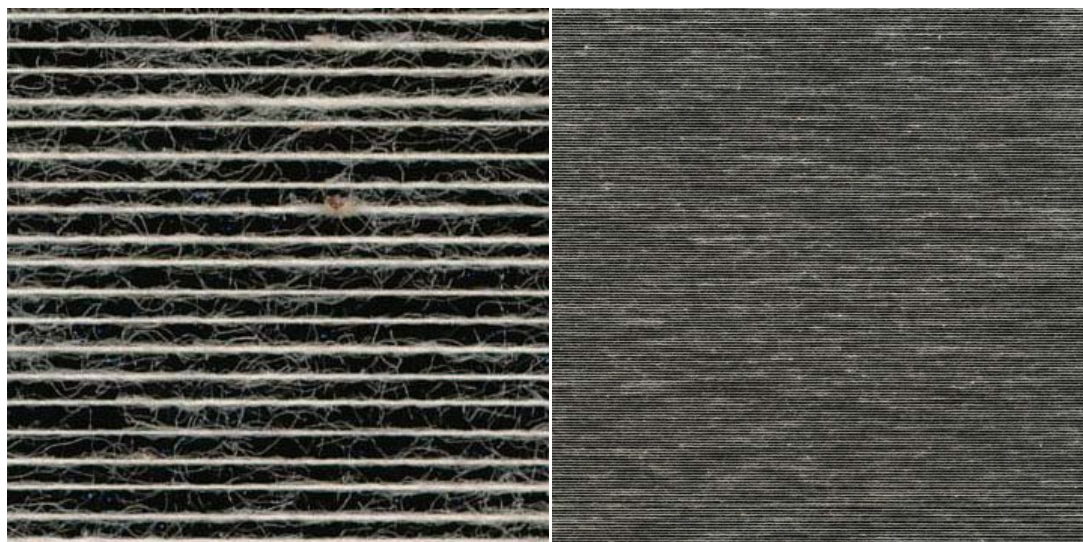
[\(b\)](#) shows the whole board image in a low resolution, corresponding to a relatively far observation distance. Though the details of yarn are not clear, several regions apparently attract our attention, which may consist of neps and thick places of yarn.

Therefore, in yarn surface grading, both low-resolution and high-resolution information are valuable for yarn classification. In this study, a two-scale model

(i.e. low-resolution, high-resolution) will be proposed in order for a complete and accurate yarn classification. Likewise, the concept and model can be also applied

to more number of scales (e.g. three- or four- scale) by adopting different observation distances or image resolutions. Therefore, it will be generally defined

as multi-scale model in this study.



(a) high resolution

(b) low resolution

Figure 5.7 Yarn board image with different resolutions.

In this study, the yarn board will be observed at two different distances: Scale 1 at the observation distance of 1m, and Scale 2 at the least distance of human distinct vision, 0.25m. [Figure 5.8](#) shows the relation of visual distance and resolution. In [Figure 5.8](#), h is the object with two pitch/points at its ends, d is viewing distance and α is visual angle of human eye. According to [Figure 5.8](#), the relation between observation distance d and image resolution P can be formulated as [161]:

$$P = \frac{1}{h} = \frac{1}{2 \times d \times \tan \frac{\alpha}{2}} \quad (5.8)$$

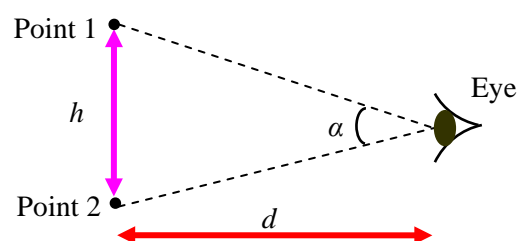


Figure 5.8 Visual distance and resolution.

Generally, the minimum distinct angle of the human eye is about 1' (minute of arc, or 1/60 of a degree) [161], and the least distance of distinct vision for normal eye is 0.25m [162]. Accordingly, the resolution p_1 for the minimum angle (1') in Scale 2 can be calculated as:

$$p_1 = \frac{1}{2 \times 0.25 \times \tan\left(\frac{1}{2} \times \frac{1}{60}\right)} = 13751 \text{ dot per meter} = 349 \text{ dot per inch (DPI)} \quad (5.9)$$

For the observation distance of 1m, the resolution p_2 of minimum angle (1') in Scale 1 can be calculated as:

$$p_2 = \frac{1}{2 \times 1 \times \tan\left(\frac{1}{2} \times \frac{1}{60}\right)} = 3438 \text{ dot per meter} = 87 \text{ dot per inch (DPI)} \quad (5.10)$$

Table 5.2 shows the relationship of observation distance and image resolution.

According to Equations (5.9) and (5.10), the calculated resolutions of two scales are 87dpi for 1m (Scale 1) and 349dpi for 0.25m (Scale 2) respectively. In this study, the approximative resolutions of 100dpi for 1m (Scale 1) and 300dpi for 0.25m (Scale 2), are, therefore, used to analyze yarn image on the black board.

Table 5.2 The observation distance and image resolution.

Scale	Observation distance (m)	Image resolution (dpi)	
		calculated value	adopted value in this study
Scale 1	1	87	100
Scale 2	0.25	349	300

Figure 5.9 shows the proposed strategy of feature extraction based on multi-scale information. Two attention models: SR model and AIM model will be used to analyze the yarn board image in Scale 1 and Scale 2, respectively. Eight features will be extracted from saliency value and saliency region for yarn classification.

The meanings of the eight features are listed in Table 5.3.

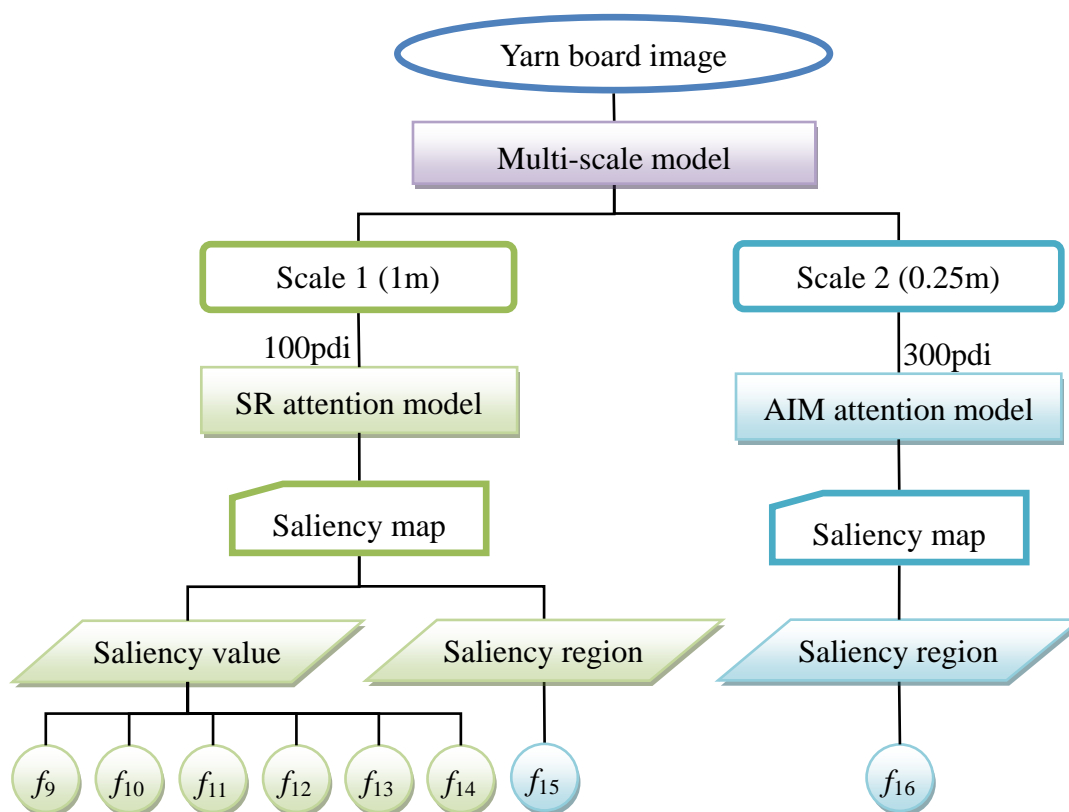


Figure 5.9 Proposed strategy for feature extractions from saliency value and region.

Table 5.3 Features and their meanings

Feature	Meaning
f_9 :	Mean of saliency value in scale 1
f_{10} :	Standard deviation of saliency value in scale 1
f_{11} :	Third-order moment of saliency value in scale 1
f_{12} :	Interquartile range (IQR) of saliency value in scale 1
f_{13} :	50 th percentile of saliency value in scale 1
f_{14} :	95 th percentile of saliency value in scale 1
f_{15} :	Mean of relative CV of diameter in saliency regions of scale 1 (SR)
f_{16} :	Mean of relative CV of diameter in saliency regions of scale 2 (AIM)

5.2.3. Extended spectral residual (SR) approach

In order to obtain large regions of yarn fault, the yarn image $I(x)$ is blurred to form an input image $I_b(x)$ by using a circular averaging filter $h_b(x)$.

$$I_b(x) = I(x) \times h_b(x) \quad (5.11)$$

Then, the log spectrum $L_b(f)$ of the blur image $I_b(x)$ can be written as

$$L_b(f) = \log(R(F[I_b(x)])) \quad (5.12)$$

where F denotes the Fourier transform and $R(F[I_b(x)])$ is the amplitude of $I_b(x)$.

In the SR method [125] mentioned in Section 2.3.2.1, the log spectrum $L(f)$ (in

Equation (2.21)) of each image $I(x)$ is smoothed and used as a benchmark for the measurement of image conspicuity or saliency. However, for yarn evaluation considered in this study, this kind of individual benchmarks is not appropriate because yarn of different qualities cannot be differentiated as the smoothed log spectrum is different for each image. Therefore, a general or standardized log spectrum or benchmark is needed in order for a comparison among the yarns with different qualities. Supposing $I_i(x)$ is the i^{th} image of the same yarn count with different qualities (A, B+, B, C+, C, D+, D and D-), the average log spectrum of these images can be calculated as

$$A(f) = \frac{1}{N} \sum_{i=1}^N \log(A_i(f)) = \frac{1}{N} \sum_{i=1}^N \log(R(F[I_i(x)])) \quad (5.13)$$

where $A_i(f)$ is the amplitude of the i^{th} image $I_i(x)$ in the database with N images.

Then the average log spectrum $A(f)$ can be smoothed and defined as the generalized log spectrum $A'(f)$:

$$A'(f) = h_n(f) \times A(f) \quad (5.14)$$

where $h_n(f)$ is an average filter with a $n \times n$ matrix.

Based on the benchmark $A'(f)$, the spectral residual $R_s(f)$ of image can be obtained by

$$R_s(f) = L_b(f) - A'(f) \quad (5.15)$$

Correspondingly, the image residual $R_I(x)$ can be formulated by transforming spectral residual back to spatial domain:

$$R_I(x) = F^{-1}[\exp(R_s(f) + \Im(F[I_b(x)]))]^2 \quad (5.16)$$

where F^{-1} denotes the inverse Fourier transform and $\Im(F[I_b(x)])$ is phase spectrum of image $I_b(x)$.

Further, the image residual indicates the conspicuity of the image. Since the quality of A-grade yarn is the best and the qualities for the others are progressively lower, yarn samples with more conspicuity (larger difference) will be assigned to a lower grade.

Finally, the saliency map $S(x)$ can be obtained by applying a series of Gaussian filter $g(x)$ to image residual $R_I(x)$:

$$S(x) = g(x) \times R_I(x) \quad (5.17)$$

5.2.4. Attention based on information maximization (AIM model)

As for AIM model [130] mentioned in [Section 2.3.2.1](#), the structure of AIM model

exhibits considerable agreement with the organization of human visual system [130].

With consideration of the definition of context, AIM can compute the saliency on the entire color image. It is suitable to be used in large-scale and high-resolution image for detecting the detailed information of yarn board image, and especially, it is sensitive to color visible fiber. Hence, in this study, AIM method will be employed to generate saliency map of detailed yarn information in Scale 2 (observed at 0.25m, image resolution of 300dpi) for multi-scale detection.

5.2.5. Probabilistic Neural Networks (PNNs)

Probabilistic neural network (PNN), as a kind of radial basis function networks (RBF), was originally proposed by Specht [163-164]. For the characteristics of simplicity and efficiency, PNN is particularly suitable for multiple-class classification problems [165]. Figure 5.10 shows the architecture of probabilistic neural network [166]. On receiving a pattern x from the input layer, the neuron x_{ij} of the pattern layer computes its output:

$$\phi_{ij}(x) = \frac{1}{(2\pi)^{d/2} \sigma^d} \exp\left[-\frac{(x - x_{ij})^T (x - x_{ij})}{2\sigma^2}\right] \quad (5.18)$$

where d denotes the dimension of the pattern vector x , σ is the smoothing parameter, and x_{ij} is the neuron vector.

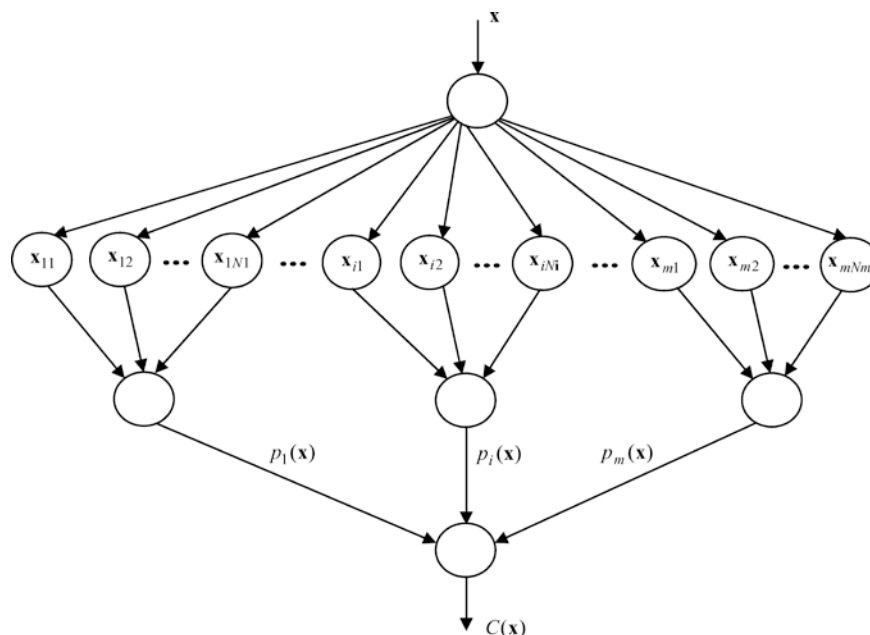


Figure 5.10 Architecture of probabilistic neural network (PNN) [166].

In this study, the PNN provided in MathWorks MATLAB software is employed to classify the yarn surface appearance. The following syntax is used to design a probabilistic neural network in MATLAB:

$$\text{net} = \text{newpnn}(P, T, \text{spread}) \quad (5.19)$$

where P is $R \times Q$ matrix of Q input vectors, T is $S \times Q$ matrix of Q target class vectors and spread is the spread of radial basis functions (the first-layer biases are all set to $0.8326/\text{spread}$, resulting in radial basis functions that cross 0.5 at weighted inputs of $\pm \text{spread}$).

The architecture of probabilistic neural network in Matlab is shown in [Figure 5.11](#).

It consists of three layers of an input layer, a hidden layer (Radial basis layer) and an

output layer (Competitive layer). When an input is presented, the first layer computes distances from the input vector to the training input vectors, and then produces a vector whose elements indicate how close the input is to a training input. The second layer sums these contributions for each class of inputs to produce a vector of probabilities. Finally, a compete transfer function on the output of the second layer picks the maximum of these probabilities, and then produces 1 for that class and 0 for the other classes. [167]

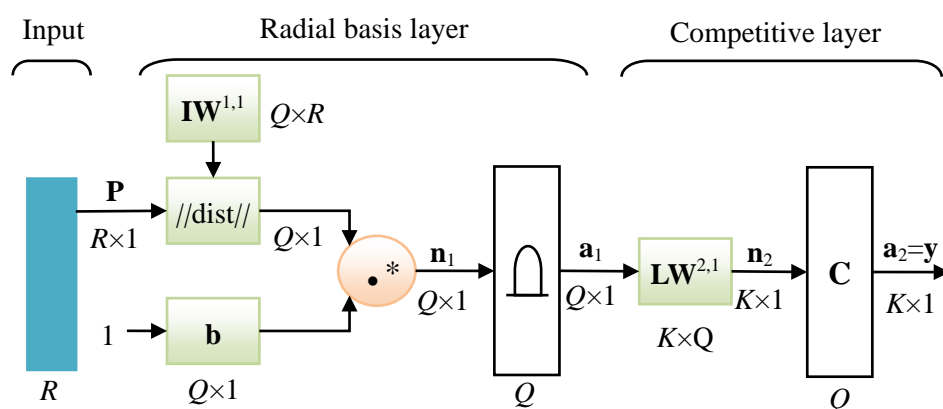


Figure 5.11 Architecture of probabilistic neural network (PNN) in Matlab. [167]

where R is number of element in input vector, Q is number of input/target pairs (number of neurons in Radial basis layer), $IW^{1,1}$ is input weights of first layer, $\|dist\|$ is the Euclidean distance weight function, b is bias vector, $LW^{1,2}$ is the second-layer weights, $\mathbf{a}_1 = e^{-n_1^2}$, \square is competitive transfer function for calculating a layer's output from its net input, and K is number of classes in input data (number of neurons in Competitive layer).

5.3. Implementation

In this section, the methodology and working principle of the proposed method will

be described. The yarn diameter, yarn hairiness, spectral residual map and multi-scale saliency regions will be formulated from the original yarn board image. Then the statistical features of all the yarn samples will be extracted and used as input of PNN to classify the grades of yarn surface appearance.

5.3.1. Segmentation of yarn body and hairs

5.3.1.1. Image processing

Yarn evenness or regularity is an important measure for yarn quality, which can be defined as the variation in weight or the variation in thickness per unit length of the yarn [168]. It is one of the most important features for yarn surface grading. Therefore, in this study, yarn body will be identified and extracted from the yarn board image for formulating statistical measures of yarn evenness. Besides, yarn hairiness image will also be obtained by removing the yarn body from the original image for formulating statistical measures of fuzziness. The main steps for the segmentation of yarn board image are described in Figure 5.12.

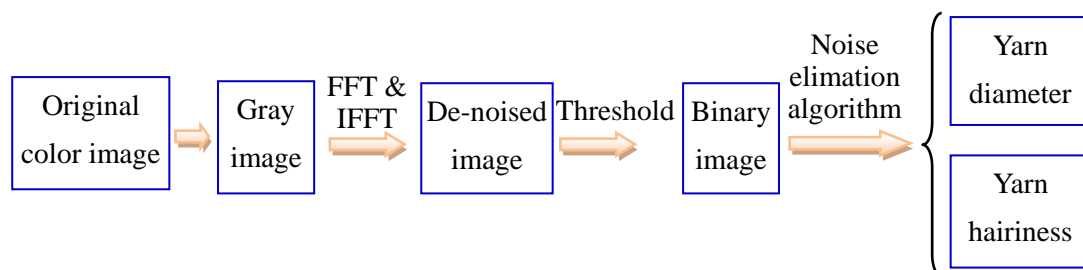
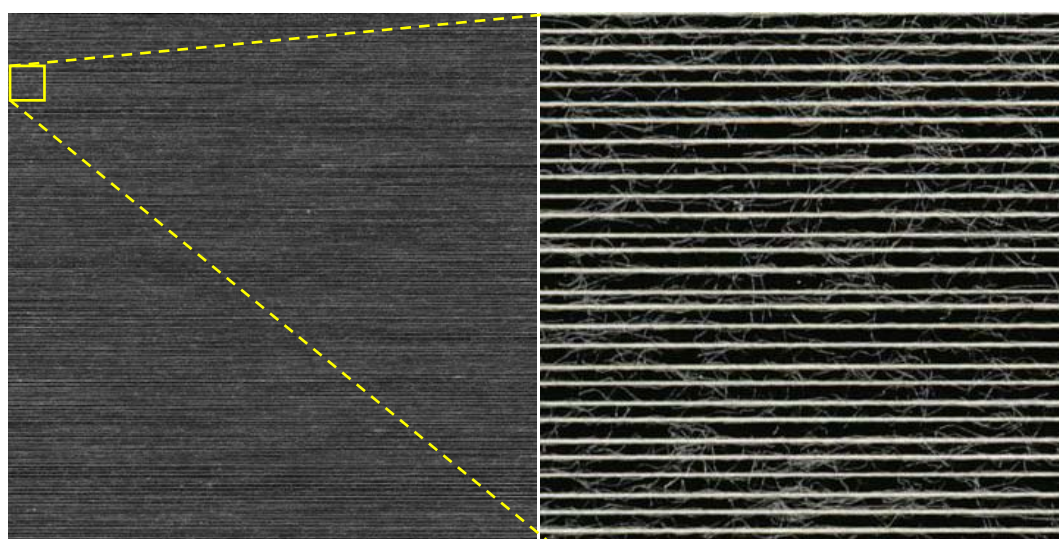


Figure 5.12 Steps for the segmentation of yarn board image.

Figure 5.13(a) shows an example of 60Ne yarn board image with a size of 7×7 inches (49 inch²). In order to demonstrate the working principle of the proposed processing method, a small part of Figure 5.13(a) is extracted and employed for yarn segmentation, as shown in Figure 5.13(b). It can be noted that the image contains a number of parallel yarn bodies, black background and randomly distributed yarn hairs. In order to extract yarn body, the hairs has to be completely removed. It is a challenging task because the hairs are not only large in number but also present a random distribution. For doing this, as shown in Figure 5.12, the original color image of yarn board needs to be converted to gray image for further processing.



(a) a 60Ne yarn board image

(b) a magnified local view of Figure 5.13(a)

Figure 5.13 Example of yarn board image.

The Fast Fourier transform (FFT) will be used to remove the majority of yarn hairs by transforming the gray image to the frequency domain. Figure 5.14(a) shows the

log spectrum image of Figure 5.13(b). It appears to be a 3D distribution with low frequency components composed of yarn bodies and background and high frequency related to yarn hairiness. Therefore, yarn hairiness can be removed by a low pass filter. In this study, Butterworth low pass filter (at $D_0=0.7$, $n=5$) is employed to delete the effect of high-frequency terms and the resultant log spectrum is shown in Figure 5.14(b). After that, the resultant log spectrum is transformed back to the spatial domain for constructing a de-noised image of Figure 5.13(b), as shown in Figure 5.15 (a). Compared to the original image, the brightness of the image after FFT analysis is decreased, and the image is blurry and contains less hairiness. In order to extract yarn body, the de-noised image should be further converted to a binary image. Figure 5.15 (b) shows a histogram of Figure 5.15 (a), which shows a global threshold is suitable to convert the de-noised image to a binary image.

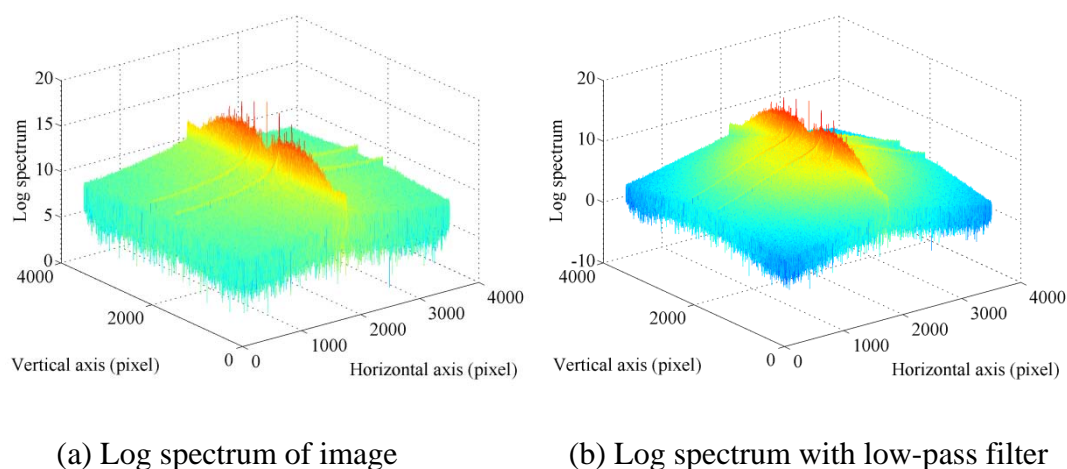


Figure 5.14 Yarn board image in frequency domain by FFT.

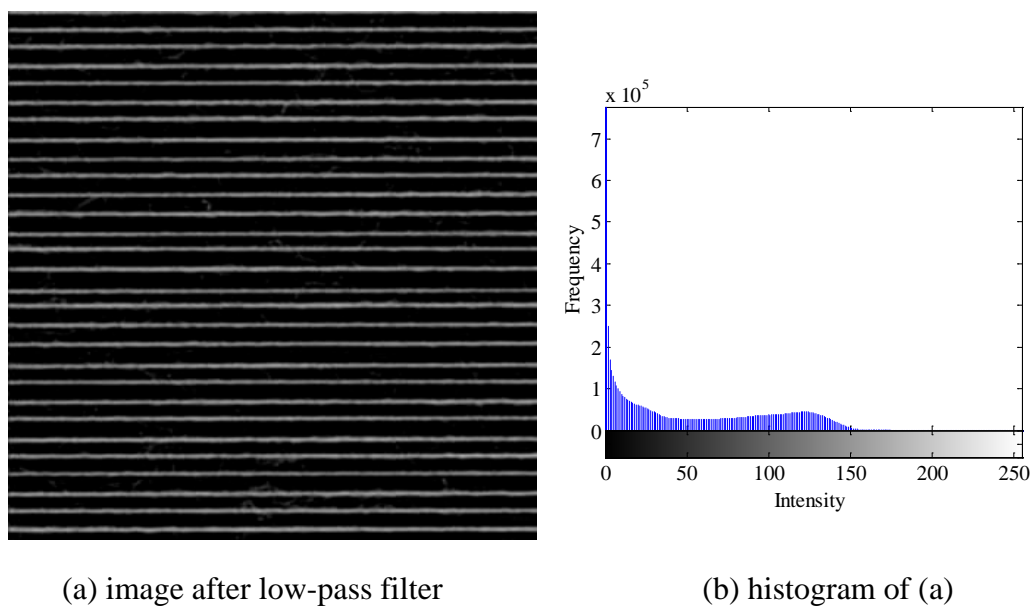


Figure 5.15 De-noised image using FFT and BLPF.

In this study, the Otsu's method is used for this purpose and the resultant binary image is shown in Figure 5.16. As shown in Figure 5.16, though majority hairs of original image are eliminated, there are still many individual yarn hairs which cannot be removed by FFT-IFFT processing.

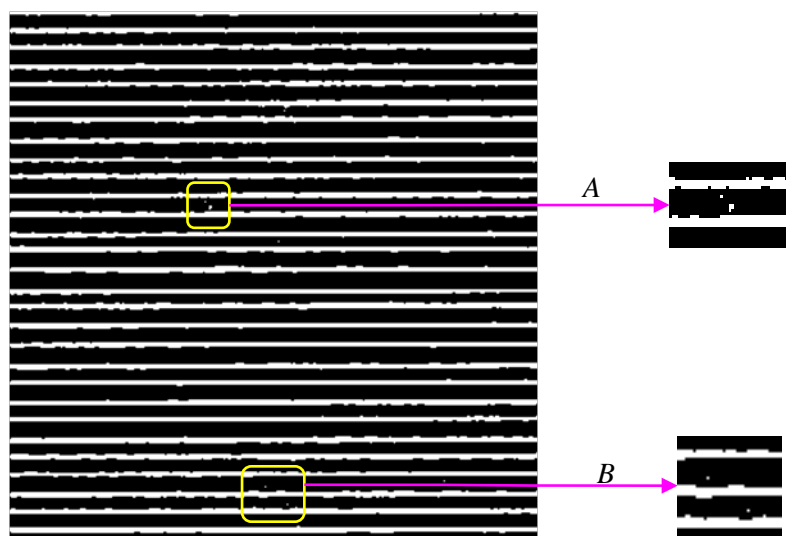


Figure 5.16 Binary image.

In order to completely remove the remaining hairs and other noises, a connected components labeling algorithm is employed. All the connected components of white pixels in the binary image are labeled and the size of each connected component is computed [96]. Since the size of the yarn body is much larger than those of the noises, the connected components with the larger size than width of image are treated as the yarn body, and the other connected components are eliminated. The final binary image of yarn body can be obtained, as shown in [Figure 5.17 \(a\)](#). Besides, the hairiness could be obtained by deleting the yarn body from the original image, as shown in [Figure 5.17 \(b\)](#).

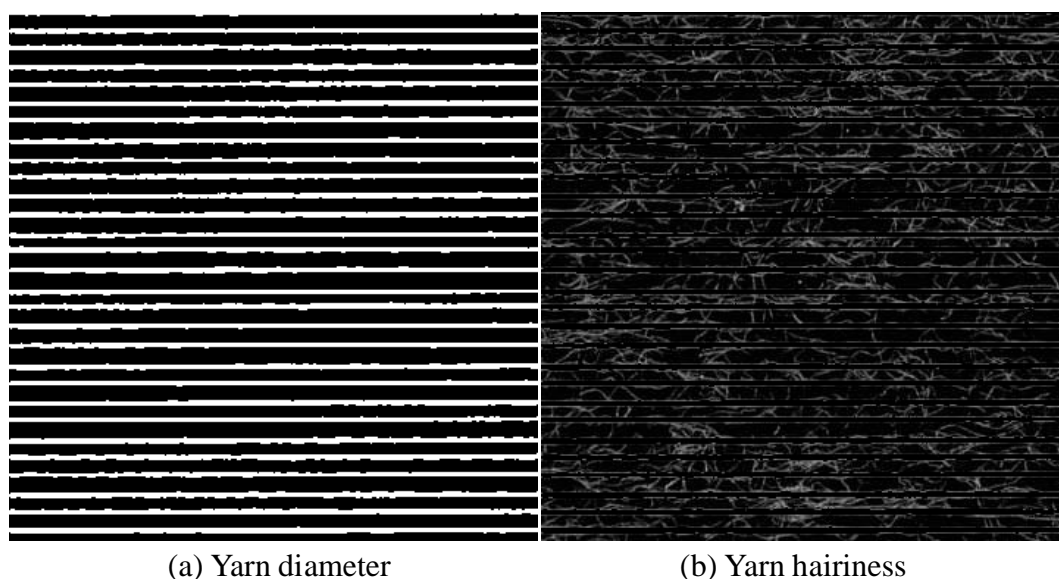


Figure 5.17 Separated yarn board image

Based on [Figure 5.17 \(a\)](#), yarn boundaries can be easily identified, as shown in [Figure 5.18\(a\)](#). Accordingly, diameter of all yarn bodies can be calculated and its

histogram is shown in Figure 5.18(b). It can be noted that the diameter of the yarn samples ranges from 1 pixel to 12 pixels. The yarn diameter is mostly concentrated between 2 and 5 pixels (99.9654% of all), with a mean diameter of about 3 pixels.

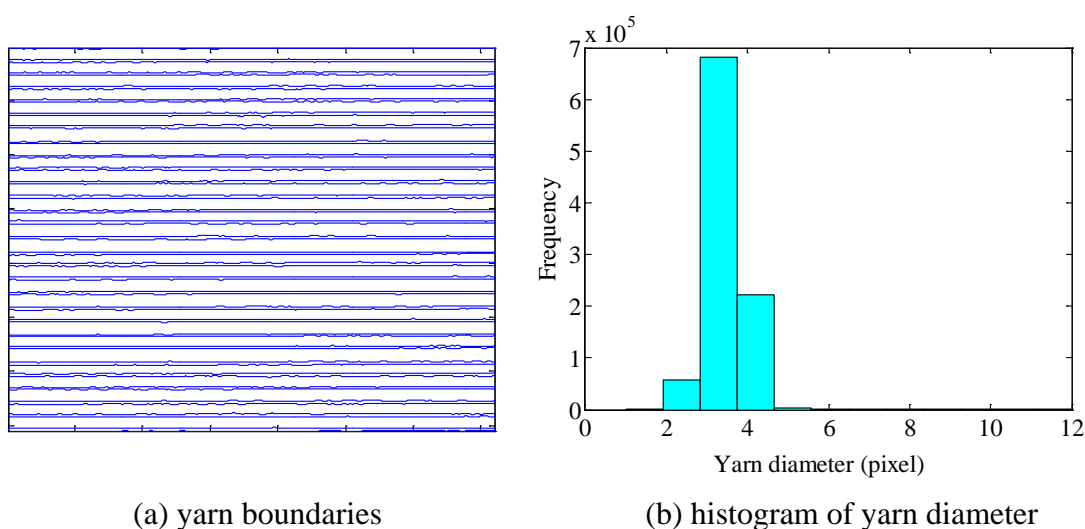


Figure 5.18 Histogram of yarn diameter.

5.3.1.2. Feature extraction

In yarn surface grading, there are six series of photographic standard used for evaluating different yarn counts and each yarn count sample should be evaluated with respect to its own photograph standard. Therefore, yarn count is considered as an important feature for yarn grading in the proposed computer method. Based on the results in Section 5.3.1.1, the mean value of yarn diameters will be extracted as a feature f_1 of yarn count for evaluation:

$$f_1 = \bar{d} = \frac{1}{L} \sum_{i=1}^L d_i \quad (5.20)$$

where d_i is i^{th} diameter, \bar{d} is the mean value of d_i , and L is the total length of yarn (in pixel).

In addition, the following four dimensionless statistical measures of yarn diameter will be formulated to present the irregularity of yarn evenness.

(1) The coefficient of variation (CV), f_2 , is formulated to measure the variability of yarn diameter:

$$f_2 = \text{CV} = \frac{\sqrt{\frac{1}{L} \sum_{i=1}^n (d_i - \bar{d})^2}}{\frac{1}{L} \sum_{i=1}^n d_i} \quad (5.21)$$

(2) Thick place is a kind of yarn fault having 50% more than the mean diameter of yarn. Therefore, the third feature f_3 is calculated as a measure of thick places in percentage relative to yarn length:

$$f_3 = \frac{T_k}{L} \quad (5.22)$$

where T_k is the number of thick places (in pixel).

(3) Thin place is also a yarn fault having 50% less than the mean diameter of yarn. Thus the fourth feature f_4 is calculated as a measure of thin places in percentage relative to yarn length:

$$f_4 = \frac{T_n}{L} \quad (5.23)$$

where T_n is number of thin places (in pixel).

(4) Neps is another yarn fault having 200% more than mean diameter of yarn. The fifth feature f_5 is calculated as a measure of neps in percentage relative to yarn length:

$$f_5 = \frac{T_p}{L} \quad (5.24)$$

where T_p is number of neps (in pixel).

Besides the above statistical measures, two more statistical measures, skewness and kurtosis, will be employed to describe the distribution patterns of yarn diameter.

The skewness of yarn diameter is used to measure the asymmetry of yarn diameters around its mean value. When yarn diameter is spread out to the left of mean, the skewness is negative, otherwise it is positive [169]. For a symmetric distribution, like normal distribution, the skewness is zero. The skewness of the distribution of yarn diameters forms the sixth feature f_6 and it can be defined as

$$f_6 = \frac{\frac{1}{n} \sum_{i=1}^n (d_i - \bar{d})^3}{\left(\sqrt{\frac{1}{n} \sum_{i=1}^n (d_i - \bar{d})^2} \right)^3} \quad (5.25)$$

Kurtosis is a measure for the degree of peakedness/flatness of a distribution or how outlier-prone the distribution is. The kurtosis of the normal distribution is 3. Distributions that are more (or less) outlier-prone than the normal distribution have kurtosis greater (or less) than 3. [170] The kurtosis of the distribution of yarn diameter forms the seventh feature f_7 and it can be defined as

$$f_7 = \frac{\frac{1}{n} \sum_{i=1}^n (d_i - \bar{d})^4}{\left(\frac{1}{n} \sum_{i=1}^n (d_i - \bar{d})^2 \right)^2} \quad (5.26)$$

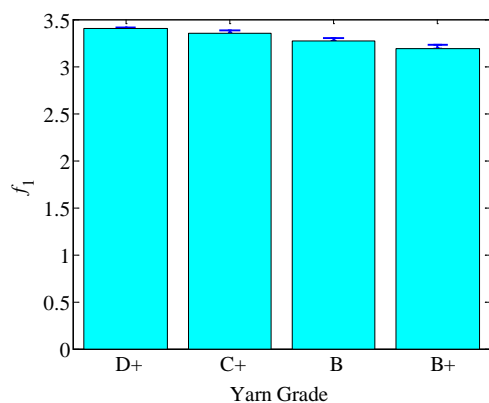
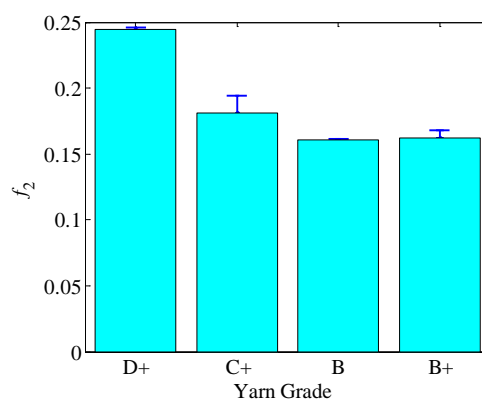
Besides the yarn diameter, information obtained from yarn hairiness will also be used for digital grading of yarn surface appearance. Particularly, the entropy of yarn hairiness extracted from the gray-scale image of hairiness (e.g. Figure 5.17 (b)) will be formulated as a statistical measure for the randomness of hairiness [171]:

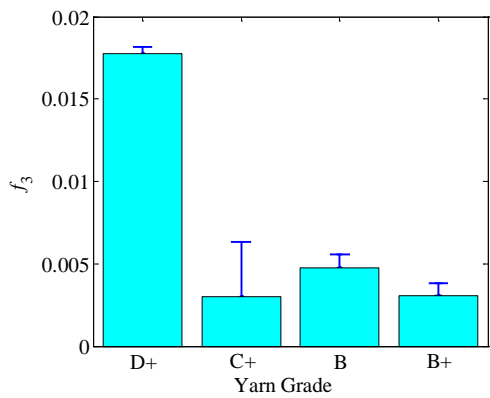
$$f_8 = - \sum_{k=0}^{M-1} (p_k \times \log_2 p_k) \quad (5.27)$$

where M is the number of gray levels of image (256 in this study) and p_k is the probability associated with gray level k .

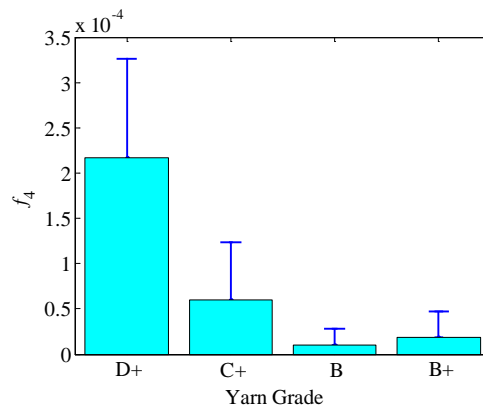
So far, eight features f_1 to f_8 related to yarn diameter and hairiness are extracted from two yarn images (Figure 5.17), as shown in Table 5.1. Feature f_1 is the mean of yarn diameter, which is considered as a global feature for yarn count. Features f_2 to

f_5 present the irregularity of yarn diameter, including CV of yarn diameter (f_2), thick place (f_3), thin place (f_4) and neps (f_5). Features f_6 and f_7 are statistical measures of the distribution pattern of yarn diameters: skewness (f_6) and kurtosis (f_7). And features f_8 is a measure of the texture of hairiness image. Figure 5.19 shows the bar charts of the statistical results (mean and standard deviation) of these features for a series of 60Ne yarn samples constructed in Section 5.3.4. For the 60Ne yarn samples, the mean of diameter f_1 , CV of diameter f_2 and entropy of hairiness f_8 appear to be good features for differentiating various grades of yarn. Their values are generally decreased with the increase of yarn surface quality, or in other words, the better the yarn quality, the lower the value. While the measures for thick places, thin places, neps, skewness and kurtosis ($f_3 \sim f_7$) do not present a linear tendency for different yarn grades. The features will be further analyzed in the following experimental section for yarn classification.

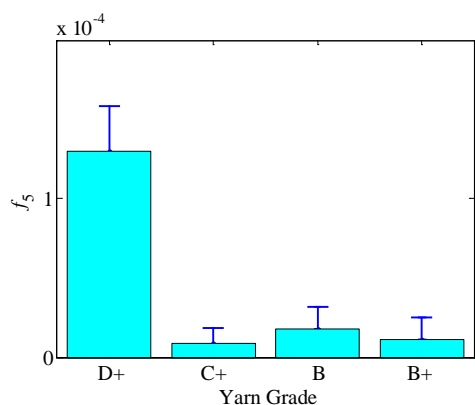
(a) f_1 : mean of diameter(b) f_2 : CV of diameter



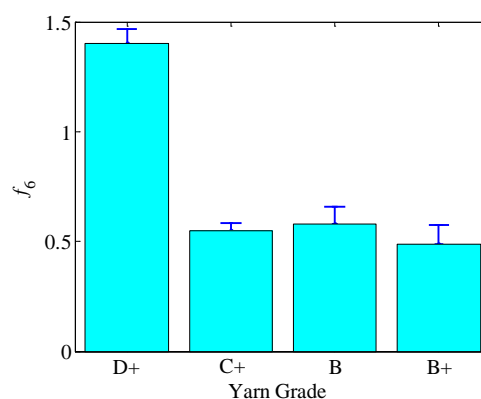
(c) f_3 : percentage of thick places



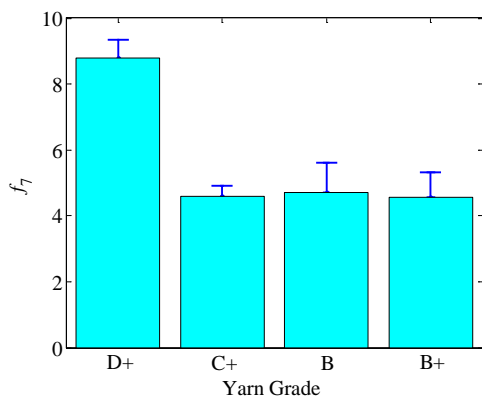
(d) f_4 : percentage of thin places



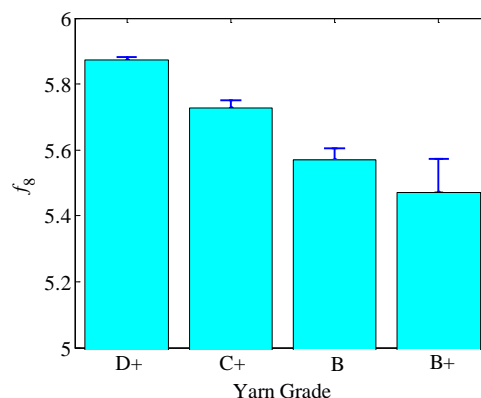
(e) f_5 : percentage of neps



(f) f_6 : skewness of diameter



(g) f_7 : kurtosis of diameter



(h) f_8 : entropy of hairiness

Figure 5.19 Bar charts of features extracted from diameter and hairs (60Ne).

5.3.2. Image residual of extended SR model

5.3.2.1. Image processing

Based on [Section 5.2.3](#), the extended SR method is applied to the yarn board image at Scale 1 (100dpi which is equivalent to an observation distance of 1m) for image analysis. For a particular yarn image, the smoothed average shape of the log spectrum of all yarn samples $A'(f)$ instead of its own smoothed log spectrum will be considered as a general shape of log spectrum for image processing. [Figure 5.20 \(a\)](#) shows the average log spectrum of all 60Ne yarn images in the database (see [Section 5.3.4](#)) and it is then smoothed by a circular averaging filter with a square matrix of side 7 pixels, as shown in [Figure 5.20 \(b\)](#). The smoothed shape of the average log spectrum will be used as a benchmark of 60Ne yarns.

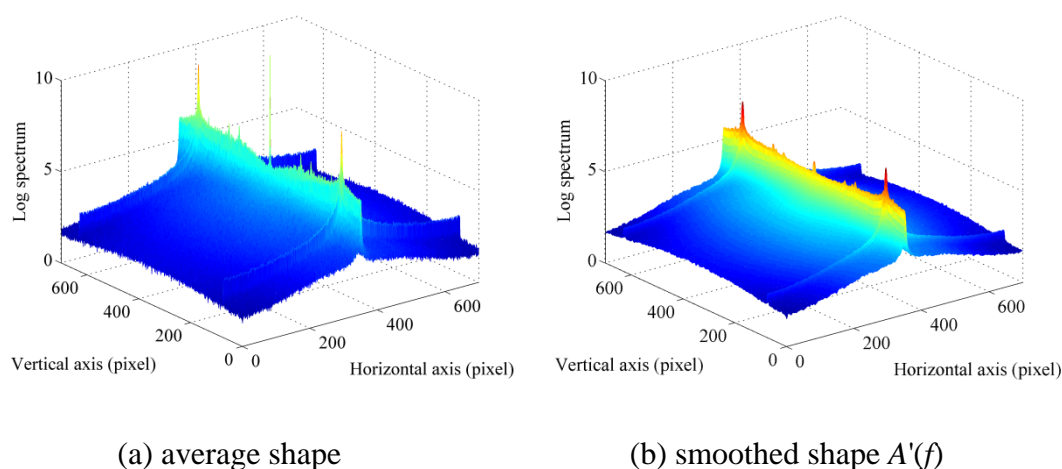
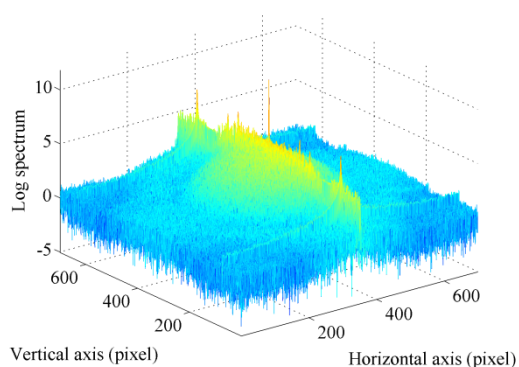


Figure 5.20 General shape of log spectrum of all 60Ne yarn samples.

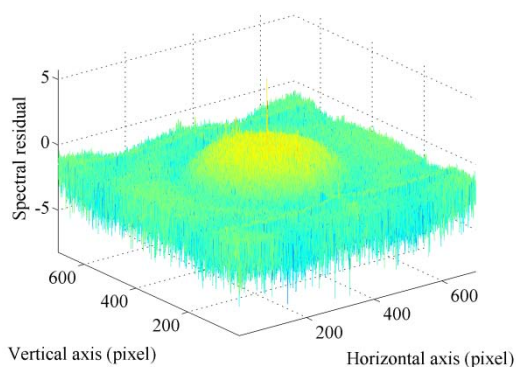
Here, a B+ grade image sample of 60Ne yarn shown in [Figure 5.21 \(a\)](#) is employed to illustrate the results of the proposed method. For the region-based yarn fault, the blurred image of [Figure 5.21 \(a\)](#) is obtained by using a circular averaging filter with a square matrix of side 5 pixels, as shown in [Figure 5.21 \(b\)](#). Based on [Equations \(5.12\)~\(5.16\)](#), the log spectrum $L_b(f)$, spectral residual $R_s(f)$ and image residual $R_I(x)$ of the B+ yarn image can be obtained, as shown in [Figure 5.22 \(a\) ~ \(c\)](#). The image residual indicates the conspicuity of the image relative to the same benchmark. As shown in [Figure 5.22\(c\)](#), the larger value of image residual presents higher conspicuity. In order to compare the level of conspicuity, the residual image is sorted as a 1D signal, as shown in [Figure 5.22 \(d\)](#), for further feature extraction.

(a) 100dpi image $I(x)$ (b) blurred image $I_b(x)$

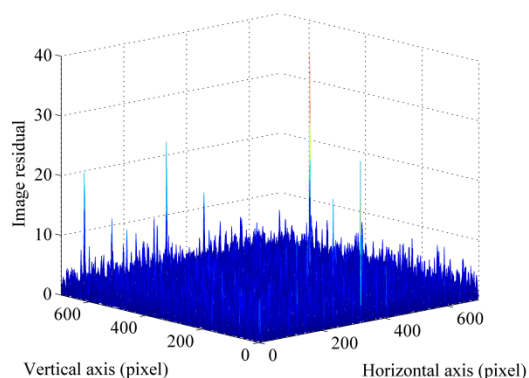
Figure 5.21 A 60Ne yarn sample with B+ grade



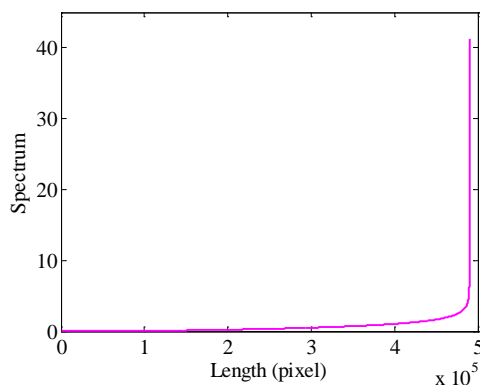
(a) log spectrum $L_b(f)$



(b) spectral residual $R_s(f)$



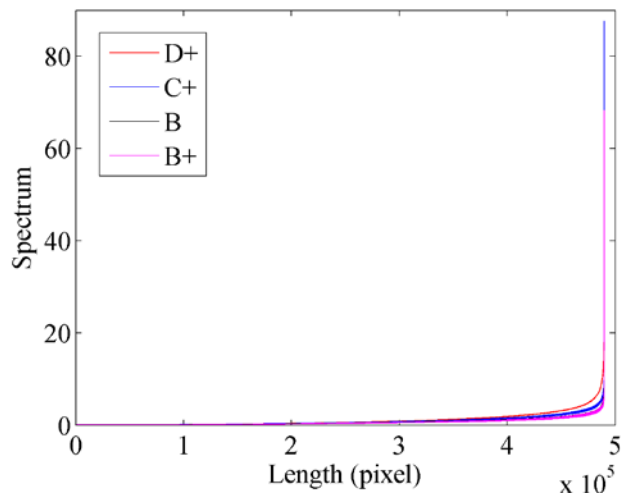
(c) image residual $R_I(x)$



(d) sort curve C of (c)

Figure 5.22 Image processing by SR method for the B+ grade 60Ne yarn.

In order to formulate feasible features for yarn grading, the ordered curves of image residual of all 60Ne yarn samples in the database are generated, as shown in Figure 5.23(a). Figure 5.23(b) shows a local magnified view of Figure 5.23(a), corresponding to 50th percentile ~ 95th percentile of the data. It can be noted that the curves of different grades of yarn present different tracks and thus can be well differentiated by appropriate measures.



(a) whole curves for all 60Ne images

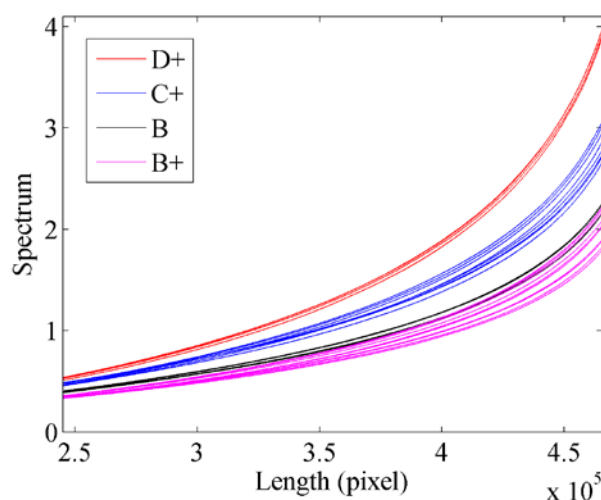
(b) 50th to 95th percentile of the curves

Figure 5.23 Ordered curve of spectral residual of all 60Ne images.

5.3.2.2. Feature extraction

Based on the tendency of the curves in [Figure 5.23](#), the following six statistical features can be extracted from the ordered curve C of image residual to present the characteristics of the yarn board images for further classification:

(1) f_9 is the mean value of C :

$$f_9 = \bar{C} = \frac{1}{n} \sum_{i=1}^n C_i \quad (5.28)$$

(2) f_{10} is standard deviation of C :

$$f_{10} = \sqrt{\frac{1}{n-1} \sum_{i=1}^n (C_i - \bar{C})^2} \quad (5.29)$$

(3) f_{11} is third-order moment of C :

$$f_{11} = \frac{1}{n} \sum_{i=1}^n (C_i - \bar{C})^3 \quad (5.30)$$

(4) f_{12} is inter-quartile range of C .

(5) f_{13} is the 50th percentile of C .

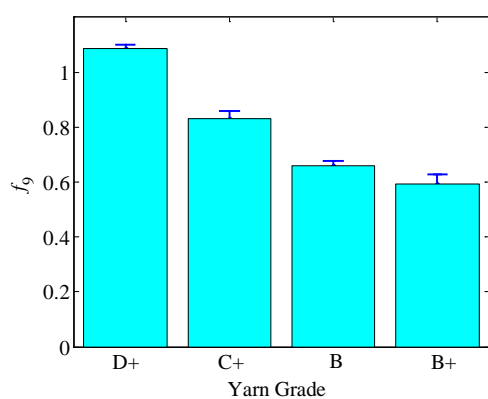
(6) f_{14} is the 95th percentile of C .

Figure 5.24 shows bar charts of the proposed six measures for 60Ne yarn samples in

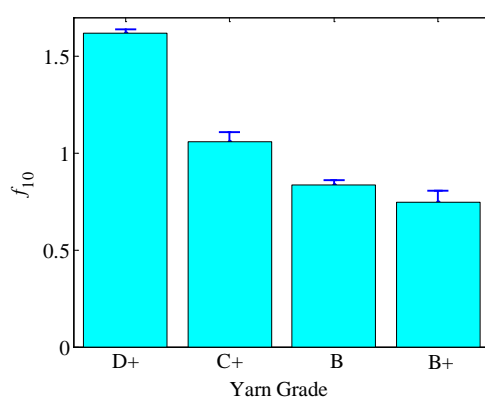
Figure 5.23. It can be noted that all the measures or features f_9 to f_{14} present a

declined trend with the increase of yarn quality. Therefore, they are potential good

features for yarn classification.



(a) f_9 : mean



(b) f_{10} : standard deviation

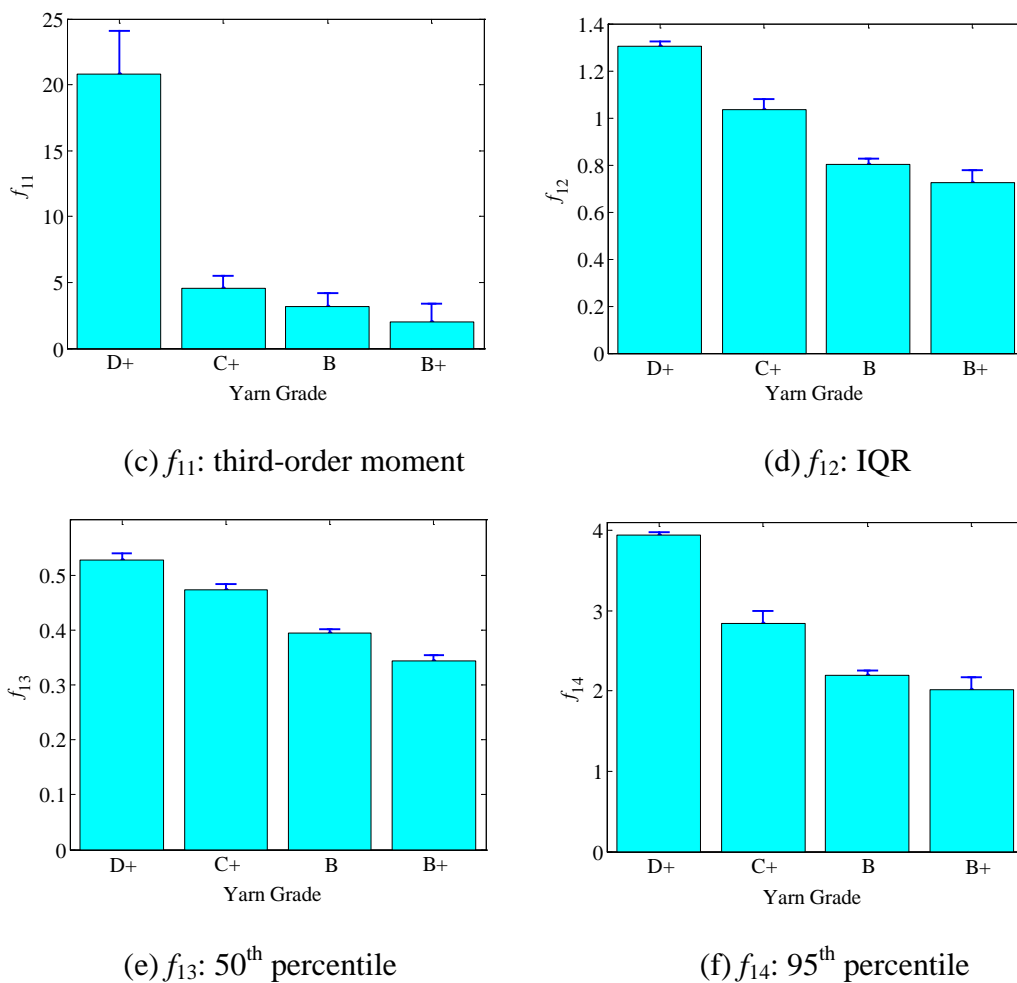


Figure 5.24 Bar charts of the features extracted from image residual of 60Ne yarns.

5.3.3. Image conspicuity from multi-scale attention models

In this section, the yarn board image will be analyzed using multi-scale attention models, and the features from different scales will be extracted from the relevant saliency map by using attention model.

5.3.3.1. Image processing

According to the multi-scale analysis proposed in [Section 5.2.2](#), in this study, yarn

board image with a resolution of 100dpi and 300dpi will be used to simulate the visual inspection at different observation distances of 1m and 0.25m, respectively. Therefore, two saliency maps at different scales will be generated by the extended SR method at Scale 1 (100dpi or at 1m) and AIM method at Scale 2 (300dpi or at 0.25m).

In scale 1, SR method works on the blurred gray image with a relatively low resolution, so the global defects, especially the neps and thick places, can be well identified, but the details of yarn (e.g. yarn hairiness) and foreign matter may be neglected. Therefore, the AIM method is employed for analysis in Scale 2, with high-resolution color image. Beside the thick places and neps, the fuzziness of hairiness and foreign matters can be detected. Saliency map in Scale 1 can detect large regions of defect while in Scale 2, saliency map can detect the detailed information of yarn faults. In the following analysis, the B+ grade yarn shown in [Figure 5.13\(a\)](#), will be employed to demonstrate the working principle of multi-scale attention model. According to [Equation \(5.17\)](#), the SR saliency map $S(x)$ in scale 1 can be obtained by applying a Gaussian filter $g(x)$ to image residual $R_f(x)$. Then, with its image residual map in [Figure 5.22 \(c\)](#), the SR saliency map of the B+ grade yarn in Scale 1 can be obtained, as shown in [Figure 5.25](#).

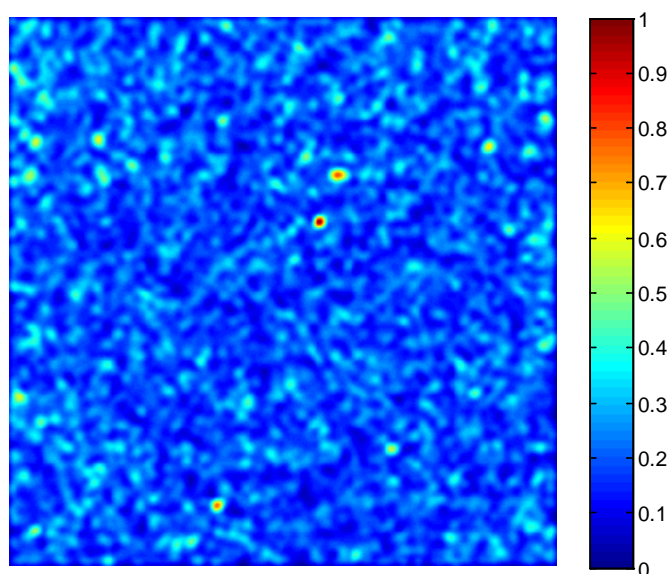


Figure 5.25 Original SR saliency map.

According to the algorithms proposed in [Section 2.3.2.1](#), AIM method can work on high-resolution image. However, because of the huge amount of computation involved, it needs more memory and time for processing. So the size of image should be considered. In this study, the yarn board images are obtained from yarn samples with a size of 7 by 7 inches at the resolution of 300dpi. In order to make the method workable and efficient, the whole image is divided into 4 pieces of images and each piece of image should be processed individually. This kind of treatment is consistent with human visual inspection behavior on yarn board at a closer observation distance. If the examiner inspects yarn board closely, it is impossible to view all the contents of whole board simultaneously. Actually, the examiner will inspect the details of yarn board section by section. [Figure 5.26](#) shows the four pieces of AIM saliency map for the B+ grade yarn sample.

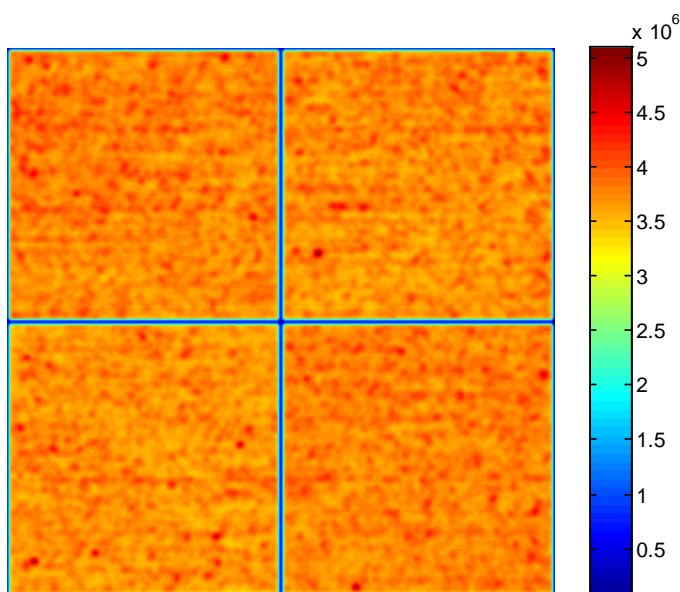


Figure 5.26 Original AIM saliency map divided into 4 pieces.

In [Figure 5.25](#) and [Figure 5.26](#), the regions with a high saliency value should be the zones of yarn fault. In this study, 95th percentile of the saliency value is chosen as the threshold to decide the target saliency regions. Then, the maximum saliency values in each target saliency regions are sorted and the top 20 regions are extracted for further analysis. [Figure 5.27](#) shows an example saliency map containing the top 20 saliency regions. Besides, four representative saliency regions (A_1 , B_1 , C_1 and D_1) are also enlarged in [Figure 5.27](#) for a better view of distribution of salient objects. It is noted that the larger saliency value means higher conspicuity of detected objects. Furthermore, yarn image and extracted yarn body are also shown in [Figure 5.27](#) corresponding to these salient regions. It is apparently that all salient regions contain certain yarn faults. More specifically, region B_1 contains thick places while

the other three regions involve different levels of nepts.

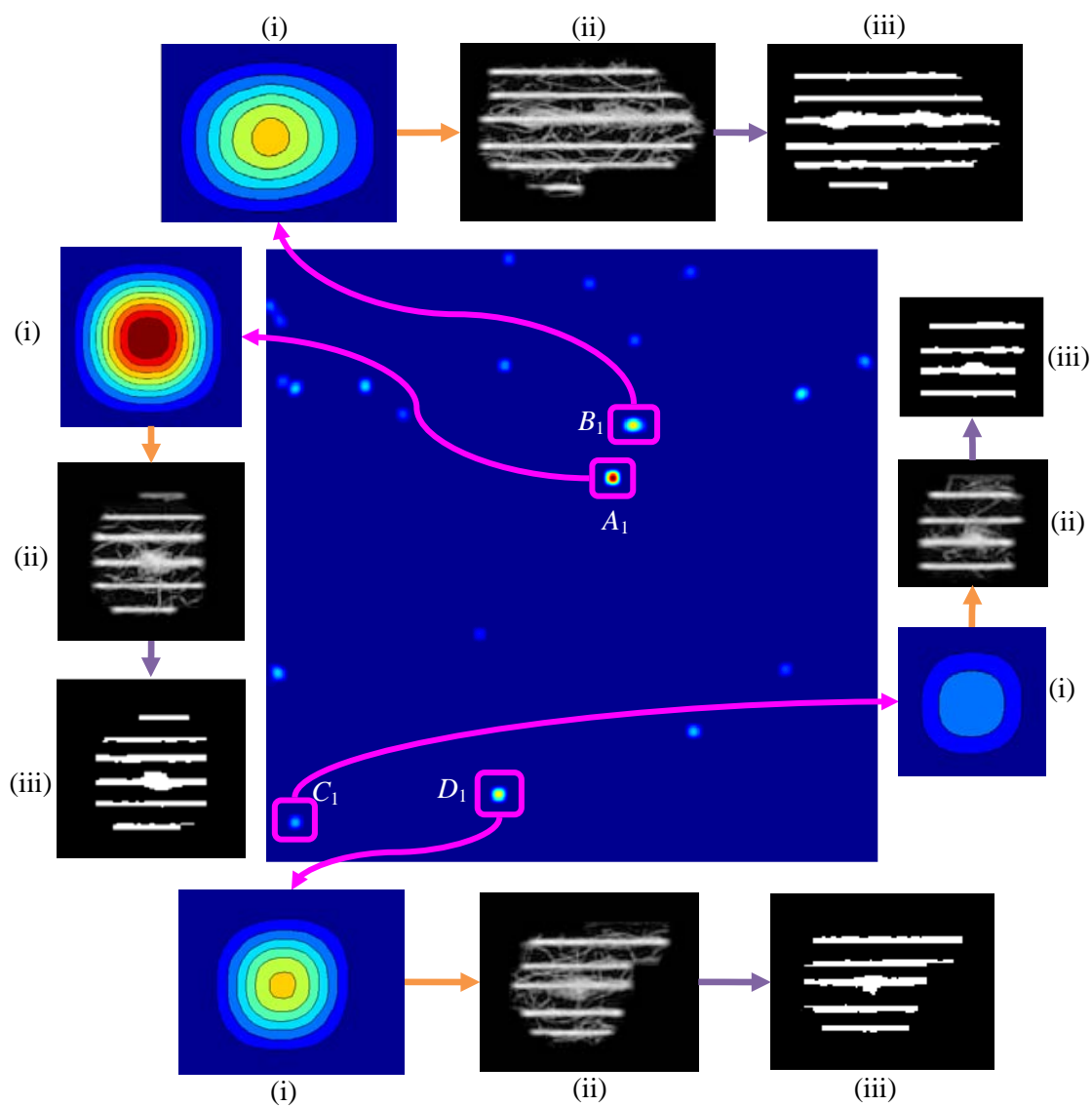


Figure 5.27 Saliency map by SR method in Scale 1 (resolution of 100dpi).

(i) saliency value image, (ii) yarn image, (iii) yarn body image.

Similarly, in AIM method, the threshold (95th percentile) will also be used for each piece of saliency map to obtain the target saliency regions and the top 5 regions in each piece will be selected (total 20 saliency regions for a whole image), as shown in

Figure 5.28. In Figure 5.28, four typical salient regions (A_2 , B_2 , C_2 and D_2) are also enlarged for a better view together with their original yarn images and the yarn bodies. It can be noted that regions A_2 and B_2 include neps and thick place respectively while fuzziness is recognized in region C_2 and a foreign matter is detected in region D_2 .

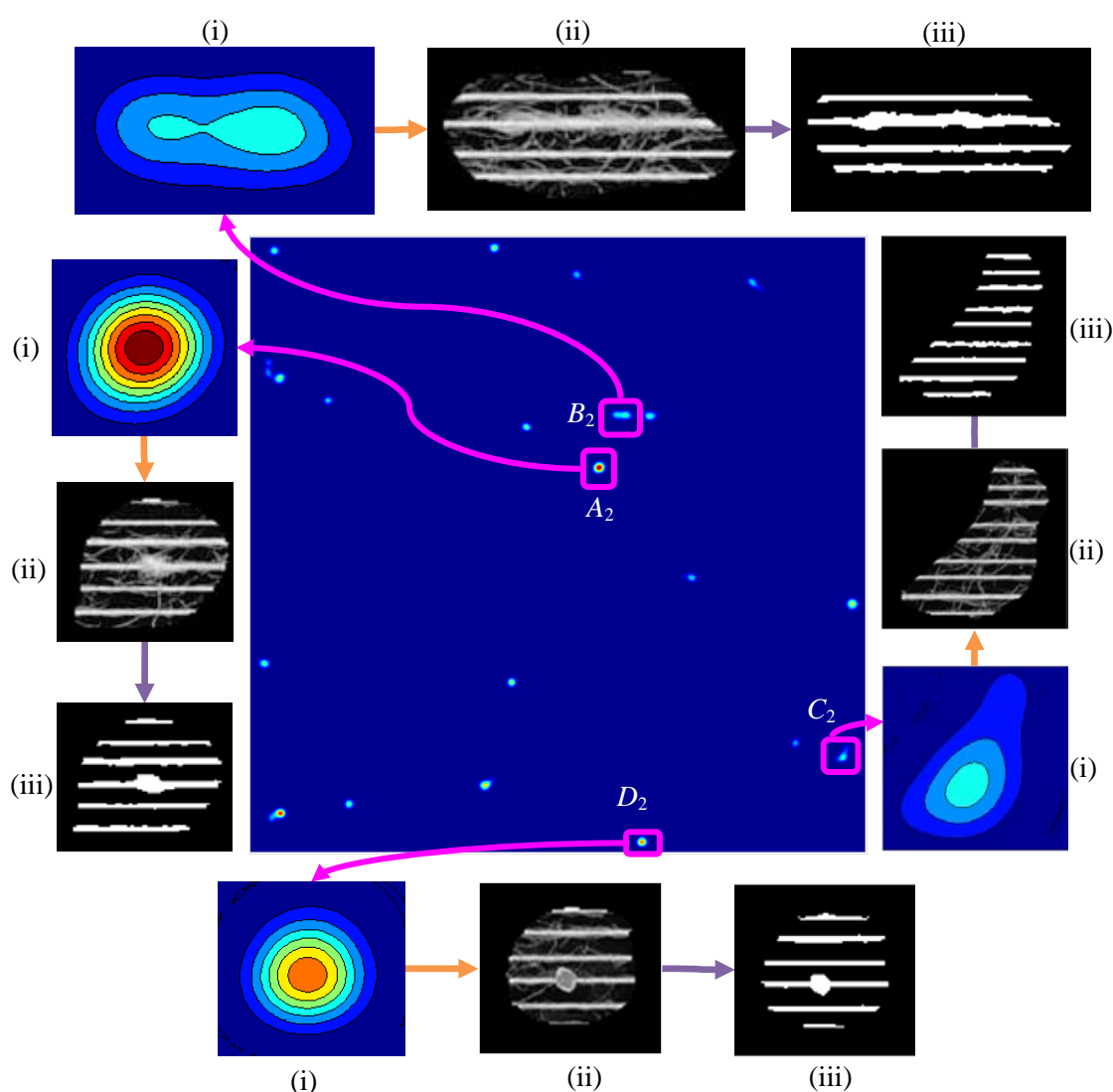


Figure 5.28 Saliency map by AIM model in Scale 2 (resolution of 300dpi).

(i) saliency value image, (ii) yarn image, (iii) yarn body image.

From [Figure 5.27](#) and [Figure 5.28](#), attention models (SR and AIM) at two different scales are feasible and capable in detecting various yarn faults by considering and comparing all adjacent yarn elements in the color yarn board image. It is not only coincided with human visual inspection of yarn grading, but also superior to other methods where only a simple component (e.g. yarn diameter) is considered.

5.3.3.2. Feature extraction

For the SR saliency map in [Figure 5.27](#) and the AIM saliency map in [Figure 5.28](#), the standard deviation of yarn diameters in each salient region (total 20 regions) is calculated. It is supposed to present a higher value for lower quality of yarn surface. Therefore, the following features will be extracted from yarn diameter in the salient region at Scale 1 and Scale 2 respectively, for yarn classification:

$$f_{15} = \frac{1}{t} \sum_{i=1}^t \frac{S_{1i}}{\bar{d}} \quad (5.31)$$

$$f_{16} = \frac{1}{t} \sum_{i=1}^t \frac{S_{2i}}{\bar{d}} \quad (5.32)$$

where $t = 20$, S_{1i} and S_{2i} are the standard deviation of yarn diameters in i^{th} saliency region in Scale 1 and Scale 2, respectively, and \bar{d} is the mean of yarn diameter in the whole board image.

Actually, the features f_{15} and f_{16} are the mean values of CV of the yarn diameters in the top 20 saliency regions. [Figure 5.29](#) shows bar charts of the features extracted from the top 20 saliency regions of multi-scales for the 60Ne yarn samples (total 26 samples) in the database. It can be noted that the values of features f_{15} and f_{16} present a declined trend with the increase of yarn quality. Therefore, they are potential good features for yarn classification.

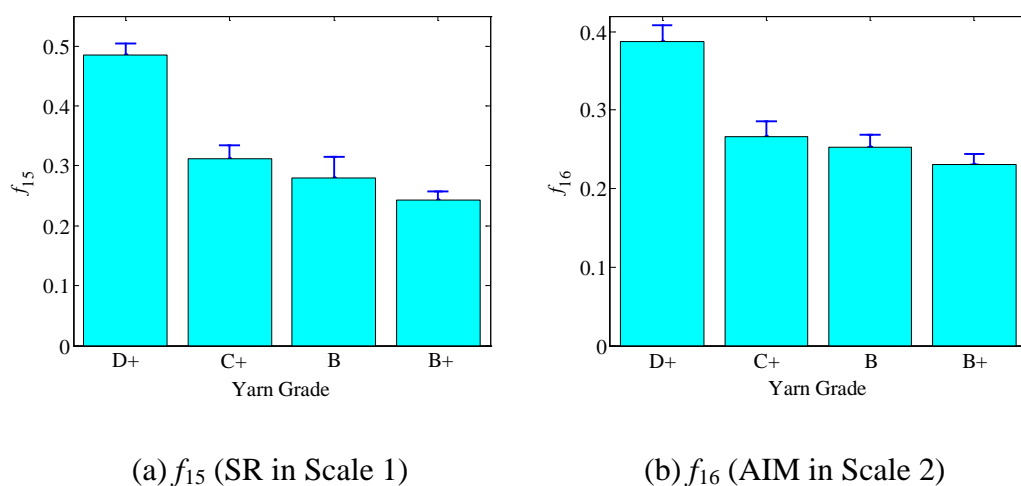


Figure 5.29 Features of 60Ne yarns extracted from the top 20 regions in multi-scale.

5.3.4. Database construction of yarn board images

In order for a full evaluation of the proposed method, in this study, a series of spun yarns with eight different counts (7Ne, 10Ne, 16Ne, 20Ne, 30Ne, 40Ne, 60Ne and 80Ne), and different qualities of surface appearance were produced by using different spinning methods and parameters, as listed in [Table 5.5](#). [Figure 5.30](#)

shows the system for image acquisition of the yarn black board, which consists of a yarn board winder, a scanner, a computer and image acquisition software. The yarn sample is wound on a black board by the yarn board winder, and then a digital yarn board image can be obtained by the scanner.



Figure 5.30 System for image acquisition.

The yarn samples were prepared and wound on the black board according to ASTM D2255 [51]. Table 5.4 shows the relevant requirements for preparation of yarn samples. Once the yarn samples were prepared, three experienced yarn graders were invited to give a visual evaluation on each sample according to the photographic standards of ASTM D2255, and assign a grade for each yarn. The grading results from the three experts were averaged as a benchmark for evaluation of the proposed computer method.

Table 5.4 Requirements for preparations of specimens

Series	Range of yarn counts (Ne)	Wraps per inch (tolerance: $\pm 10\%$)	Spun yarn appearance standard (board with photos)
Series 1-79	1 to 12	20	ADJD225501
Series 2-79	12 to 24	22	ADJD225502
Series 3-79	24 to 36	26	ADJD225503
Series 4-79	36 to 50	32	ADJD225504
Series 5-79	50 to 75	38	ADJD225505
Series 6-79	75 to 135	48	ADJD225506

The size of standard image is 9.5×5.5 inches (52.25 inch^2). In order to keep a similar quantity of yarn information, the size of digital yarn image is fixed as 7×7 inches (49 inch^2). In this study, the digital color yarn images are acquired by using CanoScan 8800F scanner with a resolution of 500dpi and a size of 7×7 inches. [Table 5.5](#) shows the details of yarn image database obtained from different yarn counts and surface qualities. In [Table 5.5](#), yarn counts range from 7Ne to 80Ne, covering most spun yarn counts of textiles. Eight levels of yarn grades (A, B+, B, C+, C, D+, D and D-) are considered in the construction of database. However, samples of two extremely poor grades (D and D-) are not presented in the table because of the difficulties in preparation of such samples. There are total 296 yarn samples in the database with more samples obtained from coarse yarn count and better surface quality. [Figure 5.31](#) shows four example images of 60Ne yarn with

different grades in the database.

Table 5.5 Database of yarn images for grading system

Yarn count (Ne)	Yarn grade (index)								Total	Frequency
	D-	D	D+	C	C+	B	B+	A		
	(60)	(70)	(80)	(90)	(100)	(110)	(120)	(130)		
7	0	0	8	8	4	4	14	8	46	16%
10	0	0	0	4	6	6	12	16	44	15%
16	0	0	0	6	12	4	12	4	38	13%
20	0	0	0	4	2	8	8	16	38	13%
30	0	0	20	0	0	0	16	8	44	15%
40	0	0	0	4	8	0	4	8	24	8%
60	0	0	4	0	8	4	10	0	26	9%
80	0	0	0	8	8	8	12	0	36	12%
Total	0	0	32	34	48	34	88	60	296	
Frequency	0%	0%	11%	11%	16%	11%	30%	20%		



(a) grade B+



(b) grade B

estimate the performance of the PNN classifier. More specifically, LOOCV is used to iteratively train and validate the classifier with different training and testing samples. In each round, a single sample is used as validation data and the remaining samples are used as training data. This will repeat K rounds in this study until all the samples have been used once as validation data.

F-measure is a statistical measure to evaluate the performance of a classifier for multi-class classification. It consists of precision and recall. Precision is the probability that a retrieved document is relevant and recall is the probability that a relevant document is retrieved in a search. [Table 5.6](#) gives a confusion matrix for a multiclass problem, where L is the number of classes, n_{ij} is the number of sample which predicts class C_i to class C_j . For the i^{th} class C_i , its precision P_i , recall R_i and F1-measure are defined as [\[172\]](#)

$$P_i = \frac{n_{ii}}{\sum_{j=1}^L n_{ij}} \quad , \quad R_i = \frac{n_{ii}}{\sum_{i=1}^L n_{ij}} \quad , \quad \text{F1-measure} = \frac{2R_i P_i}{R_i + P_i} \quad (5.33)$$

And the F1-measure of all L classes could be calculated as [\[172\]](#)

$$\text{F1-measure} = \frac{2 \sum_{i=1}^L R_i \sum_{i=1}^L P_i}{L \left(\sum_{i=1}^L R_i + \sum_{i=1}^L P_i \right)} \quad (5.34)$$

Table 5.6 Confusion matrix for multi-classification problem.

	<i>j</i>	<i>i</i>	Actual class				
			C_1	C_2	•	•	•
Predicted class	C_1	n_{11}	n_{12}	•	•	•	n_{1L}
	C_2	n_{21}	n_{22}	•	•	•	n_{2L}
	•	•	•	•	•	•	•
	•	•	•	•	•	•	•
	•	•	•	•	•	•	•
	C_L	n_{L1}	n_{L2}	•	•	•	n_{LL}

In addition, the test performance of classifiers can be also determined by the overall classification accuracy, which is calculated by the number of correct decisions divided by the total number of samples [173]:

$$\text{Accuracy} = \frac{\sum_i n_{ii}}{\sum_i \sum_j n_{ij}} \quad (5.35)$$

In this study, two types of classification will be evaluated, namely eight-grade and five-grade. In ASTM D2255, five-grade yarn classification is recognized for yarn grading of commercial shipment, while for quality control and research purpose, yarn classification can be refined into eight grades. So, in this study, both kinds of classification system will be adopted for performance evaluation of the proposed method. In eight-grade classification, eight yarn grades will be considered in yarn

grading, including A, B+, B, C+, C, D+, D and D-. In five-grade classification ([Section 5.3.5.3](#)), five yarn grades will be involved, including A, B, C, D and D-.

5.3.5.2. Eight-grade classification

The algorithms proposed in [Section 5.3.1~Section 5.3.3](#), are implemented on all 296 yarn board images in the database constructed in [Section 5.3.4](#). For each yarn board image, 16 statistical features are extracted to present the characteristics of yarn surface appearance of the sample. Detailed information about the extracted features and yarn grade (index) for all these 296 yarn samples is listed in [Appendix F](#). With these 16 features extracted from yarn board image, probabilistic neural network (PNN) is trained and used for yarn eight-grade classification on all 296 yarn samples of the database by using LOOCV. The spread of radial basis function is the sole adjustable parameter for construction of PNN. If the spread is near zero, the network acts as a nearest neighbor classifier. As spread becomes larger, the designed network takes into account several nearby design vectors [167]. [Figure 5.32](#) shows the spread-accuracy curve for spread selection in the eight-grade yarn classification. It can be noted that the accuracy has a sharp increase for small values of spread from 0 to 0.02. Afterwards, the accuracy has a very small increase from 91.22% to 92.23%. When the spread is between 0.056 and 0.074, the accuracy tends to keep stable at

92.23%. So the spread is set at 0.06 in the experiment.

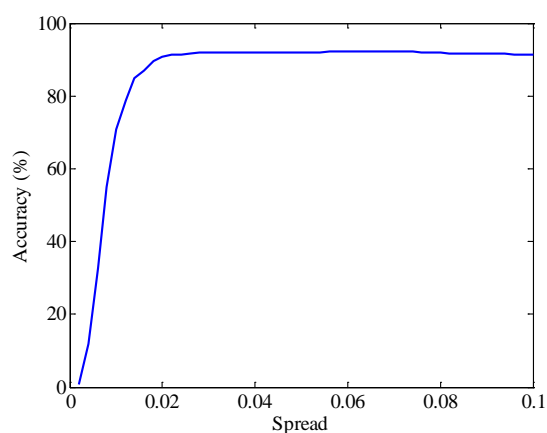


Figure 5.32 Spread-accuracy curve for spread selection (296 samples, 8 grades).

With the spread of 0.06, the resultant confusion matrix for eight-grade yarn classification (16 features, 296 samples) is shown in [Table 5.7](#) for demonstrating the classification performance of the proposed method. Each row of the table indicates the numbers of each grade in a predicted class while each column shows the numbers of each grade in an actual class. Therefore, this matrix summarizes both correct and incorrect classifications. The diagonal elements are counts of correct predictions and off-diagonal elements present the counts of incorrect predictions. From [Table 5.7](#), it can be noted that 273 samples out of the total 296 samples are correctly classified, presenting a high classification accuracy of 92.23%. Particularly, among the 23 misclassified samples, 17 samples were classified to their neighboring grades. For example, a yarn of B+ grade was misclassified to B grade. Only 6

yarn samples (2% of total samples) were incorrectly classified to non-neighboring grades (e.g. a C-grade yarn sample was misclassified to B grade).

Table 5.7 Confusion matrix for classification performance (spread = 0.06).

Confusion matrix	Actual grade						Total
	D+	C	C+	B	B+	A	
D+	32	0	1	0	0	0	33
C	0	29	0	0	0	0	29
C+	0	3	41	1	0	0	45
B	0	1	3	33	1	0	38
B+	0	1	3	0	83	5	92
A	0	0	0	0	4	55	59
Total	32	34	48	34	88	60	296
Precision (P_i)	1.0000	0.8529	0.8542	0.9706	0.9432	0.9167	
Recall (R_i)	0.9697	1.0000	0.9111	0.8684	0.9022	0.9322	
F1-measure	0.9846	0.9206	0.8817	0.9167	0.9222	0.9244	0.9269
Accuracy							0.9223

Besides the accuracy value (i.e. 92.23%) in Table 5.7, precision, recall and F1-measure are also calculated to evaluate the classification performance for each class. The precision of grade D+ is 1, indicating all D-grade yarn samples are correctly classified. For grades B, B+ and A, their precisions are all greater than 0.9, showing that the majority of their samples are correctly classified with only a

small percentage of samples misclassified. The worst cases are C and C+ grades with their precision values of 0.8529 and 0.8542 respectively. The F1-measures for all yarn grades are generally larger than 0.9 except for C+ grade. The overall F1-measure is 0.9269, which again indicates a good classification results of the proposed computer method.

In order to evaluate the importance of individual extracted features, each single feature is considered as a single input of PNN to exam the accuracy of classification, and the results are listed in [Table 5.8](#). It can be noted that the accuracy of mean diameter (f_1) is the highest (52.37%), followed by the CV of yarn diameter (f_2), mean of relative CV of diameter in saliency region in scale 1 (f_{15}), 50 percentile of SR saliency value (f_{13}) and mean of SR saliency value (f_9) with the accuracy of 49.66%, 44.26%, 43.92% and 42.91%, respectively. As discussed in [Section 5.3.1](#) to [Section 5.3.3](#), f_1 to f_8 are features extracted from yarn body and hairiness, f_9 to f_{14} are features extracted from saliency values, and f_{15} to f_{16} are related to multi-scale saliency regions. Therefore, from [Table 5.8](#), each category of features (i.e. $f_1 - f_8$, $f_9 - f_{14}$, $f_{15} - f_{16}$) makes a good contribution to the yarn grade classification.

Table 5.8 Importance of individual feature

Feature source		Single input feature f_i	Accuracy	Rank
Yarn body and hairiness	Diameter	f_1	0.5237	1
		f_2	0.4966	2
		f_3	0.3953	12
		f_4	0.3480	15
		f_5	0.3784	13
		f_6	0.4189	6
		f_7	0.2973	16
	Hairs	f_8	0.4054	9
Multi-scale model and saliency	Residual	f_9	0.4291	5
		f_{10}	0.3987	10
		f_{11}	0.3514	14
		f_{12}	0.3987	11
		f_{13}	0.4392	4
		f_{14}	0.4189	7
	Conspicuity	f_{15}	0.4426	3
		f_{16}	0.4122	8

In this study, two types of PNN neural network, i.e. global PNN and individual PNN for each yarn count, are developed for yarn classification. [Table 5.9](#) shows the classification results for global and individual PNN neural networks. In global network, all of the samples of each category are combined together for training and

testing. The result shows that 92.23% testing samples can be correctly classified, which accords with the accuracy value obtained from confusion matrix in Table 5.7.

Afterwards, eight PNN neural networks are also individually built up for their own classifications. For each individual network, only the yarn images in the corresponding category are used for training and testing. It can be noted that different individual networks have different performance. The 20Ne and 60Ne individual networks perform better than the global PNN, with the classification accuracy of 94.74% and 96.15%, respectively. The classification accuracy of 7Ne, 16Ne and 30Ne individual networks is all higher than 90%. However, the 10Ne, 40Ne and 80Ne individual networks present a worse performance with a low accuracy of around 80%.

Table 5.9 Classification results for eight-grade network (accuracy)

	Individual networks		Global network
Yarn count	7Ne	91.30%	92.23%
	10Ne	79.55%	
	16Ne	92.11%	
	20Ne	94.74%	
	30Ne	90.91%	
	40Ne	83.33%	
	60Ne	96.15%	
	80Ne	83.33%	

5.3.5.3. Five-grade classification

Besides the above refined eight-grade classification, the proposed method is also evaluated for five-grade classification which is commonly used in textile industry.

The five-grade classification only involves grades A, B, C, D and D-. For this purpose, 296 yarn samples in the database (Table 5.5) will be re-organized.

Samples of grade B+ and grade B will be grouped together as grade B samples.

Similarly, C+ and C are combined as C, D+ and D are combined as grade D. The distribution of 5-grade yarn samples is listed in Table 5.10.

Table 5.10 Database of yarn images for five-grade system

Yarn count (Ne)	Yarn grade (index)					Total	Frequency
	D-	D	C	B	A		
	(60)	(70-80)	(90-100)	(110-120)	(130)		
7	0	8	12	18	8	46	16%
10	0	0	10	18	16	44	15%
16	0	0	18	16	4	38	13%
20	0	0	6	16	16	38	13%
30	0	20	0	16	8	44	15%
40	0	0	12	4	8	24	8%
60	0	4	8	14	0	26	9%
80	0	0	16	20	0	36	12%
Total	0	32	82	122	60	296	
Frequency	0%	11%	28%	41%	20%		

The classification results for five-grade of yarn samples are shown in [Table 5.11](#).

Similar to eight-grade classification, a global PNN network and eight individual PNN networks are constructed for classification of general and count-based yarn grades. Compared with the eight-grade classification results in [Table 5.9](#), the five-grade presents a higher classification accuracy in terms of global network and the individual networks of 7Ne, 16Ne and 40Ne. For the other individual networks, the accuracies are same as those of eight-grade classification. The accuracy of global network of five-grade is 93.58% which is slightly higher than that for eight-grade individual networks. The accuracies of the individual network for 7Ne, 16Ne and 40Ne are higher than those of eight-grade by 4.35%, 5.26% and 8.34%, respectively.

Table 5.11 Classification results for five-grade network (accuracy)

Individual network		Global network
Yarn count	7Ne	95.65%
	10Ne	79.55%
	16Ne	97.37%
	20Ne	94.74%
	30Ne	90.91%
	40Ne	91.67%
	60Ne	96.15%
	80Ne	83.33%
		93.58%

5.4. Development of yarn grading system

In this section, an intelligent system will be designed and developed for yarn surface grading using MATLAB Graphical User Interface (GUI). The system covers all aspects of yarn surface evaluation, including image acquisition, image processing, feature extraction and yarn classification. As shown in Figure 5.33, the whole system consists of sample preparation, image acquisition and grading system. First, a yarn sample will be wound onto the black board and then it is scanned by a scanner to obtain a digital image, and finally, the yarn image will be input to a grading system for image processing and yarn classification.

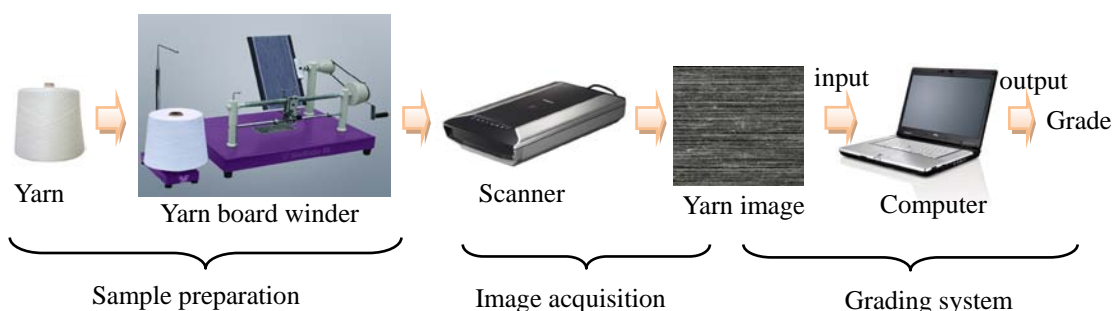


Figure 5.33 Outline for yarn grading system.

5.4.1. Main interface

The digital yarn grading system starts with a main interface as shown in Figure 5.34.

The system is designed to integrate four modules of *Image Acquisition*, *Image Loading*, *Image Processing* and *Yarn Classification*. Figure 5.35 shows the flow chart of system, which will be further discussed in the following sections.



Figure 5.34 Main interface of the digital yarn grading system.

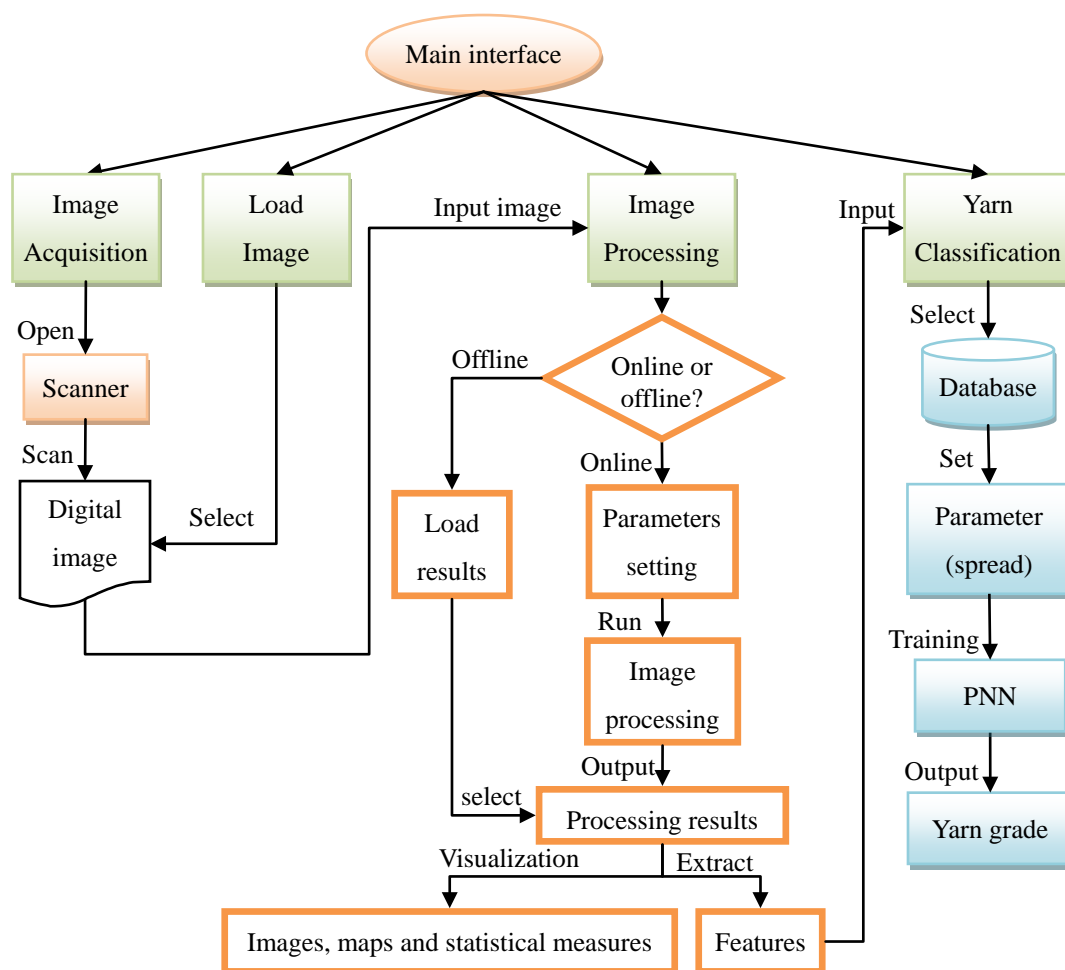


Figure 5.35 Flow chart of the digital yarn grading system.

5.4.2. Image acquisition and image loading

Yarn images have to be prepared for digital evaluation and classification. In image acquisition, new yarn board samples will be scanned in the size of 7×7 inches with a resolution of 500dpi by a digital scanner, as shown in Figure 5.36. For existing yarn board images of the same size and resolution, they can also be directly loaded into the system for further processing, as shown in Figure 5.37 and Figure 5.35.

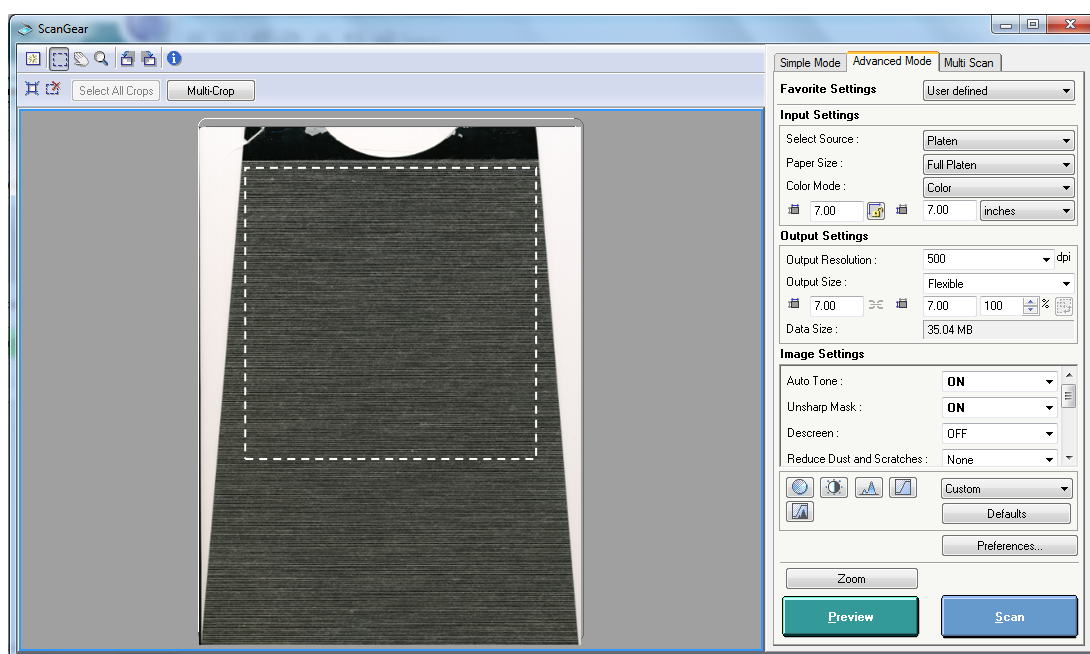


Figure 5.36 Digital image acquisition

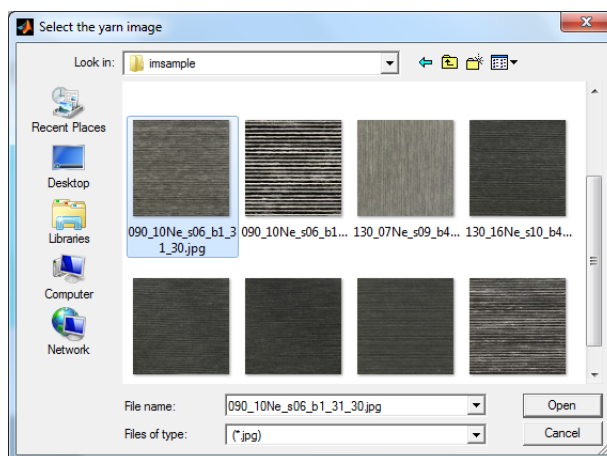
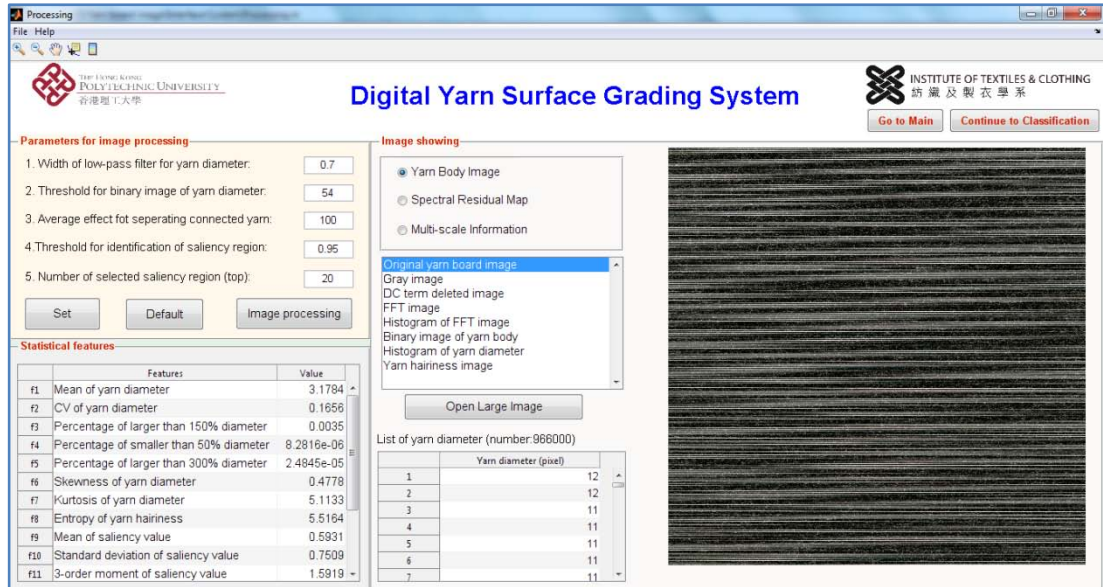


Figure 5.37 Image loading.

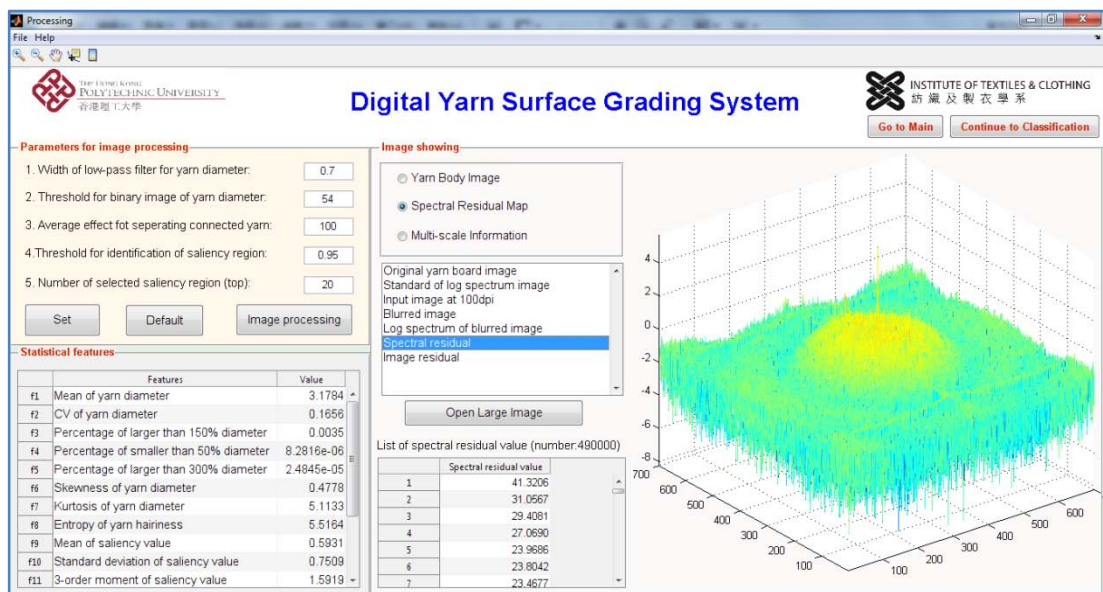
5.4.3. Image processing

With the input digital image, the computer method proposed in [Section 5.2](#) will be implemented for image processing and used for extraction of the statistical features for yarn classification. Two modules (online or offline processing) are designed and developed in image processing. Offline is used for the case where the image processing of the sample has been done before and the results of image processing can be reloaded for further processing, while online module is used for the case where the sample has never been processed, as shown in the flow chart of [Figure 5.35](#).

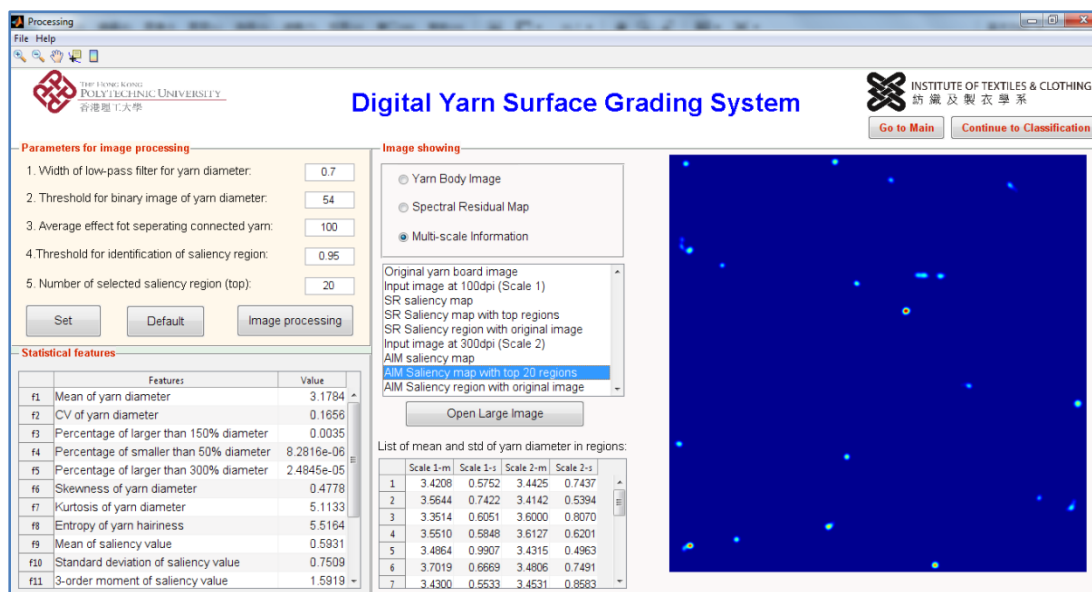
[Figure 5.38](#) shows the interfaces for image processing and feature extraction. The parameters for image processing and feature extraction are also included in the interface. The optimal values used in [Section 5.3](#) are set as default ones for image processing and they can be also adjusted here if necessary. The sixteen features extracted from yarn image are also listed in the interface together with their values. Besides the parameters setting and the extracted features, image processing results related to yarn body image, image residual map and multi-scale information can also be generated in the interface, as shown in [Figure 5.38 \(a\)](#), [\(b\)](#) and [\(c\)](#), respectively.



(a) Yarn body image related results



(b) Residual map related results



(c) Multi-scale information related results

Figure 5.38 Interface for image processing and feature extraction.

Table 5.12 lists the visualized images and maps involved in the image processing.

There are total 24 images/maps which can be visualized in the interface, with 8 for yarn body image, 7 for image residual map and 9 for multi-scale information.

Moreover, other detailed data such as sorted yarn diameter (in pixel) for each point, sorted values for image residual, and the means and standard deviations of yarn diameters in the top 20 saliency regions obtained by SR method and AIM method, are also listed in the interface, as shown in Figure 5.38.

Table 5.12 Visualized maps for selected button.

Button	Visualized maps
Yarn Body Image	Original yarn board image
	Gray image
	DC term deleted image
	FFT image
	Histogram of FFT image
	Binary image of yarn body
	Histogram of yarn diameter
	Yarn hairiness image
Spectral Residual Map	Original yarn board image
	Standard of log spectrum image
	Input image at 100dpi
	Blurred image
	Log spectrum of blurred image
	Spectral residual
	Image residual
Multi-scale Information	Original yarn board image
	Input image at 100dpi (Scale 1)
	SR saliency map
	SR Saliency map with top regions
	SR Saliency region with original image
	Input image at 300dpi (Scale 2)
	AIM saliency map
	AIM Saliency map with top 20 regions
	AIM Saliency region with original image

5.4.4. Yarn classification

Figure 5.39 shows the interface of yarn classification. The sixteen features extracted from the previous step and their normalized values are shown as the input to probabilistic neural network (PNN). Two PNNs, i.e. global and individual neural networks, can be used to classify yarn qualities. The global neural network is constructed for general yarn grading. In this network, all of the samples of each category are combined together for training and testing. The individual neural network is built for each category of different yarn counts. For the individual one, only the yarn images in the corresponding category are used for training and testing. Besides, two types of yarn grading, i.e. five-grade classification (A, B, C, D, D-) and eight-grade classification (A, B+, B, C+, C, D+, D, D-), can be selected and applied for surface quality evaluation of the samples. In this study, the default spread is set as 0.06 for PNN in the system, which can also be adjusted in the interface for classification. With the implementation of PNN, the final yarn grade and grade index can be obtained and displayed, as shown in Figure 5.39. Other information like yarn length, diameter and evenness are also displayed for reference in the panel.

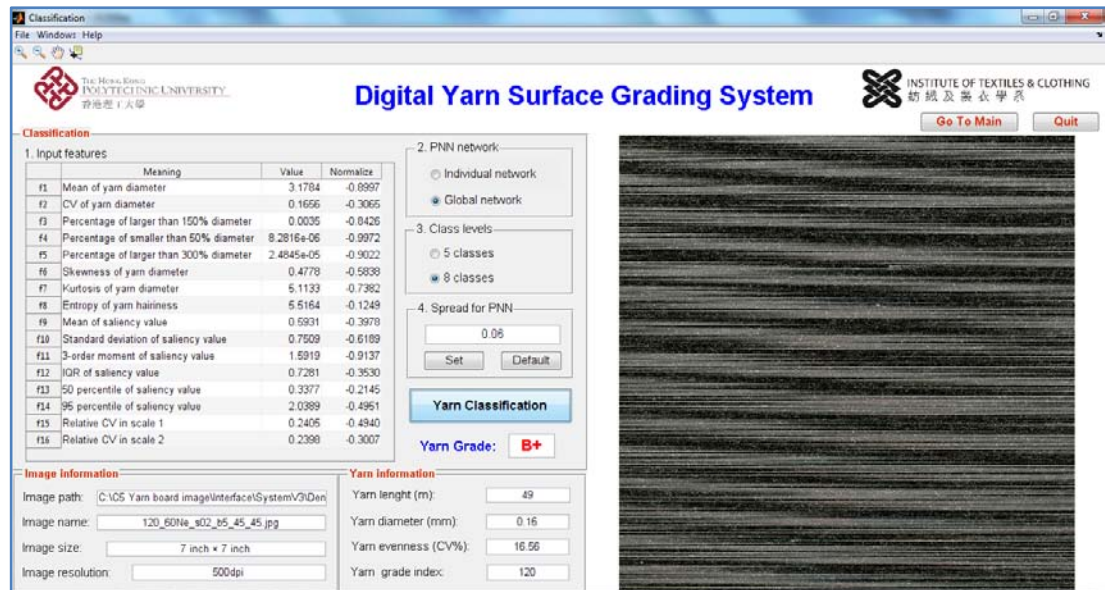


Figure 5.39 Interface of yarn classification.

The diameter D of cotton yarn can be estimated by the following equation [142]:

$$D_1 = 0.03568 \sqrt{\frac{N_{\text{tex}}}{\gamma}} = 0.037 \sqrt{N_{\text{tex}}} \quad (\text{mm}) \quad (5.36)$$

where γ is yarn density and yarn count $N_{\text{tex}} = \frac{590.5}{N_e}$.

As the yarn image is acquired with the resolution of 500dpi, the corresponding yarn diameter in pixel in the image can be calculated as:

$$D_2 = D_1 \times \frac{500}{25.4} \quad (\text{pixel}) \quad (5.37)$$

Therefore, the diameter of these eight series of yarn involved in this study can be calculated and predicted by Equations (5.36) and (5.37), and the results are listed in

Table 5.13. Besides, the yarn diameters in the image were also obtained by the proposed method in pixel and the relevant mean data D_3 were also shown in **Table 5.13** for comparison. It can be noted that the predicted diameter D_2 and measured data D_3 by the proposed method have a good agreement and their differences are all within 1 pixel.

Table 5.13 Relation of yarn count and yarn diameter (cotton).

Yarn count (Ne)	Predicted diameter		Measured mean diameter D_3 (pixel)	Difference $D_3 - D_2$ (pixel)
	D_1 (mm)	D_2 (pixel)		
7	0.37	7.23	7.81	0.58
10	0.31	6.05	6.78	0.73
16	0.24	4.78	5.61	0.83
20	0.22	4.28	5.14	0.86
30	0.18	3.49	4.07	0.58
40	0.15	3.03	3.78	0.75
60	0.13	2.47	3.29	0.82
80	0.11	2.14	3.07	0.93

5.5. Conclusions

In this chapter, intelligent digital evaluation method and system have been developed for the objective and automatic evaluation of yarn surface appearance with computer vision and artificial intelligence. It consists four modules of image acquisition,

image processing, feature extraction and yarn classification. In image processing, a multi-scale attention model is proposed to imitate the visual inspection of human on the yarn board image from different observation distances.

Following the standard of ASTM D2255, various features from influential factors of yarn unevenness, fuzziness, neppiness and visible foreign matter are all considered for yarn surface grading. For doing this, the Spectral Residual method [125] is employed and extended to establish a general benchmark for the comparison among different grades of yarn. Besides, Fourier transform is used for accurate segmentation of yarn body and hairs and multi-scale attention models are proposed and developed for obtaining image conspicuity. Total 16 features (8 from yarn diameter and hairiness, and 8 from the image conspicuity) are extracted accordingly to present the yarn surface characteristics and then used to classify and grade yarn surface qualities using Probabilistic Neural Network (PNN). Moreover, two types of PNN classifier, i.e. global and individual PNN networks, and two types of yarn grading, i.e. five-grade and eight-grade classifications, are designed and used for various yarn classifications.

In order to evaluate the performance of the proposed method, a database of yarn board images is constructed. The database contains 296 samples with various

surface qualities and yarn counts (7~80Ne). With the proposed method and 16 extracted digital features, the classification accuracy of global five-grade classifier for the database is 93.58%, which is slightly higher than that of eight-grade classifier (92.23%). Both of them achieve good grading performance. Compared with the global classifier, the performance of individual classifiers varies with yarn counts: good results for 7Ne, 16Ne, 20Ne, 30Ne, 40Ne and 60Ne and fair results for 10Ne and 80Ne. Moreover, the importance of individual feature for yarn grading is analyzed by considering each feature as a single input of PNN. And the classification results of individual feature show that each category of features obtained from yarn body, hairiness, saliency value and multi-scale saliency regions, makes a good contribution to the yarn grade classification.

Finally, an intelligent system is also designed and developed for yarn surface grading. This system integrates the whole progress of yarn analysis and shows all important characteristic results with an interactive and user-friendly interface. This computerized technology and system is potential for commercialization and application in textile testing laboratories and spinning mills for yarn surface quality control and assurance.

Chapter 6 Conclusions and Suggestions for Future Research

6.1. Conclusions

The work described in this thesis has been concerned with theoretical modelling and numerical analysis of yarn formation in spinning triangle, automatic and efficient image analysis of yarn internal structure, and intelligent and objective evaluation of yarn surface appearance on black board. The conclusions of this thesis are given as follows.

6.1.1. Theoretical modeling and numerical simulation of spinning triangle for yarn formation analysis

In yarn fabrication, fibers are eventually twisted into the yarn at the spinning triangle. The mechanical performance of fibers in spinning triangle influences the yarn structure and physical performance. Previous studies were mainly based on force method and energy method. Due to the limitations of these methods, some important parameters, such as the inclined angle of spinning tension, the fiber contact of bottom roller, yarn torque and the torsional distribution, cannot be considered. Therefore, in this study, a FEM model has been developed for

theoretical modeling and numerical analysis of spinning triangle. Firstly, a static FEM model of spinning triangle was developed with consideration of inclined spinning tension, fiber contact with bottom roller, yarn torque and fiber buckling. In this model, initial strains of fibers are formulated and applied by considering the effect of initial deformation of fibers based on the equation of mass conservation. Besides, the algorithm of element birth and death is employed to address the phenomenon of fiber buckling.

A series of numerical simulation were carried out to analyze the fiber tension distribution and torsional distribution under the effects of various spinning parameters, such as yarn count, yarn twist, spinning tension, inclined angle of spinning tension and the contact length of fiber with bottom roller. Simulation results were also compared with previous theoretical analysis of Najjar [20] (without fiber buckling) and Hua et al [22, 23] (with and without fiber buckling), and the experimental measurements of Bennett & Postle [14] (yarn torque). The comparison results showed that the proposed static model of spinning triangle is well agreed with the previous results by the energy methods and in a better agreement with the experimental data than the other models for yarn torque.

As most textile fibers show viscoelastic behavior and the fibers in the spinning

triangle are subject to dynamic loads and impacts, based on the above static FEM model, a dynamic FEM model has been further developed with consideration of fiber mass and damping for a more complete and accurate estimation of the fiber mechanical behavior in spinning triangle. The dynamic properties of spinning triangle, such as natural modes, natural frequency, mode shapes, harmonic analysis, resonant responses, have been studied. The response of fiber tension was also numerically studied under a time-varying spinning tension. The results showed that the consideration of dynamic parameters of fiber mass and damping has a notable influence on the amplitude and attenuation of fiber response in the dynamic process.

6.1.2. Automatic and efficient processing of tracer fiber images for yarn structure analysis

In tracer fiber technology for analysis of yarn internal structure, tracer fiber images are consecutively captured from two views of a moving yarn (containing tracer fiber) in the liquid. In the past, image mosaic and segmentation involved in tracer fiber image analysis were mainly based on manual operation due to two challenging technical problems: fluctuation of two views of the yarn and high pattern similarity of tracer fiber images. Therefore, this study has developed an integrated image processing method for automatic image mosaic and segmentation for yarn structure

analysis. In this method, several special statistical measures are extracted from tracer fibers and gradient yarn image, and then combined as a decision function, so as to search the optimal position for image mosaic. An extended Pan-Tompkins algorithm is also developed for tracer fiber detection in image mosaic and segmentation. Moreover, a baseline fitting method is employed to fit the background of image for eliminating the effect of uneven light condition.

A series of yarn samples with tracer fiber involved were prepared and produced at different yarn counts and twists, and then were acquired under a microscope for evaluation of the proposed method. Besides, an objective evaluation method is proposed for measuring the precision of image mosaic and segmentation of the proposed method with respect to the conditional manual method. In the experiment, total 50 series of tracer fiber images (total 872 images) were acquired from five different-count yarns. The experimental results showed that the proposed method works well for mosaic and segmentation of different yarn counts and is generally in good agreement with the manual method. Moreover, the efficiency of the proposed computer method is much higher than that of manual method for both image mosaic and segmentation. The results also showed that the relative mosaic error in horizontal direction is smaller than that in the vertical direction, and most vertical mosaic differences between the proposed method and manual method are just a few

pixels. The relative segmentation error of detected tracer fiber (1%~3%) is smaller than that for yarn boundary (2%~8%).

Based on the above developed computer algorithms, an intelligent system for automatic image analysis of yarn internal structure is also designed and developed for implementing and visualizing the whole image processing of tracer fiber images with an interactive and user-friendly interface. The system consists of five modules, including video acquisition, image acquisition, image mosaic, image segmentation and parameter analysis. In each module, the processing parameters can be adjusted (the empirical values obtained from the experiment of this study are set as default values), and the corresponding results of each step can be visually inspected in the interface. Users can control the whole process by simple operation and obtain final yarn structural parameters and charts for yarn structural analysis. The developed method and system can be used for different academic and research purposes, such as the analysis of yarn structural characteristics for an innovative spinning method and the study of effect of spinning parameters on fiber arrangement inside the yarn.

6.1.3. Intelligent and objective evaluation of yarn board images for yarn surface appearance analysis

ASTM D2255 presents a widely accepted standard method for the evaluation of yarn

surface appearance in textiles. In this method, yarn is subjectively evaluated and graded by visual inspection of experienced experts. Although some digital methods have been developed for yarn grading, none of them can fully imitate human visual behaviors in the inspection of yarn segments on a blackboard. In this study, the concept of multi-scale and attention models are proposed and employed for analyzing yarn images scanned from the yarn blackboard. A multi-scale attention model has been developed, which can fully imitate human observation at different observation distances for both a whole and a detailed analyses of yarn information. In Scale 1 at 1m observation distance, a spectral residual model is applied and extended to detect the conspicuity contents of the whole yarn image at 100dpi based on a general log spectrum obtained from all grades of yarn. In Scale 2 at a closer observation distance (0.25m), the AIM attention model is used to generate the saliency map at 300dpi for the detailed yarn information, especially for the detection of color foreign matter. In addition, with the periodic pattern of yarn board image, an integrated computer method composed of Fourier transform, Butterworth filtering and inverse Fourier transform is used to separate yarn body and hairs for further analysis.

Moreover, a database of yarn board images was constructed for evaluating the performance of the proposed method. These images were sampled from eight yarn

counts and different grades of yarn surface appearance, producing a total of 296 yarn board images.

Sixteen digital features are then extracted from yarn body image, yarn hairiness image and the multi-scale saliency maps, covering all factors (fuzziness, neppiness, unevenness and visible foreign matter) for yarn surface appearance evaluation. The digital features extracted from the database were used for training and testing of Probabilistic Neural Network (PNN) for yarn classification. Two kinds of PNNs, namely global and individual PNN, are designed and used for different yarn classification based on all yarn counts and individual yarn count, respectively. Moreover, PNNs can be used for two kinds of classification, i.e. eight-grade (A, B+, B, C+, C, D+, D and below D) and five-grade (A, B, C, D and below D). The former is a refined system and thus can be used for quality control and research purpose while the latter one accords well with the normal practice in textile industry. The accuracy of global PNN for five-grade classification is 93.58%, which is slightly higher than that for eight-grade classification (92.23%). Both of them achieve good classification performance in yarn surface grading. For the individual PNNs, similar to the global PNN, the performance of five-grade classification is generally better than that of eight-grade classification. Most of individual PNNs have accuracies over 90%, demonstrating a good performance in yarn classification.

Individual PNNs also present a comparable classification capacity with the global PNN, with higher accuracy on certain counts (e.g. 20Ne, 60Ne) and lower accuracy on the others.

Moreover, the importance analysis of individual feature for yarn grading was carried out and the results showed that each category of features, obtained from yarn body, hairiness, saliency value and multi-scale saliency regions, makes a good contribution to the yarn grade classification.

Based on the above developed algorithms, an intelligent digital evaluation system is also designed and developed for the computerized measurement and evaluation of yarn surface quality. The system consists of hardware for sample preparation and image acquisition, and software for image analysis and yarn grading. The hardware includes a yarn board winder, a scanner and a computer while the software integrates all the digital algorithms developed in this study. The system covers and integrates all aspects of yarn surface evaluation, including image acquisition, image processing, feature extraction and yarn classification. In the evaluation system, various operational parameters and processing results can be visualized and adjusted in the interface of each module. The system also provides two types of PNN (i.e. global and individual) and two types of classification (i.e. eight-grade and five-grade) for

digital yarn classification. Besides yarn grading, the statistical measures of yarn, such as the mean value and CV of yarn diameter, and yarn image processing results, such as the yarn body image, hairiness image, saliency maps and yarn saliency regions, can all be displayed and inspected for a more detailed analysis of yarn image. This computerized system is tailor-made for yarn board grading and thus potential for application in textile testing laboratories and spinning mills for yarn surface quality control and assurance.

6.2. Limitations of the study and suggestions for future research

The achievements of this study have been summarized as above. The potential challenges and limitations arising from this study will be described in this section together with the recommendations for further work

6.2.1. Instant measurement of fiber dynamic behavior inside the spinning triangle

In this study, a dynamic model of spinning triangle was developed by using finite element method with consideration of the dynamic characteristics of fiber for the analysis of its geometric and mechanical performance. The experimental work for spinning triangle, such as the measurements of dynamic spinning tension, fiber

tension forces and geometrical profile of spinning triangle, should be carried out in the future for the refinement of the developed FEM dynamic model of spinning triangle. However, it is extremely difficult to accurately measure the dynamic parameters of fibers inside the spinning triangle, particularly for individual fiber tension and torque. Therefore, an extensive and systematic work has to be carried out for developing a dedicated digital measurement and analysis system to enable the experimental validation of the theoretical analysis, the examination of dynamic performances and the quantification of the dynamic behavior of individual fibers in spinning triangle by incorporating high-tech sensing technology, high-resolution and high-speed photography and advanced image processing methods.

In this study, a simplified model is built up for the fiber frictional contact with bottom roller. It is assumed that the contact area of fiber with bottom roller is flat and the lengths for contact fibers are same. Actually, the fiber will contact the bottom roller along the arc surface of bottom roller and the contact height for individual fiber may be different. In the future, more complex conditions of contact case should be considered for a more realistic simulation.

In addition, fiber migration and inter-fiber forces are ignored in the developed FEM models and numerical simulations. This is because consideration of the two factors

will bring substantial technical challenges and computational complexities in the theoretical modeling. Actually, fiber migration occurs in the spinning triangle and its formation is determined by the fiber performance in spinning triangle. And such migration will affect yarn properties such as yarn strength and yarn torque. As fiber migration and inter-fiber forces are real matters in yarn formation at spinning triangle, it is suggested to formulate the two factors in the spinning triangle models in future so as for obtaining a more realistic and meaningful result.

6.2.2. Algorithm and measurement optimizations for yarn structural analysis

In this study, 50 series of tracer fiber images were produced from five yarn counts (10~60Ne), and used for evaluation of the proposed algorithms of mosaic and segmentation. For the 60Ne yarn, its tracer fiber and yarn hairs are thicker and less in number than the other coarse yarn images because of a larger magnification of microscope adopted in image acquisition. Although the thicker and less yarn hairs form a good feature for matching function of gradient image, they bring big noises for tracer fiber detection in the proposed algorithms. Under this situation, the matching function from gradient image will be more important. Therefore, for fine yarns (e.g. 60Ne or higher), the weights in decision function should be adjusted with

a higher weight assigned to the component of gradient image. Future work is thus recommended for systematic analysis and optimization of such decision function weights with respect to various operational parameters, such as yarn count, twist and even light conditions.

In the tracer fiber image used in this study, the intensities of background, yarn body and tracer fiber follow the sequence from light to dark. Besides this three-level gray image, an image with whiter yarn body and the blacker background and tracer fiber can also be obtained by adjusting the light conditions. Under this situation, the contrast between yarn body and background, and yarn body and tracer fiber, becomes larger, which will be helpful for achieving higher precision in the identification of yarn boundaries and tracer fiber. However, the tracer fiber, which is closer to the edge of the yarn, is easily mixed with the background in the image. For solving this problem, color tracer fiber is suggested to be used in the tracer fiber measurement because it can be easily detected from color image for further processing.

In addition, because the tracer fiber just takes a very small percentage in the yarn, in the video acquisition, most images do not contain tracer fibers, or in other words, tracer fibers will occasionally appear, and sometimes even two or more tracer fibers

appear simultaneously in one image (which are invalid tracer fibers). Therefore, developing a method to automatically detect the status of tracer fiber (i.e. non-present, single, multiple), is important and meaningful work for the image acquisition. It will not only release the operator from the long-time observation but also increase the efficiency of image acquisition. Moreover, the tracer fiber is the most important feature in the proposed algorithm, so the fiber ends are not included in this study. In the future, if the state of tracer fiber can be detected, the fiber end should also be included and analyzed.

6.2.3. Development of global yarn database and high-resolution image for precise yarn surface classification

Firstly, in this study, 296 yarn samples were acquired from eight different yarn counts for yarn grading. Although we spent a lot of time to produce and prepare different quality yarns, the samples still cannot cover all the grades. Extremely poor-quality yarns (D and D-) are hard to be obtained mainly due to the limitation of material sources. Besides, the number of samples for each grade and each yarn count is not equal to each other. The imbalanced multi-class distribution of samples may pose a drawback for the proposed method. It is, therefore, suggested to produce a global yarn sample database so as to cover all the yarn grades and

balance the sample distribution for the multi-class classification in future.

Secondly, in the analysis of yarn diameter, the resolution of yarn board image is 500dpi. Even with this resolution, the mean diameter of fine yarn, such as 60Ne and 80Ne yarn, is only 2~3 pixels. Although the diameter obtained by the proposed method is very close to the theoretical value, a small noise or processing error may lead to a large relative error. The image resolution is currently limited by the computational efficiency. With the rapid development of computer and computational sciences, it is believed that adoption of higher resolutions in yarn board image will be feasible in the future for a more precise analysis of yarn surface appearance.

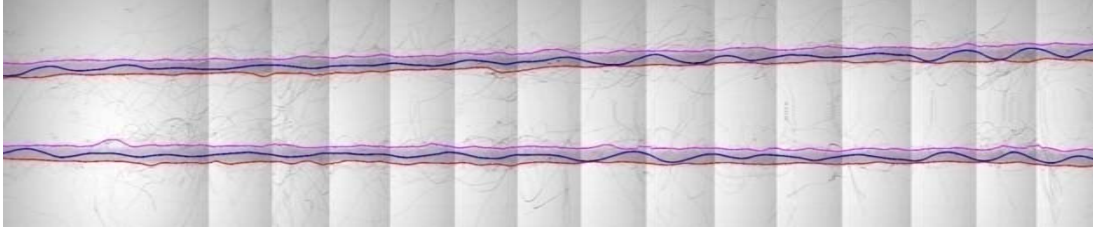
6.2.4. Integration of spinning triangle, yarn internal structure and surface appearance for a better analysis of yarn quality

The fiber behavior in spinning triangle, yarn internal structure and surface appearance of yarn are three important aspects for the analysis of yarn properties. Fiber migration occurs in the spinning triangle during yarn formation, so the fiber behavior in spinning triangle determines the fiber arrangement inside the yarn body. The theoretical model of spinning triangle should be further extended to provide some indications for fiber migration. The fiber migration and surface appearance

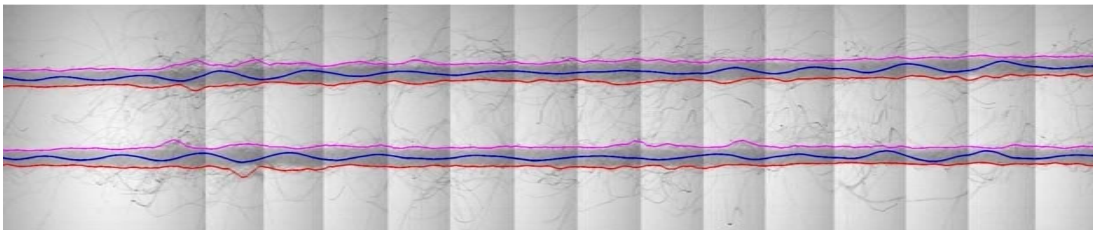
are two important yarn structural factors. They have a close relationship and affect with each other, which should be integrated and simultaneously analyzed for a better analysis of yarn structure and quality in the future.

Appendices

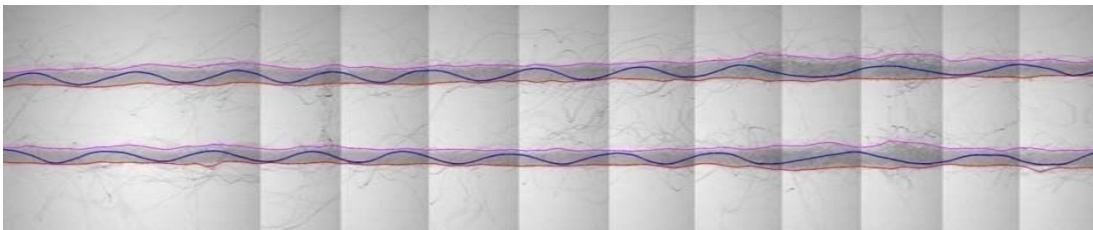
Appendix A: Results of the image mosaic and segmentation



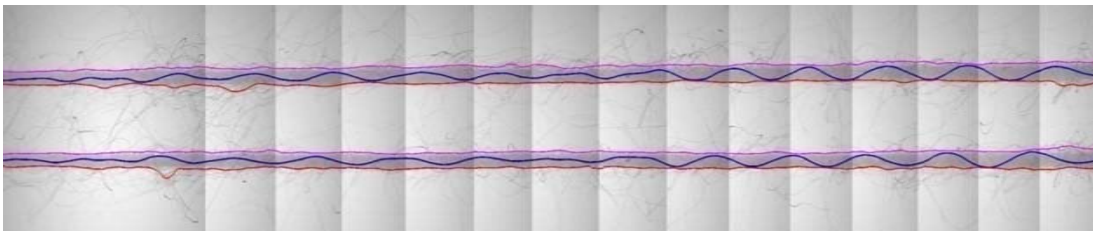
(1) 10Ne yarn-sample 1 (10Ne-s1)



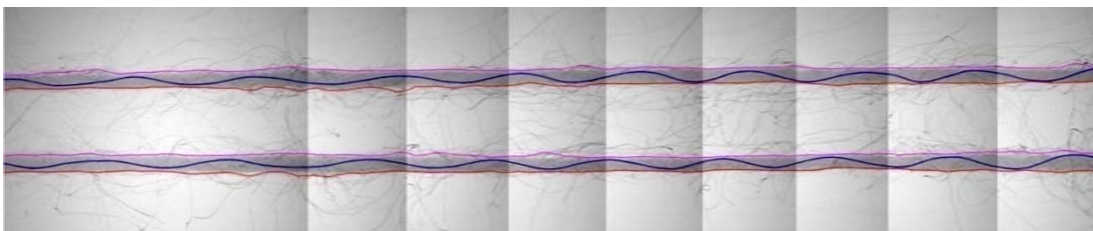
(2) 10Ne yarn-sample 2 (10Ne-s2)



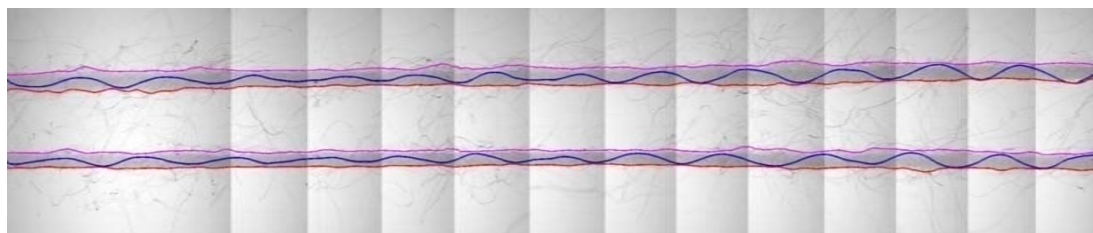
(3) 10Ne yarn-sample 3 (10Ne-s3)



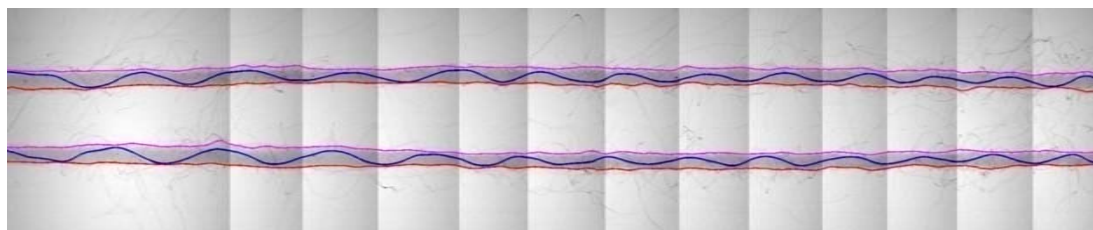
(4) 10Ne yarn-sample 4 (10Ne-s4)



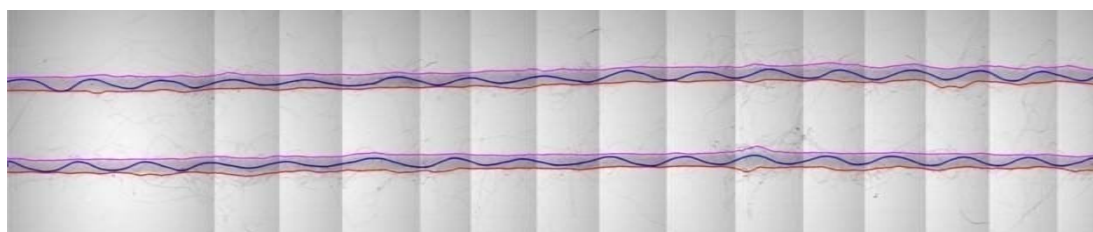
(5) 10Ne yarn-sample 5 (10Ne-s5)



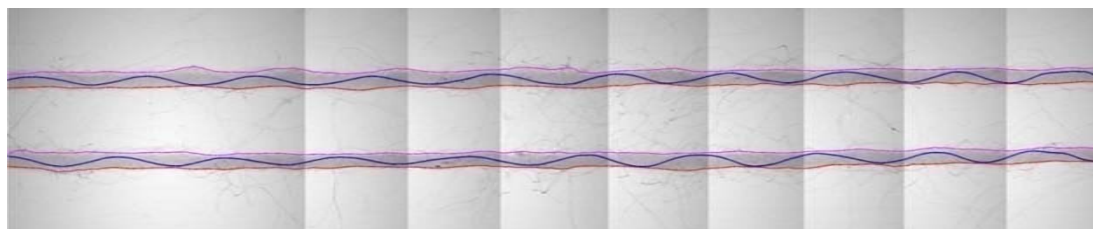
(6) 10Ne yarn-sample 6 (10Ne-s6)



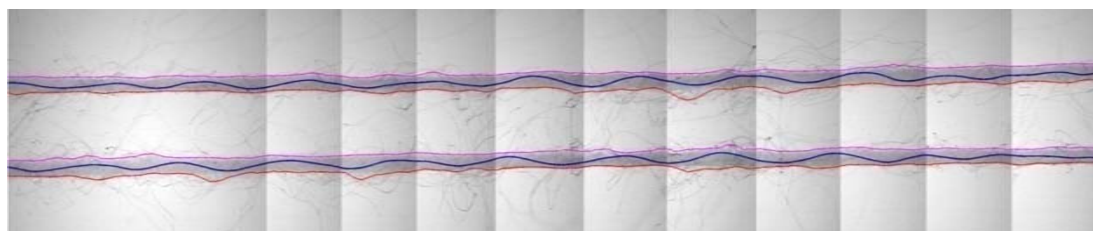
(7) 10Ne yarn-sample 7 (10Ne-s7)



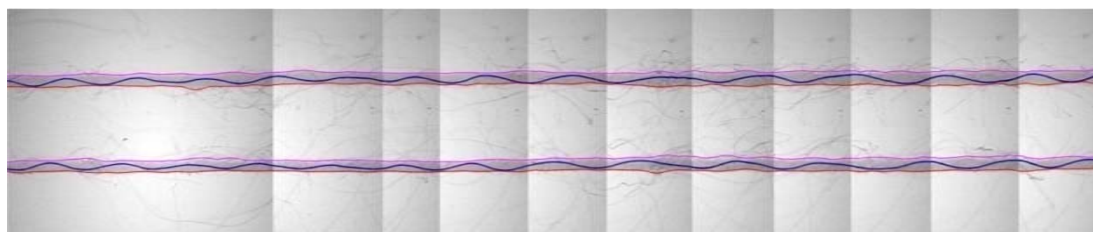
(8) 10Ne yarn-sample 8 (10Ne-s8)



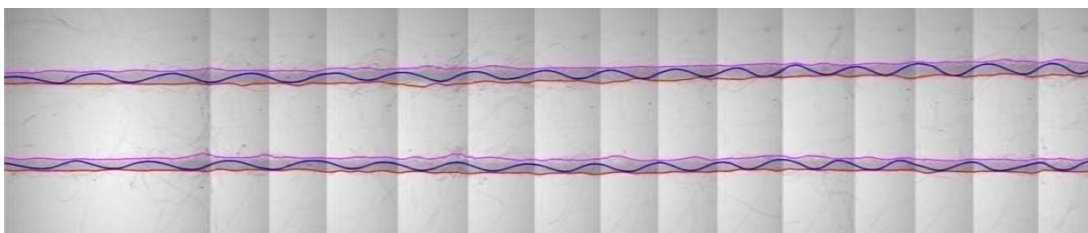
(9) 10Ne yarn-sample 9 (10Ne-s9)



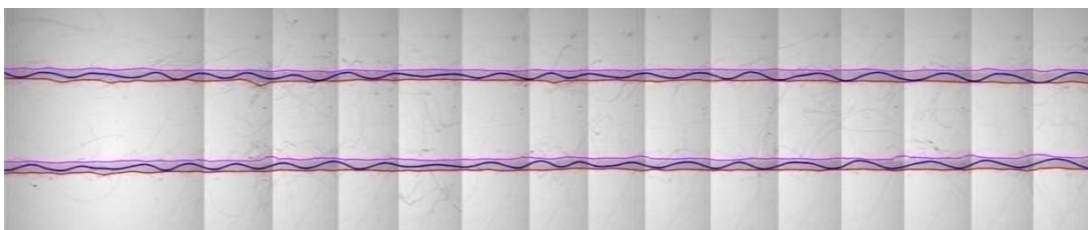
(10) 10Ne yarn-sample 10 (10Ne-s10)



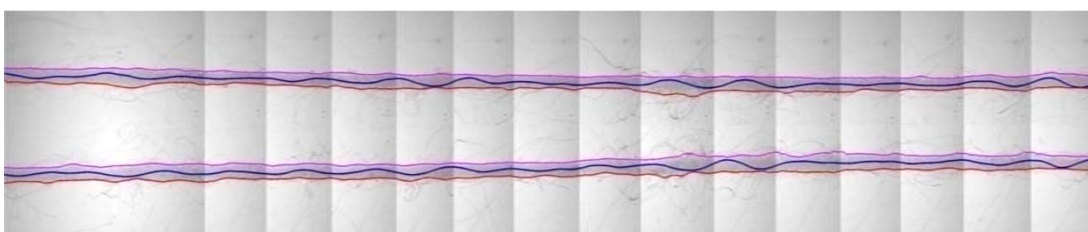
(11) 20Ne yarn-sample 1 (20Ne-s1)



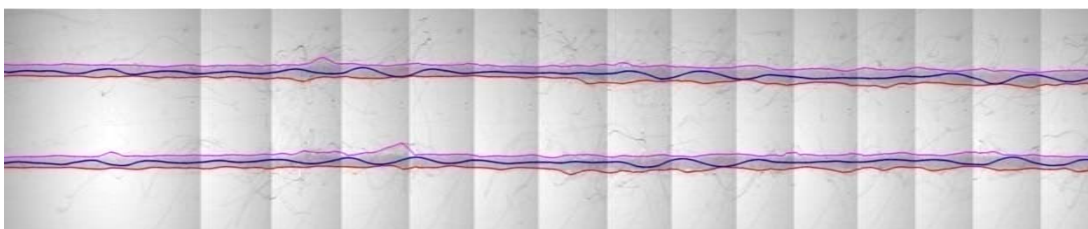
(12) 20Ne yarn-sample 2 (20Ne-s2)



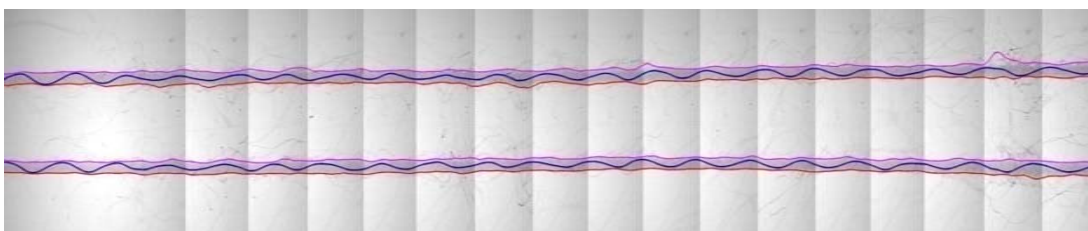
(13) 20Ne yarn-sample 3 (20Ne-s3)



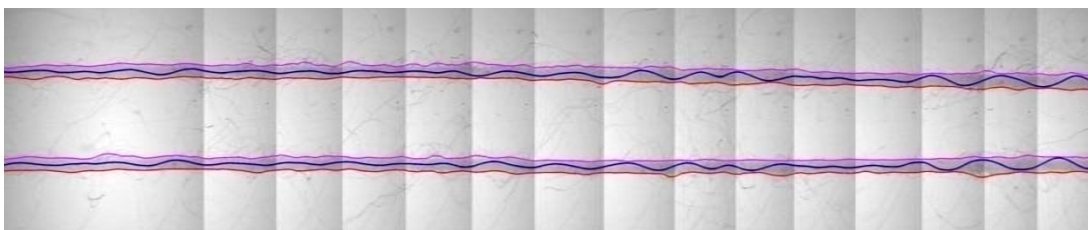
(14) 20Ne yarn-sample 4 (20Ne-s4)



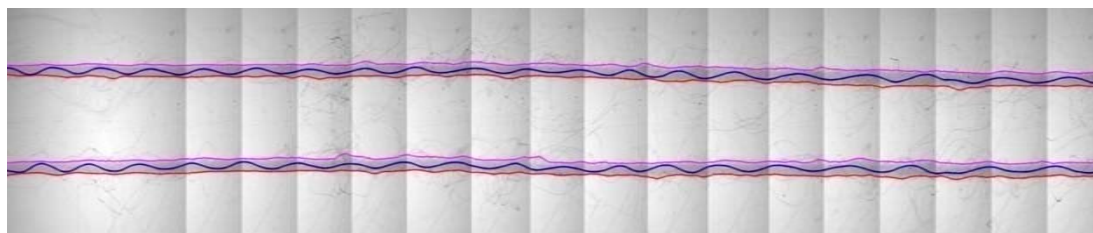
(15) 20Ne yarn-sample 5 (20Ne-s5)



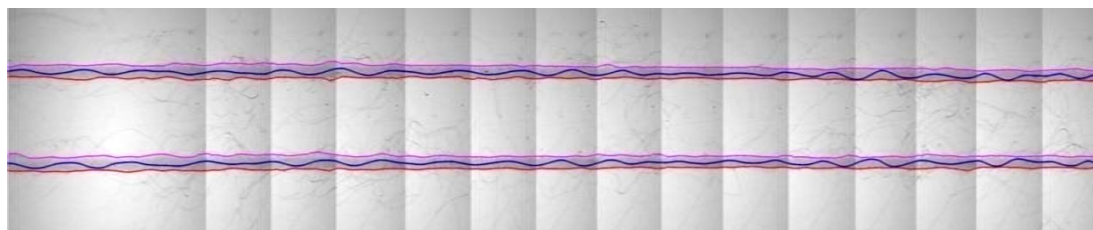
(16) 20Ne yarn-sample 6 (20Ne-s6)



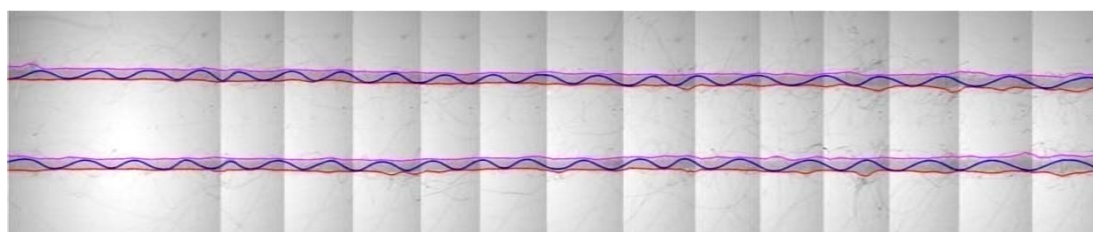
(17) 20Ne yarn-sample 7 (20Ne-s7)



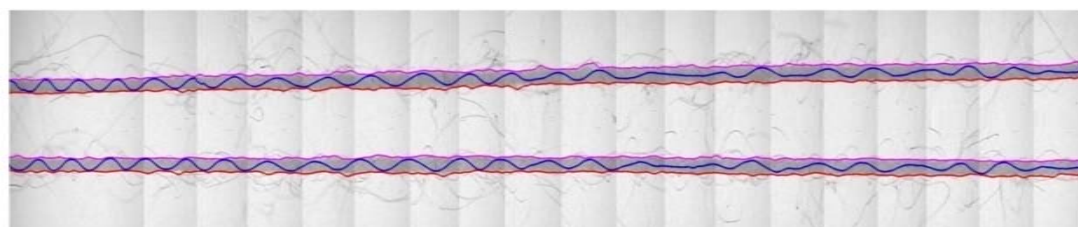
(18) 20Ne yarn-sample 8 (20Ne-s8)



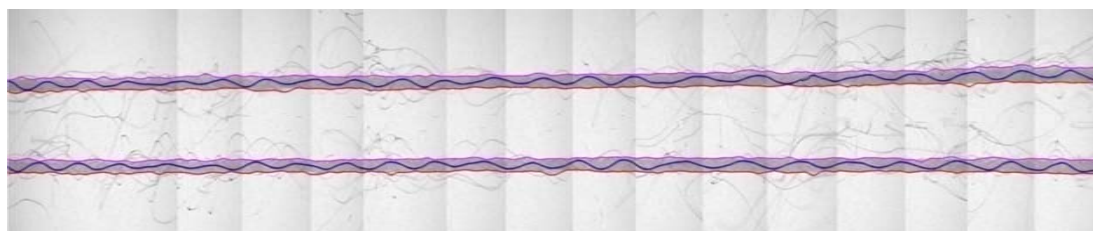
(19) 20Ne yarn-sample 9 (20Ne-s9)



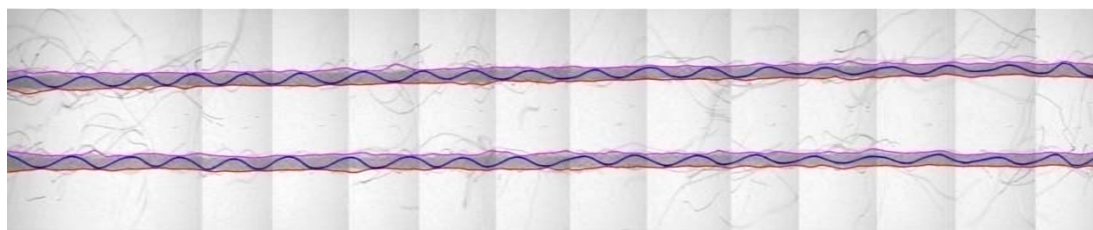
(20) 20Ne yarn-sample 10 (20Ne-s10)



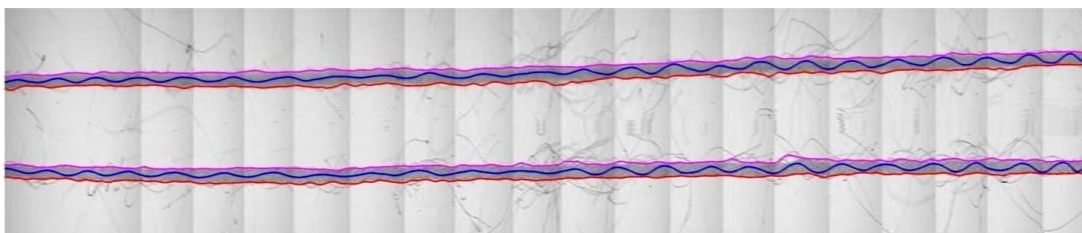
(21) 30Ne yarn-sample 1 (30Ne-s1)



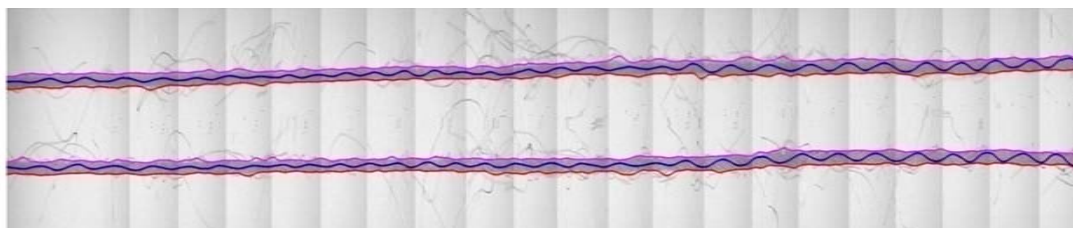
(22) 30Ne yarn-sample 2 (30Ne-s2)



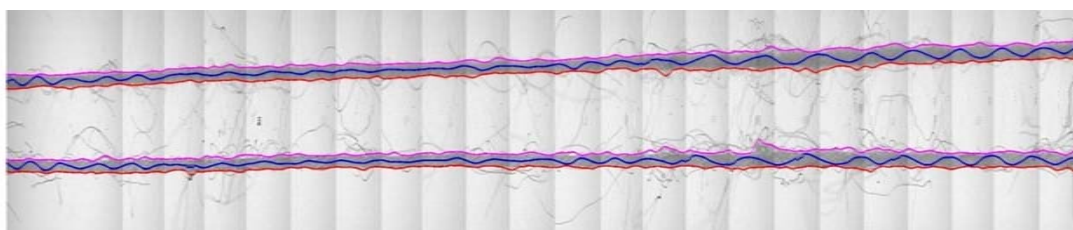
(23) 30Ne yarn-sample 3 (30Ne-s3)



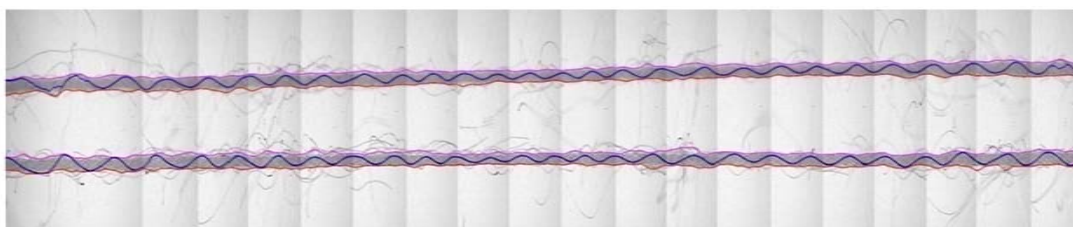
(24) 30Ne yarn-sample 4 (30Ne-s4)



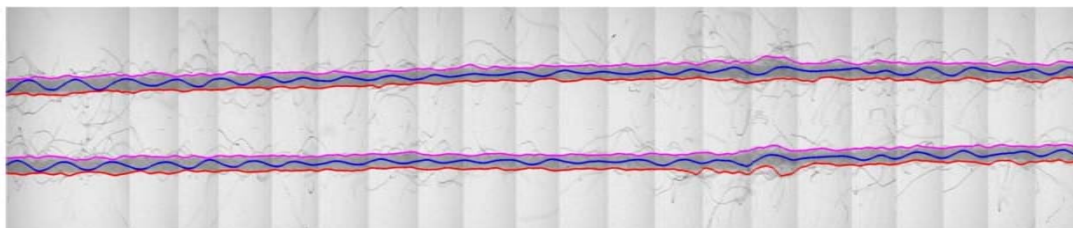
(25) 30Ne yarn-sample 5 (30Ne-s5)



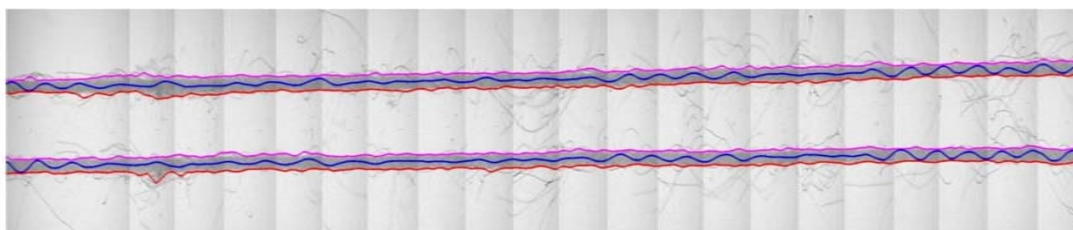
(26) 30Ne yarn-sample 6 (30Ne-s6)



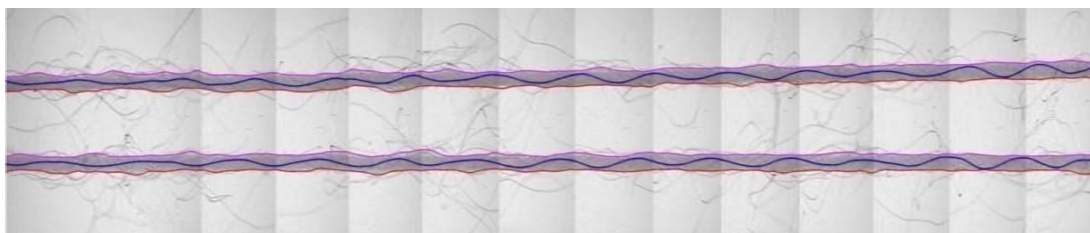
(27) 30Ne yarn-sample 7 (30Ne-s7)



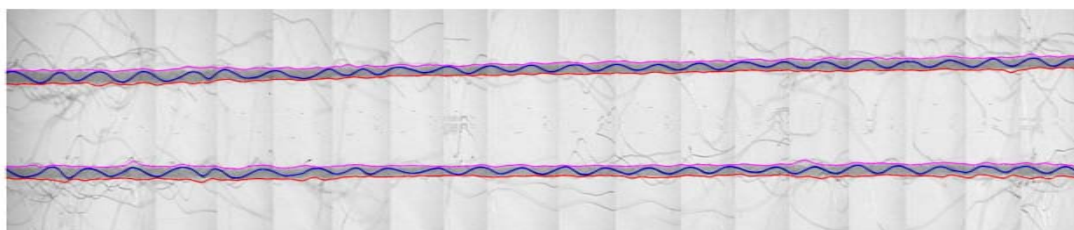
(28) 30Ne yarn-sample 8 (30Ne-s8)



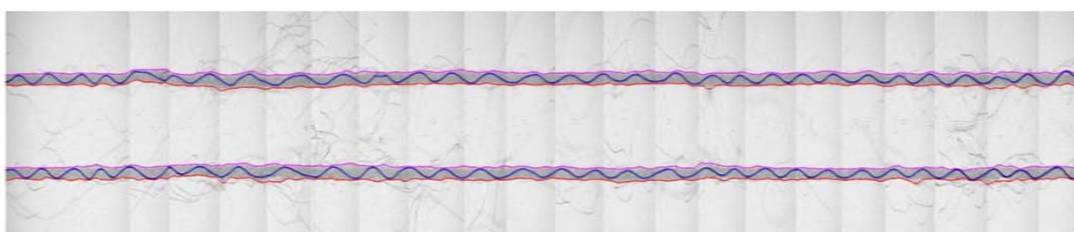
(29) 30Ne yarn-sample 9 (30Ne-s9)



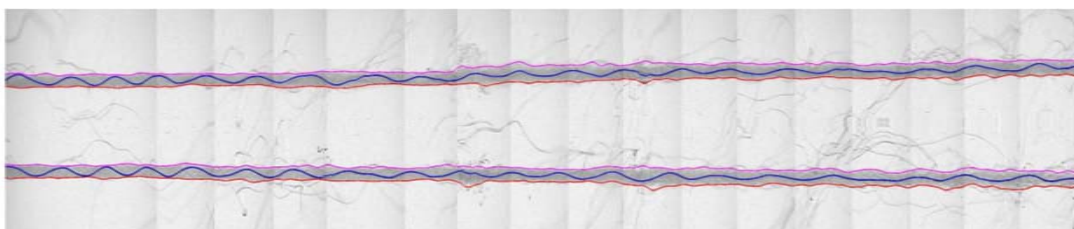
(30) 30Ne yarn-sample 10 (30Ne-s10)



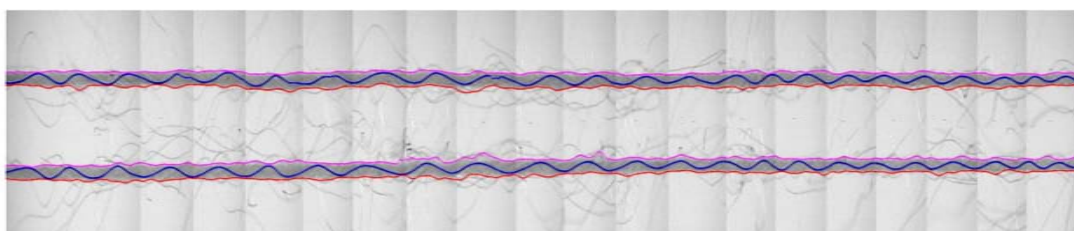
(31) 40Ne yarn-sample 1 (40Ne-s1)



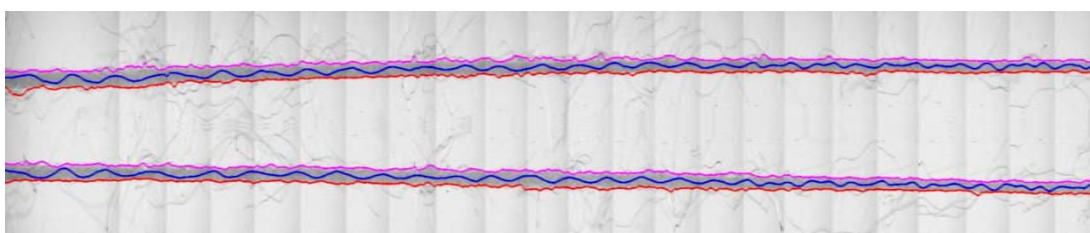
(32) 40Ne yarn-sample 2 (40Ne-s2)



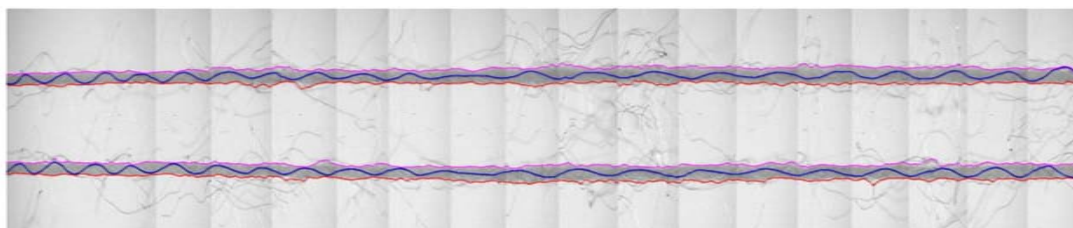
(33) 40Ne yarn-sample 3 (40Ne-s3)



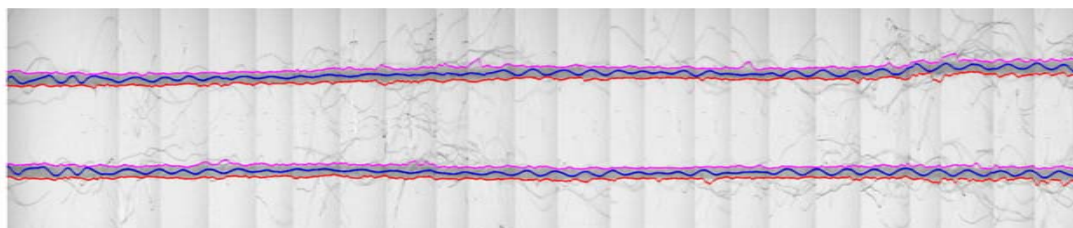
(34) 40Ne yarn-sample 4 (40Ne-s4)



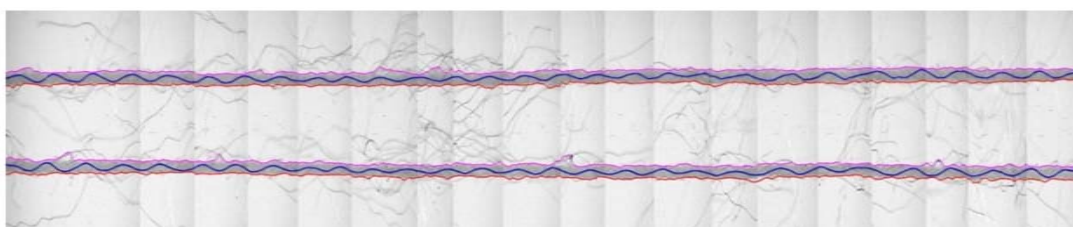
(35) 40Ne yarn-sample 5 (40Ne-s5)



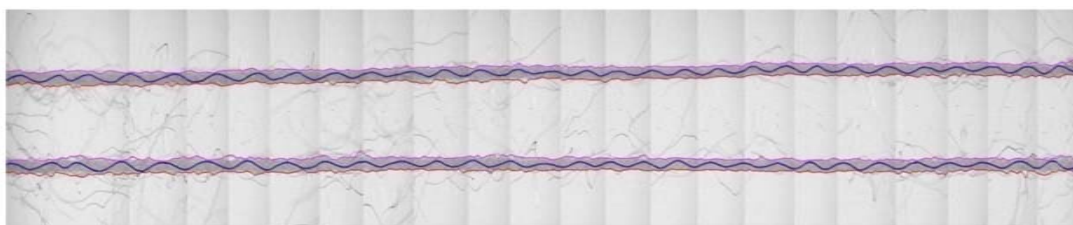
(36) 40Ne yarn-sample 6 (40Ne-s6)



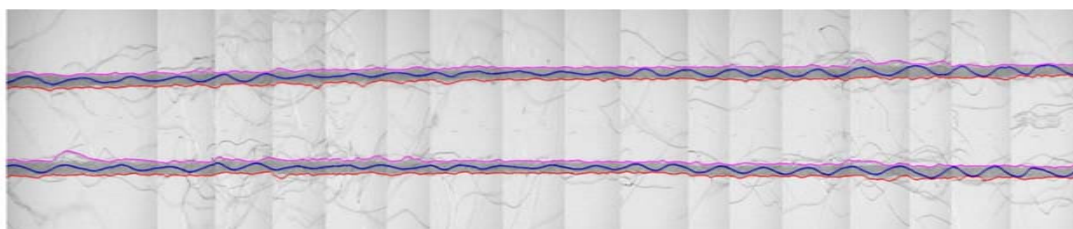
(37) 40Ne yarn-sample 7 (40Ne-s7)



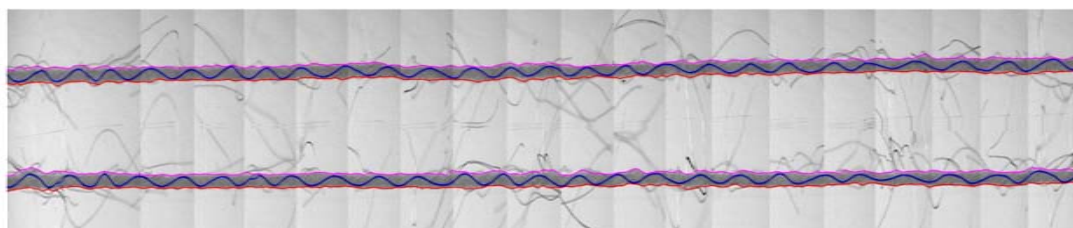
(38) 40Ne yarn-sample 8 (40Ne-s8)



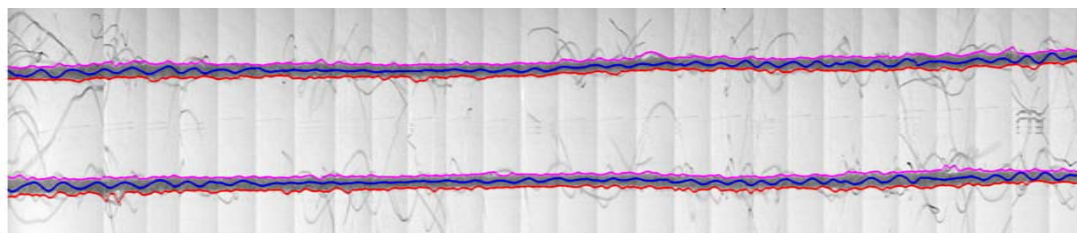
(39) 40Ne yarn-sample 9 (40Ne-s9)



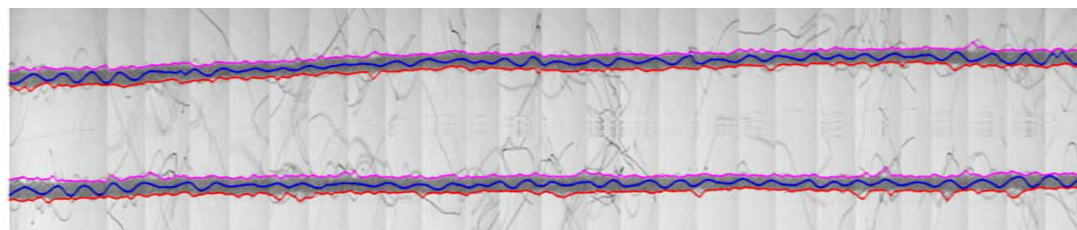
(40) 40Ne yarn-sample 10 (40Ne-s10)



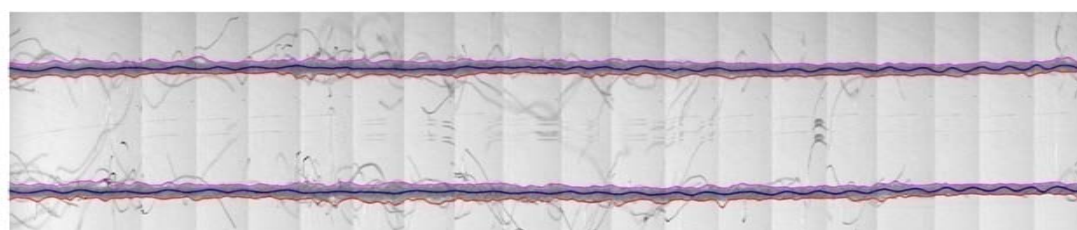
(41) 60Ne yarn-sample 1 (60Ne-s1)



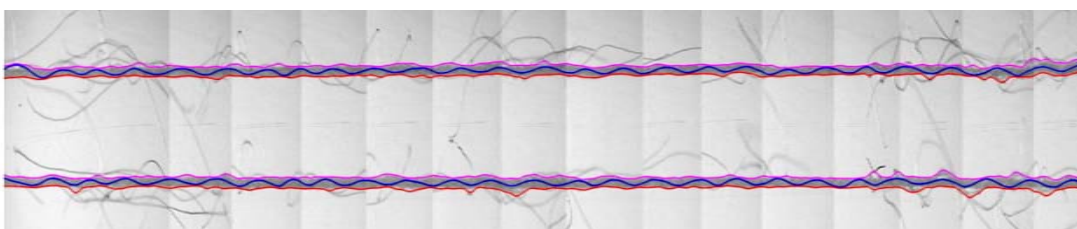
(42) 60Ne yarn-sample 2 (60Ne-s2)



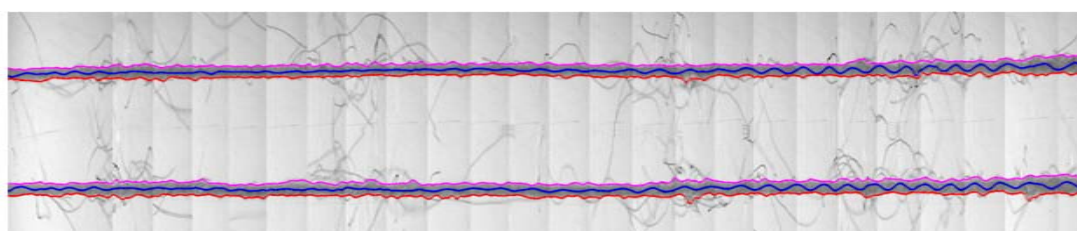
(43) 60Ne yarn-sample 3 (60Ne-s3)



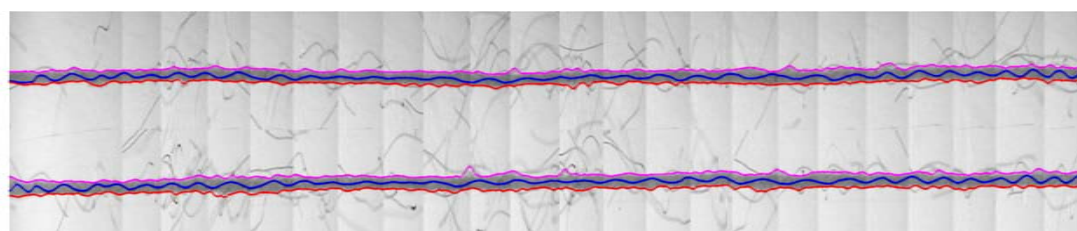
(44) 60Ne yarn-sample 4 (60Ne-s4)



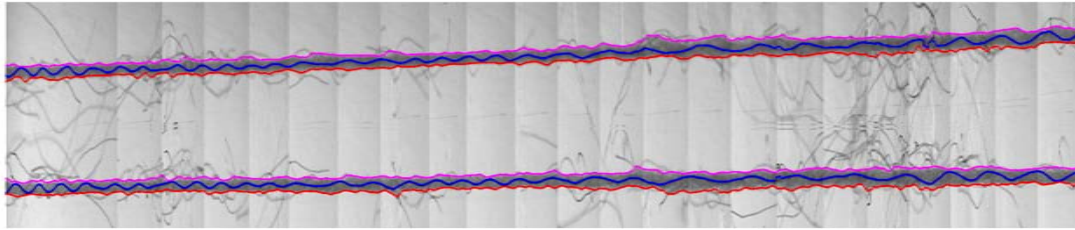
(45) 60Ne yarn-sample 5 (60Ne-s5)



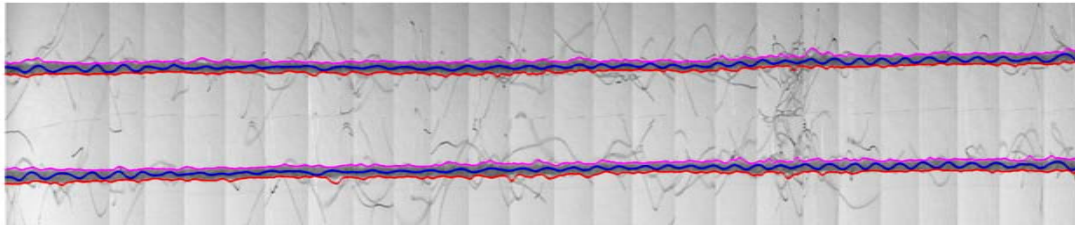
(46) 60Ne yarn-sample 6 (60Ne-s6)



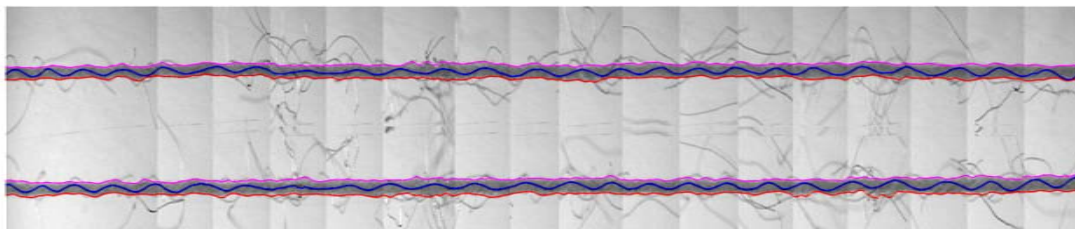
(47) 60Ne yarn-sample 7 (60Ne-s7)



(48) 60Ne yarn-sample 8 (60Ne-s8)



(49) 60Ne yarn-sample 9 (60Ne-s9)



(50) 60Ne yarn-sample 10 (60Ne-s10)

Appendix B: Evaluation results of the image mosaic

Yarn count	Sample No	Number of images	z^c-z^m (pixels)	y^c-y^m (pixels)	x^c-x^m (pixels)	Ez_i (%)		Ey_i (%)		Ex_i (%)	
						M	SD	M	SD	M	SD
10Ne	s1	15	0~9	0~2	0~4	0.59	0.48	1.79	2.02	3.79	3.91
	s2	15	1~8	0~1	0~2	0.57	0.31	1.28	1.33	1.28	1.67
	s3	11	1~7	0~2	0~3	0.77	0.39	2.11	2.08	3.16	2.72
	s4	15	1~7	0~2	0~2	0.76	0.29	2.73	2.15	2.10	2.14
	s5	9	1~6	1~1	0~1	0.69	0.26	2.94	0.00	1.84	1.52
	s6	13	1~9	0~2	0~3	0.83	0.48	3.10	2.57	3.33	2.39
	s7	13	0~9	0~3	0~2	0.71	0.53	4.29	3.28	2.53	1.75
	s8	15	0~7	0~3	0~2	0.74	0.31	4.05	3.50	3.57	2.76
	s9	9	2~9	0~2	0~3	1.14	0.37	3.13	2.89	3.91	3.23
	s10	11	1~8	0~2	0~2	0.62	0.45	1.82	2.56	2.73	2.65
20Ne	s1	11	0~7	0~2	0~3	0.73	0.39	4.44	2.34	4.07	3.68
	s2	15	2~7	0~3	0~3	0.77	0.27	2.71	3.36	3.20	3.44
	s3	15	2~9	0~2	0~2	0.88	0.32	3.87	4.16	3.87	3.04
	s4	15	3~9	0~3	0~2	0.93	0.26	2.71	3.08	2.46	2.11
	s5	15	2~10	0~2	0~1	1.01	0.42	2.30	2.26	2.04	1.83
	s6	17	1~7	0~2	0~3	0.68	0.25	3.94	3.16	4.40	3.09
	s7	15	1~10	0~3	0~2	0.91	0.46	3.57	2.80	3.06	2.75
	s8	17	1~8	0~2	0~2	0.77	0.31	3.66	2.94	2.37	2.43
	s9	15	0~9	0~2	0~1	0.71	0.38	3.02	2.69	2.75	1.80
	s10	14	2~8	1~4	0~3	0.88	0.32	8.58	4.20	6.51	3.29
30Ne	s1	19	1~13	0~3	0~4	0.82	0.50	3.47	2.81	4.34	3.06
	s2	15	1~11	0~3	0~3	0.95	0.56	3.57	3.43	4.59	3.55
	s3	13	3~7	1~3	0~5	0.91	0.24	5.11	2.56	4.30	5.02
	s4	19	1~10	0~4	0~3	1.02	0.46	3.33	3.62	4.07	3.34

Appendices

	s5	21	1~11	0~4	0~5	0.90	0.43	3.89	4.07	4.44	4.59
	s6	23	2~14	0~1	0~3	1.01	0.55	2.35	1.47	3.08	2.72
	s7	19	2~10	0~7	0~4	1.08	0.31	6.13	5.36	5.75	3.74
	s8	21	0~13	0~2	0~3	0.93	0.59	2.88	2.30	3.64	2.88
	s9	21	0~15	0~4	0~3	0.92	0.59	3.06	3.05	3.55	3.12
	s10	13	1~10	0~4	0~3	0.68	0.53	2.94	3.55	3.92	2.61
40Ne	s1	17	1~9	0~3	0~4	0.77	0.41	3.70	3.83	5.79	4.05
	s2	21	2~12	0~5	0~4	1.06	0.42	6.43	5.26	4.11	3.89
	s3	17	1~13	0~1	0~2	0.96	0.53	1.56	1.61	2.73	2.52
	s4	19	0~9	0~4	0~6	0.81	0.45	5.20	3.16	4.30	4.82
	s5	23	1~11	0~3	0~3	0.89	0.48	1.99	2.98	3.98	2.58
	s6	17	0~14	0~3	0~3	0.90	0.55	3.41	3.11	3.03	2.71
	s7	23	0~13	0~3	0~2	0.87	0.49	2.92	2.84	2.44	2.03
	s8	19	0~11	0~2	0~2	0.78	0.57	3.07	1.63	3.26	2.50
	s9	21	0~8	0~2	0~2	0.72	0.38	3.39	2.21	2.42	2.31
	s10	17	2~8	0~3	0~5	0.82	0.35	2.71	3.04	4.38	4.34
60Ne	s1	19	1~14	0~5	0~11	0.90	0.54	5.74	4.09	6.30	9.14
	s2	27	1~15	0~3	0~4	1.19	0.61	3.02	2.98	3.71	2.94
	s3	26	1~13	0~4	0~4	1.11	0.54	4.13	3.78	5.29	3.83
	s4	19	0~15	0~2	0~3	1.04	0.68	3.07	2.62	3.83	3.53
	s5	15	0~8	0~7	0~4	0.79	0.41	7.14	8.29	7.14	5.29
	s6	25	0~13	0~2	0~3	0.93	0.54	2.38	2.72	2.83	3.33
	s7	23	0~10	0~3	0~4	0.96	0.47	3.08	2.54	4.06	4.02
	s8	23	0~16	0~4	0~4	1.16	0.79	3.08	3.54	4.87	3.90
	s9	25	0~8	0~3	0~3	0.66	0.41	3.83	3.23	4.50	3.19
	s10	17	1~12	0~3	0~5	0.92	0.51	5.21	3.21	5.42	5.00

Note: The absolute error is presented by the range of difference (z^c-z^m , y^c-y^m and x^c-x^m) and the relative error is presented by the mean (M) and standard deviation (SD) of Ez_i , Ey_i and Ex_i .

Appendix C: Evaluation results of the image segmentation

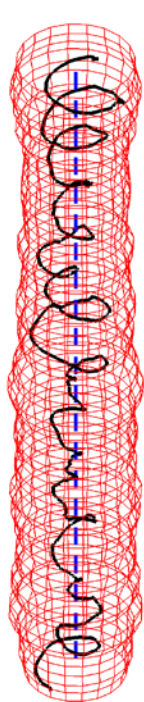
Yarn count	Sample No	D (pixels)	d (pixels)	Δd_y (%)	Δd_x (%)	Δl_1 (%)	Δl_2 (%)	Δl_3 (%)	Δl_4 (%)	Δl_5 (%)	Δl_6 (%)
10Ne	s1	32	31	6.35	6.86	4.51	1.45	5.93	4.67	1.17	4.23
	s2	38	39	7.25	7.78	4.30	1.16	4.69	3.74	0.91	5.53
	s3	37	36	5.35	6.54	3.52	1.39	4.30	4.10	0.95	5.17
	s4	33	33	8.07	5.75	4.87	1.50	6.84	3.32	1.06	4.57
	s5	33	34	6.95	6.64	4.09	1.37	6.36	4.58	0.97	5.13
	s6	35	34	6.44	4.75	4.13	1.81	5.12	4.42	1.26	4.31
	s7	33	32	5.99	5.73	4.70	1.86	4.59	3.81	1.38	4.56
	s8	31	30	6.54	6.70	3.20	2.04	6.00	3.38	1.08	6.42
	s9	32	30	7.62	4.71	4.48	1.91	5.37	3.92	1.34	4.40
	s10	33	33	8.21	6.97	3.49	1.18	7.09	4.26	0.99	5.12
20Ne	s1	27	24	8.42	9.60	4.66	1.94	7.79	5.18	1.41	6.10
	s2	28	27	8.42	7.92	2.83	2.05	7.82	4.39	1.33	5.25
	s3	23	22	7.48	6.37	4.29	2.15	9.30	4.64	1.81	6.53
	s4	29	27	5.74	7.09	3.39	1.73	6.21	3.71	1.77	5.25
	s5	27	27	9.09	8.86	3.87	2.14	9.72	5.39	1.89	6.63
	s6	27	26	7.77	9.68	5.08	2.05	3.57	6.11	2.07	4.33
	s7	27	26	7.68	7.41	5.42	1.62	3.59	6.46	1.18	3.63
	s8	28	27	6.36	8.49	3.74	1.33	5.76	5.37	1.04	5.08
	s9	25	25	7.92	5.54	4.47	1.92	6.56	4.32	1.60	5.01
	s10	25	24	8.04	7.83	6.11	2.08	9.35	4.15	1.37	7.82
30Ne	s1	32	30	5.31	5.57	3.85	1.88	2.53	3.31	1.44	3.03
	s2	28	26	5.67	7.84	4.14	1.86	2.72	3.38	1.94	5.43
	s3	30	29	5.56	9.00	4.75	1.75	2.62	6.14	1.86	3.91
	s4	29	28	5.40	6.69	3.71	1.58	3.81	4.29	1.59	3.18

Appendices

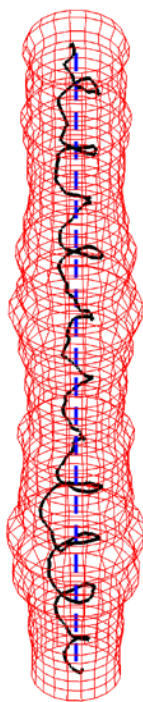
	s5	27	26	7.87	6.31	5.27	1.59	4.30	3.80	1.50	3.28
	s6	30	29	4.55	7.74	3.76	1.87	2.74	4.80	1.68	3.93
	s7	29	27	7.08	10.63	5.76	3.20	3.14	6.34	1.86	5.19
	s8	33	31	5.20	8.11	3.59	1.48	2.67	3.38	1.63	5.67
	s9	31	29	7.09	6.05	5.19	1.78	2.98	3.70	1.65	3.68
	s10	34	32	5.15	6.06	4.00	1.50	2.25	2.76	1.52	3.94
40Ne	s1	27	24	9.88	8.69	9.10	1.77	3.38	6.25	2.15	4.49
	s2	27	25	9.14	12.28	7.34	2.24	3.60	6.14	1.84	6.67
	s3	31	29	7.47	9.51	6.43	2.35	2.98	5.79	1.74	4.53
	s4	31	28	8.02	10.97	6.12	2.04	4.14	5.62	1.78	5.94
	s5	32	29	10.08	8.34	8.53	1.58	3.62	5.11	1.82	4.38
	s6	32	30	7.85	8.32	6.82	1.79	3.43	4.55	1.78	5.10
	s7	27	25	8.40	10.23	6.47	1.95	4.42	6.70	1.70	4.83
	s8	29	27	7.12	8.97	6.59	1.64	2.90	5.96	1.38	4.60
	s9	30	27	7.94	13.36	6.23	1.45	3.30	7.79	1.40	6.25
	s10	29	27	6.75	7.44	5.13	1.53	3.87	4.93	1.23	3.78
60Ne	s1	29	28	6.78	6.20	3.41	2.34	4.55	4.28	2.01	3.38
	s2	28	27	6.39	7.10	4.30	1.84	4.05	3.81	1.72	5.09
	s3	31	30	7.22	9.09	4.79	2.11	4.59	5.21	1.25	5.34
	s4	29	28	7.70	6.94	4.58	1.60	4.17	3.76	1.18	4.61
	s5	22	22	7.82	10.09	5.45	2.97	4.60	5.67	3.16	6.78
	s6	28	26	8.68	9.68	5.19	1.76	4.81	5.59	1.94	5.49
	s7	27	26	6.94	8.13	4.38	1.98	3.70	4.20	1.81	4.92
	s8	28	28	6.94	6.59	4.04	2.58	4.72	3.81	1.64	4.21
	s9	24	23	9.49	9.22	5.37	1.86	4.96	5.67	1.59	5.12
	s10	29	27	8.00	7.37	4.74	1.54	3.99	3.77	1.52	4.56

Note: D and d are the mean of d_x^m & d_y^m and d_x & d_y , respectively. Δd_y , Δd_x , and Δl_i ($i=1,2,3,4,5,6$) are the relative measures calculated by [Equations \(4.30\)](#) and [\(4.31\)](#).

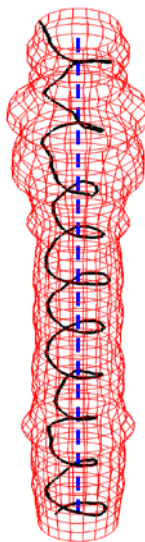
Appendix D: 3D configurations of tracer fiber in yarn



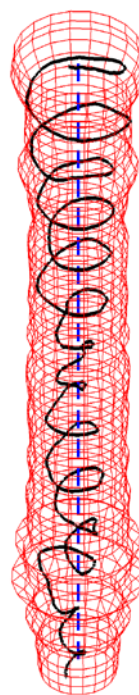
(1) 10Ne-s1



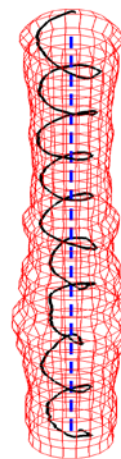
(2) 10Ne-s2



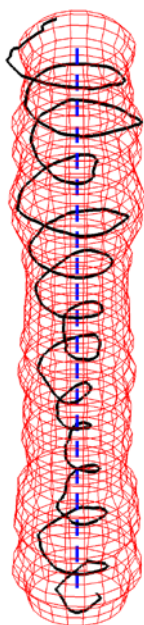
(3) 10Ne-s3



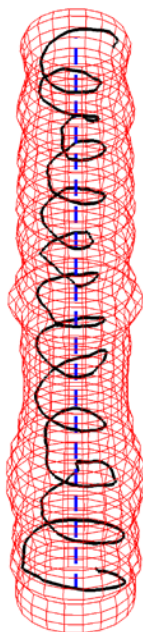
(4) 10Ne-s4



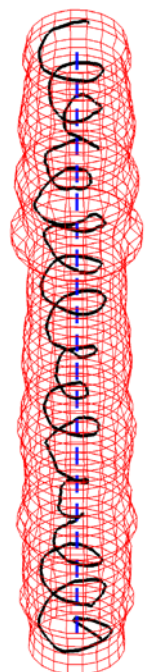
(5) 10Ne-s5



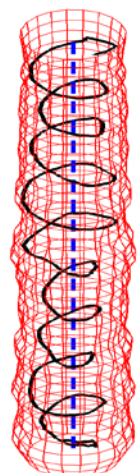
(6) 10Ne-s6



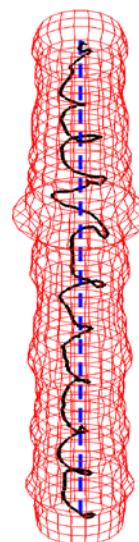
(7) 10Ne-s7



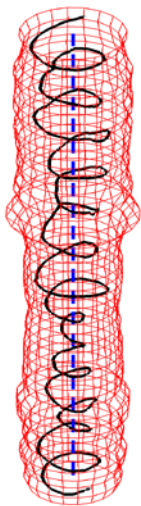
(8) 10Ne-s8



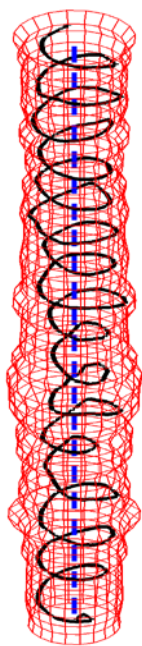
(9) 10Ne-s9



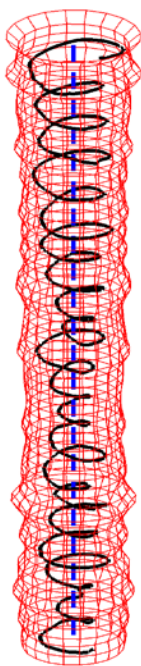
(10) 10Ne-s10



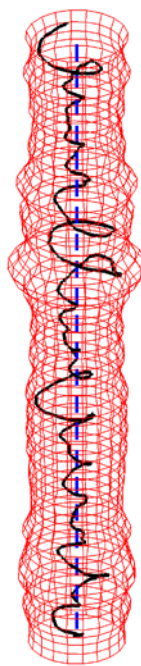
(11) 20Ne-s1



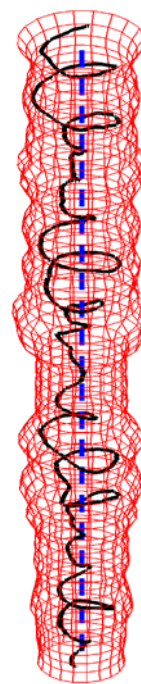
(12) 20Ne-s2



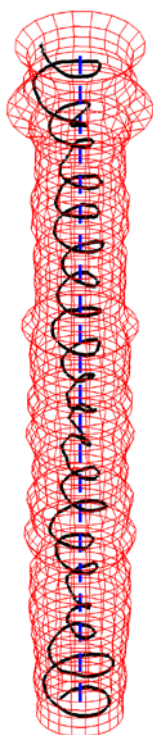
(13) 20Ne-s3



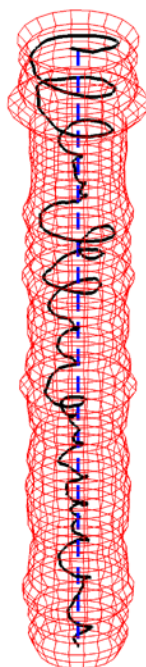
(14) 20Ne-s4



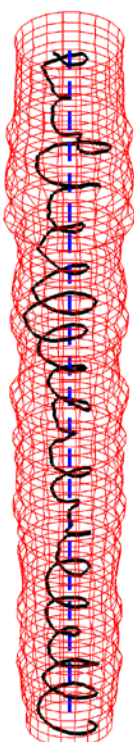
(15) 20Ne-s5



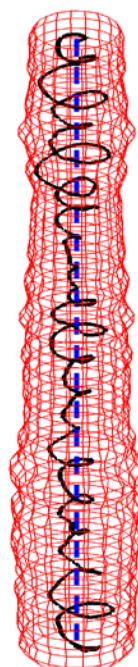
(16) 20Ne-s6



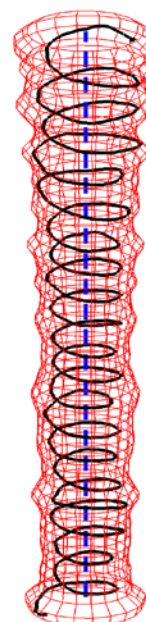
(17) 20Ne-s7



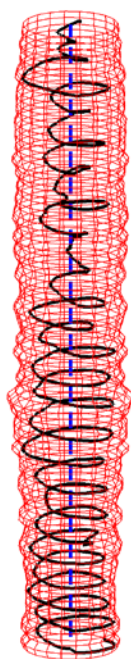
(18) 20Ne-s8



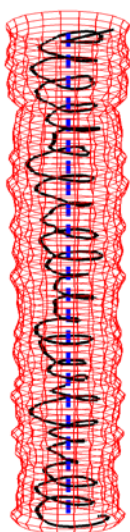
(19) 20Ne-s9



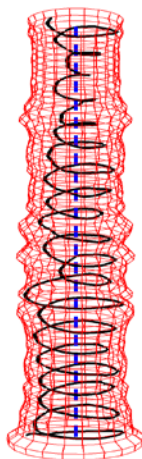
(20) 20Ne-s10



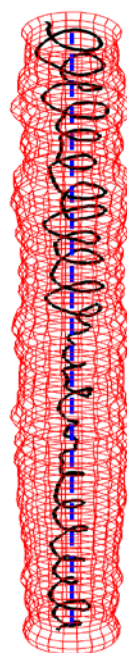
(21) $^{30}\text{Ne-s1}$



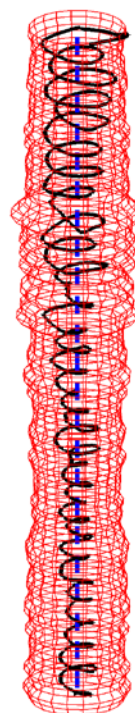
(22) $^{30}\text{Ne-s2}$



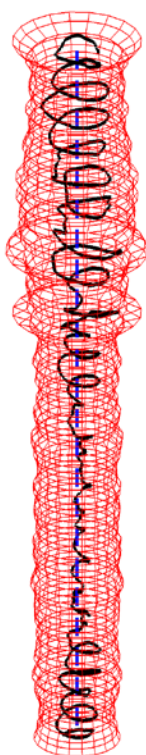
(23) $^{30}\text{Ne-s3}$



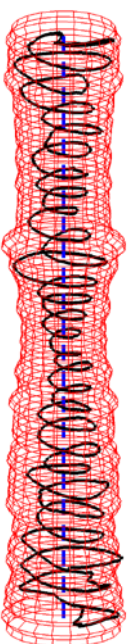
(24) $^{30}\text{Ne-s4}$



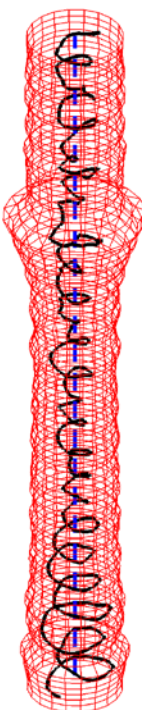
(25) $^{30}\text{Ne-s5}$



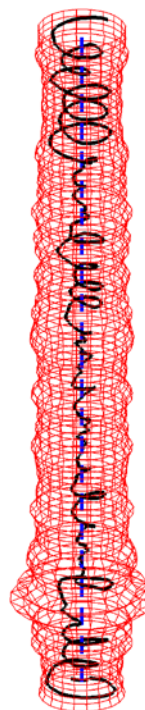
(26) $^{30}\text{Ne-s6}$



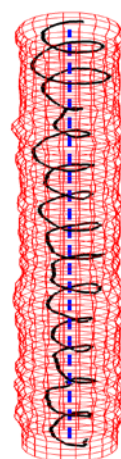
(27) $^{30}\text{Ne-s7}$



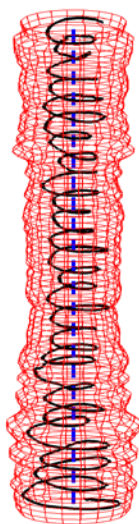
(28) $^{30}\text{Ne-s8}$



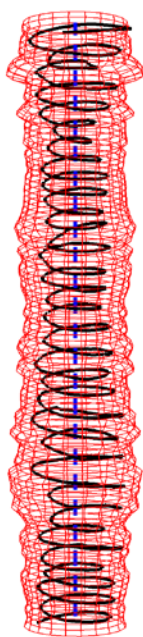
(29) $^{30}\text{Ne-s9}$



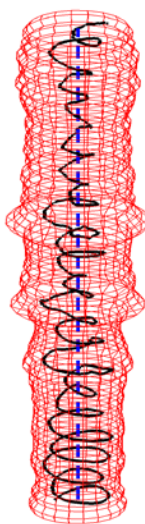
(30) $^{30}\text{Ne-s10}$



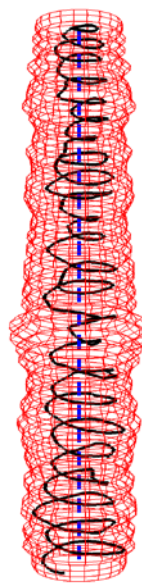
(31) 40Ne-s1



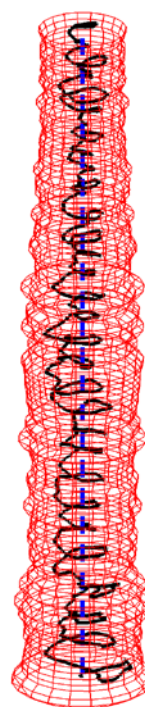
(32) 40Ne-s2



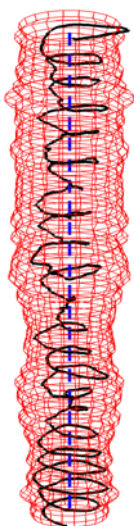
(33) 40Ne-s3



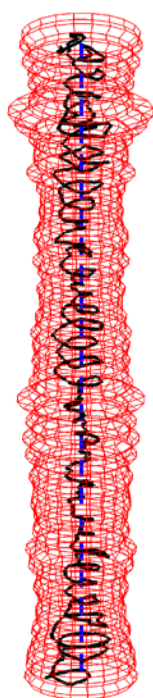
(34) 40Ne-s4



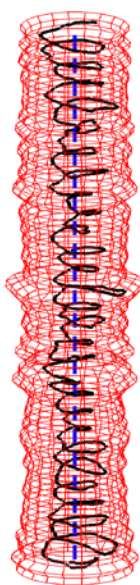
(35) 40Ne-s5



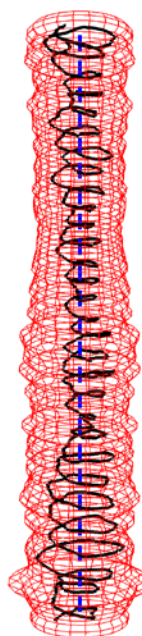
(36) 40Ne-s6



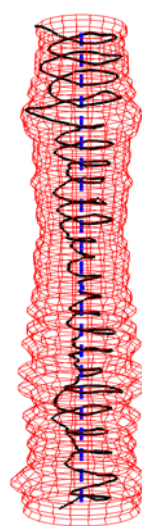
(37) 40Ne-s7



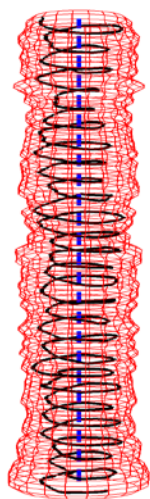
(38) 40Ne-s8



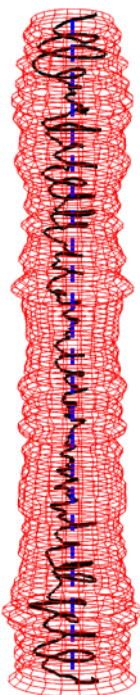
(39) 40Ne-s9



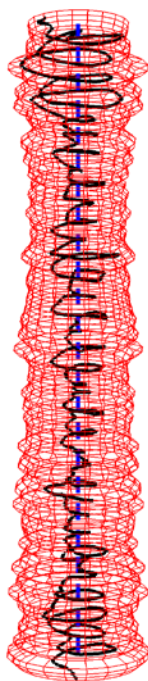
(40) 40Ne-s10



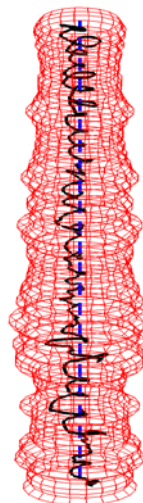
(41) 60Ne-s1



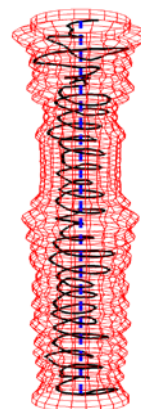
(42) 60Ne-s2



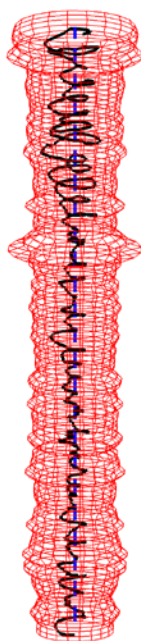
(43) 60Ne-s3



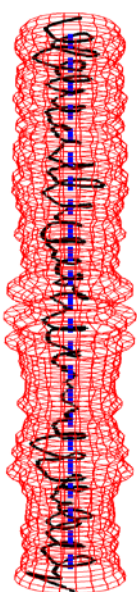
(44) 60Ne-s4



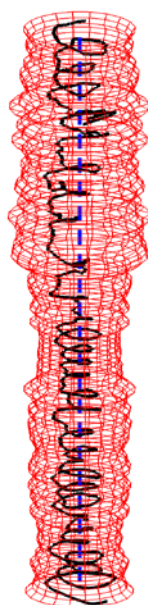
(45) 60Ne-s5



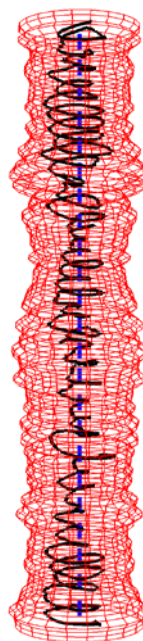
(46) 60Ne-s6



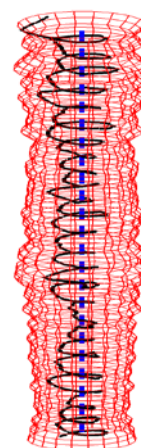
(47) 60Ne-s7



(48) 60Ne-s8



(49) 60Ne-s9



(50) 60Ne-s10

Appendix E: Time taken and the migration parameters

Yarn count	Sample No	Yarn length (mm)	Time taken		Yarn diameter		Fiber migration			
			t_m (s)	t_s (s)	Mean (mm)	CV (%)	MFP	RMSD	MMI (cm ⁻¹)	EMF (cm ⁻¹)
10Ne	s1	32.43	456	21	0.2547	11.04	0.2186	0.2161	6.4972	4.3398
	s2	33.08	443	22	0.3205	14.06	0.1434	0.1091	3.8525	5.0982
	s3	25.90	323	16	0.2958	17.83	0.4116	0.2016	7.2918	5.2202
	s4	32.97	458	22	0.2712	12.16	0.3466	0.2573	6.3676	3.5725
	s5	21.91	266	13	0.2794	12.82	0.3479	0.1619	6.0476	5.3922
	s6	29.80	395	19	0.2794	11.18	0.4382	0.3004	8.7541	4.2061
	s7	29.94	387	19	0.2629	11.77	0.3770	0.2050	7.0936	4.9938
	s8	32.18	367	21	0.2465	11.07	0.2901	0.1915	6.7380	5.0776
	s9	22.43	254	14	0.2465	9.41	0.4381	0.1931	7.0467	5.2666
	s10	25.77	320	16	0.2712	13.77	0.1685	0.1078	5.0736	6.7953
20Ne	s1	23.78	324	15	0.1890	11.33	0.3129	0.1919	8.0763	6.0737
	s2	30.62	456	21	0.2126	11.91	0.4875	0.2255	10.1837	6.5185
	s3	31.54	447	22	0.1732	9.74	0.3151	0.2056	7.8944	5.5408
	s4	31.47	450	21	0.2126	12.16	0.1478	0.1721	5.4504	4.5713
	s5	32.09	453	22	0.2126	15.44	0.2562	0.2393	6.3560	3.8334
	s6	34.97	518	19	0.2047	12.65	0.2511	0.1671	6.5379	5.6460
	s7	31.75	443	18	0.2047	11.16	0.1831	0.1958	5.5239	4.0721
	s8	35.27	442	26	0.2126	10.77	0.2024	0.1367	5.4921	5.7974
	s9	31.81	453	22	0.1969	13.23	0.1945	0.1836	7.0616	5.5509
	s10	29.60	454	20	0.1890	15.74	0.5820	0.1960	13.1493	9.6849
30Ne	s1	30.94	568	31	0.1583	9.25	0.4160	0.2554	13.2630	7.4951
	s2	24.99	441	26	0.1372	9.73	0.2905	0.1694	13.5883	11.5810
	s3	21.70	382	24	0.1530	12.08	0.4525	0.1976	13.5950	9.9296
	s4	30.62	712	37	0.1478	10.26	0.1993	0.1538	8.7746	8.2329

	s5	33.49	774	39	0.1372	10.53	0.2215	0.1847	9.0807	7.0970
	s6	35.73	865	25	0.1530	16.71	0.2066	0.1732	8.9705	7.4756
	s7	30.51	693	23	0.1425	12.26	0.4225	0.2374	18.0555	10.9782
	s8	33.47	764	27	0.1636	13.95	0.1840	0.1529	6.1124	5.7682
	s9	33.44	767	27	0.1530	12.69	0.1739	0.1975	8.3535	6.1055
	s10	21.58	463	19	0.1689	7.71	0.2664	0.1535	7.1858	6.7574
40Ne	s1	24.83	500	22	0.1086	13.06	0.3303	0.1608	14.1187	12.6696
	s2	30.07	646	25	0.1131	11.50	0.4373	0.1656	17.4678	15.2293
	s3	24.56	503	22	0.1312	14.67	0.2196	0.1799	12.3727	9.9242
	s4	27.46	568	23	0.1267	13.14	0.3371	0.1734	13.8943	11.5628
	s5	33.19	695	29	0.1312	16.72	0.1734	0.1209	11.1366	13.2990
	s6	24.80	506	24	0.1357	15.15	0.3423	0.2343	17.5678	10.8205
	s7	33.02	716	30	0.1131	15.33	0.1739	0.1475	14.9102	14.5918
	s8	27.55	684	26	0.1222	12.36	0.2336	0.1467	15.1398	14.8973
	s9	29.95	839	27	0.1222	13.50	0.2550	0.1658	14.2879	12.4356
	s10	24.54	419	24	0.1222	14.85	0.2803	0.2281	18.2206	11.5283
60Ne	s1	23.70	571	29	0.1157	10.53	0.4323	0.1694	19.6632	16.7519
	s2	32.98	841	31	0.1116	13.40	0.1396	0.1317	11.3832	12.4794
	s3	32.11	815	28	0.1240	13.66	0.2027	0.1824	14.8064	11.7180
	s4	23.86	576	23	0.1157	16.68	0.0792	0.0711	7.7399	15.7230
	s5	19.37	448	20	0.0909	16.91	0.3042	0.1692	20.5649	17.5402
	s6	30.46	768	42	0.1074	15.56	0.1081	0.1108	10.9187	14.2191
	s7	27.94	730	25	0.1074	12.97	0.1620	0.1398	12.4062	12.8104
	s8	28.50	705	33	0.1157	17.40	0.2042	0.1480	17.7844	17.3450
	s9	30.37	761	27	0.0950	13.87	0.1657	0.1329	13.1688	14.3010
	s10	21.03	516	27	0.1116	11.59	0.2010	0.1438	13.1527	13.2030

t_m and t_s : time taken for image mosaic and segmentation, MFP: mean fiber position, RMSD: RMS deviation, MMI: mean migration intensity, EMF: equivalent migration frequency.

Appendix F: Features of yarn board image(1) Features extracted from yarn diameter and hairs: $f_1 \sim f_8$

Sample No	Index	f_1	f_2	f_3	f_4	f_5	f_6	f_7	f_8
7Ne_S1	80	7.8382	0.2040	0.0246	0.0001	0.0000	0.8774	4.7594	5.7112
7Ne_S2	80	7.7764	0.2008	0.0207	0.0001	0.0000	0.8716	4.9620	5.7271
7Ne_S3	80	7.8591	0.2170	0.0302	0.0002	0.0000	0.8435	4.6441	5.6309
7Ne_S4	80	7.8830	0.2112	0.0288	0.0001	0.0000	0.7967	4.3914	5.6022
7Ne_S5	80	7.2240	0.1834	0.0190	0.0003	0.0000	0.9783	5.7430	6.0365
7Ne_S6	80	7.1832	0.1769	0.0161	0.0001	0.0000	0.9919	5.7345	6.0310
7Ne_S7	80	7.1828	0.1804	0.0170	0.0002	0.0000	1.0433	6.2599	6.0417
7Ne_S8	80	7.1397	0.1795	0.0155	0.0019	0.0000	0.8607	5.6623	6.0495
7Ne_S9	90	7.7367	0.1901	0.0155	0.0003	0.0000	0.8242	4.8495	5.9258
7Ne_S10	90	7.8128	0.1901	0.0181	0.0003	0.0000	0.8464	4.9248	5.8902
7Ne_S11	90	7.5792	0.1839	0.0110	0.0003	0.0000	0.8351	5.1857	5.9565
7Ne_S12	90	7.6083	0.1817	0.0113	0.0002	0.0000	0.7834	4.6689	5.9379
7Ne_S13	90	7.4659	0.1641	0.0056	0.0001	0.0000	0.7890	4.8324	5.9723
7Ne_S14	90	7.4422	0.1620	0.0050	0.0001	0.0000	0.8197	5.2328	5.9787
7Ne_S15	90	7.4027	0.1543	0.0039	0.0002	0.0000	0.7788	5.2245	5.9907
7Ne_S16	90	7.4655	0.1547	0.0042	0.0002	0.0000	0.7558	4.9637	5.9629
7Ne_S17	100	7.5166	0.1562	0.0043	0.0002	0.0000	0.7081	4.6151	5.9632
7Ne_S18	100	7.5334	0.1539	0.0040	0.0001	0.0000	0.6977	4.5914	5.9509
7Ne_S19	100	7.4473	0.1623	0.0052	0.0001	0.0000	0.7780	5.0032	5.9851
7Ne_S20	100	7.4242	0.1614	0.0048	0.0002	0.0000	0.7435	4.8604	5.9994
7Ne_S21	110	7.9805	0.1675	0.0096	0.0001	0.0000	0.4867	3.5440	5.3821
7Ne_S22	110	7.9694	0.1678	0.0099	0.0000	0.0000	0.4964	3.5022	5.3464
7Ne_S23	110	7.9051	0.1708	0.0099	0.0004	0.0000	0.5033	3.6569	5.4575
7Ne_S24	110	7.9843	0.1635	0.0083	0.0000	0.0000	0.4575	3.4794	5.3857
7Ne_S25	120	8.0076	0.1702	0.0024	0.0003	0.0000	0.4487	3.7002	5.4755
7Ne_S26	120	8.0599	0.1692	0.0027	0.0009	0.0000	0.3645	3.5226	5.4718
7Ne_S27	120	8.1274	0.1738	0.0036	0.0004	0.0000	0.3553	3.2746	5.3369
7Ne_S28	120	8.1042	0.1767	0.0037	0.0006	0.0000	0.4080	3.3804	5.3709
7Ne_S29	120	8.3254	0.1303	0.0004	0.0000	0.0000	0.2394	3.2190	5.7067
7Ne_S30	120	8.3121	0.1320	0.0004	0.0001	0.0000	0.2217	3.2025	5.7112
7Ne_S31	120	8.3803	0.1218	0.0005	0.0001	0.0000	0.2943	3.5617	5.7100
7Ne_S32	120	8.4245	0.1193	0.0002	0.0000	0.0000	0.2336	3.1889	5.6898

Sample No	Index	f_1	f_2	f_3	f_4	f_5	f_6	f_7	f_8
7Ne_S33	120	7.6749	0.1304	0.0006	0.0000	0.0000	0.3236	3.3203	5.6730
7Ne_S34	120	7.6886	0.1306	0.0006	0.0000	0.0000	0.2977	3.2879	5.6173
7Ne_S35	120	7.6401	0.1338	0.0005	0.0004	0.0000	0.2020	3.4040	5.6367
7Ne_S36	120	7.6697	0.1327	0.0006	0.0001	0.0000	0.2905	3.3568	5.5968
7Ne_S37	120	7.6361	0.1228	0.0012	0.0000	0.0000	0.3845	3.9293	5.5820
7Ne_S38	120	7.6034	0.1213	0.0003	0.0000	0.0000	0.3093	4.0304	5.6464
7Ne_S39	130	8.3714	0.1269	0.0006	0.0000	0.0000	0.2541	3.4442	5.7368
7Ne_S40	130	8.3565	0.1249	0.0006	0.0000	0.0000	0.3125	3.5379	5.7306
7Ne_S41	130	8.5127	0.1328	0.0007	0.0001	0.0000	0.1847	3.1647	5.7115
7Ne_S42	130	8.5221	0.1290	0.0009	0.0000	0.0000	0.2523	3.4502	5.6905
7Ne_S43	130	7.7848	0.1232	0.0004	0.0000	0.0000	0.2428	3.2585	5.6879
7Ne_S44	130	7.8878	0.1212	0.0004	0.0000	0.0000	0.2431	3.1609	5.6405
7Ne_S45	130	7.8790	0.1238	0.0005	0.0000	0.0000	0.2428	3.1822	5.6621
7Ne_S46	130	7.8717	0.1243	0.0005	0.0000	0.0000	0.2336	3.2235	5.6412
10Ne_S47	90	7.3396	0.2021	0.0117	0.0001	0.0000	0.8926	4.9605	5.5316
10Ne_S48	90	7.3345	0.2076	0.0139	0.0001	0.0000	0.9537	5.2330	5.5540
10Ne_S49	90	7.3228	0.2125	0.0336	0.0001	0.0000	0.8871	4.7686	5.4539
10Ne_S50	90	7.2725	0.2186	0.0347	0.0002	0.0000	0.8997	4.8625	5.5220
10Ne_S51	100	6.3742	0.1808	0.0145	0.0002	0.0000	1.1076	6.4271	6.1385
10Ne_S52	100	6.3414	0.1849	0.0149	0.0002	0.0000	1.1233	6.3913	6.1627
10Ne_S53	100	6.4350	0.1785	0.0140	0.0002	0.0000	1.0821	6.7912	6.1136
10Ne_S54	100	6.4403	0.1813	0.0146	0.0010	0.0000	1.0199	6.5577	6.1125
10Ne_S55	100	6.4456	0.1807	0.0153	0.0005	0.0000	0.9713	5.7860	6.0783
10Ne_S56	100	6.3905	0.1817	0.0146	0.0003	0.0000	1.1192	6.6591	6.1161
10Ne_S57	110	6.2446	0.1599	0.0068	0.0001	0.0000	1.0496	6.7331	6.1448
10Ne_S58	110	6.1454	0.1643	0.0064	0.0001	0.0000	1.1179	7.4736	6.2110
10Ne_S59	110	6.2650	0.1582	0.0065	0.0001	0.0000	1.0301	6.7390	6.0728
10Ne_S60	110	6.2600	0.1573	0.0066	0.0001	0.0000	1.0444	6.8994	6.0703
10Ne_S61	110	6.3745	0.1617	0.0085	0.0001	0.0000	0.9226	5.7531	6.0963
10Ne_S62	110	6.3116	0.1660	0.0083	0.0005	0.0000	0.9343	6.0288	6.1591
10Ne_S63	120	7.0823	0.1823	0.0082	0.0000	0.0000	0.4115	3.3798	5.4116
10Ne_S64	120	7.0697	0.1799	0.0076	0.0000	0.0000	0.4382	3.3165	5.3600
10Ne_S65	120	7.1631	0.1885	0.0117	0.0001	0.0000	0.3945	3.2901	5.2646
10Ne_S66	120	7.1396	0.1854	0.0100	0.0000	0.0000	0.4108	3.2228	5.1893
10Ne_S67	120	6.9474	0.1336	0.0014	0.0000	0.0000	0.4321	4.1344	5.6456
10Ne_S68	120	7.0000	0.1323	0.0010	0.0004	0.0000	0.2676	3.8082	5.6205

Appendices

Sample No	Index	f_1	f_2	f_3	f_4	f_5	f_6	f_7	f_8
10Ne_S69	120	6.7817	0.1378	0.0005	0.0000	0.0000	0.2994	3.5211	5.6096
10Ne_S70	120	6.7823	0.1371	0.0005	0.0000	0.0000	0.2922	3.4025	5.5930
10Ne_S71	120	6.8607	0.1458	0.0008	0.0001	0.0000	0.3370	3.2846	5.6715
10Ne_S72	120	6.9131	0.1443	0.0010	0.0000	0.0000	0.3171	3.2626	5.6180
10Ne_S73	120	6.8481	0.1437	0.0012	0.0001	0.0000	0.3734	3.4799	5.6503
10Ne_S74	120	6.8609	0.1400	0.0011	0.0000	0.0000	0.3475	3.4531	5.6270
10Ne_S75	130	6.7838	0.1266	0.0006	0.0000	0.0000	0.3583	3.7257	6.0329
10Ne_S76	130	6.7740	0.1296	0.0008	0.0000	0.0000	0.4577	4.6172	6.0701
10Ne_S77	130	6.9779	0.1350	0.0013	0.0000	0.0000	0.3927	3.7576	6.0323
10Ne_S78	130	6.9803	0.1363	0.0016	0.0000	0.0000	0.4493	4.1335	6.0434
10Ne_S79	130	6.9530	0.1363	0.0019	0.0000	0.0000	0.5247	4.3656	6.0242
10Ne_S80	130	6.8657	0.1394	0.0010	0.0000	0.0000	0.4000	3.7035	6.0757
10Ne_S81	130	6.7786	0.1682	0.0028	0.0000	0.0000	0.4630	3.5168	5.3610
10Ne_S82	130	6.7853	0.1713	0.0036	0.0000	0.0000	0.5049	3.5805	5.4596
10Ne_S83	130	6.7951	0.1719	0.0042	0.0001	0.0000	0.5380	3.6513	5.3086
10Ne_S84	130	6.8120	0.1715	0.0040	0.0000	0.0000	0.5414	3.8170	5.3510
10Ne_S85	130	6.7816	0.1769	0.0046	0.0000	0.0000	0.5361	3.7054	5.2574
10Ne_S86	130	6.8035	0.1760	0.0043	0.0000	0.0000	0.5517	4.2400	5.2857
10Ne_S87	130	6.8921	0.1298	0.0007	0.0003	0.0000	0.3174	3.7378	5.6338
10Ne_S88	130	6.8329	0.1292	0.0007	0.0001	0.0000	0.4303	4.2201	5.7270
10Ne_S89	130	6.8846	0.1356	0.0005	0.0003	0.0000	0.2702	3.4996	5.6690
10Ne_S90	130	6.9068	0.1355	0.0006	0.0000	0.0000	0.3249	3.3391	5.6323
16Ne_S91	90	5.4864	0.2253	0.0222	0.0001	0.0000	1.6749	10.1918	6.0622
16Ne_S92	90	5.4618	0.2138	0.0170	0.0001	0.0000	1.2505	7.2091	6.1125
16Ne_S93	90	6.6860	0.2054	0.0107	0.0002	0.0000	0.8053	4.5665	5.2307
16Ne_S94	90	6.6868	0.2083	0.0121	0.0002	0.0000	0.8554	4.6760	5.2872
16Ne_S95	90	6.8246	0.2204	0.0174	0.0004	0.0000	0.8478	4.9015	5.1980
16Ne_S96	90	6.8355	0.2189	0.0185	0.0004	0.0000	0.7558	4.0965	5.2888
16Ne_S97	100	5.2638	0.1930	0.0250	0.0001	0.0001	1.6817	11.0849	6.1568
16Ne_S98	100	5.2222	0.1960	0.0236	0.0000	0.0002	1.9805	14.4067	6.2028
16Ne_S99	100	5.3333	0.1903	0.0276	0.0001	0.0001	1.3975	9.1959	6.1742
16Ne_S100	100	5.3002	0.1909	0.0248	0.0000	0.0001	1.5079	10.6072	6.2458
16Ne_S101	100	5.0766	0.1899	0.0172	0.0000	0.0000	1.3388	8.8119	6.2293
16Ne_S102	100	5.0468	0.1942	0.0189	0.0000	0.0000	1.3664	8.2710	6.2430
16Ne_S103	100	5.1708	0.1914	0.0214	0.0000	0.0000	1.2611	7.7671	6.2570
16Ne_S104	100	5.1557	0.1894	0.0199	0.0000	0.0000	1.2555	7.7667	6.2539

Sample No	Index	f_1	f_2	f_3	f_4	f_5	f_6	f_7	f_8
16Ne_S105	100	5.8103	0.1871	0.0174	0.0000	0.0000	0.9235	5.4981	6.1430
16Ne_S106	100	5.8150	0.1897	0.0186	0.0000	0.0000	1.0088	5.9421	6.1255
16Ne_S107	100	5.9055	0.1840	0.0200	0.0000	0.0000	1.0384	6.4181	6.1826
16Ne_S108	100	5.8686	0.1827	0.0185	0.0000	0.0000	1.0508	6.3250	6.1775
16Ne_S109	110	5.5119	0.1877	0.0080	0.0000	0.0000	0.8618	5.6572	5.3166
16Ne_S110	110	5.5453	0.1838	0.0076	0.0000	0.0000	0.8670	7.0557	5.2837
16Ne_S111	110	5.4999	0.1828	0.0071	0.0003	0.0000	0.7460	5.0091	5.3090
16Ne_S112	110	5.5405	0.1778	0.0063	0.0000	0.0000	0.7553	5.1721	5.2976
16Ne_S113	120	5.0415	0.1506	0.0051	0.0000	0.0000	0.8812	6.9722	5.9550
16Ne_S114	120	5.0646	0.1483	0.0045	0.0000	0.0000	0.8310	7.0352	5.9380
16Ne_S115	120	5.0835	0.1498	0.0057	0.0000	0.0000	0.8809	6.7588	6.0611
16Ne_S116	120	5.0752	0.1509	0.0056	0.0000	0.0000	0.8215	5.9568	6.0636
16Ne_S117	120	5.8256	0.1593	0.0058	0.0000	0.0000	0.4709	3.7409	5.5760
16Ne_S118	120	5.8205	0.1568	0.0054	0.0000	0.0000	0.5055	4.0442	5.5356
16Ne_S119	120	5.8396	0.1601	0.0060	0.0000	0.0000	0.4652	3.7365	5.4951
16Ne_S120	120	5.7937	0.1638	0.0054	0.0004	0.0000	0.4258	3.8420	5.6205
16Ne_S121	120	5.8207	0.1604	0.0053	0.0000	0.0000	0.4224	3.6451	5.6626
16Ne_S122	120	5.8596	0.1580	0.0052	0.0000	0.0000	0.3860	3.5299	5.6041
16Ne_S123	120	5.8226	0.1649	0.0064	0.0000	0.0000	0.4501	3.7863	5.6067
16Ne_S124	120	5.8727	0.1605	0.0062	0.0000	0.0000	0.4575	3.7844	5.5204
16Ne_S125	130	5.2006	0.1489	0.0039	0.0000	0.0000	0.3703	3.5431	5.4098
16Ne_S126	130	5.2722	0.1493	0.0054	0.0000	0.0000	0.4263	3.7190	5.3202
16Ne_S127	130	5.2907	0.1476	0.0053	0.0000	0.0000	0.3792	3.5399	5.2419
16Ne_S128	130	5.3420	0.1489	0.0009	0.0000	0.0000	0.4144	3.7351	5.1950
20Ne_S129	90	5.9823	0.2124	0.0365	0.0000	0.0000	0.9073	5.0677	5.2931
20Ne_S130	90	6.0465	0.2215	0.0152	0.0026	0.0001	0.9810	6.0284	5.3613
20Ne_S131	90	6.0471	0.2308	0.0178	0.0045	0.0000	0.8832	4.8046	5.2537
20Ne_S132	90	6.0179	0.2258	0.0167	0.0040	0.0001	0.9302	5.2157	5.2226
20Ne_S133	100	5.0864	0.2186	0.0272	0.0001	0.0000	1.2726	7.4527	6.0001
20Ne_S134	100	5.0598	0.2279	0.0310	0.0001	0.0001	1.4400	8.4233	6.0928
20Ne_S135	110	4.9478	0.1645	0.0069	0.0000	0.0000	0.9928	6.8483	5.9761
20Ne_S136	110	4.9585	0.1656	0.0068	0.0000	0.0000	1.0665	7.8131	5.9553
20Ne_S137	110	4.9219	0.1684	0.0071	0.0000	0.0001	1.1243	8.7399	6.0374
20Ne_S138	110	4.9233	0.1676	0.0071	0.0000	0.0000	1.1622	8.4696	6.0245
20Ne_S139	110	5.2722	0.1976	0.0269	0.0000	0.0000	0.8968	5.2543	5.1245
20Ne_S140	110	5.3048	0.1948	0.0283	0.0000	0.0000	0.9168	5.4176	4.9402

Appendices

Sample No	Index	f_1	f_2	f_3	f_4	f_5	f_6	f_7	f_8
20Ne_S141	110	5.2677	0.2022	0.0289	0.0000	0.0000	0.9512	5.7929	5.0902
20Ne_S142	110	5.2683	0.2015	0.0288	0.0000	0.0000	0.9768	5.8902	4.9635
20Ne_S143	120	5.0420	0.1856	0.0136	0.0000	0.0000	0.9794	6.2462	6.1660
20Ne_S144	120	5.1017	0.1854	0.0158	0.0000	0.0000	1.0141	6.2404	6.1169
20Ne_S145	120	5.1282	0.1921	0.0201	0.0000	0.0000	1.0886	6.3280	6.0872
20Ne_S146	120	5.0837	0.1920	0.0180	0.0000	0.0000	1.1420	7.0072	6.1386
20Ne_S147	120	4.9943	0.1651	0.0050	0.0000	0.0000	0.6292	4.6870	5.8582
20Ne_S148	120	4.9673	0.1654	0.0049	0.0000	0.0000	0.6857	4.9936	5.9748
20Ne_S149	120	5.1073	0.1617	0.0057	0.0000	0.0000	0.5982	4.4387	5.8229
20Ne_S150	120	5.0525	0.1651	0.0056	0.0000	0.0000	0.5875	4.3577	5.9224
20Ne_S151	130	5.0496	0.1453	0.0015	0.0000	0.0000	0.3783	4.1961	6.0501
20Ne_S152	130	5.0288	0.1494	0.0019	0.0000	0.0000	0.4050	4.1587	6.1120
20Ne_S153	130	5.1706	0.1457	0.0023	0.0000	0.0000	0.3902	4.0847	5.9581
20Ne_S154	130	5.2216	0.1431	0.0024	0.0000	0.0000	0.3177	3.5098	5.9226
20Ne_S155	130	4.9876	0.1411	0.0016	0.0000	0.0000	0.5324	5.2923	6.0035
20Ne_S156	130	5.0050	0.1391	0.0015	0.0000	0.0000	0.4994	5.1329	5.9920
20Ne_S157	130	4.8917	0.1394	0.0010	0.0000	0.0000	0.4009	4.1310	6.0688
20Ne_S158	130	4.9350	0.1378	0.0013	0.0000	0.0000	0.4438	4.7337	6.0148
20Ne_S159	130	5.3930	0.1487	0.0011	0.0000	0.0000	0.4914	4.3277	5.9057
20Ne_S160	130	5.3808	0.1494	0.0010	0.0000	0.0000	0.5595	5.4974	5.9751
20Ne_S161	130	5.2842	0.1483	0.0052	0.0000	0.0000	0.4505	4.1545	5.9774
20Ne_S162	130	5.2663	0.1481	0.0045	0.0000	0.0000	0.4397	4.1864	5.9815
20Ne_S163	130	4.5498	0.1397	0.0025	0.0000	0.0000	0.4576	4.4653	5.7246
20Ne_S164	130	4.5849	0.1378	0.0028	0.0000	0.0000	0.4924	4.7111	5.6653
20Ne_S165	130	4.5775	0.1398	0.0031	0.0000	0.0000	0.6683	6.6613	5.8632
20Ne_S166	130	4.5396	0.1408	0.0031	0.0000	0.0000	0.6663	6.3348	5.8767
30Ne_S167	80	4.0658	0.1899	0.0066	0.0020	0.0002	1.7189	18.0792	5.5597
30Ne_S168	80	4.1180	0.1894	0.0078	0.0016	0.0002	1.5216	13.6182	5.5463
30Ne_S169	80	4.0913	0.1874	0.0076	0.0009	0.0002	1.5578	13.6059	5.6102
30Ne_S170	80	4.1071	0.1782	0.0054	0.0006	0.0001	1.2557	11.2656	5.5412
30Ne_S171	80	4.1056	0.2115	0.0137	0.0015	0.0002	1.6339	11.9394	5.7279
30Ne_S172	80	4.1125	0.2054	0.0120	0.0015	0.0001	1.5212	11.5536	5.6641
30Ne_S173	80	4.1575	0.2136	0.0152	0.0020	0.0002	1.6717	12.3447	5.7390
30Ne_S174	80	4.1754	0.2121	0.0157	0.0017	0.0002	1.5151	10.6282	5.6785
30Ne_S175	80	4.1749	0.2391	0.0234	0.0042	0.0004	1.7403	11.8703	5.7809
30Ne_S176	80	4.1992	0.2330	0.0228	0.0032	0.0002	1.4363	8.6385	5.7058

Sample No	Index	f_1	f_2	f_3	f_4	f_5	f_6	f_7	f_8
30Ne_S177	80	4.1642	0.2490	0.0264	0.0058	0.0005	1.8913	13.2158	5.7637
30Ne_S178	80	4.1622	0.2462	0.0252	0.0054	0.0004	1.7830	11.4250	5.7502
30Ne_S179	80	4.1370	0.2241	0.0177	0.0025	0.0002	1.6381	11.3145	5.7305
30Ne_S180	80	4.1733	0.2252	0.0199	0.0025	0.0001	1.4808	9.0663	5.7099
30Ne_S181	80	4.1591	0.2153	0.0159	0.0020	0.0001	1.3873	9.0801	5.7083
30Ne_S182	80	4.1879	0.2165	0.0174	0.0019	0.0002	1.4579	9.9551	5.6995
30Ne_S183	80	4.2838	0.2529	0.0342	0.0054	0.0002	1.4872	8.2634	5.9987
30Ne_S184	80	4.2365	0.2459	0.0299	0.0041	0.0002	1.5166	8.5863	6.0280
30Ne_S185	80	4.3364	0.2474	0.0357	0.0039	0.0001	1.3980	7.7933	6.0119
30Ne_S186	80	4.3602	0.2519	0.0394	0.0034	0.0001	1.4952	8.3050	6.0177
30Ne_S187	120	3.9422	0.1633	0.0094	0.0000	0.0000	0.5872	6.1048	5.8768
30Ne_S188	120	3.9705	0.1621	0.0107	0.0000	0.0000	0.6049	6.2936	5.8189
30Ne_S189	120	3.8838	0.1682	0.0096	0.0000	0.0000	0.6074	5.5644	5.8020
30Ne_S190	120	3.9431	0.1647	0.0105	0.0000	0.0000	0.6264	6.3533	5.7330
30Ne_S191	120	3.8946	0.1674	0.0088	0.0000	0.0000	0.5183	5.6873	5.9301
30Ne_S192	120	3.8685	0.1685	0.0080	0.0000	0.0000	0.5440	5.5204	5.9799
30Ne_S193	120	3.9554	0.1712	0.0140	0.0000	0.0000	0.4780	4.4907	5.9967
30Ne_S194	120	3.9834	0.1686	0.0140	0.0000	0.0000	0.5448	5.2179	5.9560
30Ne_S195	120	3.9708	0.1641	0.0113	0.0000	0.0000	0.5114	5.1639	5.8320
30Ne_S196	120	3.9312	0.1677	0.0105	0.0000	0.0000	0.6686	6.8590	5.9559
30Ne_S197	120	3.9507	0.1703	0.0133	0.0000	0.0000	0.7138	6.5636	5.8681
30Ne_S198	120	3.9870	0.1660	0.0135	0.0000	0.0000	0.5841	5.4635	5.8236
30Ne_S199	120	4.0079	0.1653	0.0013	0.0007	0.0000	0.4375	4.4841	5.8403
30Ne_S200	120	3.9719	0.1679	0.0120	0.0000	0.0000	0.6179	6.2822	5.9202
30Ne_S201	120	4.0366	0.1657	0.0017	0.0008	0.0000	0.6510	6.9066	5.8462
30Ne_S202	120	4.0439	0.1657	0.0018	0.0005	0.0000	0.6432	6.9334	5.8291
30Ne_S203	130	4.0525	0.1544	0.0007	0.0002	0.0000	0.4149	5.6260	5.8968
30Ne_S204	130	3.9817	0.1555	0.0057	0.0000	0.0000	0.4830	7.3492	6.0265
30Ne_S205	130	4.2667	0.1491	0.0014	0.0000	0.0000	0.4470	4.6107	5.9480
30Ne_S206	130	4.2816	0.1491	0.0013	0.0000	0.0000	0.4473	4.6845	5.8980
30Ne_S207	130	3.9366	0.1631	0.0098	0.0000	0.0000	0.5946	6.1881	6.0775
30Ne_S208	130	3.8902	0.1647	0.0083	0.0000	0.0000	0.5306	5.4205	6.1334
30Ne_S209	130	3.8831	0.1635	0.0071	0.0000	0.0000	0.5237	5.9305	6.0625
30Ne_S210	130	3.9343	0.1620	0.0082	0.0000	0.0000	0.5445	6.3209	6.0020
40Ne_S211	90	3.9311	0.2237	0.0403	0.0000	0.0002	1.5493	9.9223	5.9010
40Ne_S212	90	3.8986	0.2362	0.0416	0.0000	0.0005	1.9413	13.3301	5.9850

Appendices

Sample No	Index	f_1	f_2	f_3	f_4	f_5	f_6	f_7	f_8
40Ne_S213	90	4.0118	0.2238	0.0134	0.0049	0.0001	1.6466	11.9060	5.9568
40Ne_S214	90	4.0511	0.2261	0.0154	0.0042	0.0001	1.6209	10.4764	5.9175
40Ne_S215	100	3.6723	0.1835	0.0091	0.0000	0.0000	0.9613	7.1979	5.8671
40Ne_S216	100	3.6468	0.1914	0.0096	0.0000	0.0003	1.6697	17.6966	5.9445
40Ne_S217	100	3.6683	0.1895	0.0101	0.0000	0.0000	1.1512	8.8304	5.9434
40Ne_S218	100	3.7013	0.1871	0.0102	0.0000	0.0001	1.1485	9.6181	5.9289
40Ne_S219	100	3.8545	0.1771	0.0113	0.0000	0.0000	0.5796	5.0868	5.8419
40Ne_S220	100	3.8475	0.1830	0.0124	0.0000	0.0001	1.0484	11.4245	5.9360
40Ne_S221	100	3.7813	0.1779	0.0085	0.0000	0.0000	0.4551	4.0214	5.9381
40Ne_S222	100	3.8220	0.1800	0.0098	0.0000	0.0000	0.6287	5.9019	5.8792
40Ne_S223	120	3.7759	0.1824	0.0103	0.0000	0.0000	0.8415	7.5721	5.9895
40Ne_S224	120	3.7350	0.1849	0.0096	0.0000	0.0000	0.7827	6.5040	6.0751
40Ne_S225	120	3.7770	0.1770	0.0089	0.0000	0.0000	0.6769	5.7643	5.9945
40Ne_S226	120	3.8178	0.1767	0.0098	0.0000	0.0000	0.7240	6.4235	5.9782
40Ne_S227	130	3.7792	0.1587	0.0036	0.0000	0.0000	0.2945	3.9555	5.8261
40Ne_S228	130	3.7944	0.1569	0.0029	0.0000	0.0000	0.2308	3.7137	5.8181
40Ne_S229	130	3.8971	0.1568	0.0051	0.0000	0.0000	0.2474	3.7108	5.8592
40Ne_S230	130	3.9089	0.1548	0.0047	0.0000	0.0000	0.2530	4.0576	5.8491
40Ne_S231	130	3.5145	0.1656	0.0017	0.0000	0.0000	0.6731	5.9075	5.4585
40Ne_S232	130	3.5048	0.1677	0.0018	0.0001	0.0001	0.7740	7.6473	5.6079
40Ne_S233	130	3.5925	0.1647	0.0021	0.0000	0.0000	0.5806	6.0026	5.5620
40Ne_S234	130	3.6232	0.1614	0.0018	0.0000	0.0000	0.4186	4.5364	5.4926
60Ne_S235	80	3.4032	0.2428	0.0175	0.0002	0.0001	1.3860	8.7344	5.8805
60Ne_S236	80	3.4162	0.2433	0.0179	0.0002	0.0002	1.4933	9.5080	5.8669
60Ne_S237	80	3.3924	0.2460	0.0174	0.0004	0.0001	1.3821	8.8004	5.8815
60Ne_S238	80	3.4053	0.2454	0.0182	0.0002	0.0001	1.3394	8.1520	5.8610
60Ne_S239	100	3.3103	0.1695	0.0109	0.0000	0.0000	0.5867	4.9471	5.7479
60Ne_S240	100	3.3485	0.1666	0.0008	0.0000	0.0000	0.5296	3.9194	5.6887
60Ne_S241	100	3.3640	0.1689	0.0010	0.0000	0.0000	0.5684	4.5121	5.7250
60Ne_S242	100	3.3856	0.1690	0.0010	0.0000	0.0000	0.5896	4.7297	5.7152
60Ne_S243	100	3.3766	0.1906	0.0022	0.0001	0.0000	0.4984	4.6847	5.7050
60Ne_S244	100	3.3356	0.1920	0.0022	0.0001	0.0000	0.5293	4.6124	5.7362
60Ne_S245	100	3.3381	0.1961	0.0027	0.0002	0.0000	0.5212	4.4590	5.7540
60Ne_S246	100	3.3800	0.1947	0.0031	0.0001	0.0000	0.5763	4.8928	5.7446
60Ne_S247	110	3.2646	0.1614	0.0047	0.0000	0.0000	0.5458	4.4839	5.5888
60Ne_S248	110	3.3130	0.1598	0.0058	0.0000	0.0000	0.5087	3.5807	5.5278

Sample No	Index	f_1	f_2	f_3	f_4	f_5	f_6	f_7	f_8
60Ne_S249	110	3.2301	0.1614	0.0037	0.0000	0.0000	0.5713	4.9535	5.6094
60Ne_S250	110	3.2774	0.1607	0.0047	0.0000	0.0000	0.6888	5.7576	5.5511
60Ne_S251	120	3.1923	0.1663	0.0041	0.0000	0.0000	0.4283	4.2632	5.4769
60Ne_S252	120	3.1435	0.1662	0.0030	0.0000	0.0000	0.3671	4.2917	5.5815
60Ne_S253	120	3.1837	0.1648	0.0038	0.0000	0.0000	0.4246	4.2718	5.5266
60Ne_S254	120	3.1630	0.1675	0.0033	0.0001	0.0000	0.5363	6.4864	5.5850
60Ne_S255	120	3.1784	0.1656	0.0035	0.0000	0.0000	0.4778	5.1133	5.5036
60Ne_S256	120	3.1409	0.1684	0.0034	0.0000	0.0000	0.3559	4.2635	5.5849
60Ne_S257	120	3.1905	0.1553	0.0016	0.0000	0.0000	0.5108	4.0386	5.3808
60Ne_S258	120	3.2351	0.1560	0.0029	0.0000	0.0000	0.5848	4.0076	5.3185
60Ne_S259	120	3.2163	0.1552	0.0024	0.0000	0.0000	0.6170	4.6656	5.4012
60Ne_S260	120	3.2473	0.1566	0.0025	0.0000	0.0000	0.5536	4.1830	5.3493
80Ne_S261	90	2.9822	0.2118	0.0085	0.0024	0.0001	0.4583	6.2683	5.6819
80Ne_S262	90	3.0241	0.2088	0.0104	0.0012	0.0000	0.4743	5.5167	5.6135
80Ne_S263	90	3.0874	0.2080	0.0138	0.0006	0.0000	0.5147	5.2845	5.7665
80Ne_S264	90	3.0227	0.2054	0.0091	0.0016	0.0000	0.4643	5.8002	5.6215
80Ne_S265	90	2.9207	0.1856	0.0025	0.0006	0.0000	0.2164	5.8171	5.2492
80Ne_S266	90	3.0420	0.1797	0.0054	0.0001	0.0000	0.5720	7.2335	5.3567
80Ne_S267	90	2.8962	0.1861	0.0025	0.0008	0.0001	0.2229	6.4483	5.3007
80Ne_S268	90	3.0875	0.1749	0.0056	0.0000	0.0000	0.5965	7.0996	5.3038
80Ne_S269	100	3.0965	0.1627	0.0022	0.0000	0.0000	0.5558	7.0548	5.2892
80Ne_S270	100	3.1092	0.1636	0.0022	0.0000	0.0000	0.5247	6.4422	5.2503
80Ne_S271	100	3.0989	0.1596	0.0019	0.0000	0.0000	0.5490	6.6545	5.3623
80Ne_S272	100	3.1448	0.1590	0.0021	0.0000	0.0000	0.4969	4.9814	5.2953
80Ne_S273	100	3.1009	0.1772	0.0049	0.0000	0.0000	0.5621	6.6660	5.6552
80Ne_S274	100	3.1581	0.1732	0.0057	0.0000	0.0000	0.6144	6.8303	5.5555
80Ne_S275	100	3.1928	0.1743	0.0070	0.0000	0.0000	0.6520	6.6609	5.6313
80Ne_S276	100	3.2438	0.1714	0.0094	0.0000	0.0000	0.6244	5.0912	5.5954
80Ne_S277	110	3.0336	0.1668	0.0027	0.0000	0.0000	0.3695	6.0489	5.6312
80Ne_S278	110	3.0411	0.1676	0.0024	0.0002	0.0000	0.4719	7.5293	5.6210
80Ne_S279	110	3.0280	0.1679	0.0029	0.0000	0.0000	0.4785	7.5391	5.6294
80Ne_S280	110	3.0988	0.1643	0.0035	0.0000	0.0000	0.5424	6.2138	5.5882
80Ne_S281	110	3.1691	0.1704	0.0051	0.0000	0.0000	0.5256	5.3827	5.5337
80Ne_S282	110	3.1274	0.1718	0.0044	0.0000	0.0000	0.5499	6.1763	5.6303
80Ne_S283	110	3.1985	0.1673	0.0054	0.0000	0.0000	0.6157	5.9945	5.5928
80Ne_S284	110	3.2255	0.1685	0.0058	0.0000	0.0000	0.5948	5.8488	5.5274

Appendices

Sample No	Index	f_1	f_2	f_3	f_4	f_5	f_6	f_7	f_8
80Ne_S285	120	3.0443	0.1726	0.0035	0.0001	0.0000	0.3651	5.8295	5.3339
80Ne_S286	120	3.0180	0.1780	0.0044	0.0000	0.0000	0.3736	5.8344	5.4631
80Ne_S287	120	3.0937	0.1699	0.0038	0.0000	0.0000	0.4368	5.5872	5.4056
80Ne_S288	120	3.1312	0.1709	0.0046	0.0000	0.0000	0.3922	4.6926	5.3888
80Ne_S289	120	3.0151	0.1735	0.0037	0.0000	0.0000	0.2977	5.4525	5.3576
80Ne_S290	120	3.0253	0.1770	0.0046	0.0000	0.0000	0.3451	5.1951	5.4264
80Ne_S291	120	3.0247	0.1733	0.0034	0.0000	0.0000	0.2744	5.1741	5.3718
80Ne_S292	120	3.0114	0.1782	0.0041	0.0001	0.0000	0.4198	7.0188	5.4594
80Ne_S293	120	3.0001	0.1638	0.0009	0.0000	0.0000	0.0829	4.6975	5.5079
80Ne_S294	120	3.0277	0.1616	0.0010	0.0001	0.0000	0.1562	4.7401	5.4552
80Ne_S295	120	3.0112	0.1654	0.0012	0.0003	0.0000	0.1371	5.1098	5.4305
80Ne_S296	120	3.0167	0.1626	0.0014	0.0000	0.0000	0.1554	4.7973	5.4918

(2) Features extracted from multi-scale attention model: $f_9 \sim f_{16}$

Sample No	Index	f_9	f_{10}	f_{11}	f_{12}	f_{13}	f_{14}	f_{15}	f_{16}
7Ne_S1	80	0.7849	1.0449	3.3615	0.9819	0.4037	2.8217	0.3045	0.2313
7Ne_S2	80	0.7680	1.0314	3.4609	0.9527	0.3949	2.7744	0.2993	0.2224
7Ne_S3	80	0.7726	1.0970	4.7150	0.9487	0.3679	2.8723	0.3202	0.2854
7Ne_S4	80	0.7557	1.0645	3.7963	0.9244	0.3596	2.8204	0.2824	0.2459
7Ne_S5	80	0.8808	1.0527	2.8806	1.1028	0.5278	2.9365	0.2803	0.1917
7Ne_S6	80	0.8561	1.0394	3.4496	1.0680	0.5089	2.8632	0.2671	0.1995
7Ne_S7	80	0.8545	1.0476	3.3127	1.0634	0.5045	2.8691	0.3245	0.2309
7Ne_S8	80	0.8512	1.0399	3.1030	1.0653	0.4981	2.8688	0.2811	0.1963
7Ne_S9	90	0.9352	1.0920	3.3441	1.1690	0.5809	3.0442	0.2936	0.2237
7Ne_S10	90	0.9200	1.0759	3.3043	1.1458	0.5750	2.9836	0.2998	0.2200
7Ne_S11	90	0.9412	1.0889	3.3088	1.1667	0.5945	3.0273	0.2665	0.2195
7Ne_S12	90	0.9285	1.0549	2.7351	1.1547	0.5924	2.9830	0.2465	0.1803
7Ne_S13	90	0.8374	0.9759	2.4011	1.0430	0.5194	2.7314	0.2504	0.1828
7Ne_S14	90	0.8333	0.9776	2.3659	1.0381	0.5134	2.7271	0.2584	0.2082
7Ne_S15	90	0.8256	0.9739	2.5844	1.0200	0.5122	2.6944	0.2459	0.2020
7Ne_S16	90	0.8223	0.9622	2.3390	1.0182	0.5127	2.6753	0.2494	0.1948
7Ne_S17	100	0.8298	0.9578	2.1007	1.0322	0.5194	2.6983	0.2157	0.1688
7Ne_S18	100	0.8132	0.9402	2.1218	1.0131	0.5097	2.6408	0.2457	0.1721
7Ne_S19	100	0.8628	0.9724	2.0684	1.0719	0.5505	2.7678	0.2180	0.1908
7Ne_S20	100	0.8731	0.9981	2.8039	1.0855	0.5570	2.8054	0.2247	0.1769
7Ne_S21	110	0.5884	0.7771	1.5499	0.7218	0.3153	2.0842	0.2003	0.1778

Sample No	Index	f_9	f_{10}	f_{11}	f_{12}	f_{13}	f_{14}	f_{15}	f_{16}
7Ne_S22	110	0.5710	0.7610	1.5361	0.6983	0.3067	2.0125	0.2067	0.1939
7Ne_S23	110	0.6022	0.7808	1.3976	0.7378	0.3291	2.1153	0.2279	0.2007
7Ne_S24	110	0.5795	0.7582	1.5084	0.7101	0.3180	2.0270	0.2012	0.1862
7Ne_S25	120	0.6147	0.7947	1.6931	0.7534	0.3437	2.1155	0.2308	0.1949
7Ne_S26	120	0.6405	0.8331	2.0097	0.7865	0.3536	2.2302	0.2121	0.1967
7Ne_S27	120	0.5914	0.7797	1.5434	0.7225	0.3213	2.0735	0.1989	0.2017
7Ne_S28	120	0.6197	0.8529	3.1888	0.7551	0.3267	2.2068	0.2084	0.2059
7Ne_S29	120	0.7472	0.8139	1.1562	0.9312	0.4912	2.3558	0.1442	0.1526
7Ne_S30	120	0.7565	0.8260	1.2285	0.9427	0.4978	2.3868	0.1380	0.1409
7Ne_S31	120	0.7584	0.8122	1.2029	0.9377	0.5116	2.3492	0.1626	0.1565
7Ne_S32	120	0.7506	0.7989	1.0283	0.9249	0.5076	2.3226	0.1350	0.1312
7Ne_S33	120	0.5721	0.6764	0.8528	0.6992	0.3507	1.8883	0.1344	0.1429
7Ne_S34	120	0.5506	0.6589	0.8082	0.6704	0.3338	1.8316	0.1308	0.1389
7Ne_S35	120	0.5586	0.6644	0.7686	0.6844	0.3386	1.8579	0.1388	0.1389
7Ne_S36	120	0.5470	0.6548	0.7278	0.6713	0.3298	1.8196	0.1220	0.1503
7Ne_S37	120	0.5588	0.6881	0.9548	0.6806	0.3290	1.8777	0.1308	0.1174
7Ne_S38	120	0.5700	0.7016	1.1649	0.6933	0.3395	1.9098	0.1341	0.1312
7Ne_S39	130	0.7899	0.8058	1.0345	0.9578	0.5582	2.3629	0.1465	0.1452
7Ne_S40	130	0.7781	0.7940	1.0318	0.9439	0.5518	2.3128	0.1541	0.1456
7Ne_S41	130	0.8363	0.8296	1.0327	1.0152	0.6052	2.4572	0.1411	0.1448
7Ne_S42	130	0.8381	0.8336	1.1433	1.0072	0.6093	2.4470	0.1546	0.1569
7Ne_S43	130	0.5946	0.6942	0.8309	0.7231	0.3689	1.9506	0.1237	0.1308
7Ne_S44	130	0.5963	0.7089	0.9729	0.7197	0.3664	1.9677	0.1364	0.1412
7Ne_S45	130	0.6037	0.7084	1.0572	0.7262	0.3800	1.9556	0.1335	0.1361
7Ne_S46	130	0.5920	0.6894	0.8967	0.7184	0.3724	1.9182	0.1362	0.1336
10Ne_S47	90	0.6893	1.0164	4.0439	0.8307	0.3135	2.6167	0.2936	0.2483
10Ne_S48	90	0.7363	1.1186	5.6139	0.8770	0.3256	2.8172	0.3482	0.2711
10Ne_S49	90	0.6762	1.0386	4.5923	0.7983	0.2966	2.5916	0.3332	0.2528
10Ne_S50	90	0.7134	1.0875	5.5554	0.8502	0.3172	2.7270	0.3633	0.3153
10Ne_S51	100	0.8032	1.0696	3.7684	0.9989	0.4213	2.8572	0.3183	0.2084
10Ne_S52	100	0.8277	1.0815	3.8429	1.0308	0.4458	2.9058	0.3371	0.2231
10Ne_S53	100	0.8107	1.0957	4.6672	1.0061	0.4214	2.8836	0.2979	0.2418
10Ne_S54	100	0.8011	1.0950	4.9168	0.9881	0.4168	2.8397	0.3599	0.2685
10Ne_S55	100	0.7714	1.0480	3.7495	0.9484	0.3960	2.7787	0.2620	0.2250
10Ne_S56	100	0.7989	1.0911	4.8599	0.9874	0.4125	2.8613	0.3584	0.2473
10Ne_S57	110	0.7381	0.9745	3.0976	0.9149	0.3981	2.5837	0.2858	0.2348

Appendices

Sample No	Index	f_9	f_{10}	f_{11}	f_{12}	f_{13}	f_{14}	f_{15}	f_{16}
10Ne_S58	110	0.7796	1.0127	3.4203	0.9675	0.4319	2.6950	0.3146	0.2605
10Ne_S59	110	0.6891	0.9339	3.0164	0.8492	0.3634	2.4333	0.3081	0.2374
10Ne_S60	110	0.6953	0.9614	3.7106	0.8551	0.3623	2.4601	0.2951	0.2362
10Ne_S61	110	0.7292	0.9451	2.4446	0.9084	0.3942	2.5694	0.2566	0.2208
10Ne_S62	110	0.7807	1.0063	3.2922	0.9754	0.4314	2.7048	0.2601	0.2433
10Ne_S63	120	0.5742	0.7803	1.7217	0.7031	0.2964	2.0697	0.2381	0.2047
10Ne_S64	120	0.5677	0.7747	1.5901	0.6896	0.2933	2.0483	0.2001	0.1960
10Ne_S65	120	0.5409	0.7681	1.8441	0.6541	0.2667	1.9886	0.2313	0.2073
10Ne_S66	120	0.5218	0.7332	1.4518	0.6326	0.2578	1.9188	0.2140	0.2106
10Ne_S67	120	0.5709	0.7322	1.0924	0.7014	0.3144	2.0044	0.1665	0.1596
10Ne_S68	120	0.5817	0.7535	1.2520	0.7103	0.3171	2.0456	0.1377	0.1486
10Ne_S69	120	0.5336	0.7101	1.1893	0.6504	0.2847	1.8933	0.1644	0.1563
10Ne_S70	120	0.5363	0.7224	1.3308	0.6520	0.2841	1.9062	0.1616	0.1515
10Ne_S71	120	0.5574	0.7042	0.9402	0.6880	0.3114	1.9384	0.1534	0.1547
10Ne_S72	120	0.5377	0.6826	0.9031	0.6581	0.3022	1.8647	0.1490	0.1574
10Ne_S73	120	0.5356	0.6857	0.9313	0.6537	0.2977	1.8668	0.1446	0.1439
10Ne_S74	120	0.5332	0.6714	0.8550	0.6497	0.3030	1.8388	0.1655	0.1400
10Ne_S75	130	0.7306	0.8385	1.4516	0.9126	0.4591	2.3650	0.1747	0.1509
10Ne_S76	130	0.7730	0.8775	1.7961	0.9631	0.4948	2.4732	0.1813	0.1663
10Ne_S77	130	0.7783	0.8761	1.5218	0.9759	0.4946	2.5081	0.1712	0.1516
10Ne_S78	130	0.8126	0.8965	1.5560	1.0163	0.5309	2.5719	0.1837	0.1577
10Ne_S79	130	0.7652	0.8795	1.6786	0.9583	0.4801	2.4810	0.2080	0.1791
10Ne_S80	130	0.7966	0.8886	1.5734	0.9968	0.5138	2.5429	0.1536	0.1600
10Ne_S81	130	0.4913	0.6910	1.2681	0.5944	0.2461	1.7960	0.2086	0.1884
10Ne_S82	130	0.5234	0.7355	1.3203	0.6338	0.2566	1.9306	0.2254	0.1991
10Ne_S83	130	0.5144	0.7477	1.6333	0.6146	0.2461	1.9108	0.1998	0.2080
10Ne_S84	130	0.5147	0.7616	3.0140	0.6206	0.2489	1.9003	0.2099	0.2127
10Ne_S85	130	0.4879	0.7179	1.9095	0.5859	0.2344	1.8104	0.2239	0.2087
10Ne_S86	130	0.5006	0.7190	1.4503	0.6073	0.2407	1.8589	0.2584	0.2162
10Ne_S87	130	0.5266	0.6813	1.1197	0.6340	0.2975	1.8150	0.1668	0.1525
10Ne_S88	130	0.5616	0.7323	1.3941	0.6795	0.3126	1.9483	0.1798	0.1767
10Ne_S89	130	0.5556	0.7230	1.5482	0.6758	0.3083	1.9321	0.1521	0.1512
10Ne_S90	130	0.5485	0.7031	1.0644	0.6668	0.3079	1.8982	0.1529	0.1457
16Ne_S91	90	0.7051	1.0477	5.3936	0.8498	0.3332	2.6148	0.4419	0.3210
16Ne_S92	90	0.7455	1.0931	5.4241	0.9029	0.3552	2.7449	0.3638	0.2876
16Ne_S93	90	0.6137	0.9512	3.8880	0.7205	0.2747	2.3279	0.3304	0.2760

Sample No	Index	f_9	f_{10}	f_{11}	f_{12}	f_{13}	f_{14}	f_{15}	f_{16}
16Ne_S94	90	0.6412	0.9920	4.3154	0.7550	0.2831	2.4491	0.3471	0.3057
16Ne_S95	90	0.6279	0.9929	5.0302	0.7337	0.2752	2.4065	0.3914	0.3171
16Ne_S96	90	0.6753	1.0428	4.8792	0.7945	0.2930	2.6056	0.3166	0.3056
16Ne_S97	100	0.7176	1.0996	7.0412	0.8582	0.3403	2.6322	0.4519	0.3491
16Ne_S98	100	0.7539	1.1551	7.9344	0.8999	0.3563	2.7649	0.4808	0.3172
16Ne_S99	100	0.7496	1.0921	5.9425	0.9123	0.3622	2.7476	0.4225	0.3005
16Ne_S100	100	0.8049	1.1397	6.0706	0.9872	0.3990	2.9281	0.4218	0.3119
16Ne_S101	100	0.7622	1.1017	5.2444	0.9299	0.3571	2.8537	0.3427	0.3045
16Ne_S102	100	0.7747	1.1166	4.8455	0.9417	0.3612	2.9075	0.4030	0.2642
16Ne_S103	100	0.7984	1.1109	4.3862	0.9850	0.3867	2.9490	0.3691	0.2817
16Ne_S104	100	0.7818	1.1010	4.8142	0.9584	0.3789	2.8939	0.3538	0.2912
16Ne_S105	100	0.8209	1.0817	3.6778	1.0255	0.4298	2.9337	0.2854	0.2524
16Ne_S106	100	0.8101	1.0972	4.3869	1.0000	0.4206	2.8927	0.3344	0.2527
16Ne_S107	100	0.8793	1.1673	5.4191	1.0893	0.4698	3.1101	0.3070	0.2628
16Ne_S108	100	0.8554	1.1291	4.4702	1.0613	0.4528	3.0460	0.3171	0.2835
16Ne_S109	110	0.4597	0.7567	2.8883	0.5359	0.1975	1.7578	0.3512	0.2884
16Ne_S110	110	0.4430	0.7134	2.5156	0.5189	0.1919	1.7081	0.2963	0.2627
16Ne_S111	110	0.4697	0.7505	2.2728	0.5480	0.2028	1.8119	0.2793	0.2428
16Ne_S112	110	0.4591	0.7495	3.1621	0.5356	0.2013	1.7472	0.3010	0.2597
16Ne_S113	120	0.5253	0.7518	1.7515	0.6400	0.2568	1.9218	0.2877	0.2434
16Ne_S114	120	0.5085	0.7246	1.6933	0.6189	0.2519	1.8594	0.2787	0.2264
16Ne_S115	120	0.5743	0.8023	1.8030	0.7028	0.2843	2.0987	0.2841	0.2221
16Ne_S116	120	0.5897	0.8256	1.9345	0.7201	0.2896	2.1643	0.2410	0.1963
16Ne_S117	120	0.5189	0.7155	1.1884	0.6284	0.2629	1.8882	0.1775	0.1760
16Ne_S118	120	0.5152	0.7278	1.4552	0.6160	0.2573	1.8856	0.2069	0.1762
16Ne_S119	120	0.4980	0.6885	1.1016	0.5989	0.2539	1.8098	0.2149	0.1864
16Ne_S120	120	0.5385	0.7384	1.3715	0.6545	0.2733	1.9643	0.2006	0.1782
16Ne_S121	120	0.5259	0.7117	1.1396	0.6402	0.2723	1.9021	0.1962	0.1746
16Ne_S122	120	0.5213	0.7063	1.1211	0.6312	0.2709	1.8802	0.1917	0.1794
16Ne_S123	120	0.5299	0.7324	1.3312	0.6431	0.2689	1.9271	0.2077	0.1876
16Ne_S124	120	0.5000	0.6858	1.0726	0.6051	0.2551	1.8143	0.1993	0.1789
16Ne_S125	130	0.3854	0.5414	0.5173	0.4617	0.1903	1.4254	0.1602	0.1604
16Ne_S126	130	0.3836	0.5521	0.6787	0.4565	0.1881	1.4136	0.1923	0.1752
16Ne_S127	130	0.3760	0.5420	0.5837	0.4463	0.1831	1.3873	0.1535	0.1646
16Ne_S128	130	0.3793	0.5495	0.7611	0.4488	0.1858	1.3993	0.1920	0.1868
20Ne_S129	90	0.5563	0.9007	3.5608	0.6432	0.2336	2.1643	0.3384	0.3091

Appendices

Sample No	Index	f_9	f_{10}	f_{11}	f_{12}	f_{13}	f_{14}	f_{15}	f_{16}
20Ne_S130	90	0.6051	1.0224	8.8614	0.7016	0.2475	2.3606	0.3632	0.3169
20Ne_S131	90	0.5722	0.9347	3.8756	0.6615	0.2310	2.2571	0.3804	0.3022
20Ne_S132	90	0.5794	0.9773	5.5173	0.6618	0.2337	2.2689	0.3760	0.3251
20Ne_S133	100	0.6382	1.0054	5.4975	0.7553	0.2797	2.4274	0.4104	0.3396
20Ne_S134	100	0.6915	1.0822	6.0242	0.8195	0.3020	2.6336	0.4119	0.3140
20Ne_S135	110	0.5494	0.8031	2.1282	0.6655	0.2593	2.0465	0.3010	0.2763
20Ne_S136	110	0.5464	0.8294	3.2156	0.6531	0.2547	2.0253	0.3373	0.2551
20Ne_S137	110	0.5767	0.8514	2.7622	0.6950	0.2718	2.1369	0.3420	0.2757
20Ne_S138	110	0.5714	0.8585	3.1795	0.6843	0.2689	2.1194	0.3429	0.2668
20Ne_S139	110	0.4658	0.7989	2.8003	0.5287	0.1776	1.8648	0.3256	0.2680
20Ne_S140	110	0.4338	0.7683	2.8684	0.4836	0.1621	1.7459	0.3717	0.3086
20Ne_S141	110	0.4628	0.8307	3.8347	0.5162	0.1721	1.8576	0.3954	0.3353
20Ne_S142	110	0.4431	0.8325	5.3756	0.4871	0.1638	1.7704	0.3834	0.3427
20Ne_S143	120	0.7124	1.0053	3.3752	0.8717	0.3400	2.6545	0.3263	0.2569
20Ne_S144	120	0.6805	0.9615	3.0668	0.8342	0.3241	2.5407	0.3197	0.2527
20Ne_S145	120	0.6983	0.9922	3.0878	0.8549	0.3257	2.6329	0.3205	0.2401
20Ne_S146	120	0.7319	1.0523	4.1774	0.8924	0.3406	2.7518	0.3193	0.2464
20Ne_S147	120	0.5799	0.8424	2.1122	0.7064	0.2646	2.1991	0.2558	0.2309
20Ne_S148	120	0.6286	0.8925	2.2889	0.7725	0.2903	2.3754	0.2782	0.2202
20Ne_S149	120	0.5664	0.8130	1.8776	0.6926	0.2624	2.1402	0.2315	0.2251
20Ne_S150	120	0.6011	0.8597	2.1228	0.7373	0.2790	2.2804	0.2274	0.2138
20Ne_S151	130	0.6103	0.8128	1.7959	0.7635	0.3177	2.1887	0.1886	0.1952
20Ne_S152	130	0.6348	0.8327	1.6367	0.7948	0.3306	2.2827	0.2098	0.1759
20Ne_S153	130	0.5784	0.7808	1.9778	0.7198	0.2995	2.0835	0.2290	0.2035
20Ne_S154	130	0.5676	0.7493	1.1679	0.7058	0.2944	2.0494	0.1970	0.1745
20Ne_S155	130	0.5443	0.7337	1.4296	0.6745	0.2809	1.9626	0.2487	0.2201
20Ne_S156	130	0.5399	0.7308	1.5319	0.6674	0.2799	1.9372	0.2071	0.1905
20Ne_S157	130	0.5636	0.7559	1.6314	0.7027	0.2930	2.0142	0.1798	0.1577
20Ne_S158	130	0.5403	0.7251	1.2539	0.6692	0.2802	1.9430	0.2163	0.1992
20Ne_S159	130	0.5986	0.7982	1.7695	0.7453	0.3134	2.1367	0.2306	0.2098
20Ne_S160	130	0.6220	0.8295	1.9224	0.7743	0.3263	2.2121	0.2175	0.2152
20Ne_S161	130	0.6103	0.8137	1.8572	0.7611	0.3193	2.1756	0.2102	0.2006
20Ne_S162	130	0.6069	0.7956	1.4492	0.7562	0.3206	2.1678	0.2042	0.2000
20Ne_S163	130	0.4235	0.6054	0.8173	0.5164	0.2003	1.5808	0.2193	0.1973
20Ne_S164	130	0.4184	0.5963	0.7210	0.5102	0.1977	1.5642	0.2212	0.1857
20Ne_S165	130	0.4604	0.6579	1.2270	0.5630	0.2229	1.7008	0.2692	0.2261

Sample No	Index	f_9	f_{10}	f_{11}	f_{12}	f_{13}	f_{14}	f_{15}	f_{16}
20Ne_S166	130	0.4717	0.6727	1.2682	0.5777	0.2291	1.7360	0.2225	0.2263
30Ne_S167	80	0.5247	0.8942	4.7461	0.5903	0.2312	1.9682	0.5019	0.4070
30Ne_S168	80	0.5270	0.8493	3.0788	0.6001	0.2375	1.9754	0.4504	0.3470
30Ne_S169	80	0.5232	0.8200	2.7963	0.6016	0.2455	1.9346	0.4191	0.3269
30Ne_S170	80	0.4988	0.7834	2.5810	0.5751	0.2379	1.8227	0.4181	0.3057
30Ne_S171	80	0.6329	1.0485	8.5291	0.7267	0.2679	2.4400	0.5176	0.3760
30Ne_S172	80	0.5896	0.9458	4.0096	0.6795	0.2544	2.2559	0.4796	0.3258
30Ne_S173	80	0.6641	1.0992	7.4098	0.7595	0.2799	2.5643	0.5121	0.4339
30Ne_S174	80	0.6365	1.0376	5.4579	0.7319	0.2694	2.4524	0.5185	0.3786
30Ne_S175	80	0.7263	1.2269	9.9908	0.8251	0.2898	2.8636	0.5904	0.4403
30Ne_S176	80	0.6779	1.1242	6.3272	0.7729	0.2696	2.6821	0.4848	0.3712
30Ne_S177	80	0.7214	1.2191	8.3429	0.8100	0.2773	2.8960	0.5462	0.4675
30Ne_S178	80	0.7153	1.2141	8.6643	0.8055	0.2757	2.8492	0.5390	0.4617
30Ne_S179	80	0.6656	1.1095	7.1816	0.7591	0.2685	2.6125	0.5361	0.4176
30Ne_S180	80	0.6696	1.0987	5.8305	0.7664	0.2713	2.6381	0.4516	0.3654
30Ne_S181	80	0.6584	1.0927	8.6140	0.7559	0.2707	2.5802	0.4633	0.3483
30Ne_S182	80	0.6538	1.0626	5.8554	0.7521	0.2735	2.5425	0.4937	0.4069
30Ne_S183	80	0.7925	1.1525	6.4139	0.9573	0.3826	2.9196	0.4960	0.3630
30Ne_S184	80	0.7940	1.1277	5.4564	0.9681	0.3939	2.8810	0.5102	0.3614
30Ne_S185	80	0.7947	1.1254	5.3800	0.9644	0.3986	2.8744	0.4652	0.3697
30Ne_S186	80	0.8204	1.1715	6.0698	0.9896	0.4056	3.0045	0.5048	0.3729
30Ne_S187	120	0.5966	0.8019	1.7170	0.7305	0.3127	2.1369	0.2901	0.2608
30Ne_S188	120	0.5805	0.7881	1.7404	0.7046	0.3045	2.0770	0.2671	0.2537
30Ne_S189	120	0.5720	0.7784	1.5030	0.6990	0.2918	2.0820	0.2773	0.2545
30Ne_S190	120	0.5483	0.7620	1.6555	0.6616	0.2804	1.9856	0.3015	0.2839
30Ne_S191	120	0.5834	0.7578	1.4598	0.7291	0.3162	2.0513	0.2536	0.2408
30Ne_S192	120	0.6154	0.7974	1.7384	0.7711	0.3347	2.1599	0.2909	0.2395
30Ne_S193	120	0.6338	0.7954	1.3401	0.7984	0.3521	2.2073	0.2273	0.2167
30Ne_S194	120	0.6177	0.7824	1.6547	0.7747	0.3454	2.1361	0.2727	0.2535
30Ne_S195	120	0.5873	0.7944	1.7290	0.7208	0.3019	2.1279	0.2452	0.2312
30Ne_S196	120	0.6468	0.8763	2.2251	0.7967	0.3330	2.3320	0.2971	0.2649
30Ne_S197	120	0.6372	0.8940	2.8722	0.7820	0.3153	2.3282	0.3026	0.2772
30Ne_S198	120	0.6075	0.8331	1.8679	0.7465	0.3050	2.2185	0.2772	0.2394
30Ne_S199	120	0.5654	0.7169	1.1578	0.7032	0.3175	1.9592	0.2484	0.2117
30Ne_S200	120	0.5959	0.7595	1.4235	0.7406	0.3337	2.0645	0.2927	0.2507
30Ne_S201	120	0.5709	0.7310	1.5644	0.7063	0.3238	1.9656	0.3384	0.2683

Appendices

Sample No	Index	f_9	f_{10}	f_{11}	f_{12}	f_{13}	f_{14}	f_{15}	f_{16}
30Ne_S202	120	0.5619	0.7300	1.7411	0.6901	0.3190	1.9225	0.3017	0.2798
30Ne_S203	130	0.5740	0.7170	1.2028	0.7135	0.3280	1.9623	0.2539	0.2282
30Ne_S204	130	0.6277	0.7821	1.5823	0.7794	0.3632	2.1300	0.3032	0.2714
30Ne_S205	130	0.6443	0.7712	1.2157	0.7904	0.3874	2.1493	0.2315	0.1853
30Ne_S206	130	0.6113	0.7329	1.1432	0.7483	0.3690	2.0389	0.2184	0.1914
30Ne_S207	130	0.6814	0.8636	1.7414	0.8569	0.3730	2.3940	0.3108	0.2399
30Ne_S208	130	0.7035	0.8870	1.8077	0.8882	0.3852	2.4688	0.2683	0.2158
30Ne_S209	130	0.6743	0.8696	1.9697	0.8496	0.3630	2.3808	0.3058	0.2281
30Ne_S210	130	0.6372	0.8144	1.6111	0.8042	0.3458	2.2380	0.2749	0.2187
40Ne_S211	90	0.6728	1.0619	7.5914	0.7931	0.3040	2.5282	0.4303	0.3553
40Ne_S212	90	0.7350	1.1866	9.2686	0.8597	0.3255	2.7470	0.5893	0.4365
40Ne_S213	90	0.7088	1.0802	6.6365	0.8468	0.3365	2.5907	0.4990	0.3972
40Ne_S214	90	0.6995	1.1114	8.7376	0.8240	0.3252	2.5744	0.5218	0.4225
40Ne_S215	100	0.6059	0.9087	2.5476	0.7196	0.2662	2.3463	0.3271	0.2611
40Ne_S216	100	0.6538	1.0222	5.4656	0.7761	0.2818	2.5100	0.4601	0.3544
40Ne_S217	100	0.6538	0.9900	3.6394	0.7774	0.2847	2.5321	0.3745	0.2841
40Ne_S218	100	0.6476	0.9838	4.4416	0.7747	0.2855	2.4850	0.3904	0.3127
40Ne_S219	100	0.5693	0.7469	1.2752	0.7123	0.3015	2.0338	0.2944	0.2799
40Ne_S220	100	0.6191	0.8252	2.1008	0.7764	0.3263	2.1972	0.3691	0.2548
40Ne_S221	100	0.6019	0.7845	1.4279	0.7578	0.3143	2.1634	0.2488	0.2239
40Ne_S222	100	0.5817	0.7888	2.1532	0.7292	0.3015	2.0861	0.3516	0.2552
40Ne_S223	120	0.6318	0.8700	2.4947	0.7850	0.3140	2.3098	0.3332	0.2839
40Ne_S224	120	0.6816	0.9141	2.3868	0.8571	0.3451	2.4731	0.3203	0.3019
40Ne_S225	120	0.6330	0.8510	2.2809	0.7913	0.3263	2.2853	0.3189	0.2683
40Ne_S226	120	0.6200	0.8368	1.9641	0.7714	0.3186	2.2389	0.3216	0.2828
40Ne_S227	130	0.5673	0.7714	1.4303	0.6957	0.2854	2.0771	0.2124	0.1995
40Ne_S228	130	0.5577	0.7510	1.2551	0.6870	0.2834	2.0344	0.2045	0.1866
40Ne_S229	130	0.5901	0.7705	1.2249	0.7309	0.3108	2.1142	0.1853	0.1832
40Ne_S230	130	0.5935	0.7873	1.8167	0.7377	0.3104	2.1252	0.2025	0.1996
40Ne_S231	130	0.4228	0.6184	0.9601	0.5168	0.1946	1.5937	0.3320	0.2640
40Ne_S232	130	0.4662	0.6822	1.4578	0.5720	0.2159	1.7545	0.3680	0.3088
40Ne_S233	130	0.4459	0.6489	1.4308	0.5457	0.2133	1.6563	0.2686	0.2570
40Ne_S234	130	0.4281	0.6058	0.8535	0.5259	0.2072	1.5839	0.2307	0.2196
60Ne_S235	80	1.0971	1.6151	18.2244	1.3172	0.5364	3.9661	0.4894	0.3586
60Ne_S236	80	1.0842	1.6410	25.4211	1.3020	0.5273	3.9161	0.5021	0.4059
60Ne_S237	80	1.0967	1.6299	20.9421	1.3175	0.5354	3.9682	0.4912	0.3891

Sample No	Index	f_9	f_{10}	f_{11}	f_{12}	f_{13}	f_{14}	f_{15}	f_{16}
60Ne_S238	80	1.0646	1.5968	18.6025	1.2765	0.5097	3.8847	0.4595	0.3962
60Ne_S239	100	0.8238	1.0475	4.8356	1.0210	0.4772	2.7787	0.3042	0.2714
60Ne_S240	100	0.7860	0.9864	3.1988	0.9676	0.4562	2.6564	0.2669	0.2491
60Ne_S241	100	0.8140	1.0256	6.0451	1.0025	0.4838	2.7123	0.2983	0.2528
60Ne_S242	100	0.8203	1.0352	4.7064	1.0051	0.4857	2.7287	0.3150	0.2782
60Ne_S243	100	0.8237	1.0543	3.6959	1.0261	0.4582	2.8611	0.3130	0.2571
60Ne_S244	100	0.8472	1.0940	4.5554	1.0628	0.4648	2.9498	0.3340	0.2837
60Ne_S245	100	0.8727	1.1111	4.0822	1.1013	0.4777	3.0561	0.3271	0.2384
60Ne_S246	100	0.8663	1.1269	5.4956	1.0840	0.4768	3.0148	0.3332	0.2975
60Ne_S247	110	0.6753	0.8401	2.7735	0.8244	0.4034	2.2539	0.2592	0.2510
60Ne_S248	110	0.6493	0.8063	2.2362	0.7855	0.3918	2.1508	0.2552	0.2333
60Ne_S249	110	0.6715	0.8483	3.2035	0.8216	0.3975	2.2385	0.2773	0.2600
60Ne_S250	110	0.6476	0.8522	4.5975	0.7803	0.3863	2.1481	0.3307	0.2691
60Ne_S251	120	0.5891	0.7464	1.5531	0.7221	0.3371	2.0209	0.2455	0.2427
60Ne_S252	120	0.6268	0.7851	1.5166	0.7792	0.3548	2.1691	0.2377	0.2338
60Ne_S253	120	0.6087	0.7545	1.3492	0.7549	0.3510	2.0819	0.2284	0.2303
60Ne_S254	120	0.6374	0.8633	5.8796	0.7907	0.3568	2.1993	0.2718	0.2562
60Ne_S255	120	0.5931	0.7509	1.5919	0.7281	0.3377	2.0389	0.2405	0.2398
60Ne_S256	120	0.6367	0.8073	1.6393	0.7918	0.3553	2.2193	0.2412	0.2250
60Ne_S257	120	0.5641	0.6851	1.0968	0.6829	0.3384	1.8833	0.2195	0.2133
60Ne_S258	120	0.5448	0.6767	1.3671	0.6475	0.3310	1.7923	0.2467	0.2258
60Ne_S259	120	0.5725	0.7205	1.7997	0.6860	0.3438	1.8952	0.2516	0.2175
60Ne_S260	120	0.5538	0.6894	2.1247	0.6563	0.3390	1.8190	0.2472	0.2279
80Ne_S261	90	0.7955	0.9755	4.8599	0.9491	0.4917	2.5952	0.3632	0.2989
80Ne_S262	90	0.7678	0.9180	2.5005	0.9159	0.4764	2.5008	0.3452	0.3063
80Ne_S263	90	1.0344	1.3468	7.8471	1.2965	0.5570	3.6440	0.3209	0.2957
80Ne_S264	90	0.7829	0.9349	3.0442	0.9302	0.4902	2.5489	0.3707	0.3152
80Ne_S265	90	0.5991	0.7479	2.9029	0.6728	0.3800	1.8957	0.3306	0.3001
80Ne_S266	90	0.7424	1.1031	7.4127	0.8739	0.3741	2.6735	0.3706	0.3125
80Ne_S267	90	0.5919	0.7371	2.2270	0.6604	0.3742	1.8846	0.3493	0.3120
80Ne_S268	90	0.6888	0.9827	5.5684	0.8056	0.3662	2.4353	0.3333	0.3006
80Ne_S269	100	0.7062	0.9027	4.2508	0.8341	0.4274	2.3278	0.3060	0.2615
80Ne_S270	100	0.7010	0.8888	3.5581	0.8283	0.4213	2.3172	0.2969	0.2641
80Ne_S271	100	0.7269	0.9067	3.7044	0.8537	0.4476	2.3703	0.2977	0.2693
80Ne_S272	100	0.6965	0.8329	2.3566	0.8130	0.4367	2.2596	0.2663	0.2290
80Ne_S273	100	0.9421	1.2307	9.2613	1.1556	0.5406	3.1798	0.3561	0.3035

Appendices

Sample No	Index	f_9	f_{10}	f_{11}	f_{12}	f_{13}	f_{14}	f_{15}	f_{16}
80Ne_S274	100	0.8754	1.1290	6.4844	1.0631	0.5039	2.9708	0.2803	0.2664
80Ne_S275	100	0.9776	1.2307	7.3340	1.1876	0.5812	3.2512	0.3456	0.2890
80Ne_S276	100	0.9431	1.1821	6.2444	1.1388	0.5635	3.1320	0.3014	0.2607
80Ne_S277	110	0.8461	1.0691	3.9891	1.0530	0.4789	2.9167	0.2607	0.2598
80Ne_S278	110	0.8415	1.0818	5.6890	1.0374	0.4829	2.8663	0.3291	0.2786
80Ne_S279	110	0.8616	1.1251	6.6892	1.0709	0.4829	2.9729	0.3185	0.2802
80Ne_S280	110	0.8358	1.0629	4.1998	1.0274	0.4754	2.8730	0.2725	0.2430
80Ne_S281	110	0.8374	1.0492	5.4421	1.0022	0.5053	2.7678	0.3318	0.2645
80Ne_S282	110	0.9136	1.1539	6.9024	1.1169	0.5405	3.0474	0.3346	0.2834
80Ne_S283	110	0.9220	1.1443	9.1096	1.1140	0.5679	2.9998	0.2940	0.2641
80Ne_S284	110	0.8730	1.0847	7.4333	1.0418	0.5404	2.8350	0.3107	0.2698
80Ne_S285	120	0.7444	1.0111	4.1807	0.9078	0.3905	2.6587	0.2632	0.2500
80Ne_S286	120	0.8016	1.1020	5.1044	0.9754	0.4132	2.8839	0.2927	0.2610
80Ne_S287	120	0.7970	1.0511	4.5418	0.9603	0.4379	2.7871	0.2776	0.2303
80Ne_S288	120	0.7797	1.0250	4.2709	0.9302	0.4310	2.7251	0.2360	0.2139
80Ne_S289	120	0.7319	0.9799	2.9004	0.8918	0.3841	2.6150	0.2531	0.2367
80Ne_S290	120	0.7630	1.0274	3.3171	0.9316	0.3971	2.7532	0.2524	0.2345
80Ne_S291	120	0.7312	0.9669	2.6589	0.8950	0.3878	2.6144	0.2282	0.2252
80Ne_S292	120	0.7729	1.0971	11.1570	0.9351	0.4024	2.7746	0.2770	0.2487
80Ne_S293	120	0.7286	0.8802	1.7578	0.8856	0.4334	2.4519	0.2155	0.2057
80Ne_S294	120	0.7090	0.8594	1.6884	0.8586	0.4206	2.3855	0.1982	0.1943
80Ne_S295	120	0.7110	0.8798	2.0450	0.8680	0.4131	2.4300	0.2239	0.2147
80Ne_S296	120	0.7428	0.9203	2.0718	0.9080	0.4273	2.5543	0.2023	0.1965

References

1. Cheng K.P.S. and Yu C. A Study of Compact Spun Yarns. *Textile Research Journal* 73 (4): 345-349 (2003).
2. Krifa M. and Ethridge M D. Compact Spinning Effect on Cotton Yarn Quality: Interactions with Fiber Characteristics. *Textile Research Journal* 76 (5): 388-399 (2006).
3. Miao M., Cai Z. and Zhang Y. Influence of Machine Variables on Two-Strand Yarn Spinning Geometry. *Textile Research Journal* 63 (2): 116-120 (1993).
4. Zhang L. and He J. Geometry Condition for Optimal Two-strand Yarn Spinning Part I: Sirospun. *Textile Research Journal* 79 (3): 243-246 (2009).
5. Najar S.S., Khan Z. and Wang X. TheN Solo-Siro Spun Process for Worsted Yarns. *Journal of the Textile Institute* 97: 205-210 (2006).
6. Chang L. and Wang X. Comparing the Hairiness of Solospun and Ring Spun Worsted Yarns. *Textile Research Journal* 73:640-644 (2003).
7. Gharahaghaji A.A., Zargar E.N., Ghane M. and Hossaini A. Cluster-spun Yarn a New Concept in Composite Yarn Spinning. *Textile Research Journal* 80: 19-24 (2010).
8. Xu B.G. and Tao X.M. Techniques for Torque Modification of Singles Ring Spun Yarns. *Textile Research Journal* 78 (10): 869-879 (2008).
9. Xu B., Tao X. and Leung C.S. A Comparative Study of Knitted Fabrics and Garments Produced by the Modified Low Twist and Conventional Ring Yarns.

References

- Fibers and Polymers 11(6): 899-904 (2010).
10. Tang H.B., Xu B.G. and Tao X.M. A New Analytical Solution of the Twist Wave Propagation Equation with Its Application In a Modified Ring Spinning System. Textile Research Journal 80(7): 636-641 (2010).
 11. Tang H.B., Xu B.G., Tao X.M. and Feng J. Mathematical Modeling and Numerical Simulation of Yarn Behavior in a Modified Ring Spinning System. Applied Mathematical Modelling 35 (1): 139-151 (2011).
 12. Lord P.R. The Structure of Open-end Spun Yarn. Textile Research Journal 41: 778-784 (1971).
 13. Bennett J.M. and Postle R. A Study of Yarn Torque and Its Dependence on the Distribution of Fiber Tensile Stress in the Yarn. 1. Theoretical Analysis. Journal of the Textile Institute 70: 121-132 (1979).
 14. Bennett J.M. and Postle R. A Study of Yarn Torque and its Dependence on the Distribution of Fiber Tensile Stress in the Yarn. Part II: Experimental. Journal of the Textile Institute 70: 133-141 (1979).
 15. Fujino K., Uno M., Shiomi A., Yanggawa Y., and Kitada Y. A Study on the Twist Irregularity of Yarn Spun on the Ring Spinning Frame. Journal of the Textile Machinery Society of Japan 8 (3): 51-62 (1962).
 16. Pavlov Y.V. Structural Transformations in the Fiber Assembly at the Twist Threshold at the Instant of Rupture. Technology of the textile industry U.S.S.R. 4: 57-63 (1965).
 17. El-Shiekh A. "On the Mechanics of Fiber Migration". PhD Thesis, Massachusetts

- Institute of Technology, 1965.
18. Huang X.C. "Prediction of Yarn Breakage Rates". PhD Thesis, University of Leeds, 1991.
 19. Krause H.W., Soliman H.A. and Tian J.L. Investigation of the Strength of the Spinning Triangle in Ring Spinning. *Melliand Textilberichte* 72: 499-502 (1991).
 20. Najar S.S. "An Analysis of the Twist Triangle in Ring Spinning". PhD Thesis, University of New South Wales, Australia, 1996.
 21. Hua T. "Production, Properties and Structures of Short Staple Low Torque Singles Ring Yarn for Weaving". PhD Thesis, The Hong Kong Polytechnic University, 2006.
 22. Hua T., Tao X.M., Cheng K.P.S. and Xu B.G. Effects of Geometry of Ring Spinning Triangle on Yarn Torque Part I: Analysis of Fiber Tension Distribution. *Textile Research Journal* 77 (11): 853-863 (2007).
 23. Hua T., Tao X.M., Cheng K.P.S. and Xu B.G. Effects of Geometry of Ring Spinning Triangle on Yarn Torque: Part II: Distribution of Fiber Tension within a Yarn and Its Effects on Yarn Residual Torque. *Textile Research Journal* 80 (2): 116-123 (2010).
 24. Hajiani F., Jeddi A.A. A. and Gharehaghaji A. A. An Investigation on the Effects of Twist on Geometry of the Electrospinning Triangle and Polyamide 66 Nanofiber Yarn Strength. *Fibers and Polymers* 13(2): 244-252 (2012).
 25. Feng J., Xu B.G., Tao X.M. and Hua T. Theoretical Study of a Spinning Triangle with Its Application in a Modified Ring Spinning System. *Textile Research*

References

- Journal 80 (14): 1456-1464 (2010).
26. Su X.Z., Gao W.D., Liu X.J., Xie C.P. and Xu B.J. Theoretical Study of Fiber Tension Distribution at the Spinning Triangle. *Textile Research Journal* 83 (16): 1728-1739 (2013).
 27. Liu X., Su X. and Zhang H. Theoretical Study of Spinning Triangle with Fiber Concentric Circular Cones Arrangement at Front Nip Line. *The Journal of The Textile Institute*: 1-6 (2014), DOI: 10.1080/00405000.2014.922245.
 28. Badehnoush A. and Yazdi A.A. Real-time Yarn Evenness Investigation via Evaluating Spinning Triangle Area Changes. *Journal of the Textile Institute* 103 (8): 850-861 (2012).
 29. Alagha M.J., Oxenham W. and Iypc C. The Use of an Image Analysis Technique for Assessing the Structural Parameters of Friction Spun Yams. *Journal of the Textile Institute* 85: 383-388 (1993).
 30. Basal G. and Oxenham W. Effect of Some Parameters on the Structure and Properties of Vortex Spun Yarn. *Textile Research Journal* 76: 492-9 (2006).
 31. Morton W.E. and Yen K.C. The Arrangement of Fibres in Fibro Yarns. *Journal of the Textile Institute* 43: T60-6 (1952).
 32. Yang K., Tao X.M., Xu B.G., and Lam K.C. Structure and Properties of Low Twist Short-staple Singles Ring Spun Yarns. *Textile Research Journal* 77 (9): 675-685 (2007).
 33. Kato H., Konda F., Okamura M., Merati, A.A. and Saeki H. Yarn Tail Structure in Friction Spinning. *Textile Research Journal* 69 (3): 214-219 (1999).

34. Soltani P. and Johari M.S. A Study on Siro-, Solo-, Compact-, and Conventional Ring-spun Yarns. Part I: Structural and Migratory Properties of the Yarns. *Journal of the Textile Institute* 103 (6): 622-628 (2011).
35. Ganesan S. and Ramakrishnan G. Fiber Migration in Compact Spun Yarns. <http://spinningarticles.freehostia.com/FIBRE%20MIGRATION%20IN%20COMPACT%20SPUN%20YARNS.htm> (March 2015).
36. Basal G. and Oxenham W. Comparison of Properties and Structures of Compact and Conventional Spun Yarns. *Textile Research Journal* 76: 567-75 (2006).
37. Ghosh A., Ishtiaque S.M. and Rengasamy R.S. Analysis of Spun Yarn Failure. Part I: Tensile Failure of Yarns as a Function of Structure and Testing Parameters. *Textile Research Journal* 75 (10): 731-740 (2005).
38. Hearle J.W.S and Gupta G.S. Migration of Fibres in Yarns, Part-III: A Study of Migration in a Staple Fibre Rayon Yarn. *Textile Research Journal* 35: 788-95 (1965).
39. Grishanov S.A., Harwood R.J. and Bradshaw M.S. A Model of Fibre Migration in Staple-fibre Yarn. *Journal of the Textile Institute. Part 1, Fibre science and textile technology* 90(3): 298-321 (1999).
40. Huh Y., Kim Y.R. and Oxenham W. Analyzing Structural and Physical Properties of Ring, Rotor, and Friction Spun Yarns. *Textile Research Journal* 72: 156-63 (2002).
41. Ishtiaque S.M., Kumar A., Das A. and Tholeti P.B. Development of Image Processing based System to Study Yarn Structure during Extension. *Journal of the*

References

- Textile Institute. 101 (8): 687-698 (2010).
42. Kumar A., Ishtiaque S.M. and Das A. Effect of Yarn Extension on Migration Parameters of Fibres in Yarns. *Journal of the Textile Institute* 103 (5): 575-581 (2011).
 43. Kumar A., Ishtiaque S.M. and Das A. Influence of Yarn Extension on Longitudinal Structural Characteristics of Fibres. *Journal of the Textile Institute* 103 (8): 836-843 (2011).
 44. Guo Y., Tao X.M., Xu B.G., Choi K.F., Hua T. and Wang S.Y. A Continuous Measurement System for Yarn Structures by an Optical Method. *Measurement Science and Technology* 21: 115706 (2010).
 45. Huh Y., Kim Y.R. and Ryu W.Y. Three-dimensional Analysis of Migration and Staple Yarn Structure. *Textile Research Journal* 71: 81-9 (2001).
 46. Riding G. Filament Migration in Single Yarns. *Journal of the Textile Institute* 55: T9-17 (1964).
 47. Zou Z., Cheng L., Xi B., Luo Y. and Liu, Y. Investigation of Fiber Trajectory Affected by Some Parameter Variables in Vortex Spun Yarn. *Textile Research Journal*, 0040517513509873 (2014).
 48. Zhang H.W., Chen D.S. and Wang Y.B. Fiber Migration and Twist Radial Distribution in Rotor Spun Yarns. *Textile Research Journal* 73: 945-8 (2003).
 49. Fu P., Cheng L., Wang S. and Zhou Y. Hi-scope Video Microscope System for Studies on Structure of Compact Spun Yarns. *Melliand China* 3: 27-32 (2006).
 50. Primentas A. and Iype C. The Configuration of Textile Fibers in Staple Yarns.

- Journal of Textile and Apparel, Technology and Management 1 (4): 1-8 (2001).
51. ASTM D 2255/D2255M-09. "Standard Test Method for Grading Yarn for Appearance", 2009.
 52. Semnani D., Latifi M., Tehran M.A., Pourdeyhimi B. and Merati A.A. Grading of Yarn Surface Appearance Using Image Analysis and an Artificial Intelligence Technique. *Textile Research Journal* 76 (3): 187-196 (2006).
 53. Semnani D., Latifi M., Tehran M.A., Pourdeyhimi B. and Merati A.A. Effect of Yarn Appearance on Apparent Quality of Weft Knitted Fabric. *The Journal of the Textile Institute* 96 (5): 295-301 (2005).
 54. Semnani D., latifi M., Tehran M.A., Pourdeyhimi B. and Merati A.A. Development of Appearance Grading Method of Cotton Yarns for Various Types of Yarns. *Research Journal of Textile and Apparels* 9 (4): 86-93 (2005).
 55. Liang Z., Xu B., Chi Z. and Feng D. Intelligent Characterization and Evaluation of Yarn Surface Appearance using Saliency Map Analysis, Wavelet Transform and Fuzzy ARTMAP Neural Network. *Expert Systems with Applications* 39 (4): 4201-4212 (2012).
 56. Liang Z., Xu B., Chi Z. and Feng D.D. Relative Saliency Model over Multiple Images with an Application to Yarn Surface Evaluation, *IEEE Transactions on Cybernetics* 44 (8): 1249-1258 (2014).
 57. Lien H.C. and Lee. Applying Pattern Recognition Principles to Grading Textile Yarns. *Textile Research Journal* 72 (4): 320 (2002).
 58. Amin A.E. A Novel Classification Model for Cotton Yarn Quality based on

References

- Trained Neural Network using Genetic Algorithm. *Knowledge-Based Systems* 39: 124-132 (2012).
59. Uster® CLASSIMAT 5, The yarn classification system. http://www.uster.com/fileadmin/customer/Instruments/Brosch%C3%BCren/en_USTER_CLASSIMAT_5_web_brochure.pdf (March 2015).
60. Rong G.H., Slater K.L. and Fei R.C. The Use of Cluster Analysis for Grading Textile Yarns. *Journal of the Textile Institute* 85 (3): 389-396 (1994).
61. Bonneau D., Gordon Jr K.W., Lawson J.B. and Nevel A. System for Electronically Grading Yarn. U.S. Patent No. 5541734 (1996).
62. Bonneau D., Gordon Jr K.W., Lawson J.B. and Nevel A. System and Method for Electronically Displaying Yarn Qualities. U.S. Patent No. 5570188 (1996).
63. Bonneau D., Gordon Jr K.W. and Nevel A. System and Method for Electronically Evaluating Predicted Fabric Qualities. U.S. Patent No. 6130746 (2000).
64. Nevel A., Gordon Jr K.W. and Bonneau D. System and Method for Electronically Evaluating Predicted Fabric Qualities. U.S. Patent No. 6741726 (2004).
65. Yarn Analysis System, <http://www.lawsonhemphill.com/lh-481-yarn-analysis-system.html>. (September 2014)
66. Madenci E. and Guven I. "The Finite Element Method and Applications in Engineering Using ANSYS", Springer, New York, N.Y., 2006.
67. Pan J. and Tompkins W.J. A Real-time QRS Detection Algorithm. *IEEE Trans Biomed Eng*, BME-32 (3): 230-236 (1985).

68. Sidek K.A. and Khalil I. Enhancement of Low Sampling Frequency Recordings for ECG Biometric Matching using Interpolation. *Computer Methods and Programs in Biomedicine* 109(1): 13-25 (2013).
69. <http://www.rieter.com> (December 2012).
70. Xu B.G. and Tao X.M. Integrated Approach to Dynamic Analysis of Yarn Twist Distribution in Rotor Spinning Part I: Steady State. *Textile Research Journal* 73 (1): 79-89 (2003).
71. Guo B., Tao X. and Lo T. A Mechanical Model of Yarn Twist Blockage in Rotor Spinning. *Textile Research Journal* 70: 11 (2000).
72. Long J., Xu B. and Tao X. A Nonlinear Dynamic Model for Periodic Motion of Slender Threadline Structures. *CMES* 72 (4): 273-297 (2011).
73. Yang R.H., Wang S.Y. Determination of the Convergent Point in the Rotor-spun Composite Yarn Spinning Process. *Textile Research Journal* 79: 555 (2009).
74. <http://www.rieter.com/en/rikipedia/articles/alternative-spinning-systems/the-various-spinning-methods/open-end-spinning-processes/the-basic-principle-of-yarn-formation/> (December 2012).
75. Lord P.R. "Handbook of Yarn Production". Cambridge: Woodhead Publishing: Textile Institute; Boca Raton: CRC Press, 2003.
76. Zhang M., Atkinson K.R. and Baughman, R.H. Multifunctional Carbon Nanotube Yarns by Downsizing an Ancient Technology. *Science* 306: 1358-1361 (2004).
77. Jia J., Zhao J., Xu G., Di J., Yong Z., Tao Y., Fang C., Zhang Z., Zhang X., Zheng L. and Li Q. A Comparison of the Mechanical Properties of Fibers Spun From

References

- Different Carbon Nanotubes. *Carbon* 49: 1333-1339 (2011).
78. Tran C.D., Humphries W., Smith S.M., Huynh C. and Lucas S. Improving the Tensile Strength of Carbon Nanotube Spun Yarns using a Modified Spinning Process. *Carbon* 47: 2662-2670 (2009).
79. Ali U., Zhou Y., Wang X. and Lin T. Direct Electrospinning of Highly Twisted, Continuous Nanofiber Yarns. *Journal of the Textile Institute* 103: 80-88 (2012).
80. Timoshenko S.P. "Theory of Elastic Stability". McGraw-Hill, New York, 1961.
81. Jiang X.Y., Hu J.L., Cheng K.P.S. and Postle R. Determining the Cross-Sectional Packing Density of Rotor Spun Yarns. *Textile Research Journal* 75: 233 (2005).
82. Zheng S., Zou Z., Shen W. and Cheng L. A Study of the Fiber Distribution in Yarn Cross Section for Vortex-spun Yarn. *Textile Research Journal* 82 (15): 1579-1586 (2012).
83. Chiu S., Chen J. and Lee J. Fiber Recognition and Distribution Analysis of PET/Rayon Composite Yarn Cross Sections Using Image Processing Techniques. *Textile Research Journal* 69 (6): 417-422 (1999).
84. Chiu S. and Liaw J. Fiber Recognition of PET/Rayon Composite Yarn Cross-sections Using Voting Techniques. *Textile Research Journal* 75 (5): 442-448 (2005).
85. Wan Y., Yao L., Zeng P. and Xu B. Shaped Fiber Identification Using a Distance-Based Skeletonization Algorithm. *Textile Research Journal* 80 (10): 958-968 (2010).
86. Xu B. and Huang Y. Image Analysis for Cotton Fibers Part II: Cross-Sectional

- Measurements. *Textile Research Journal* 74 (5): 409-416 (2004).
87. Levin A., Zomet A., Peleg S. and Weiss Y. Seamless Image Stitching in the Gradient Domain. *ECCV 2004, Lecture Notes in Computer Science* 3024: 377-389 (2004).
88. Goshtasby A.A. "Image Registration: Principles, Tools and Methods." Springer Science & Business Media. (2012).
89. Lowe D.G. Distinctive Image Features From Scale-invariant Keypoints. *International Journal of Computer Vision* 60 (2): 91-110 (2004).
90. Juan L. and Gwun O. SURF Applied in Panorama Image Stitching. *Image Processing Theory, Tools and Applications*: 495-499 (2010).
91. Yang F., Wei L.L., Zhang Z.W. and Tang H.M. Image Mosaic based on Phase Correlation and Harris Operator. *Journal of Computational Information Systems* 8 (6): 2647-2655 (2012).
92. Hugin - Panorama Photo Stitcher. <http://hugin.sourceforge.net/> (August 2014).
93. Mills A. and Dudek G. Image Stitching with Dynamic Elements. *Image Vision Comput* 27 (10): 1593-1602 (2009).
94. <http://www.arcsoft.com/topics/panorama-maker/stitch-video-frames.html> (August 2011).
95. Ozkaya Y.A., Acar M. and Jackson M.R. Digital Image Processing and Illumination Techniques for Yarn Characterization. *Journal of Electronic Imaging* 14 (2): 023001 (2005)

References

96. Xu B.G., Murrells C.M. and Tao X.M. Automatic Measurement and Recognition of Yarn Snarls by Digital Image and Signal Processing Methods. *Textile Research Journal* 78: 439-456 (2008).
97. Xu B.G., Tao X.M. and Murrells C.M. Evaluation of a Digital Image-signal Approach on the Automatic Measurement of Cotton Yarn Snarls. *Textile Research Journal* 80: 1151-1159 (2010).
98. Murrells C.M., Tao X.M., Xu B.G. and Cheng K.P.S. An Artificial Neural Network Model for the Prediction of Spirality of Fully Relaxed Single Jersey Fabrics. *Textile Research Journal* 79 (3): 227-234 (2009).
99. Fabijańska A. Yarn Image Segmentation using the Region Growing Algorithm. *Measurement Science and Technology* 22: 114024 (2011).
100. Fabijańska A. and Jackowska-Strumiłło L. Image Processing and Analysis Algorithms for Yarn Hairiness Determination. *Machine Vision and Applications* 23 (3): 527-540 (2012).
101. Fabijanska A. A Survey of Thresholding Algorithms on Yarn Images. *Perspective Technologies and Methods in MEMS Design (MEMSTECH), 2010 Proceedings of VIth International Conference: 23-26, Polyana-Svalyava (Zakarpattya), Ukraine, April 2010.*
102. Cybulska M. Assessing Yarn Structure with Image Analysis Methods. *Textile Research Journal* 69(5): 369-373 (1999).
103. Ozkaya Y.A., Acar M., Jackson M.R. Hair Density Distribution Profile to Evaluate Yarn Hairiness and its Application to Fabric Simulations. *Journal of*

- Textile Institute 98 (6): 483–490 (2007).
- 104.Ozkaya Y.A., Acar M., Jackson M.R. Simulation of Photosensor-based Hairiness Measurement using Digital Image Analysis. *Journal of Textile Institute* 99 (2): 93-100 (2008).
- 105.Chimeh M.Y., Tehran M.A., Latifi M. and Mojtahedi M.R.M. Characterizing Bulkiness and Hairiness of Air-jet Textured Yarn using Imaging Techniques. *Journal of Textile Institute* 96 (4): 251-255 (2005).
- 106.Ozkaya Y.A., Acar M., Jackson M.R. Yarn Twist Measurement using Digital Imaging. *Journal of Textile Institute* 101 (2): 91–100 (2010).
- 107.Guha A., Amarnath C., Pateria S. and Mittal R. Measurement of Yarn Hairiness by Digital Image Processing. *Journal of Textile Institute* 99 (6): 1754-2340 (2009).
- 108.Jasper W.J., Gunay M. and Suh M.W. Measurement of Eccentricity and Twist in Spun and Plied Yarns. *Journal of the Textile Institute* 96 (2): 93-97 (2005).
- 109.Carvalho V., Belsley M., Vasconcelos R. and Soares F. Yarn Hairiness and Diameter Characterization using a CMOS Line Array. *Measurement* 41 (10): 1077-1092 (2008).
- 110.Carvalho V., Belsley M., Vasconcelos R. and Soares F. A Comparison of Mass Parameters Determination using Capacitive and Optical Sensors. *Sensors and Actuators A* 167: 327-331 (2011).
- 111.Carvalho V., Cardoso P., Belsley M., Vasconcelos R. and Soares F. Yarn Irregularity Parameterisation using Optical Sensors. *Fibres & Textiles in Eastern*

References

- Europe 17 (1): 26-32 (2009).
112. Boykov Y.Y and Jolly M.P. Interactive Graph Cuts for Optimal Boundary & Region Segmentation of Objects in ND Images. Eighth IEEE International Conference on Computer Vision (ICCV 2001), Proceedings 1: 105-112 (2001).
113. Alagha M.J., Oxenham W. and Iype C. The Use of An Image Analysis Technique for Assessing the Structural Parameters of Friction Spun Yarns. . Journal of the Textile Institute 85(3): 383–388 (1994).
114. Yadav V.K., Joshi S.D., Ishtiaque S.M. and Chatterjee, J.K. Yarn Fault Classification: a Signal Processing Approach using Multiple Projections. The Journal of The Textile Institute, 106(2): 197-205 (2015).
115. Nateri A.S., Ebrahimi F. and Sadeghzade N. Evaluation of Yarn Defects by Image Processing Technique. Optik-International Journal for Light and Electron Optics 125(20): 5998-6002 (2014).
116. Kim H.J., Kim J.S., Lim J.H. and Huh Y. Detection of Wrapping Defects by a Machine Vision and its Application to Evaluate the Wrapping Quality of the Ring Core Spun Yarn. Textile Research Journal 79 (17): 1616-1624 (2009).
117. Lien H.C. and Lee S. A Method of Feature Selection for Textile Yarn Grading Using the Effective Distance Between Clusters. Textile Research Journal 72 (10): 870-878 (2002).
118. Zhou X. Study on Yarn Blackboard by Digital Image Processing Method. Modern Applied Science 1 (4): 107-111 (2007).
119. Liu J., Li Z., Lu Y. and Jiang H. Visualisation and Determination of the

- Geometrical Parameters of Slub Yarn. *Fibres & Textiles in Eastern Europe* 18 (1): 31-35 (2010).
120. Pan R., Gao W., Liu J. and Wang H. Recognition the Parameters of Slub-yarn Based on Image Analysis. *Journal of Engineered Fibers and Fabrics* 6 (1): 25-30 (2011).
121. Rong G.H. and Slater K. Analysis of Yarn Unevenness by Using a Digital Signal Processing Technique. *Journal of the Textile Institute* 86 (4): 590-599 (1995).
122. Carpenter G.A., Grossberg S., Markuzon N., Reynolds J.H. and Rosen D.B. Fuzzy ARTMAP: An Adaptive Resonance Architecture for Incremental Learning of Analog Maps. In *International joint conference on neural networks (IJCNN 1992)*: 309-314 (1992).
123. Itti L., Koch C. and Neibur E. A Model of Saliency-Based Visual Attention for Rapid Scene Analysis. *IEEE Transactions on Pattern Analysis and Machine Intelligence* 20 (11): 1254-1259 (1998).
124. Toet A. Computational versus psychophysical bottom-up image saliency: A comparative evaluation study. *IEEE Transactions on Pattern Analysis and Machine Intelligence* 33(11): 2131-2146 (2011).
125. Hou X. and Zhang L. Saliency Detection: A Spectral Residual Approach. *IEEE Conference on Computer Vision and Pattern Recognition (CVPR)*: 1-8 (June 2007).
126. Hou X., Harel J. and Koch C. Image Signature: Highlighting Sparse Salient Regions. *IEEE Transactions on Pattern Analysis and Machine Intelligence* 34(1):

References

- 194-201 (2012).
- 127.Zhang L., Tong M.H., Marks T.K., Shan H. and Cottrell G.W. SUN: A Bayesian Framework for Saliency using Natural Statistics. *Journal of Vision*, 8 (7): 32 (2008).
- 128.Riche N., Mancas M., Duvinage M., Mibulumukini M., Gosselin B. and Dutoit T. Rare2012: A Multi-Scale Rarity-Based Saliency Detection with Its Comparative Statistical Analysis. *Signal Processing: Image Communication* 28 (6): 642-658 (2013).
- 129.Bruce N. and Tsotsos J. Saliency Based on Information Maximization. *Advances in Neural Information Processing Systems*: 155-162 (2005).
- 130.Bruce N.D.B. and Tsotsos J.K. Saliency, Attention, and Visual Search: An Information Theoretic Approach. *Journal of Vision* 9 (3): 5, 1-24 (2009).
- 131.Harel J., Koch C. and Perona P. Graph-Based Visual Saliency. *Advances in Neural Information Processing Systems*: 545-552 (2006).
- 132.Walther D. and Koch C. Modeling Attention to Salient Proto-Objects. *Neural Networks* 19 (9): 1395-1407 (2006).
- 133.Cheng M.M., Zhang G.X., Mitra N.J., Huang X. and Hu S.M. Global Contrast Based Salient Region Detection. *Computer Vision and Pattern Recognition (CVPR)*: 409-416 (June 2011).
- 134.Hou X. and Zhang L. Dynamic Visual Attention: Searching for Coding Length Increments. *Advances in Neural Information Processing Systems*: 681-688 (2009).

- 135.Zhang L. Tong M.H. and Cottrell G.W. SUNDAY: Saliency Using Natural Statistics for Dynamic Analysis of Scenes. Proceedings of the 31st Annual Cognitive Science Conference. Cambridge, MA: AAAI Press: 2944-2949 (2009).
- 136.Seo H.J. and Milanfar P. Static and Space-Time Visual Saliency Detection by Self-Resemblance. *Journal of Vision* 9(12): 15 (2009).
- 137.Itti L. and Baldi P. Bayesian Surprise Attracts Human Attention. *Vision Research* 49(10): 1295-1306 (2009).
- 138.Hearle J.W.S., Grosberg P. and Backer S. "Structural Mechanics of Fibers, Yarns, and Fabrics". Wiley-Interscience, New York, 1969.
- 139.Grosberg P. and Plate D.E.A. Capstan Friction for Polymer Monofilaments with Rigidity. *Journal of the Textile Institute* 60: 268-283 (1969).
- 140.Emmanuel A. and Plate D.E.A. An Alternative Approach to Two-fold Weaving Yarn. Part II: the Theoretical Model. *Journal of the Textile Institute* 73 (3): 107-116 (1982).
- 141.Morton W.E. and Hearle J.W.S. "Physical Properties of Textile Fibres". Textile Institute, Manchester, U.K., 1993.
- 142.Zhu H., Wu F.L., Han L.Y. and Feng P.Q. "Textile Material". Textile Industry Press, Beijing, 1987.
- 143.Postle R., Burton P. and Chaikin M. The Torque in Twisted Singles Yarns. *Journal of the Textile Institute Transactions* 55 (9): T448-T461 (1964).
- 144.Theory Reference, ANSYS Release 9.0, Help System, ANSYS, Inc.

References

145. Schonung B. First Results with Individual Motor-Driven Ring Spindles, Lecture on the Occasion of the 4th Ring Spinning Colloquium on Oct. 25, 1989 in Enningen U. A. near Reutlingen, SKF Report, 13-17 (1989).
146. Dunell B.A. and Dillon J.H. The Measurement of Dynamic Modulus and Energy Losses in Single Textile Filaments Subjected to Forced Longitudinal Vibrations. *Textile Research Journal* 21 (6): 393-403 (1951).
147. Zorowski C.F. and Murayama T. Wave Propagation and Dynamic Modulus in Continuous-Filament Twisted Yarns Part I: Low Initial Yarn Tension. *Textile Research Journal* 37 (10): 852-860 (1967).
148. Petterson D.R., Stewart G.M., Odell F.A. and Maheux R.C. Dynamic Distribution of Strain in Textile Materials Under High-Speed Impact: Part I: Experimental Methods and Preliminary Results on Single Yarns. *Textile Research Journal* 30 (6): 411-421 (1960).
149. Fujino K., Kawai H. and Horino T. Experimental Study of the Viscoelastic Properties of Textile Fibers Dynamic Measurements from Subsonic to Supersonic Frequencies. *Textile Research Journal* 25 (8): 722-737 (1955).
150. Vangheluwe L. Relaxation and Inverse Relaxation of Yarns After Dynamic Loading. *Textile Research Journal* 63 (9): 552-556 (1993).
151. Muller S., Kastner M., Brummund J. and Ulbricht V. A Nonlinear Fractional Viscoelastic Material Model for Polymers. *Computational Materials Science* 50 (10): 2938-2949 (2011).
152. Christensen R.M. "Theory of Viscoelasticity". Dover Publications, Mineola, N.Y.,

- 2003.
153. Lyons W.J. Dynamic Properties of Filaments, Yarns, and Cords at Sonic Frequencies. *Textile Research Journal* 19 (3): 123-135 (1949).
154. Lawrence C.A. "Fundamentals of Spun Yarn Technology ". Boca Raton, FL: CRC Press, 2003.
155. Feng J., Xu B.G. and Tao X.M. Dynamic Analysis of Yarn Twist Propagation and Variation in a Modified Low Torque Ring Spinning System. *Proceedings of the 10th Asian Textile Conference*: 1-8. Ueda, Japan, September 2009.
156. Chung J. and Hulbert G.M. A Time Integration Algorithm for Structural Dynamics with Improved Numerical Dissipation: The Generalized- α Method. *Journal of Applied Mechanics* 60: 371 (1993).
157. Yeh Y.C. and Wang W.J. QRS Complexes Detection for ECG Signal: The Difference Operation Method. *Computer methods and programs in biomedicine* 91(3): 245-254 (2008).
158. http://en.wikipedia.org/wiki/QRS_complex (September 2012)
159. Morton W.E. The Arrangement of Fibers in Single Yarns. *Textile Research Journal* 26(5): 325-331 (1956).
160. Fourier Transform. <http://www.svi.nl/FourierTransform>. (September 2014).
161. Marques O. "Practical image and video processing using MATLAB". John Wiley & Sons, 2011.
162. Singh D. "Fundamentals Of Optics." New Delhi, 2010.

References

163. Specht D.F. Probabilistic Neural Networks for Classification, Mapping, or Associative Memory. IEEE Conference on Neural Network. Vol. I: 525-532, San Diego, July 1988.
164. Specht D.F. Probabilistic Neural Networks, Neural Networks 3: 109-118 (1990).
165. Wasserman P.D. "Advanced Methods in Neural Computing". John Wiley & Sons, Inc., 1992.
166. Guler I. and Ubeyli E.D. Multiclass Support Vector Machines for EEG-signals Classification. IEEE Transactions on Information Technology in Biomedicine 11(2): 117-126 (2007).
167. Probabilistic Neural Networks. <http://www.mathworks.com/help/nnet/ug/probabilistic-neural-networks.html> (September 2014).
168. Saville B.P. "Physical Testing of Textiles". Elsevier, 1999.
169. Skewness. <http://www.mathworks.com/help/stats/skewness.html> (April 2014).
170. Kurtosis. <http://www.mathworks.com/help/stats/kurtosis.html> (April 2014).
171. Entropy. <http://www.mathworks.com/help/images/ref/entropy.html> (April 2014).
172. Qian Y., Liang Y., Li M., Feng G. and Shi X. A Resampling Ensemble Algorithm for Classification of Imbalance Problems. Neurocomputing 143: 57-67, 2014.
173. Fatma G.N. and Elif D.U. Multiclass Support Vector Machines for EEG-signals Classification. IEEE Transactions on Information Technology in Biomedicine 11(2): 117-126 (2007).